Development of Advanced High Modulus Steels for Automotive Applications

Sulayman Khan

University of Sheffield

A thesis submitted for the degree of Doctor of Philosophy

in the

School of Chemical, Materials and Biological Engineering

2024

Abstract

The increasing demand for high-modulus steels in automotive applications is driven by the need for improved mechanical performance, such as strength and stiffness while maintaining lightweight properties for fuel efficiency. This thesis evaluates the potential of two processing techniques, vacuum induction melting (VIM) and field-assisted sintering technology (FAST), for the development of high-modulus steels through the incorporation of titanium diboride (TiB_2) as a ceramic reinforcement in a microalloyed steel (MA) matrix. The MA steel was first fabricated through VIM and subjected to thermomechanical processing (TMP), including hot rolling and plane strain compression (PSC), to refine the alloy and study phase transformations under different cooling rates. Through electron backscattered diffraction (EBSD), confirmation of prior austenite grain boundaries (PAGBs) was found in MA samples quenched from recrystallisation-stop and limit temperatures. MA steel cooled at 0.1˚C/s exhibited a pro-eutectoid phase and pearlite. The introduction of TiB_2 into the MA steel matrix, in 5 and 7.5% volume fractions, demonstrated the positive effects of grain pinning mechanisms and martensitic transformation at fast cooling rates (30˚C/s). At slower cooling rates (0.1˚C/s), differences between the 5MASC and 7.5MASC phase transformations were observed, though the grain pinning effects of TiB_2 were evident. Tensile testing and resonant frequency damping analysis (RFDA) showed a significant improvement in stiffness, with Young's modulus increasing from 208 GPa for MA steel to 239 GPa for 7.5MASC. FAST was also explored as a novel powder metallurgy route to manufacture high-modulus steels. Using S4140 as a baseline material, the FAST process demonstrated its ability to consolidate powder effectively, although additions of TiB_2 impeded full diffusion bonding, resulting in incomplete densification and brittle fracture behaviour in the MASC consolidated sample. Microscopy analysis confirmed the role of TiB_2 as a diffusion barrier. FAST demonstrated improved densification and diffusion bonding with increasing dwell time, temperature, and pressure but issues of phase inhomogeneity in larger samples and porosity were observed.

Acknowledgements

My gratitude first goes to Almighty Allah, the Most Merciful and Most Generous. The completion of this PhD would not be possible without your strength and guidance, and I will always be in debt. Alhamdullilah.

To my loving Mum and Dad, I cannot thank you enough for everything you have given me. Without your support, this PhD would have taken a lot longer to complete. Mum, there truly is nobody like you and I think people are surprised to find out that you are my mum. It is incredible that you are in the position you are in today, I always look up to you and feel inspired when I see how far you have come and how far you have yet to go. Unfortunately, I can't match your IQ and I know you like hearing that, but I can at least try. Dad, you are the foundation of our family and have tirelessly supported me to the point where I think 'ok that's too much'… I feel so blessed to have you in my life. Both of you, never change.

To Bajaan, Baaji and Hurjaan, I thank you all for making my life challenging with the sibling rivalry we have. Why are we all lunatics when we are together? And why do we constantly annoy and make fun of each other? Can you guys stop bullying me because I'm the youngest and most talented, please? On a serious note, having your company and support has gotten me through this PhD, and I really do mean that. I cherish our memories of growing up more than you think. I love you guys.

To Professor Eric J. Palmiere, as my primary supervisor, I cannot express how thankful I am for your kindness and support throughout these 4 years, how time flies. Through the ups and downs of this PhD, your guidance and wisdom have allowed me to complete this work. We have talked professionally and as friends, and I will never forget the motivation and drive you passed on to me. Your knowledge on steel metallurgy is incredible and I would be lucky to have half of that one day. I'm not sure I will meet someone like you again, but I am certainly glad that we went through this journey together. Thank you.

To Professor Martin Jackson, as my secondary supervisor, I would first like to thank you for your knowledge and guidance throughout this PhD. You have always pushed me to further understand my results and look at data from a different perspective. I am so lucky to also be a part of the STAR group that you kindly introduced me to. The research group you have established is full of impressive and talented people and the environment in the office always has a buzz. I will not forget your support and brilliant character. Thank you.

To Dr Ralf Rablbauer, as my industrial supervisor, I greatly appreciate everything you have done for me in the past 4 years. I am incredibly lucky to have been given the opportunity to undertake my research at the VW plant in Wolfsburg for 3 months, it is something I will never forget. As a person, you are extremely nice and an absolute pleasure to be around. Our discussions about life and research always left me feeling happy and uplifted. I also want to thank you for inviting me to your home and lending me your bike even though I struggled to ride it! You have a beautiful home and a lovely family and I thank you for the memories you gave me in Germany. Vielen Dank.

To Dr Yunus Azakli, now a technology platform lead for Materials Discovery and Prototyping, congratulations! Your promotion is undeniably deserved. Where do I begin? Firstly, thank you for everything you have done for me in these 4 years. From casting to sawing to hammering to milling to sandblasting to hot rolling to atomising… I could go on! Without you, this work would not exist. I cannot exaggerate enough how appreciative I am of you. You are like an older brother who always looked after me. Every time I walk into the RDC workshop I look for you because our chats are funny, educational and make my day. Please keep that high energy up and insha' Allah you will achieve more than you can imagine. Teşekkürler.

To Dean Haylock and Neil Hind, I thank you for putting up with me and my problematic samples (mainly me). I do not think you can get more genuine people than you two, and I always loved our chats about life. Cheers!

I thank Sharon Brown for accepting me into the AMS CDT programme at the young age of 21. As a nervous and introverted individual starting a PhD, I had little hope. The work you have done in organising modules and outings to make each cohort feel welcomed is substantial and has not gone unnoticed. Any problem or requirement I have is immediately dealt with by you and I show my sincerest appreciation for this.

To Simba and Milo, my two cats who have been with me since high school, you have seen me make it all the way to a PhD! So I have one thing to say to you… meow!

To those who I have missed out, I honestly apologise. Thank you all for everything.

Table of Contents

List of Figures

List of Tables

1. Introduction

1.1 Background

In the automotive industry, significant efforts are being made to reduce the weight of steel components. Over the last decade, a traditional solution for light-weighting was to use a gauge reduction method which aids manufacturers in producing thin, strong steels through data monitoring and measurements of variables such as tensile properties, temperature of the workpiece, geometric tolerances and the shape of the steel on exit through a cold/hot rolling mill. These gauges can also be used to apply uniform metallic coatings with the aid of strain gauges, data recorders and computer software. An alternative approach is to use a steel matrix composite (SMC) to improve high modulus steel (HMS) and advanced high strength steel (AHSS). Some examples of composite groups are ceramic, carbide, oxide, nitride and boride reinforcement [1]. These exhibit high Young's modulus (E) which can be retained when combined with a low alloy steel. The overall aim of this project is to achieve a high stiffness, high modulus steel with relatively low density using conventional casting and sintering techniques whilst implementing titanium diboride (TiB_2) as a composite reinforcement.

Some examples of automotive parts which use steel are chassis frames (bodies in white, BIW), engine blocks, suspension systems, connecting rods and body panels [2]. Merging a ductile matrix with a stiff composite is ideal but can prove to be technically challenging, as there needs to be thermodynamic stability during fabrication and post-process heat treatments. Borides in particular are highly popular (paired with a transition metal through eutectic solidification) when trying to achieve high strength and stiffness; this will be discussed in detail through literature findings. Ferro-boron (B) is popularly paired with ferro-titanium (Ti) as this can provide equal phase distribution when forming TiB_2 during solidification. Other metals to be studied *in situ* are vanadium and niobium, which are sparsely researched as part of the ceramic composite reinforcement group. In general, these composites work as excellent strengthening particles as there is good interfacial

bonding and a homogeneous microstructure is achieved [3]. Carbides such as TiC have been studied but it has been found that stiffness is not significantly improved compared to the likes of TiB_2 for instance, despite its excellent compatibility with hot rolling [2].

Lightweight component design is of great importance in the automotive industry, with the main goals being to improve fuel efficiency and enhance the dynamic capability of vehicles; these can include acceleration, handling and brake performance. The use of HMSs have been extensively used for the creation of stiff and light automotive components, using less material to achieve equal rigidity and structurally sound components [4]. Thermomechanical processing (TMP) and microalloying are the two main routes used to achieve this. For microalloyed steels in particular, the hardness and strength of the material can be improved based on the composition used. Thermomechanical processing routes such as quenching and tempering will produce excellent grain refinement; however, this route is higher in cost and more time-consuming. Thermomechanical processing, involving controlled rolling and cooling techniques, significantly refines the grain structure of the steel. This grain refinement enhances the mechanical properties, including tensile strength and impact resistance, making the steel more suitable for demanding automotive applications. However, the complexity and cost associated with TMP, including the need for precise temperature control and additional processing steps, can be a limitation for widespread adoption [5].

Microalloyed (MA) steels offer enhanced mechanical properties through the addition of small amounts of alloying elements. These steels are engineered to provide superior strength, toughness, and ductility without the need for extensive heat treatment processes, making them ideal for automotive applications. The key to microalloyed steels lies in the precise addition of alloying elements such as vanadium, niobium, and titanium. These elements play a crucial role in refining the grain structure and controlling the precipitation of carbides and nitrides within the steel matrix. The refinement of grain structure leads to improved mechanical

properties, including higher yield strength and better resistance to wear and fatigue. For instance, vanadium and niobium contribute to the formation of fine precipitates that inhibit grain growth during hot working, resulting in a fine-grained microstructure [6]. MA steels are often produced through controlled TMP, which combines mechanical working and thermal treatment. In manufacturing, TMP typically involves hot rolling followed by controlled cooling, which enhances the steel's toughness and strength by promoting the formation of ferrite and fine pearlite structures. The resulting microstructure is characterised by a fine dispersion of carbides, nitrides and/or carbo-nitrides, which impede dislocation movement and contribute to the steel's high strength and toughness [7].

An SMC is composed of two key elements, a matrix and particle/fibrous reinforcement. The latter is commonly referred to as the secondary phase which is typically a ceramic-based material and is found as particles in volume (vol.) fractions ranging from 5-15%. This differs significantly from an MA steel on the other hand, as it is a base steel with very small additions (<1wt.%) [8] [9] of precious metal which can form precipitates as little as 5nm. An SMC will have superior strength and durability compared to a microalloyed steel, with the possibility to fabricate lightweight components as a solution for weight reduction. However, SMCs are complex in terms of second-phase reactions, the morphology of formed particles in liquid and solid phases and the volumetric fraction of these phases can strongly influence stiffness and strength. MA steels can be formed with any steel composition as long as the alloying additions do not exceed a certain amount to the point where unfavourable phases form in volume fractions above 1%. An example would be adding too much titanium (Ti) to a medium carbon steel, where titanium nitride (TiN) is formed primarily followed by titanium carbide (TiC). The literature review in this thesis will look at carbide reinforcement as a ceramic phase within a medium carbon microalloyed steel; the particular precious metals to be studied as additions are Ti, niobium (Nb) and vanadium (V). This will allow for an understanding of these elements and their microstructural influence.

Precipitation-hardened ferritic-pearlitic (PHFP) steels are medium-carbon high manganese in composition with a microstructure made up of ferrite and pearlite. The amount of pro-eutectoid ferrite present in PHFPs can be manipulated by a controlled cooling rate [10]. Lesser amounts of ferrite improve hardness and fracture toughness; however, ductility is reduced. Carbide (-C) precipitates such as TiC, NbC and VC, form during the liquid phase in a medium-carbon steel and have high thermodynamic stability once formed. The idea of adding carbide precipitates to a base steel is to pin grain boundaries and prevent dislocation movement [10]. Ti, in particular, is excellent at higher temperatures but tends to oxidise quickly during vacuum induction melting. V and Nb in carbide form will prevent the recrystallisation of austenite grains during deformation, which is necessary as the MA steel will be coarse in grain structure due to an uncontrolled cooling rate casting method generally used during fabrication. TiB_2 exhibits similar behaviour to carbide precipitates; however, the effects of grain pinning and thermodynamic behaviour of a boride-based reinforcement are greater. The performance and characteristics of TiB_2 will be discussed later in Chapter 2.

With continuous advancements being made in the electric automotive sector, it is important to establish goals for improving vehicle efficiency through lightweight design and geometric adaptation. Structural steels are predominantly used to fabricate both internal combustion-powered and new electric vehicles due to their high modulus, stiffness and strength. Steel components such as integral chassis components, body panels and engine/motor components are responsible for most of a vehicle's total mass. This implores research into the development of HMSs with particular composite ceramic reinforcement to both enhance stiffness and reduce the overall density of steel components. With a lower density and equal/higher strength, parts can be made lighter through geometry changes. Alternatively, new composite reinforced steels can keep the same geometry as existing parts whilst exhibiting similar or greater mechanical properties all whilst reducing the weight of an electric vehicle.

1.2 Aim and Objectives

The overall aim of this project is to fabricate an SMC using field-assisted sintering technology (FAST) and/or vacuum induction melting (VIM) coupled with single-stage TMP. The feasibility of *in situ* reinforcement (TiB_2) is to be established through experimental work using facilities provided by the Henry Royce Institute (HRI). By first developing a microalloyed steel, an understanding and appreciation can be attained through microstructural analysis and mechanical testing on a uniquely fabricated steel composition. The project can then progress onto the main focus, which is to incorporate TiB_2 into the existing composition using the processing routes in parallel (VIM and FAST). The key achievable outcomes for these newly developed steels are:

I. To understand the physical metallurgy of microalloyed steels, SMCs, precipitation hardening, steel powder consolidation, TMP and etching through a comprehensively written literature review
II. To understand the process and techniques used during VIM and FAST through experimental work
III. To fabricate monolithic and atomised forms of MA steel with detailed microscopy and mechanical property analysis
IV. To conclude on the overall benefits MA steels hold, justifying it as a material used for automotive components.
V. To improve the strength and elastic modulus of the MA steel by introducing TiB_2 as an *in situ* composite reinforcement for both processing routes
VI. To control the phase transformation and grain refinement in both MA and SMC steels using TMP routes such as hot rolling and plane strain compression (PSC)
VII. To critically compare VIM and FAST to conclude their feasibility for use in the automotive sector at an industrial scale

1.3 Thesis Structure

1.3.1 Overview

This thesis comprises nine chapters, each of which contributes to the investigation and understanding of MA and MA steel composites (MASCs). Findings from the VIM processing route are found in Chapters 4 and 5 and findings from the FAST processing route are found in Chapters 6 and 7. Chapter 8 critically compares microstructural and mechanical property findings between both processing routes:

Chapter 1: A complete overview of the research topic, highlighting its significance and the necessity for research. This chapter also outlines the research aim and objectives and provides a summary of the thesis structure.

Chapter 2: The literature review explores the physical metallurgy of MA steels and SMCs. Present literature on the fabrication and analysis of composites will allow the identification of correct manufacturing parameters and will also justify the necessity of this project.

Chapter 3: This chapter outlines the methodologies used in the study, including the selection of material composition, the manufacturing of alloys using VIM and FAST, and TMP. It also covers analysis techniques for microscopy and mechanical testing. Additionally, it describes the unique methods employed for acquiring prior-austenite grain boundaries (PAGBs)

Chapter 4: Microscopy and mechanical property findings of an MA steel fabricated using VIM, followed by hot rolling and PSC, are presented and discussed. The impact of cooling rate modifications on phase transformation and grain morphology is analysed through scanning electron microscopy (SEM), tensile testing, Vickers hardness testing, and resonant frequency damping analysis (RFDA) which is used for calculating Young's modulus. The effects of cooling rate modifications on hardness, strength values (yield and ultimate), elongation, and elastic modulus are highlighted.

Chapter 5: Similarly to Chapter 4, the investigation of microscopy and mechanical properties is carried out for the same MA composition but with the additions of TiB_2 in 5% and 7.5% volume fractions. These alloys will be referred to as 5MASC and 7.5MASC. Grain refinement and phase transformation with modified cooling rates after PSC testing are also discussed. Calculations of the volume fractions of TiB_2 are also presented.

Chapter 6: Analysis of American Iron and Steel Institute (AISI) grade S4140 powder, which has a composition similar to MA steel. This composition was used at the beginning of the PhD due to restrictions on fabricating MA powder caused by COVID-19. Extensive FAST testing on S4140 is presented and analysed through microscopy, highlighting progressive densification. A discussion is also presented for the microstructure when TiB_2 powder is added in a 5% volume fraction to an S4140 matrix.

Chapter 7: The FAST processing route for MA steel powder fabricated via VIM and gas atomisation is examined. The effects of dwell time, temperature, and powder particle size are explored with comprehensive microscopical analysis. Additionally, the incorporation of a 5% volume fraction of TiB_2 powder as a reinforcing composite is investigated through mechanical testing, microscopy and X-ray energy dispersive spectroscopy (X-EDS).

Chapter 8: A critical comparison of the microstructures and mechanical properties between the VIM and FAST processing routes is presented. The feasibility of manufacturing high modulus composite steels using both methods is evaluated, with detailed discussions on their respective advantages and limitations. Concluding remarks address which processing route is better suited for mass production in the automotive industry, considering factors such as efficiency and overall material performance.

Chapter 9: This section summarises the research findings, discussing their significance and implications. It addresses the practical applications and limitations of the research. Additionally, recommendations for future work are outlined, suggesting potential directions for further investigation.

1.3.2 Flow Diagram

Figure 1 highlights a generic path of processing for VIM and FAST routes:

Figure 1: Flow diagram illustrating processing and analysis routes for VIM and FAST

2. Literature Review

This chapter will provide a comprehensive critique of the literature on reinforced steels fabricated using both vacuum induction melting (VIM) and field-assisted sintering technology (FAST) methods. It is essential to first grasp the existing research on microalloyed (MA) steels and steel matrix composites (SMCs) across various grades, and understand how different alloying elements influence the microstructure and consequently the mechanical properties. The review will begin by introducing the fundamental steel fabrication techniques relevant to this study, followed by an exploration of the physical metallurgy of austenite, grain pinning, and precipitate reinforcements in MA steels. Next, thermomechanical processing (TMP) routes will be detailed, closing with an in-depth examination of SMCs produced through VIM and FAST methods.

Many automotive components found in suspension and the chassis demand specific rigidity, which means that the stiffness of the steel used is a highlighted important parameter. Problems with current matrix composites are present in the form of damaging mechanisms. These include de-cohesion and fracture at the location of reinforcement particles. From this, it can be said that one of the most important factors for an effective reinforcement addition is to have good bonding at grain interfaces [11]. Other factors that the reinforcement has on mechanical properties are the volumetric fraction of precipitates and their size.

2.1 Fundamentals of Steelmaking

Steelmaking is an essential process in materials science, particularly for producing high-quality steels used in automotive applications. This chapter focuses on VIM and FAST, two advanced methods that are critical for creating high-modulus steels with superior properties. VIM involves melting metals in a vacuum using electromagnetic induction, which significantly reduces contamination by gases and impurities, resulting in high-purity steels. The process involves placing raw materials in a crucible within a vacuum chamber, where an alternating current

passes through a surrounding coil, inducing eddy currents in the metal. These currents generate heat, melting the metal while the vacuum environment removes undesirable elements such as hydrogen, oxygen, and nitrogen in some cases. This method allows for precise control over the alloy composition, enabling the production of steels with tailored properties. The high purity and controlled alloying are particularly beneficial for automotive steels, where specific mechanical properties are crucial [12].

FAST is a cutting-edge method for consolidating powdered materials into dense solids using electric fields and pressure. FAST significantly reduces sintering time and temperature compared to traditional methods by applying uniaxial pressure and a pulsed direct electric current (DC) to the powder material. This process generates localised heating at the contact points between particles, promoting rapid sintering and densification; this is known as Joule heating [13]. FAST enables the production of advanced steels with fine-grained microstructures, enhancing hardness, strength, and wear resistance. It also facilitates the creation of composite materials and functionally graded steels, which are highly desirable for automotive components due to their improved performance and durability [14]. VIM and FAST are respected routes for producing high-quality steels with superior mechanical properties, and both have their advantages and limitations. These techniques allow for precise control over composition and microstructure, making them indispensable for developing HMSs for automotive applications. The ongoing advancements in these methods continue to drive innovation in steelmaking, supporting the development of next-generation automotive technologies [15].

2.1.1 Vacuum Induction Melting

Vacuum Induction Melting (VIM) is a crucial process for producing high-purity steels by using electromagnetic induction in a vacuum environment. This method minimises contamination from gases and impurities, making it ideal for creating high-performance materials with specific properties. Casting and remelting metals are critical processes that result in ingots with improved cleanliness and reduced

segregation. During VIM, the induction heating generates movement, known as electromagnetic stirring [16], in the liquid metal within the furnace crucible, enhancing the mixing of alloying elements and leading to a more homogeneous final product.

In VIM, raw materials are placed in a crucible within a vacuum chamber. An alternating current passes through a coil surrounding the crucible, generating a magnetic field that induces eddy currents in the metal, thus producing heat and melting the material. The vacuum helps remove undesirable elements such as hydrogen, oxygen, and nitrogen, leading to a cleaner melt [17]. The precise control over the melt's composition and purity makes VIM suitable for producing high-performance alloys used in mechanically demanding applications, such as in the aerospace and automotive industries. The microstructure of VIM-processed materials is significantly refined due to controlled cooling rates and the absence of contamination. The grain structure of metals processed through VIM is typically finer, which enhances mechanical properties like strength, toughness, and fatigue resistance [18]. This process is particularly advantageous for producing alloys with reactive elements that are prone to oxidation or contamination in other melting environments [19].

Under normal atmospheric steelmaking conditions, detrimental non-metallic inclusions tend to precipitate during solidification, which often reduces the material's ductility. In contrast, VIM minimises these reactions because the oxygen content is extremely low. As metals solidify, the equilibrium solubility of gases decreases significantly, potentially causing gaseous development that results in unsoundness and porosity in castings. Proper vacuum techniques help minimise this gaseous progress during solidification, producing improved castings. Additionally, controlling gas content in a vacuum reduces the amount of gas in a solid solution. In steel it is well known that hydrogen causes embrittlement and flake formation; oxygen leads to various inclusions, raises the impact transition temperature, and decreases fracture toughness; nitrogen causes embrittlement and negatively affects

ageing, fatigue, and stress rupture properties, as well as decreasing impact strength [20].

Recent advancements in VIM technology focus on improving the efficiency and precision of the melting process. Innovations include the development of advanced crucible materials, improved induction coil designs, and enhanced vacuum systems that further reduce impurities. These advancements have expanded the range of materials that can be processed using VIM, allowing for the production of even more complex alloys with tailored properties [21]. The versatility of VIM extends to the production of *in situ* composite materials, where it is used to achieve uniform dispersion of reinforcing particles within a metal matrix. For instance, microalloyed steels produced through VIM exhibit improved mechanical properties due to the uniform distribution of fine carbides and other strengthening phases. This uniform distribution is crucial for applications requiring high wear resistance and structural integrity [22]. To summarise, VIM is employed to achieve several key objectives [23]:

I. Extracting unfavourable gasses
II. Removing trace elements with high vapour pressures
III. Preventing oxidation due to air exposure, thus minimising the loss of reactive elements
IV. Managing pressure-dependent reactions such as decarburisation
V. Attaining the highest standards of material cleanliness
VI. Ensuring extremely precise compositional control

2.1.2 Field-assisted Sintering Technology

Field-assisted sintering technology (FAST) operates by applying a uniaxial pressure simultaneously with a pulsed direct current (DC) to a powder compact, which is typically enclosed within a graphite die. This combination of mechanical pressure and electrical current induces Joule heating between powder particles, enabling the sintering process to occur at lower temperatures and within shorter timeframes compared to conventional sintering methods such as hot isostatic pressing (HIP) [24]. The general FAST machine apparatus is presented in Figure 2 [25]:

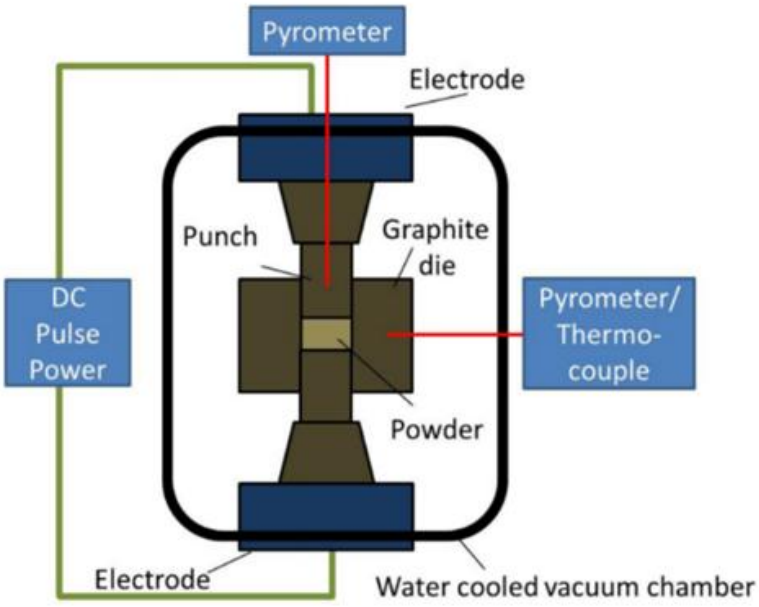

Figure 2: FAST schematic with an included mould housing [25]

The application of a pulsed electric field in FAST induces localised heating at particle contact points, leading to the initiation of plasma discharges. These discharges are believed to enhance mass transport mechanisms, such as diffusion and plastic deformation, which promote the consolidation and densification of the material. Additionally, the high heating rates achieved in FAST minimises grain growth, allowing for the retention of fine-grain microstructures. This is particularly advantageous when processing nanostructured materials or composites, where the preservation of fine-grained microstructures is crucial for maintaining enhanced strength, hardness, and toughness [26].

The ability of FAST to apply a uniaxial pressure during the sintering process plays a critical role in enhancing the densification behaviour. Applied pressure not only facilitates the rearrangement and deformation of particles but also aids in the elimination of pores and the suppression of undesired phase transformations. This pressure-assisted densification is particularly important when working with refractory materials or materials with high melting points, where achieving full densification through traditional sintering methods would require excessively high temperatures [24].

The versatility of FAST extends to its ability to process a wide range of materials, including metals, ceramics, composites, and even functionally graded materials (FGMs). The capacity to produce dense materials with favourable microstructures and controlled phase compositions has made it a valuable tool in the development of advanced materials for various applications, including aerospace, automotive, and biomedical industries. For instance, the ability to sinter materials such as tungsten carbide-cobalt (WC-Co) composites [27], which are commonly used in cutting tools, with enhanced hardness and wear resistance is a direct consequence of the precise control over microstructure afforded by FAST.

However, despite its numerous advantages, FAST also presents certain challenges. The rapid heating and cooling cycles inherent to the process can induce thermal stresses, potentially leading to cracking or other defects, particularly in brittle materials. Additionally, the use of graphite dies, while effective in conducting the electric current, can introduce carbon contamination, which may alter the properties of the sintered material [24], [28]. Thus, ongoing research in the field is focused on optimising processing parameters, such as current density, pulse duration, and applied pressure, to mitigate these challenges and fully utilise the capabilities of FAST.

2.2 Recrystallisation and Grain Pinning in Steels

Recrystallisation is a restoration process involving the replacement of deformed grains with new, relatively defect-free grains. This process is characterised by the nucleation of new grains and the migration of grain boundaries. As recrystallisation progresses, the original deformed matrix is gradually consumed by the newly formed recrystallised grains, leading to the development of a fully formed microstructure that is free from deformation and dislocation densities [29]. This process results in significant changes to the material's properties, such as a pronounced softening effect, which is generally more pronounced than that observed in other restoration processes. The softening effect associated with

recrystallisation is accompanied by notable changes in the material's strength and ductility.

Recrystallisation can occur under different conditions and can be classified accordingly. When recrystallisation occurs simultaneously with deformation, it is known as dynamic recrystallisation. In contrast, when recrystallisation occurs after the deformation process has finished, it is referred to as static recrystallisation. Dynamic recrystallisation is particularly significant in high-temperature and/or low-strain deformation processes, where it plays a vital role in controlling grain size and, consequently, the mechanical properties of the material [30]. Recrystallisation can also be demonstrated as a continuous restoration mechanism, known as continuous dynamic recrystallisation, where new grains form progressively as deformation continues. In some metals, under specific conditions of stress and temperature, the accumulation of defects and the resulting local gradients in dislocation density can lead to the nucleation of new grains without the need for prior recovery. This pathway, where nucleation occurs without preceding recovery, is referred to as discontinuous dynamic recrystallisation. This typically occurs in materials where the recovery process is slow, allowing for the build-up of dislocation density to reach levels sufficient for the nucleation of new grains [31].

The conditions under which recrystallisation occurs, including temperature, strain rate, and the nature of the material, play an important part in determining the specific recrystallisation mechanism and the resulting microstructure. Understanding these mechanisms is essential for tailoring the microstructure and properties of high modulus steels through controlled thermomechanical processing.

2.2.1 Dynamic Recrystallisation of Austenite

At elevated temperatures during plastic deformation, materials undergo a complex interaction between hardening and softening mechanisms. As the material is deformed, the introduction of dislocations increases, resulting in a hardened microstructure. However, dynamic restoration processes simultaneously work to counter this work hardening by eliminating dislocations, thus softening the material.

In materials such as austenitic steel, which possess low stacking fault energy (SFE), the recovery process is notably slow due to the challenges posed by the face-centred cubic (FCC) structure in accommodating cross-slip. This slow rate of recovery allows for a significant accumulation of defects, which generate regions with sufficient stored energy to nucleate new grains through dynamic recrystallisation without the requirement of recovery [32].

The stress-strain behaviour associated with dynamic recrystallisation is illustrative of the underlying metallurgical transformations. As stress is applied and plastic deformation progresses, the material hardens until it reaches a critical strain (ε_c), at which point dynamic recrystallisation is initiated. The start of dynamic recrystallisation shows the balance between the ongoing hardening induced by continuous deformation and the softening brought by the formation of new, defect-free grains. This interaction results in the appearance of a peak strain (ε_p) on the stress-strain curve. As deformation continues beyond this point, the fraction of the material undergoing dynamic recrystallisation steadily increases, leading to a reduction in the overall stress until the material stabilises at a steady-state strain (ε_{ss}), where a constant stress level (σ_{ss}) is maintained [33].

Dynamic recrystallisation is characterised by the nucleation of new grains at sites of high energy, such as triple junctions and austenite grain boundaries. As deformation progresses, these newly nucleated grains are subjected to further strain until they reach the critical strain necessary for another cycle of recrystallisation. This ongoing process establishes a steady-state condition in the material, where a continuous development of nucleation and limited grain growth occurs [34]. The microstructural evolution during dynamic recrystallisation often results in a distinctive "necklace" structure, where the original grain boundaries serve as sites for the formation of new grains. These grains expand until they impinge upon neighbouring grains, at which point additional grains begin to form along the new grain boundaries within the matrix. This process continues until the entire material

is recrystallised, resulting in a microstructure characterised by a fine, equiaxed grain structure that significantly influences the material's mechanical properties.

2.2.2 Static Recrystallisation of Austenite

During the hot working of austenite, when the deformation does not reach the critical strain necessary to initiate dynamic recrystallisation, and the extent of recovery is minimal, static recrystallisation can take place after the deformation process. This restoration mechanism, which typically occurs during the intervals between successive deformations, plays a crucial role in refining the microstructure and restoring the ductility of the material [29].

Static recrystallisation is a time-dependent process, in which new, strain-free grains nucleate and grow within the deformed matrix. Unlike dynamic recrystallisation, which occurs concurrently with deformation, static recrystallisation begins only after the external stress is removed, allowing the material to recover and recrystallise under thermal conditions without the influence of deformation [35]. The driving force for static recrystallisation is the stored energy from the deformation, which is concentrated in the form of dislocations within the grains. As these dislocations accumulate, they create regions of high energy that become potential nucleation sites for the formation of new grains.

The process of static recrystallisation can be described by the Avrami equation, which is commonly used to model the kinetics of phase transformations, including recrystallisation [36]:

$$X(t) = 1 - \exp\left(-kt^n\right) \quad (1)$$

where X(t) is the fraction of recrystallised material at time t, k is a rate constant that depends on the material and temperature, and n is the Avrami exponent, which provides information about the nucleation and growth mechanisms.

This equation illustrates how static recrystallisation progresses over time, with the fraction of recrystallised material increasing as the process continues until it eventually reaches completion [37]. During static recrystallisation, the newly formed grains grow at the expense of the deformed matrix, gradually consuming the original, dislocation-rich microstructure. The nucleation of these new grains typically occurs at locations with high dislocation density, such as grain boundaries, triple junctions, and other regions of high stored energy. As these grains grow, they absorb and eliminate the dislocations, resulting in a microstructure that is free of deformation-induced defects [38]. The kinetics of static recrystallisation are influenced by several factors, including temperature, initial dislocation density, grain size, and the presence of alloying elements. Higher temperatures generally accelerate the recrystallisation process, leading to faster nucleation and growth of new grains. Conversely, lower temperatures slow down the kinetics, requiring longer times for the material to fully recrystallise. Alloying elements can either promote or inhibit static recrystallisation, depending on their effect on the mobility of grain boundaries and the stability of the deformed microstructure [38]. An example of static recrystallisation is illustrated in (Figure 3) from a cold-worked steel being heated to recrystallisation temperature, A_r.

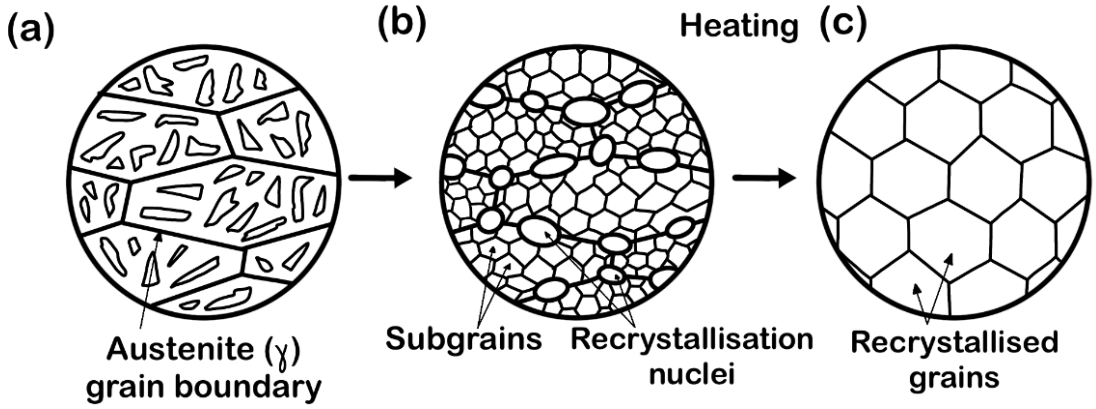

Figure 3: Schematic representation of static recrystallisation taking place on (a) cold-worked steel which had been heated to form (b)(c) recrystallised grains which grow from prior austenite grain boundaries

2.2.3 Grain Pinning Mechanism

One of the most widely recognised models that describe the relationship between grain size and strength is the Hall-Petch relationship. This relationship quantitatively expresses how decreasing grain size leads to an increase in the yield strength of a material. The Hall-Petch equation is given by:

$$\sigma_y = \sigma_0 + k_y d^{-1/2} \quad (2)$$

where σ_y is the yield strength of the material, σ_0 is the friction stress or the intrinsic strength of the material, which is a constant related to the lattice resistance to dislocation movement, k_y is the Hall-Petch slope, a material-specific constant that reflects the strengthening influence of grain boundaries and d is the average grain diameter [39]. According to the Hall-Petch relationship, as the grain size decreases, the yield strength σ_y increases. This occurs because grain boundaries act as barriers to dislocation motion, which is the primary mechanism of plastic deformation in crystalline materials. The finer the grains, the more grain boundaries there are to impede the movement of dislocations, thereby requiring higher applied stress to initiate plastic deformation [40].

Experimental studies have consistently supported the Hall-Petch relationship across a wide range of materials, including steels, aluminium alloys, and other metals [41], [42], [43], [44]. For example, in steels, grain refinement through controlled TMP or alloying can significantly enhance the yield strength without compromising ductility. This makes grain refinement a particularly favourable method for developing high-strength, high-performance steels.

At very small grain sizes, an inverse Hall-Petch effect has been observed, where further grain refinement leads to a decrease in strength. This occurrence is attributed to the grain boundary sliding that becomes dominant at extremely fine grain sizes, where the grain boundaries themselves can become sources of deformation [44].

Grain pinning by precipitates occurs when second-phase particles impede grain boundary movement, stabilising the microstructure. The effectiveness of this pinning is influenced by the size, volume fraction, and distribution of the precipitates within the matrix. This mechanism is crucial in refining grain structure and enhancing the material's mechanical properties by maintaining a finer grain size. The pinning force, F_{pin}, associated with the movement of grain boundaries directly relates to the size of precipitates in a matrix, according to Zener's theory (see Equation 3) [45]. The volume fraction of precipitates of radius r will also affect the pinning force and grain migration behaviour, as well as the number of particles per unit area (N_s). For instance, if a second phase particle is present at a migrating grain boundary, the surface energy of said boundary would reduce as the particle acting as a pinning mechanism replaces part of the original grain's perimeter.

This means that a greater amount of force (i.e., work) would be required for the grain boundary to move away from the particle.

$$F_{pin} = 4rVN_s \tag{3}$$

where the pinning force, F_{pin}, is dependent on the radius of particles, r, the volume fraction, V, and the number of particles per unit area, N_s.

$$\sigma_p = 8.995 \times 10^3 f^{3/2} d^{-1} \ln(2.417d) \tag{4}$$

Similarly, Orowan's equation (Equation 4) looks at the precipitation contribution to strengthening σ_p, where f is the volume fraction of precipitates and d is the average grain diameter [48].

2.3 Microalloyed Medium Carbon Steels

2.3.1 Hypo-eutectoid Steels

Hypo-eutectoid steels, typically containing between 0.3% and 0.6% carbon, undergo several transformations that significantly affect their microstructure and mechanical properties. During the austenitising process, the steel is heated above the critical temperature (a_3), where it exists in the austenitic phase (γ-phase) characterised by a face-centred cubic (FCC) crystal structure [46]. This homogenous austenitic phase is essential as the initial state for subsequent phase transformations. Upon cooling below the upper critical temperature (A_3), pro-eutectoid ferrite begins to precipitate along the austenite grain boundaries. This nucleation and growth occur because ferrite has a lower solubility for carbon than austenite, causing carbon to be diffused into the remaining austenite. The morphology and distribution of pro-eutectoid ferrite are influenced by the cooling rate and the initial austenite grain size.

As cooling continues to the eutectoid temperature (approximately 727˚C), the remaining austenite transforms into pearlite, a name which describes the lamellar morphology of ferrite and cementite (Fe_3C). This transformation is a cooperative growth mechanism where ferrite and cementite precipitate simultaneously in alternating lamellae, creating a characteristic lamellar microstructure. The interlamellar spacing, which is inversely related to the cooling rate, significantly affects the mechanical properties, with finer (smaller interlamellar spacing) pearlite structures enhancing strength and hardness [47]. At higher cooling rates, the austenite transformation bypasses pearlite formation and produces bainite or martensite. Bainite, formed at intermediate temperatures, consists of acicular needle-like ferrite and cementite. The structure of bainite varies from upper bainite, which forms at higher temperatures with a feathery appearance, to lower bainite, which forms at lower temperatures with a plate-like structure. Bainite provides a useful combination of hardness and ductility, making it suitable for various engineering applications [36] [38].

Martensite, formed through rapid quenching, is a supersaturated solid solution of carbon in body-centred tetragonal (BCT) iron. This diffusionless transformation involves a shear mechanism, resulting in a highly strained and hardened microstructure. Although martensite is extremely hard, it is also brittle and requires tempering to enhance toughness. During tempering, the steel is reheated to a temperature below the eutectoid point, allowing the decomposition of supersaturated martensite into equilibrium phases such as ferrite and cementite. This process relieves internal stresses, refines the carbide distribution, and restores some ductility to the steel [39] [40]. Throughout these transformations, the kinetics of precipitation and segregation phenomena play crucial roles. Alloying elements such as manganese, silicon, and chromium, commonly present in medium carbon steels, influence the transformation temperatures and the stability of various phases. These elements enhance hardenability, prevent the formation of undesirable phases, and improve the overall mechanical properties of the steel.

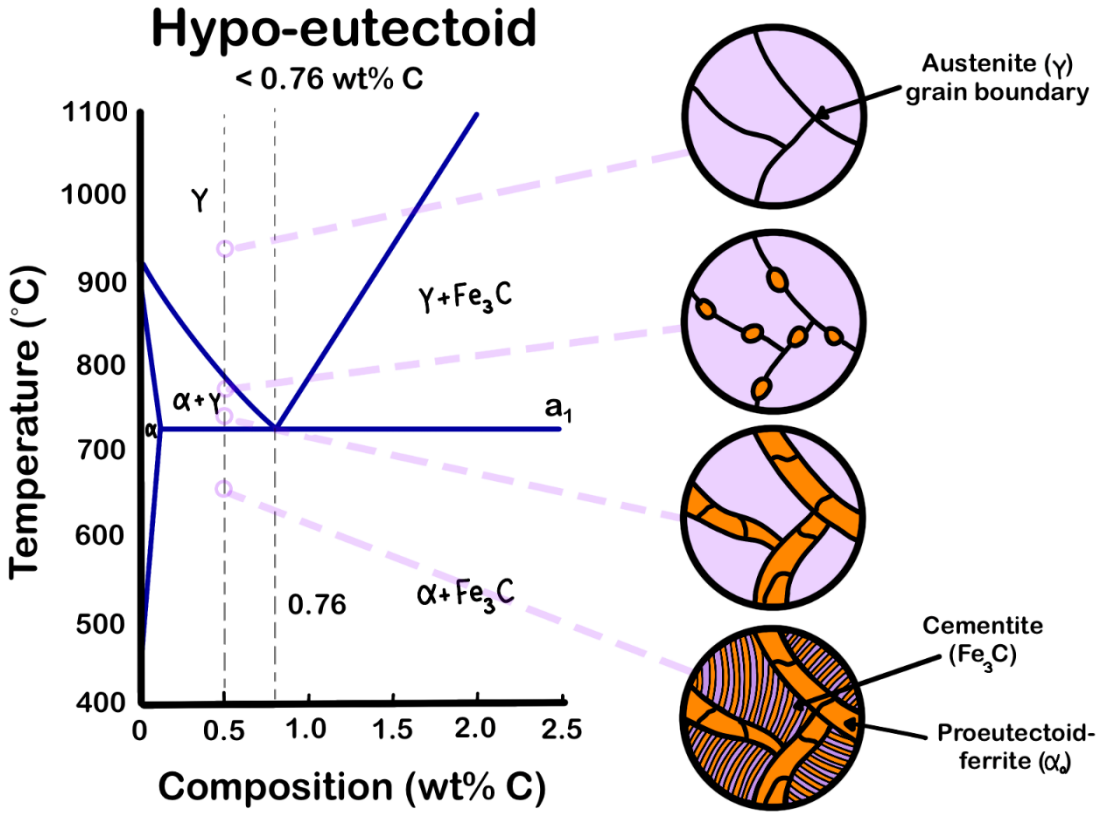

Figure 4: Phase diagram of a <0.76 wt.% C hypo-eutectoid steel which exemplifies the nucleation of pro-eutectoid ferrite and pearlite

2.3.2 Microalloyed Steels

Microalloyed (MA) steels, also known as high-strength low-alloy (HSLA) steels, represent a modern class of materials designed to achieve exceptional mechanical properties through the addition of microalloying elements and the precise control of TMP. These steels are characterised by their relatively low carbon content, typically in the range of 0.05-0.4%, combined with microalloying additions such as vanadium (V), niobium (Nb) and titanium (Ti) in concentrations usually less than 0.1 wt.% [51] [8]. These elements significantly enhance the strength, toughness, and wear resistance of the steel through complex interactions involving precipitation hardening, grain refinement, and phase transformations. The microalloying elements in these steels play distinct roles in modifying the microstructure and enhancing mechanical properties. Vanadium, niobium, and titanium are the most common microalloying elements, each contributing individually to the steel's performance:

Vanadium (V): Vanadium is known for its ability to form vanadium carbides (VC) during cooling, which precipitate within the ferrite matrix. These fine precipitates act as obstacles to dislocation movement, thereby increasing the yield strength through precipitation hardening. Vanadium also contributes to grain refinement by restricting austenite grain growth during hot working, which is essential for maintaining a fine grain structure that enhances both strength and toughness [52], [53].

Niobium (Nb): Niobium is particularly effective in impeding recrystallisation during thermomechanical processing, thereby refining the austenite grain structure. It forms niobium carbides (NbC) and niobium nitrides (NbN), which precipitate both intergranular and intragranular. The presence of Nb in a solid solution increases the strength of the steel through a combination of grain boundary strengthening and precipitation hardening. Nb also raises the recrystallisation temperature, allowing for controlled rolling practices that enhance the steel's microstructure [54].

Titanium (Ti): Titanium contributes to the formation of titanium carbides (TiC) and titanium nitrides (TiN) in the liquid state, which are effective in both grain refinement and precipitation hardening. TiN particles are particularly beneficial in preventing the coarsening of austenite grains during reheating, leading to a finer final microstructure [55]. The fine dispersion of TiC precipitates provides additional resistance to dislocation motion, further strengthening the steel [56][52].

The improved mechanical properties of microalloyed steels are largely achieved through controlled TMP, particularly controlled rolling. Controlled rolling is a process that involves accurate management of temperature and deformation conditions (strain and strain rate) to optimise the microstructure. The steel is first reheated to a temperature above the austenitisation range, typically between 1100˚C and 1250˚C, where the microalloying elements dissolve into the austenite phase [51]. This homogenises the steel and prepares it for subsequent deformation steps. During controlled hot rolling, the steel undergoes multiple stages of deformation, often in the non-recrystallisation region, where the temperature is carefully controlled to prevent the complete recrystallisation of austenite. This process enhances the dislocation density and promotes the nucleation of fine ferrite grains during subsequent cooling. The deformation is typically performed in two stages: in the high-temperature austenite region to achieve dynamic recrystallisation and in the low-temperature austenite region to control grain refinement.

After deformation, the steel is subjected to controlled cooling, where the cooling rate is an important parameter. Fast cooling rates are usually employed to avoid the formation of coarse pearlite and to encourage the formation of fine bainitic or martensitic structures, depending on the alloy composition and desired properties. The cooling rate also influences the precipitation kinetics of microalloying elements, where rapid cooling can lock microalloying elements in solid solution, to be precipitated during subsequent ageing treatments. The microstructure of microalloyed steels is largely determined by the phase transformations that occur during controlled cooling from the austenite phase. The key microstructural

components that form include ferrite, pearlite, bainite, and martensite, each contributing to the steel's mechanical properties:

Ferrite (α) Transformation: The transformation from austenite to ferrite typically begins at temperatures below the a_3 temperature and is accelerated by the presence of microalloying elements like Nb and Ti, which inhibit austenite grain growth. The resulting ferrite grains are fine and equiaxed, contributing to the steel's toughness and strength. The addition of microalloying elements delays the austenite (γ)-to-ferrite transformation, refining the final ferritic microstructure [57].

Pearlite (α+Fe_3C) Formation: Pearlite forms through a eutectoid reaction at the lower end of the cooling range and consists of alternating lamellae of α and Fe_3C. The interlamellar spacing of pearlite is inversely related to the cooling rate; finer pearlite, which forms at higher cooling rates, contributes to higher strength but reduced ductility. In microalloyed steels, the presence of alloying elements often suppresses the formation of pearlite, favouring bainite [56].

Bainite and Martensite Formation (B+M): Bainite forms at intermediate cooling rates and is characterised by its acicular structure, which provides a combination of strength and toughness. Bainitic structures are particularly desirable in applications requiring high-impact resistance. Martensite, which forms at very high cooling rates, is a supersaturated phase that significantly increases the hardness of the steel. However, martensitic steels typically require tempering to restore some ductility and reduce internal stresses.

2.3.2.1 Precipitate Reinforcement

The precipitation of carbides and nitrides in microalloyed steels occurs through a series of distinct stages during TMP. These precipitates, which can form as homogeneous, coherent, semi-coherent, or incoherent phases with respect to the steel's crystalline lattice, play a crucial role in refining the microstructure and enhancing mechanical properties. Precipitates can form not only within the grain interiors but also at grain boundaries and dislocations, where they may initiate

strain-induced precipitation during subsequent deformation [58]. The precipitation process typically begins with the nucleation of fine particles during cooling from the austenite phase, followed by growth and coarsening as the temperature decreases further. Recent literature has particularly focused on nanoprecipitates, which are of significant interest due to their substantial contribution to yield strength. These nanoprecipitates, primarily consisting of carbides and nitrides of Ti, V and Nb serve to inhibit the movement of austenitic grain boundaries, thereby retarding grain growth at elevated temperatures. This inhibition is important in maintaining a fine grain size, which directly correlates with increased strength and toughness of the steel. In particular, studies have shown that precipitates such as titanium nitride (TiN) and niobium carbonitrides (Nb (C, N)) are highly effective in pinning austenite grain boundaries and preventing grain coarsening during high-temperature processing [59]. The effectiveness of these precipitates in grain boundary pinning is highly dependent on the temperature at which carbonitrides form during steel processing. Table 1 shows the effects of microalloying elements on the mechanical and/or thermodynamic characteristics of the steel.

The stages for carbide and nitride precipitation during the processing of microalloyed steels are as follows [58]:

I. Precipitates formed during the liquid phase or immediately following solidification are typically highly stable but are generally too coarse to significantly affect austenite recrystallisation. However, the finer precipitates in this stage can slow down the coarsening of austenite grains during the reheating process.
II. During controlled rolling, strain-induced precipitation occurs, which effectively inhibits austenite recrystallisation and promotes grain refinement, leading to an enhanced microstructure.
III. Fine precipitates form during or after the austenite-to-ferrite transformation, nucleating at the austenite-ferrite interface or within the ferrite phase, resulting in a refined precipitation structure.

Table 1: Principal effects of microalloying elements [8]

Element	wt %	Effect
C	<0.25	Strengthener
Mn	0.5–2.0	Retards the austenite decomposition during accelerated cooling Decreases ductile to brittle transitions temperature Strong sulfide former
Si	0.1–0.5	Deoxidizer in molten steel Solid solution strengthener
Al	<0.02	Deoxidizer Limits grain growths as aluminum nitride
Nb	0.02–0.06	Very strong ferrite strengthener as niobium carbides/nitrides Delays austenite-ferrite transformation
Ti	0–0.06	Austenite grain control by titanium nitrides Strong ferrite strengthener
V	0–0.10	Strong ferrite strengthener by vanadium carbonitrides
Zr	0.002–0.05	Austenite grain size control Strong sulfide former
N	<0.012	Strong former of nitrides and carbonitrides with microalloyed elements
Mo	0–0.3	Promotes bainite formations Ferrite strengthener
Ni	0–0.5	Increase fracture toughness
Cu	0–0.55	Improves corrosion resistance Ferrite strengthener
Cr	0–1.25	In the presence of copper, increase atmospheric corrosion resistance
B	0.0005	Promotes bainite formation

Mengaroni et al. focus on MA steels and in particular vanadium (V) as the rich precipitate responsible for increases in yield strength in a medium carbon steel matrix [60]. In the conducted experiment, traditional industrial forging conditions were used during hot rolling and re-heating processes where variables such as deformation temperature and cooling rates were specified. The resulting microstructure was deemed as a mixture of ferrite and fine pearlite. Precipitation hardening was observed with V particles characterised as very fine (<5nm) through transmission electron microscopy (TEM). This led to yield strength levels of approximately 500MPa [60], an improvement from the base medium carbon steel by around 80MPa with approximately 1.0wt% of V.

2.4 Thermomechanical Processing

Thermomechanical processing (TMP) is a common technique that combines mechanical deformation with carefully controlled thermal cycles to engineer the microstructure and enhance the mechanical properties of metallic materials. This process is particularly vital in the production of advanced steels, where the controlled interaction between temperature, strain, and strain rate during deformation directs key phase transformations, dislocation movements, and grain boundary dynamics.

Through TMP, materials can achieve refined grain structures, precise precipitation of secondary phases, and optimised phase distributions, leading to improved yield strength, toughness, and fatigue resistance. The process's effectiveness lies in its ability to manipulate microstructural changes during stages such as dynamic recrystallisation, phase transformation, and the suppression of grain growth. For example, control of rolling temperatures and cooling rates can prevent grain coarsening and promote desirable microstructural features such as ferrite and fine pearlite [61].

2.4.1 Hot Rolling

One method of deformation is hot rolling a workpiece, so it becomes thinner, densifying the material and altering the grain structure. A key study by Guk et al. looked at the impact of hot rolling on the microstructure of a sintered SMC with ZrO_2 particles. For the experiment (Figure 5), a wedge shape sample was used with conditions 900˚C and 1100˚C for the rolling temperature, 0.5 m/s for the rolling speed and a holding time of 30 minutes [62]. The observed microstructure clearly signified a realignment of ZrO_2 particles which had been orientated along the direction of rolling. Pore shrinkage occurred up to a point where no visible pores were detected at a rolling temperature of 1100˚C. This paper also looked into the rolling strain and it was concluded that increasing strain induced during rolling decreases the number of pores as well as their volume [62].

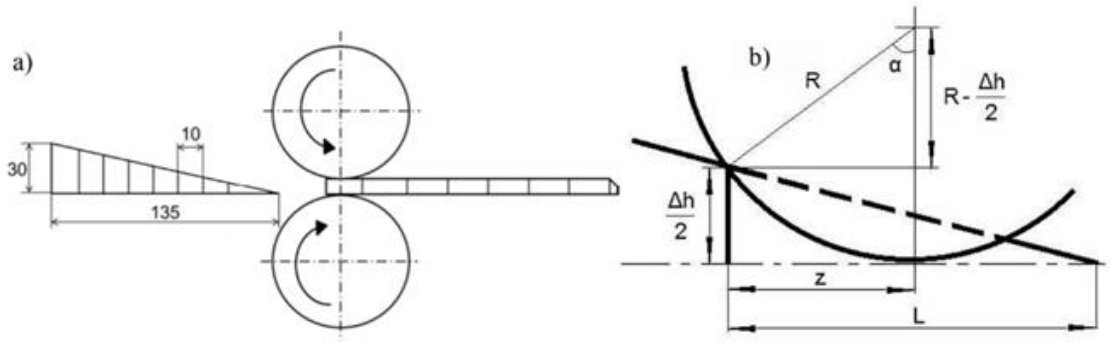

Figure 5: Representation of (a), the wedge specimen and rollers and (b), the deformation zone [62]

Lartigue-Korinek et al. [3] studied interfaces and defects from hot rolling a SMC which had titanium diboride (TiB_2) ceramic reinforcement. After forming the SMC via eutectic solidification, the material was rolled out from an initial thickness of 70 mm down to 3 mm over 45 minutes at an initial temperature of 1200˚C [3]. Plastic deformation occurred in TiB_2 particles at a temperature equivalent to 0.3 of the absolute melting temperature. Dislocations are visible in SEM after hot rolling, with larger TiB_2 particles making it more difficult for dislocations along a slip plane (identified as basal and prismatic), improving stiffness. Small amounts of damage in the form of particle fractures were observed at high strain levels, however the overall material displayed good ductility under tensile testing.

2.4.2 Plane Strain Compression (PSC)

A thermomechanical compression (TMC) machine is useful in simulating TMP techniques such as final rolling and forging. The TMC machine enables control of both deformation and temperature profiles to achieve targeted microstructures. By defining and controlling imposed strain and strain rates during deformation, as well as managing the heating and cooling temperature gradients, PSC provides a reliable and repeatable method for studying the effects of TMP on material behaviour, which is vital for the manufacturing of automotive components and other engineering applications [63].

The versatility of the TMC machine lies in its ability to accurately replicate the conditions experienced during large-scale industrial processes but in a controlled

laboratory setting. This allows researchers to investigate the effects of various parameters on the microstructure and mechanical properties of materials. For example, by adjusting the strain rate, the TMC machine can simulate the rapid deformation rates seen in high-speed rolling or forging processes. Additionally, the control over temperature profiles allows the study of dynamic recrystallisation and phase transformations.

Loveday et al. [64] provided a guide on the accurate measurement of hot flow stress under medium to high strain rates using a TMC machine. The guide highlights the importance of specimen preparation, geometry, and precise measurements to verify that the deformation passes have resulted in the correct thickness reductions corresponding to the imposed strain and strain rate. The alignment of the tool or cross-head and the accuracy of load measurements are critical to ensuring consistent and reliable results from the TMC machine. Inaccuracies in alignment can lead to significant deviations in the deformation process, as demonstrated through finite element analysis (FEA). Misalignment of the deformation tooling can cause non-uniform deformation patterns, such as U-shaped or Z-shaped distortions, leading to inconsistent deformation zones across the sample. Such inconsistencies can adversely affect the reproducibility of the experiment and the reliability of the data obtained. Therefore, maintaining precise alignment and consistent operating conditions is imperative for achieving accurate and reproducible results in PSC experiments [64]. The TMC machine's ability to impose complex strain paths and temperature histories on material makes it an invaluable tool for investigating the microstructural evolution under conditions that closely mimic industrial TMP processes. This capability is particularly useful for developing new HMS composites and optimising processing parameters to achieve desired properties such as improved strength, toughness, and ductility in automotive components.

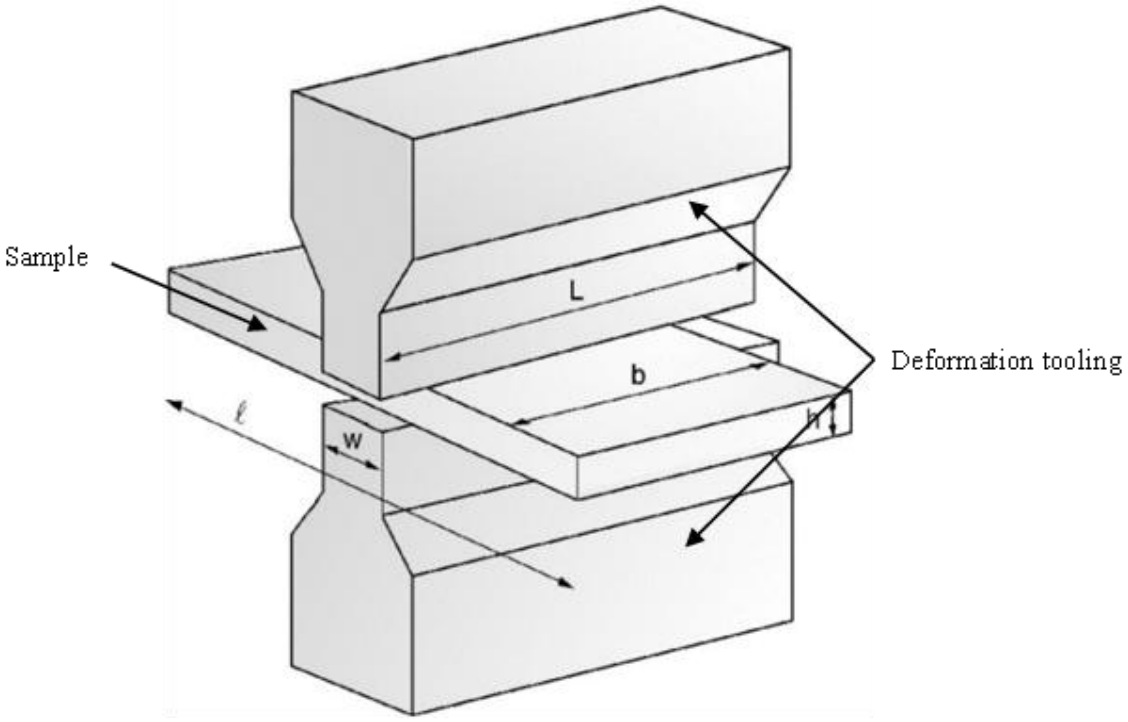

Figure 6: Schematic of a plane strain compression test containing 2 deformation tools which deform the centre of the sample [64]

2.5 Steel Matrix Composites (SMCs)

Steel matrix composites (SMCs) advance the mechanical properties of conventional steels through the incorporation of hard ceramic reinforcements, such as carbides and borides. These reinforcements significantly improve the hardness, wear resistance, and high-temperature performance of the steel matrix, making SMCs highly suitable for demanding applications in industries such as automotive, aerospace, and tool manufacturing [65], [66], [67].

Carbides, such as titanium carbide (TiC), vanadium carbide (VC), and tungsten carbide (WC), are among the most commonly used reinforcements in steel matrix composites. These carbides are characterised by their exceptional hardness and high melting points and are well known to improve the overall strength and durability of the composite. The incorporation of carbides into the steel matrix enhances wear resistance by creating a hard phase that impedes the movement of dislocations, effectively reducing the rate of material loss due to abrasion and erosion [68].

Borides, such as titanium boride (TiB_2) and chromium boride (CrB_2), also play a crucial role in reinforcing steel matrices. Borides are known for their high hardness, excellent thermal stability, and chemical inertness, which make them ideal for applications requiring high-temperature performance and resistance to corrosion. The addition of boride particles to the steel matrix results in a composite with superior elastic modulus, hardness and thermal resistance [69].

The distribution, size, and morphology of carbide and boride reinforcements within the steel matrix are significant factors that influence the overall performance of the composite. Fine, uniformly distributed particles are generally preferred as they contribute to a more homogeneous microstructure, leading to better mechanical properties. Additionally, the interfacial bonding between the steel matrix and the ceramic reinforcements plays a vital role in determining the composite's mechanical behaviour. Strong interfacial bonding ensures effective load transfer from the matrix to the reinforcements, thereby enhancing the composite's strength and toughness [68].

2.5.1 Ceramic Reinforcement

An ideal method of incorporating ceramic composites is by forming *in situ* using a ferroalloy (Fe-) combination. VIM is suitable for melting oxidation-sensitive metals such as Al and Ti as the procedure takes place in an inert atmosphere. An example of *in situ* formation has been studied by Li et al. [70] using VIM to obtain TiB_2 in an SMC. To achieve an HMS which can be produced at an industrial scale, alloys Fe-Ti and Fe-B were melted in an alumina crucible using an induction coil as the heating source. After maintaining a melt temperature of 1873K for 5 min, the liquid was poured and cooled in a cast [70]. The X-ray diffraction (XRD) pattern obtained showed peaks corresponding to that of TiB_2 in literature, meaning that using VIM to obtain a matrix composite is achievable. Importantly, the TiB_2 (at 13% volume) particles were equally distributed to give a homogeneous microstructure, where an increase in volume fraction showed more nucleation and less distance between these particles [70].

Another report by Martin Detrois et al. [71] looks at the same reinforcement technique using VIM with AISI 420 stainless steel. This martensitic steel has excellent mechanical properties as well as moderate corrosion resistance due to the high chromium content (~13%) [71] [72]. Again, homogeneous scattering of TiB_2 particles was achieved, using a temperature of 1773K. Similarly, an XRD study carried out showed peaks matching both TiB_2 and ferrite (α) phases. The obtained densities of the stainless steel (AISI 420) with the TiB_2 were similar to the theoretical values stated, with higher porosity present due to the ceramic matrix.

Bonnet et al. [11] elaborates on different reinforcing particles and their effects on Young's modulus and density of a medium carbon (0.35 wt.%) steel. These include titanium and vanadium carbide (TiC, VC - see Figure 7) as well as TiB_2 which all form during eutectic solidification.

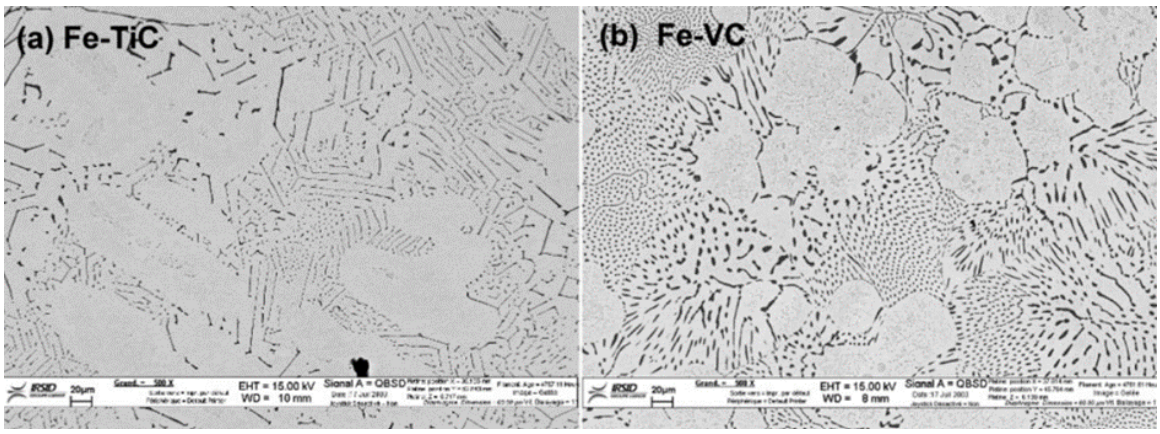

Figure 7: SEM images of (a) Fe-TiC and (b) Fe-VC as-cast microstructures formed under eutectic solidification [11]

From VIM, the results showed primary dendrites forming 10mm from the bottom of the cast piece. Increasing the fraction of composite reinforcement affects the morphology of the as-cast microstructure, which can vary from being lamellar to fibrous. Hot rolling was also performed at a thickness reduction rate of 50% with each pass, using a temperature of 900˚C to keep formability levels appropriate. As expected, both carbide and boride precipitates aligned with the rolling direction with equal distribution, before which a homogeneous heat treatment process was used (1200˚C for 30 min); no fracturing or reinforcement damage was observed.

This study also looks into specific stiffness and density measurements of TiC and VC at different fractions whilst comparing them to other composite reinforcements found in literature findings. This shows that a comprehensive analysis was carried out ensuring clarity and understanding of the chosen SMC's impact. Real-life applications such as weight savings and recycling for environmental targets were also addressed.

Another paper by Mengaroni et al. [60] studied the effects of microalloying elements in addition to base carbon steels of ferritic-pearlitic microstructure. VC precipitates are thermodynamically preferred over niobium carbide (NbC) precipitates as VC is more energetically favourable at lower temperatures, making it a better solute for dissolution and further grain refinement [73]. Similarly to Bonnet et al. [11], VIM coupled with hot rolling was used to simulate a large-scale industrial process. Nitrogen levels were kept at 40 ppm to prevent the promotion of vanadium nitride (VN) precipitates forming. After hot rolling at 1000˚C with a cooling rate of 1˚C/s, austenitisation was performed through tempering. This was done to improve the hardness of the steel by ensuring that the vanadium was fully solutionised. Figure 8 shows how Vickers hardness (HV) varies with the temperature, the value of hardness levels out as vanadium fully solutions at 980˚C. Carbon extraction replica alongside transmission electron microscopy (TEM) allowed for ferrite and pearlite phases to be easily distinguished, which was also verified through targeted electron backscatter diffraction (EBSD) analysis.

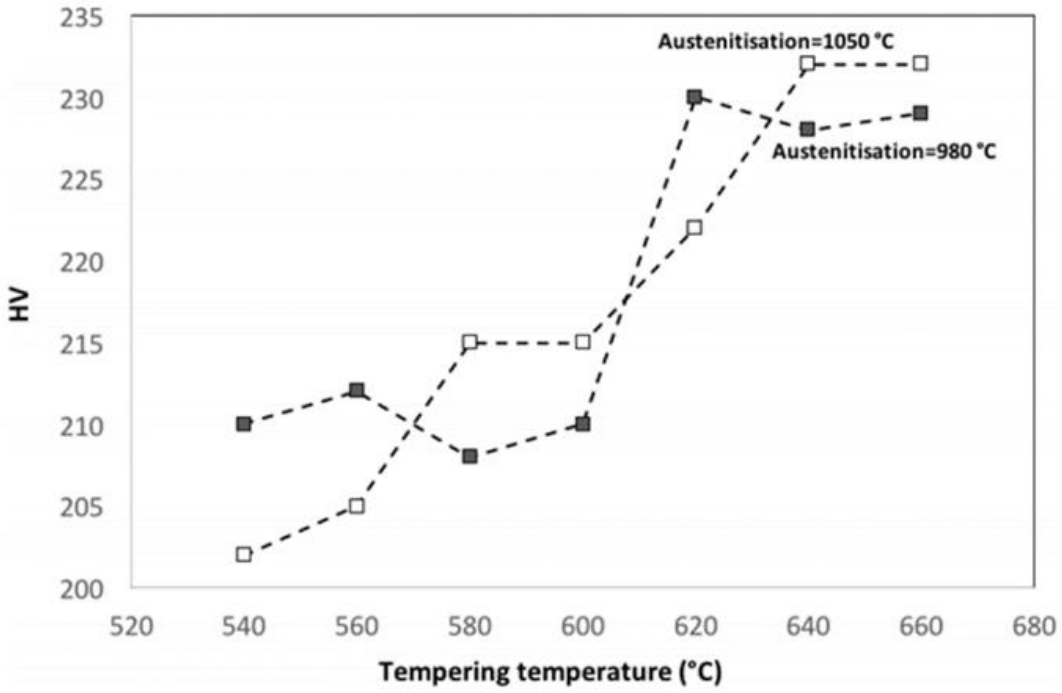

Figure 8: Change in Vickers hardness value with increasing tempering temperature [60]

Though both VC and TiC are excellent reinforcement precipitates, (Nb + Ti)C carbide reinforcement was studied by Kan et al. [66], where the aim was to combine the favourable density of Nb with the high strength of Ti. TiC is harder to homogeneously distribute due to its lower density, allowing it to float to the top of a cast piece during solidification. Carbide volume fractions of 5-10% were chosen as carbide segregation tends to occur at higher volume fractions [74]. The experiment involved arc melting 304 stainless steel followed by heat treatment at 1050˚C and water quenching. It was found that the solubility of NbC was decreased with the presence of ~5% TiC, which was demonstrated through SEM and EBSD mapping, clarifying the carbide morphology and phases present in each sample to the reader (Figure 5). When the TiC nucleated, fine particles formed, removing any acicular morphology that was present with solely NbC. Overall, it was concluded that combining Nb and Ti in a ceramic composite reduces the cost of materials, reduces the solubility of carbides in liquid-state steels and can improve particle hardness as well as sliding wear. These points were justified through a clear experimental approach presented, which included Vickers hardness and sliding wear testing.

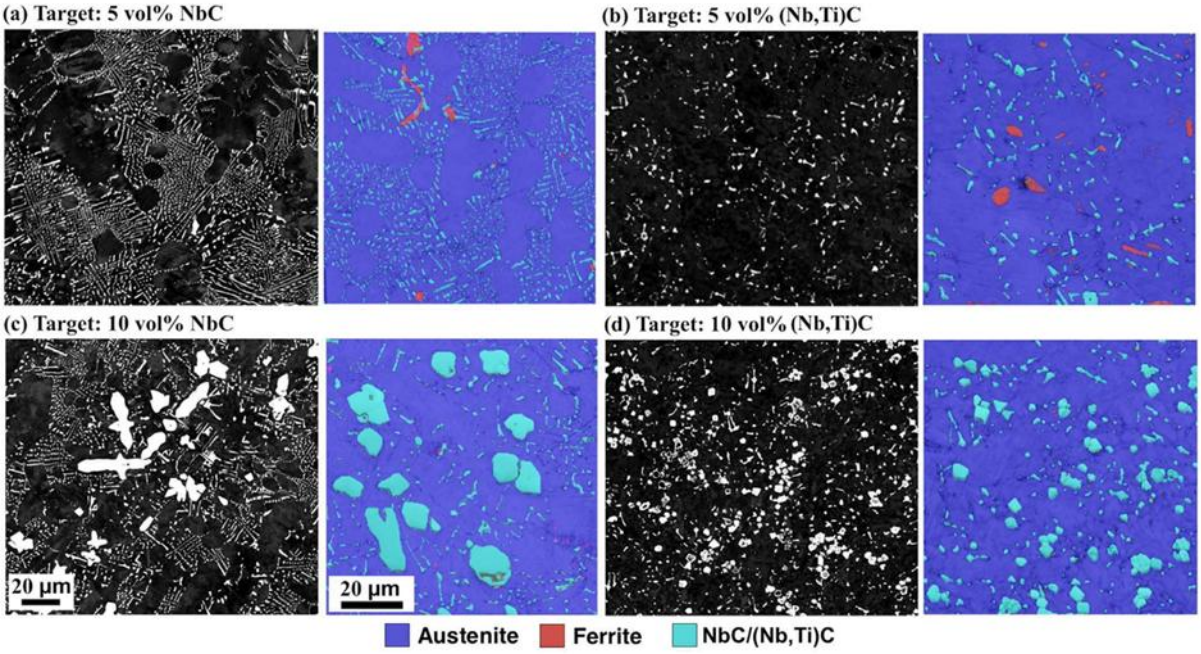

Figure 9: SEM and EBSD highlighting carbides in samples which each contain different volume fractions of Nb/Ti + C particles [66]

A study by Zhang et al. [75] investigated the strengthening effect of vanadium nitride (V-N) precipitates in an austenitic medium carbon steel. From the methodology used, controlled hot rolling at different temperatures followed by several different cooling rates was used to obtain different austenitic grain sizes. It was discovered that increasing the temperature and holding time would lead to a greater austenite grain size, which is due to pro-eutectoid ferrite nucleating. Zhang et al. [75] also performed Charpy mechanical tests on different specimens to check their compatibility with fracture splitting for automotive connecting rods. Larger amounts of ferrite would improve fracture toughness, but the wt.% of ferrite decreases at higher temperatures and holding times. Interestingly, the rate of grain size growth was found to be initially slow from temperatures 800˚C to 950˚C. This is due to the pinning effect of the V-N precipitates, which instigated greater energy as a requirement to overcome grain boundary movement. When there is a second phase particle present at the location of a grain boundary, the energy of this grain boundary decreases. This occurs as a part of the grain boundary is removed to occupy the surface area of a precipitate [45]. The SEM micrographs of each heated specimen were presented clearly (Figure 10), highlighting clear austenite grain

growth with increasing temperature. This paper concluded that particle pinning of VN slows the rate of austenite grain growth at higher temperatures (1100˚C), which was verified through experimental holding times and subsequent micrograph analysis.

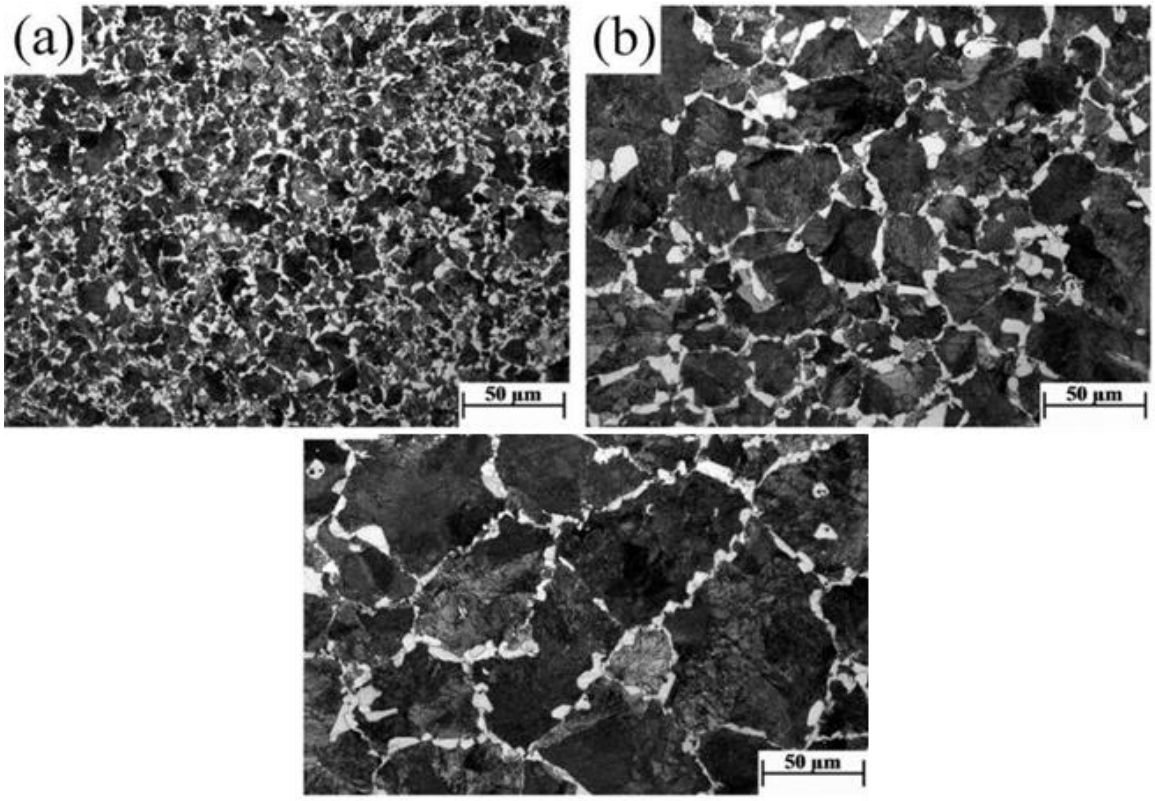

Figure 10: Prior austenite grain boundaries (PAGBs) found in a medium carbon steel at (a) 800˚C, (b) 1000˚C and (c) 1100˚C [75]

2.5.2 Boride Reinforcement

There are a number of ternary alloy systems composed of Fe-B-X (boride-based ceramic reinforcement), where 'X' is a transition metal that plays a crucial role in precipitation and strengthening mechanisms. A study by Baron et al. [1] looked at evaluating several elements to replace 'X', where it was appropriate to ensure a hexagonal lattice of XB_2 was present to ensure effective high modulus values. The paper looks at boride-compatible elements which vary from vanadium (V) and niobium (Nb) to chromium (Cr) and molybdenum (Mo). After arc melting samples and creating dog-bone test pieces to be used for mechanical testing, the following engineering stress-strain curves were obtained as shown in Figure 11 below [1]:

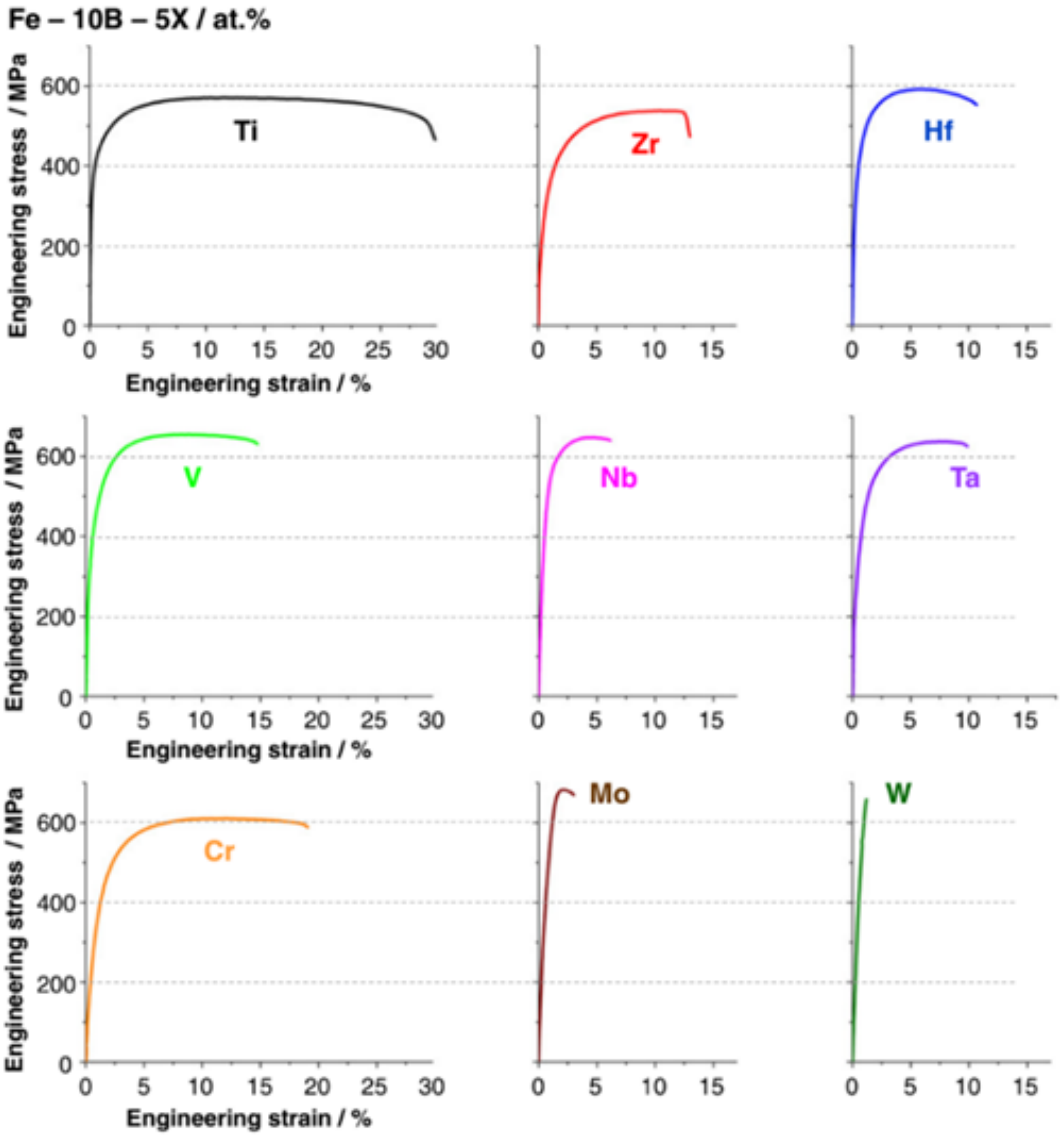

Figure 11: Engineering stress-strain plots for Fe-B-X alloys, where 'X' is the pairing element to the diboride reinforcement particle [1]

TiB_2 reinforcement is highly popular in strengthening and improving steel composites and this was justified as the Fe-B-Ti alloy showed an excellent specific modulus of around 31 GPa, yield strength of 420 MPa and ultimate tensile strength of 570 MPa. A variety of material characteristics were observed for the remaining alloys. For instance, V alloys showed great strength with less ductility which was due to a higher fraction of brittle boride particles within VB_2. Alloys which incorporated Mo, Ta, Hf and Nb highlighted spiky morphology from SEM characterisation. Alongside TiB_2, Cr and Zr were concluded to be the most promising for future alloy design [1].

To understand how TiB_2 works in a steel composite, it is important to appreciate the individual mechanical and thermal properties of this polycrystalline ceramic reinforcement. Many studies have justified the use of TiB_2 as a strengthening and stiffening addition, however the ceramic material has been independently researched by Munro [76]. The research describes the crystal structure as hexagonal, belonging to the P6/mmm space group. Identified methods of producing TiB_2 were listed, some of which being hot pressing, sintering and dynamic compaction. This highlights the flexibility of TiB_2 and its ease of production in industry. By itself, TiB_2 has an elastic modulus of around 565 GPa at room temperature which decreases with increasing temperature, however, higher values of density increase elastic modulus, as shown in Figure 12:

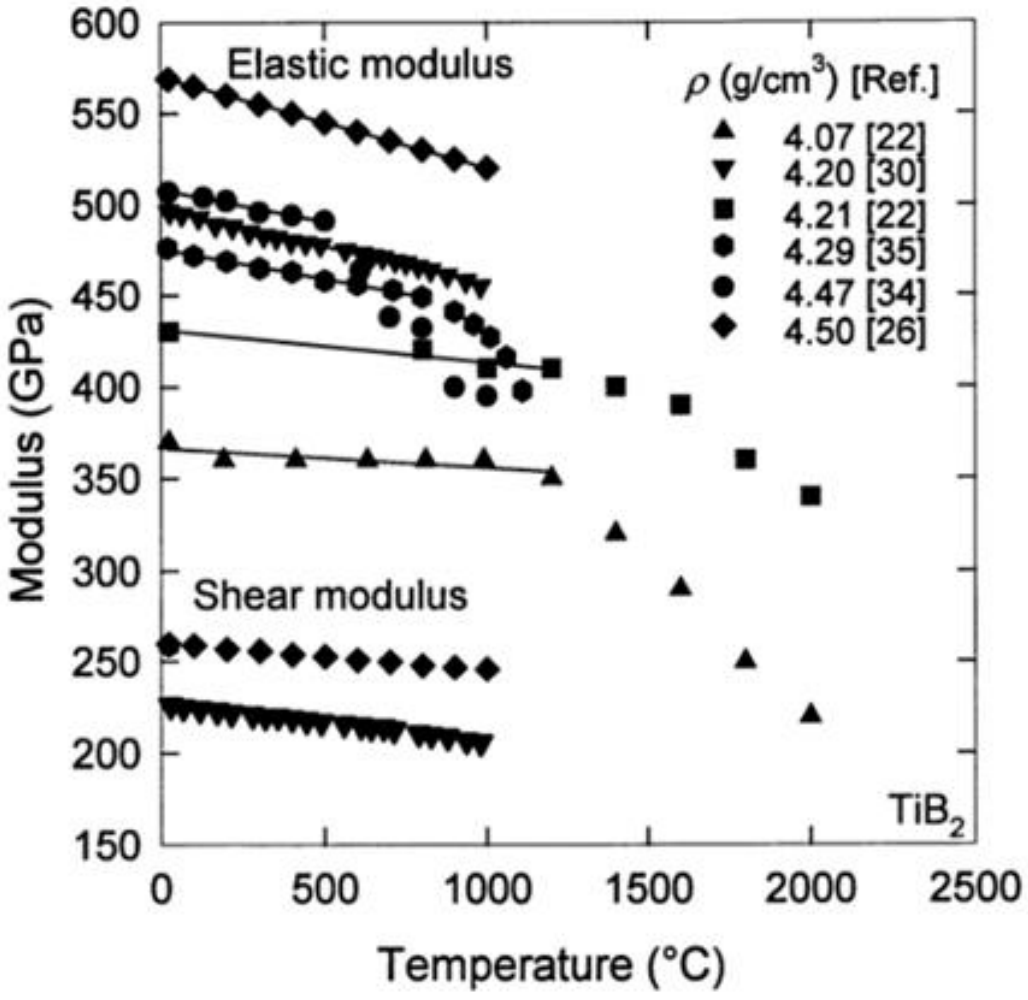

Figure 12: Temperature effects on elastic modulus at varying densities, ρ, of TiB_2 [76]

A fascinating early paper by Tanaka et al. [77] looked into predicting the ternary phase diagram of a Fe-Ti-B system. Initially, after obtaining a TiB_2 SMC through powder sintering, it was found that oxygen levels increased to a point beyond disregard. Using Thermo-Calc software, phase equilibrium was calculated, with the aid of an electron probe micro-analyser. An HMS with around 30% vol. of TiB_2 displayed fine precipitate particles using specimens created by sintering at 1523K [77]. The *in situ* TiB_2 was achieved through the synthesis of Fe-Ti and Fe-B alloys. The overall specific modulus increases with increasing volume fractions of TiB_2, agreeing with the simple theoretical assumption that TiB_2 retains its excellent stiffness in a steel matrix after hot forming processes such as sintering [77].

Li et al. [70] studied the effects of *in situ* TiB_2 reinforcements in a base low-carbon steel matrix, which was homogeneously present and fabricated using VIM. TiC and TiB_2 have high thermodynamic stability and possess excellent mechanical properties for strengthening. VIM in particular is used for the homogeneous distribution of ceramic reinforcement particles through electromagnetic stirring. Induction melting also allows for better alloy composition control and is slagless, with any oxides or gasses that have been produced being extracted out of the main chamber. TiB_2 is fabricated by mixing ferrous Ti (Fe-Ti) and ferrous boron (Fe-B), shown simply in the reaction equation below [70]. Solution-precipitation is the main mechanism which forms TiB_2 particles, which hold high thermodynamic stability once formed up to a temperature of 3498K [78].

$$FeTi + 2FeB \rightarrow TiB_2 + 3Fe \quad (5)$$

In the as-cast ingot, it was observed that the TiB_2 precipitates were distributed homogeneously but of different sizes due to different volumes of TiB_2 used. This paper shows that the greater the concentration of Ti and B in the matrix, the more stoichiometrically favourable they become for nucleation which is why they are

prominent at higher volume fractions. Interestingly, the coarse as-cast grains were refined significantly through a single-stage hot rolling process, however, the position of TiB_2 precipitates remained unchanged. This led to the results showing an ultimate tensile strength (UTS) increase from 590 MPa to 650 MPa based on 13 wt.% TiB_2.

An investigation on mechanical and tribological behaviours of TiB_2 in a reinforced AISI 420 martensitic steel was carried out by Sadhasivam et al. [79], who incorporated a TiB_2 powder in 1%, 2% and 4% volume fractions respectively. The powder was added to the crucible with the AISI 420 steel and brought up to a temperature of 1550˚C. Apparent TiB_2 and ferrite peaks were observed through XRD with no unfavourable secondary phases being present such as TiB or TiB_3. These phases are disadvantageous due to their lower thermal stability and less desirable mechanical properties.

Microscopy results highlighted an improvement in grain refinement, hardness and strength with increasing volumetric additions of TiB_2, which was homogenous in all samples due to the electromagnetic stirring effects that occur during VIM. Tensile data revealed that the tensile strength improved in all reinforcement addition amounts with linear improvements being made with more TiB_2 present. Yield strength also improved with a gradual decrease in ductility, leading to reduced fracture strain. This study identifies TiB_2 as an ideal reinforcement ceramic addition to SMCs as it does not change in morphology when mixed with a liquid state matrix and exhibits excellent mechanical properties in small wt.% additions. A more recent study by Chen et.al [67] studied the effects TiB_2 has on fracture toughness using hot rolling and tensile testing techniques. The first step was incorporating 9% and 13% volume fractions of TiB_2 using VIM with melting at 1650˚C followed by a two-step hot rolling procedure. Microstructural analysis revealed that as-cast SMCs display typical hypoeutectic structures with coarse TiB_2 particles homogenously distributed at less than 10μm in size. After rolling, the particles are aggregated and fractured in regions, particularly at higher volume fractions. This was due to the deformation

with the alignment of grains being observed in the direction of rolling. Upon tensile testing, it was clear that strength and elongation were improved with additions of TiB_2 after hot rolling. This is partially due to the grain refinement during hot rolling and the increased stiffness brought by the TiB_2 particles. At 13% volume fraction, TiB_2 particles agglomerate and are very prone to crack initiation and propagation which is not conducive to fracture resistance properties. Nevertheless, through hot-rolling and further grain refinement, fracture toughness was improved by 30%.

2.5.3 SMCs Fabricated through FAST

The fabrication of SMCs via FAST offers some noteworthy advantages. First, the rapid heating rates (often exceeding 100°C/min) and the high degree of control over the sintering environment minimise the oxidation of reactive elements, thus maintaining the integrity of the composite. The applied uniaxial pressure during sintering enhances densification by promoting particle rearrangement and deformation, leading to near-theoretical densities in the final product [80]. This high density is critical for ensuring that the mechanical properties, particularly hardness and wear resistance, are maximised. The distribution, morphology, and interface bonding of the reinforcement particles, such as carbides and borides, are critical factors influencing the overall composite performance. For example, TiB_2 offers superior thermal and chemical stability, high hardness, and excellent wear resistance. Its incorporation into the steel matrix via FAST results in a composite with an enhanced combination of toughness and hardness, suitable for high-stress, high-temperature applications. The interfacial bonding between TiB_2 particles and the steel matrix has potential to be strong as long as there is optimisation of the sintering parameters. The versatility of FAST allows for the fabrication of SMCs with tailored microstructures. By adjusting the sintering parameters such as temperature, pressure, and heating rate, it is possible to control the size and distribution of the reinforcement phases, the grain size of the matrix, and the overall porosity of the composite. This level of control is essential for optimising the mechanical properties of the composite for specific applications.

Thermal Mismatch and Interfacial Bonding in FAST

Thermal mismatch between the MA steel matrix and TiB_2 during FAST can significantly impact interfacial bonding. This mismatch arises from the differing coefficients of thermal expansion (CTE) between the steel matrix and TiB_2 particles. During the joule heating and cooling cycles of FAST, the steel matrix and TiB_2 particles expand and contract at different rates, generating thermal stresses at the interface. These stresses can lead to the formation of dislocations and microcracks around the TiB_2 particles, potentially weakening the interfacial bond.

High thermal stresses can also cause plastic deformation in the steel matrix, further compromising the integrity of the interface. The presence of microcracks and dislocations impedes effective load transfer between the matrix and the reinforcement, reducing the overall mechanical performance of the composite. Addressing this issue requires careful control of processing parameters which will be addressed in this thesis.

Literature in studying SMCs which use FAST is extensive and there are a variety of ceramic reinforcements used. One example investigates the influence of *in situ* ZrB_2 on an SMC (using FAST), studied by Iwona Sulima et al. [81]. When combined with 316L austenitic steel at different wt.%, several SEM images were obtained and analysed. The phase composition of different wt.% ZrB_2 highlighted that peaks became more prominent with increasing ZrB_2. It was deemed that the experiment was successful in combining a ceramic reinforcement with an austenitic stainless steel using SPS at a temperature of 1373K for 300 seconds, as a homogeneous microstructure was observed [81].

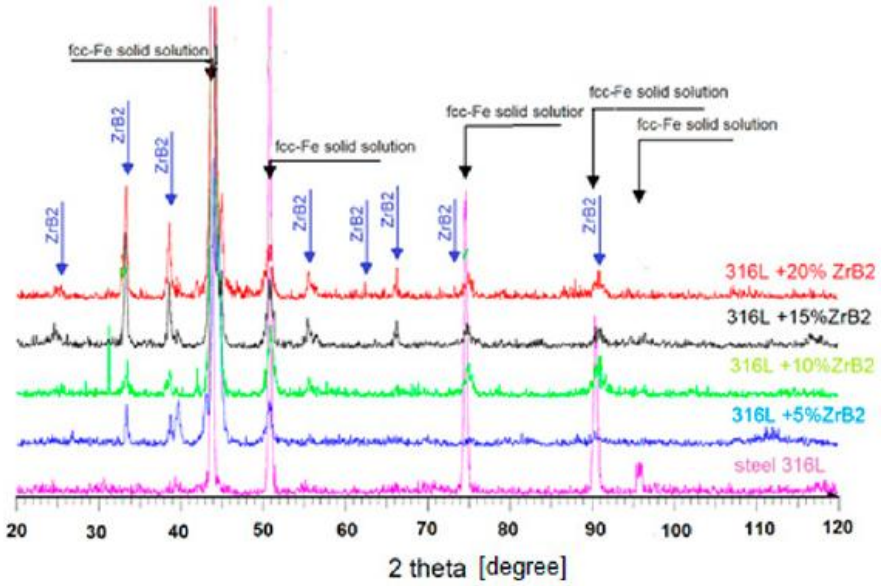

Figure 13: XRD pattern of sintered 316L with different wt.% ZrB2 ranging from 0-20% [81]

An example of a conventional sintering process used to incorporate a ceramic composite in a high-strength steel has been studied by Wang et al. [65], where a TiC-steel composite was created through a vacuum hot-press furnace using different temperatures to investigate the effect of bonding and overall microstructure. It was deduced that the TiC powder particles (50 wt.%) were uniformly distributed within the steel matrix. Measurements of relative density and porosity were obtained and it was concluded that specimens sintered at higher temperatures under the same pressure yielded higher densities and lower porosity percentages [65].

In situ TiB_2 and TiC-reinforced steel composites were studied by Binghong et al. [82]. The experimental procedure involved combining ferro-titanium and boron carbide powders using FAST, with a sintering temperature of 1100˚C at 30MPa holding pressure for 5 minutes. The 4µm composite powder thermally expanded at 650˚C, which was observed through a progressive reducing displacement between the two dies. Densification improved with increased temperatures which is assumed to be the case due to the wettability of the liquid phase being improved. It is important not to increase the temperature too close to the melting point of a material as sintering will cause excessive displacement which leads to voids or mould breakage, decreasing the effect of densification.

The SEM images obtained both from the milled powder and the sintered powder showed a homogeneous distribution. TiB_2 and TiC were observed at a particle size of 2μm, which is very fine. This small size may be because the particles had inadequate time to grow due to the quick sintering time. Binghong identifies that having a holding time past 5 minutes can lead to the growth of crystals, whilst a lower holding time will not allow for full consolidation. Both hardness and relative density show cooperative behaviour with increasing holding time (see Figure 14). A steady increment of temperature was used for the experimental runs (from 800˚C to 1050˚C) which yielded clear results and the conclusion stated that sintering temperature and hold time have vital effects on phase evolution and densification of the SMC.

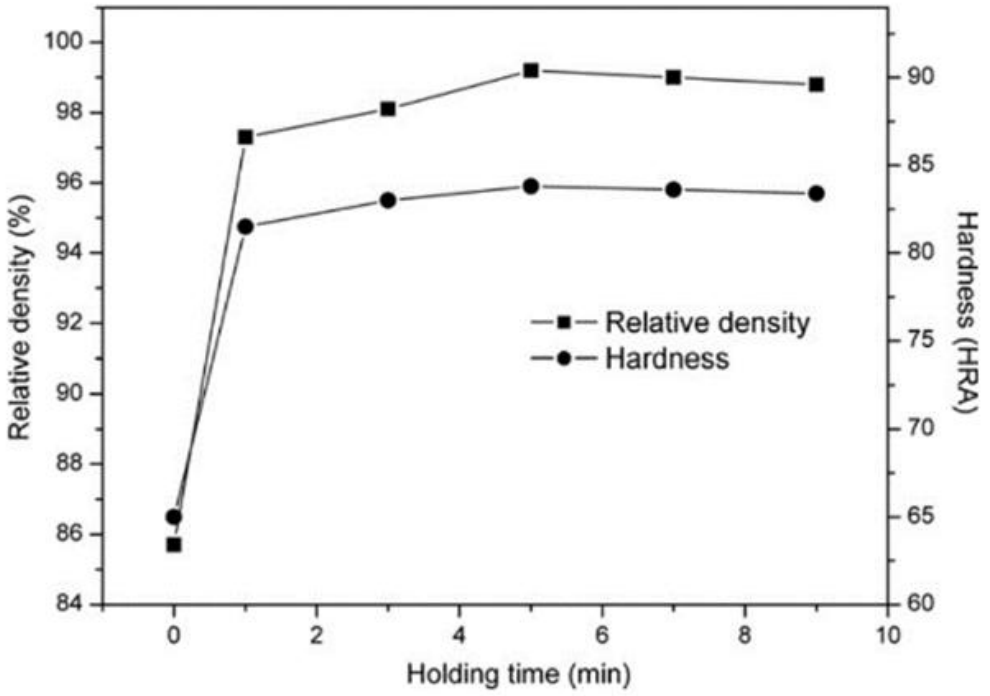

Figure 14: Relative density (%) vs holding time (min) vs hardness (HRA) at 1050˚C [82]

Sulima et al. [83] also studied the effects that FAST parameters have on the densification and properties of SMCs with TiB_2 reinforcement. This is particularly important as the fabrication of SMCs with FAST is uncommon and little has been

researched in this field, making this paper novel and significant for SMC development. A commercial 316L stainless steel powder (particle size 25μm) was sintered with different volume percentages of TiB_2 (particle size 2.5-3.5μm). The measurement of densification was carried out using Equation 6.

$$E = \rho \times C_T^2 \frac{3C_L^2 - 4C_T^2}{C_L^2 - C_T^2} \quad (6)$$

where Young's modulus (E) and the velocity of longitudinal and transversal waves (C_L, C_T) are used to calculate the density, ρ. C_L and C_T were determined as the ratio of the sample thickness and the relevant transmission time. Sulima et al. accounted for any percentage uncertainties for this calculation and the results yielded were found as shown in Figure 15. The TiB_2 was found to be homogeneously distributed in the matrix at all temperatures ranging from 1000˚C to 1100˚C, with a tendency for the particles to locate at grain boundaries.

It was clarified that the higher volumes of TiB_2 may have reduced the overall density of the matrix as the reinforcement has a lower density [84]. Microhardness values improved with greater additions of TiB_2, with an improvement of 60-80% when increasing the hold temperature from 1000˚C to 1100˚C. At 1000˚C, it was found that complete consolidation was not achieved due to a lack of intermolecular diffusion, with a porosity level of 6-18%. From tensile testing, TiB_2 reinforcement became a ductility limiting factor when exceeding 6% volume. It was also stated by Sulima that the dwell time strongly influences mechanical properties, with better bonding occurring at higher temperatures with better overall consolidation. It is important to stay under the liquid-phase temperature as reaching this state causes mould breakage and force deviation. It was concluded that for 316L the volume fraction of TiB_2 should not exceed 4% as the plastic properties become unstable. At 4% volume fraction, the highest tensile strength and satisfactory yield strength were observed and are deemed to be suitable for use in a wide range of temperatures.

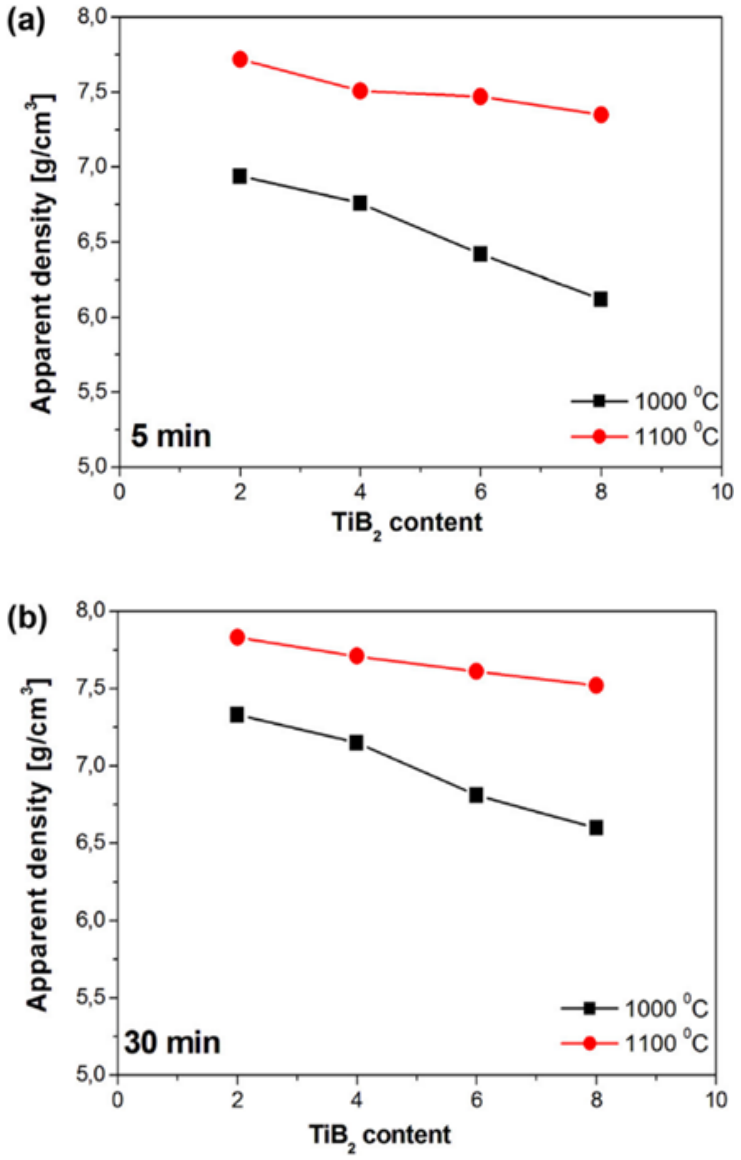

Figure 15: Apparent densities of composites at (a) 5 minutes and (b) 30 minutes dwell time [83]

A newer publication by Salustre et.al [85] focused on incorporating 12 wt.% TiB_2 in an MA steel matrix with 0.12 wt% carbon (C) using FAST. The parameters used were 5 minutes dwell time at 1000˚C and 60 MPa holding pressure. MA additions were Ti, vanadium (V) and niobium (Nb) all at 0.2 wt%. A computational diagram was created using ThermoCalc software to show the mass fraction of phases present with increasing temperature, which highlighted TiC and Fe_2B as pre-existing phases that form past the equilibrium austenitisation temperature, with TiB_2 forming and remaining stable past 1300˚C (Figure 16).

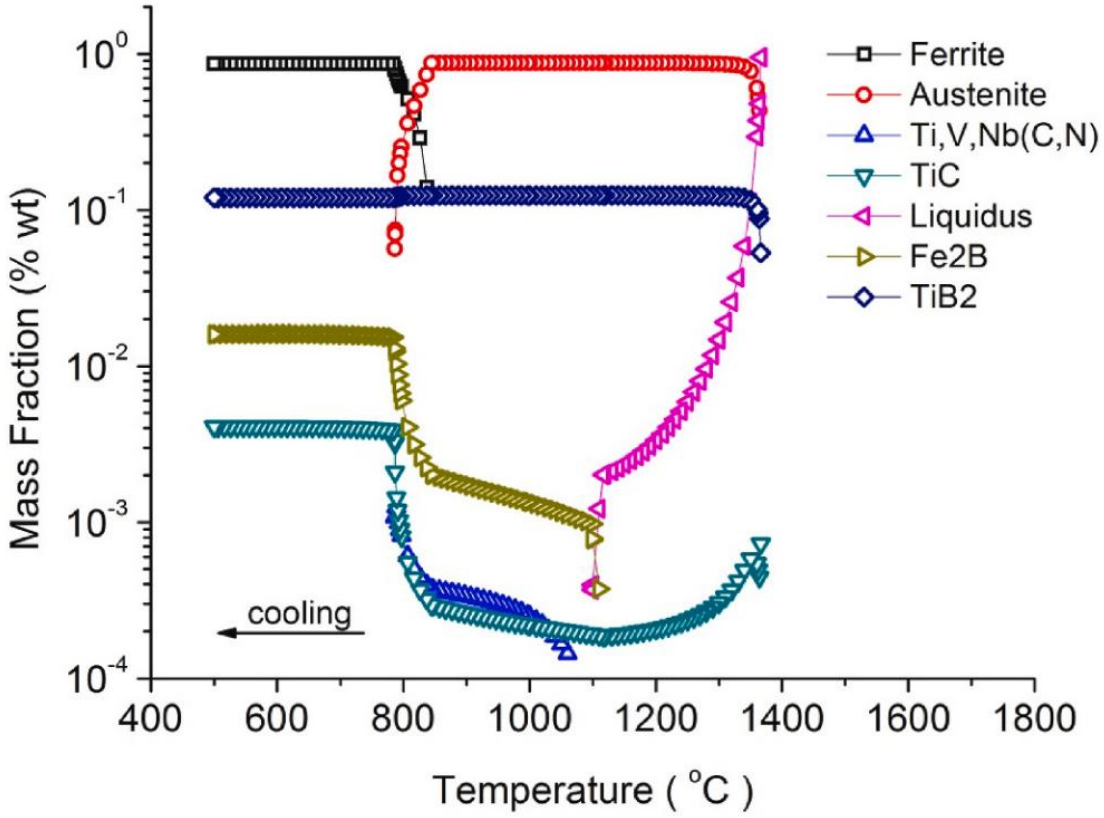

Figure 16: Phase prediction using ThermoCalc 2018b with a temperature range of 500-1400°C ***[103]***

XRD measurements confirmed the presence of ferrite, Fe_2B and TiB_2 with a homogeneous dispersion of TiB_2 particles. The sample was almost fully densified with 0.04% porosity and exhibited a 36.8% reduction in abrasive wear when compared with the original MA steel. The distribution of phases was mostly homogenous with small amounts of TiC present.

TiC in particular was not observed through XRD though was thought to form alongside Fe_2B due to stoichiometric reactions that take place with free carbon in the matrix. It is therefore vital to ensure that the wt.% additions of any alloying elements which tend to form secondary phase precipitates are carefully calculated so that there is not an excess or lack of an element, which will in turn push the formation of other phases.

Research into incorporating reinforcement into a steel matrix via the powder metallurgy (PM) route is steadily advancing, with new testing methodologies and discoveries enhancing understanding of the process. A key area of focus is the interaction between composite reinforcement powders and steel powders, particularly because the PM process is driven by solid-state mechanisms and is highly dependent on variables such as pressure, temperature, and dwell time.

Densification is a critical factor in this process, as the presence of porosity can significantly undermine the strength and wear resistance of the final composite. The relatively ductile steel matrix densifies through particle deformation and diffusion bonding when temperature and pressure are carefully controlled. However, the incorporation of hard ceramic powders like TiB_2, which has a high melting point of approximately 2970˚C, presents unique challenges. The extreme hardness and high melting point of TiB_2 can impede effective densification, making it difficult to achieve a fully dense composite material. This emphasises the importance of optimising processing parameters and understanding the complex interactions between the reinforcement and the steel matrix to ensure the desired mechanical properties are achieved.

2.6 Summary of Literature

The extensive body of literature on HMS reinforced with ceramic matrices highlights the advancements in enhancing the modulus and stiffness of various steel types, including those with austenitic and martensitic microstructures. Among the ceramic reinforcements, TiB_2 stands out as the most studied, particularly for its effectiveness in improving tensile properties and overall mechanical performance when incorporated into a largely ductile steel matrix. The abundance of tensile data and microscopy analyses available for TiB_2 composites reflects its popularity and success in providing the necessary stiffness and brittleness required in such applications. Incorporating TMP in the fabrication of SMCs has been shown to yield advantageous outcomes, particularly in terms of grain orientation and pore reduction, which are crucial for enhancing the mechanical properties of the composites.

However, despite the significant progress made with TiB_2, there remains a notable gap in research concerning the use of unique transition metals such as vanadium and niobium as additional microalloying reinforcements. These elements, when utilised in casting and sintering techniques, offer the potential for creating high modulus steels (HMS) with superior properties, particularly for automotive components, yet the area of MA steel composites (MASC) remains sparsely explored. This literature review provided key insights on FAST as a PM route for the development of SMCs, where parameters and results from previous studies will guide experimental work for this project. Such data from papers will be invaluable in advancing the development of HMS, particularly in optimising the use of novel reinforcements and refining TMP to achieve the desired balance of strength, stiffness, and ductility in steel composites. In conclusion, there remains noteworthy potential for further research, especially in comparing VIM and FAST processing routes for the fabrication of MASC alloys.

3. Methodology

3.1 Material Composition

This study looks at refining a case hardening steel which does not need additional heat treatment steps after fabrication such as quenching and tempering. These steels are referred to as precipitation-hardened ferritic-pearlitic (PHFP) steels with microalloying elements such as Ti, Nb and V added to form precipitate-strengthening mechanisms in the form of carbide and nitrides [10]. The PHFP composition was given as a recommendation from the collaborator of this project, Volkswagen. From this composition, a nearly identical microalloyed (MA) steel was fabricated using vacuum induction melting (VIM). The MA steel was then taken as a suitable matrix for the addition of Ti and B to form titanium diboride (TiB_2) as a reinforcing ceramic particle to improve mechanical properties such as Young's modulus. These alloys were studied with nominal 5 and 7.5 volume percent (vol.%) additions of TiB_2 and named as MA steel composites (MASCs). For example, '5MASC' represents a microalloyed steel matrix composite with 5 vol.% TiB_2 added. The elemental composition of these alloys can be found in Table 2.

Steel 4140 (S4140) was used for the field-assisted sintering technology (FAST) route at the beginning of this project. This was due to the unavailability of atomisation facilities during COVID-19. This alloy holds similar compositional qualities as the PHFP despite not having microalloying additions, and provided an excellent understanding of the powder metallurgy (PM) experimental procedure, allowing familiarisation of powder handling, powder analysis, sintering parameters and characterisation techniques. Importantly, all alloys studied in this project are medium-carbon (placing them in the hypo-eutectoid steel region) and high manganese steels. The elemental compositions for all alloys were externally analysed through induction-coupled plasma optical emission spectroscopy (ICP-OES), with the exception of S4140 powder which was provided with analysis by Hoganas, Sweden.

Table 2: Average elemental composition in weight percent (wt.%) of as-cast MA ingot compared to the targeted PHFP steel composition by W. Bleck et al. (PHFP) [10]*, S4140 and MASC alloys with 5 and 7.5 volume % additions of TiB_2*

Material	Fe	C	Cr	Mn	Mo	Nb	Ni	P	S	Si	Ti	V	B
MA Steel	96.56	0.47	0.13	1.37	0.06	0.030	0.17	0.013	0.010	0.72	0.03	0.18	--
5MASC	94.021	0.43	0.10	1.28	0.07	0.03	0.17	0.011	0.008	0.70	2.05	0.18	0.95
7.5MASC	92.991	0.38	0.11	1.29	0.07	0.03	0.17	0.013	0.006	0.75	2.55	0.19	1.45
S4140	97.068	0.40	1.0	0.90	0.2	--	--	0.026	0.006	0.4	--	--	--

3.2 Vacuum Induction Melting

A Consarc 10kg VIM unit was used to fabricate the MA steel and both MASC alloys with *in situ* TiB_2. VIM was also used to cast an MA steel bar which was later atomised for the PM route. All ingots were fabricated under vacuum conditions. As Figure 17 displays, the mould was assembled on the mould turntable inside the VIM chamber due to the weight of the assembly components. Boron nitride (BN) spray was used on surfaces where the molten metal is expected to come into contact with, such as the dipstick thermocouple and the inner mould walls. BN acts as a lubricating barrier, ensuring that there is no sticking during disassembling. An alumina crucible was mounted with a base steel inside along with iron pellets and ferrous refractory metals (Fe-Mo, Fe-Nb and Fe-B). The remaining alloying elements were placed in a charge (Figure 18) ready for dropping once the molten state was reached. After pumping the chamber to remove unwanted gasses, heating commenced using the power unit. The induction coil which surrounds the crucible is responsible for heating the material, where the temperature is increased by increasing the current (therefore power). A maximum temperature of 1600˚C (at a power output of 18 kW) was recorded for all alloys. After the remaining ferro- Ti, V, Si, Cr and Mn elements were dropped from the charge into the crucible, the

material was left to electromagnetically stir for 5 minutes before being poured into the mould. The cast ingot was left to cool in the chamber for approximately 4 hours before the mould was taken out and disassembled. A final clean of the chamber with isopropanol alcohol was performed to ensure that the system ventilation did not worsen over time.

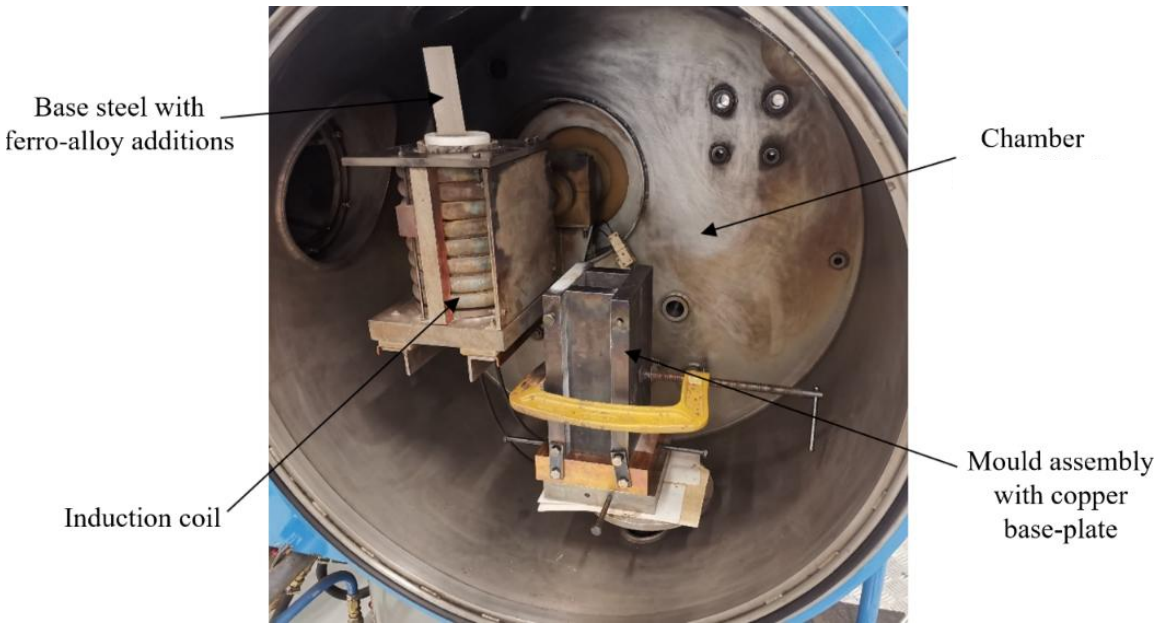

Figure 17: Labelled assembly in the Consarc 10kg VIM chamber

ICP-OES was carried out by Element, Sheffield, on the MA steel to see if the elemental composition was close to the target PHFP steel and theoretical [10]. This comparison can be found in Table 2, where a close match is obtained for most elements. It was assumed that the Ti would volatilise slightly during melting, however, the added Ti remained *in situ* leading to a slightly higher wt.% of 0.03 for the MA steel. It was expected that some Mn would volatilise and leave during melting, however most of what was added has been retained. This level of Mn is ideal as strengthening and hardening have been added to the steel without it becoming too brittle (at > 1.5 wt.%). Nb and V levels in the MA steel almost exactly match the PHFP composition, with the expectation of NbC, TiC and VC precipitates to be present in the matrix. A discussion of the MASC compositions is presented in Chapter 5, Section 5.2.

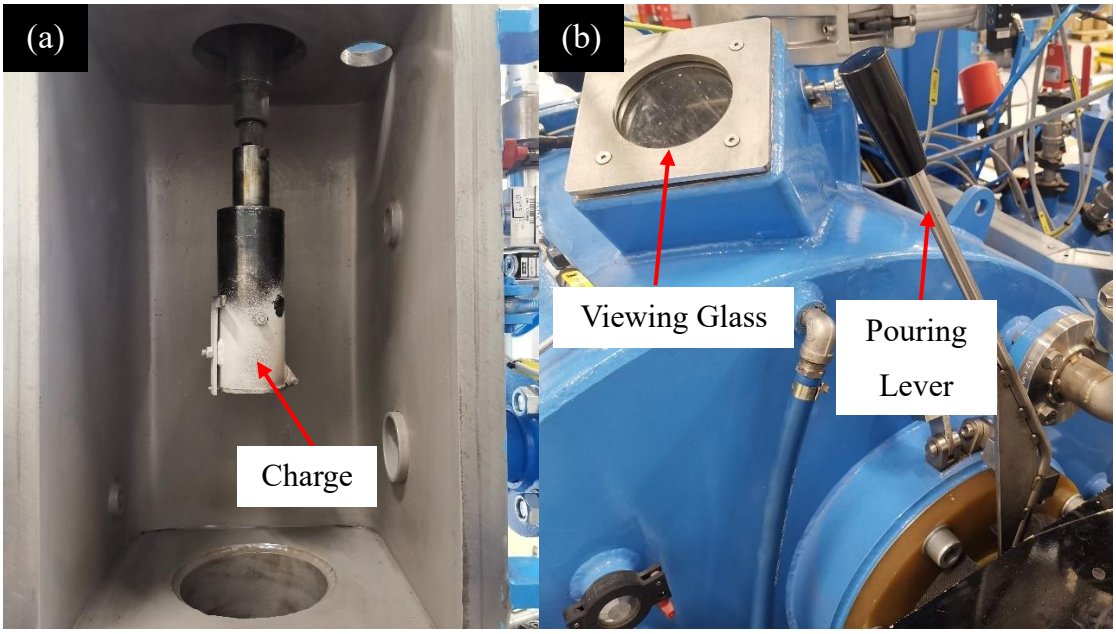

Figure 18: (a) Charge which holds the ferrous alloying elements positioned directly above the crucible and (b) viewing glass and lever for pouring the liquid alloy into the mould

3.3 Thermomechanical Processing

3.3.1 Hot Rolling

To ensure that the as-cast steel was entirely homogenised, a preliminary heat treatment was performed before the hot rolling stage, where the ingots were placed in a furnace at 1250˚C for 4 hours to ensure that all the alloying elements had been solutionised. The ingot was coating with BN as an effective barrier against oxidation. A FENN hot rolling mill with a run-out cooling table was used to reduce the thickness of the ingot to approximately 12mm; this thickness was chosen for easier post-machining as the specimens required for PSC testing need to be 10mm thick. The initial thickness of the ingot was 80mm and the rollers were set at a temperature of 200˚C (maximum temperature). This was done to ensure that the ingot does not cool too rapidly during deformation, which would lead to cracking and a poor surface finish. With each rolling pass, 5 mm thickness was reduced, meaning that a total of 14 passes were performed to get to the desired thickness. After the 7th pass, the ingot was placed back into the furnace for 10 minutes as the

temperature dropped to 918˚C (constant temperature monitoring was tracked with an infrared thermometer). Though this is still a high temperature past austenisation, it was important to keep the hot ductility of the ingot throughout the experiment. All information regarding the gap between the rollers, rotational speed, hydraulic pressure and dimensional parameters was monitored using an interactive screen (Figure 19). The ingot and rolling operation are also shown in Figure 20 alongside the final piece, which was left to cool to room temperature after the final pass.

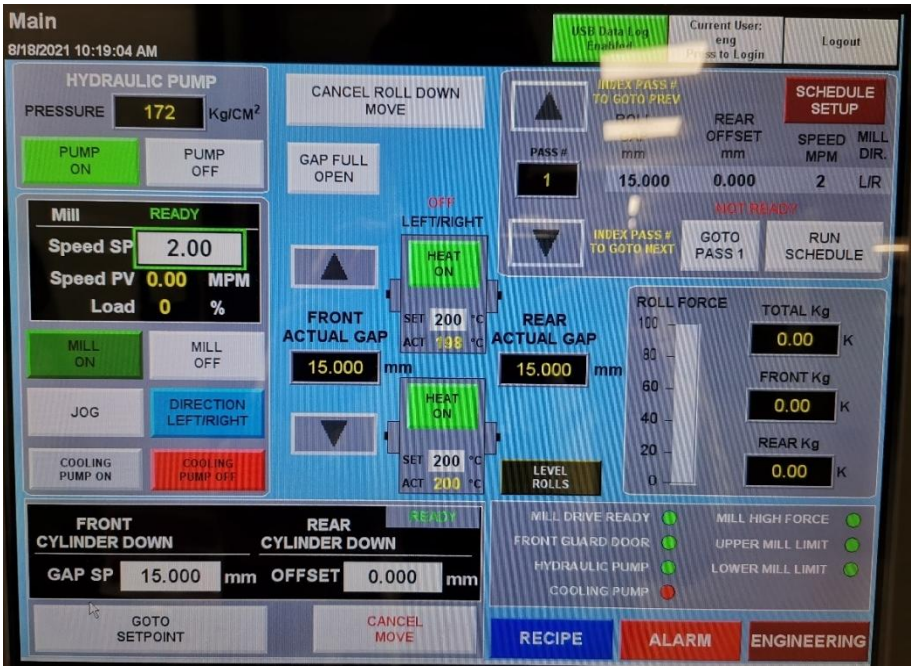

Figure 19: Live screen view on the FENN mill during hot rolling, illustrating various input/output variables and information on the reverse rollers

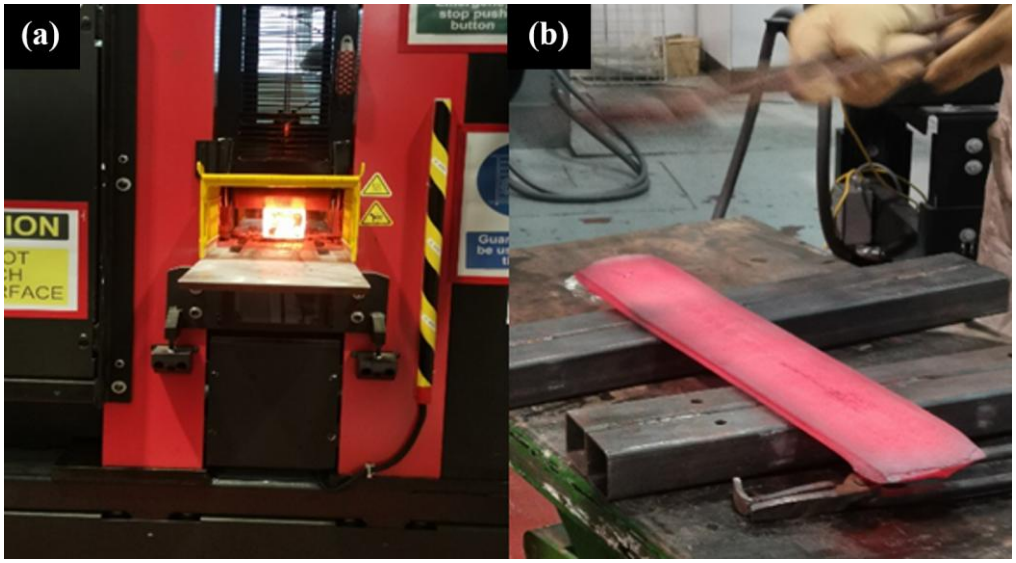

Figure 20: (a) Hot rolling of the MA ingot and (b) the final 12mm thick ingot left to air-cool

To simulate the final rolling passes in industrial processing, plane strain compression (PSC) samples were prepared from the hot-rolled ingots. The ingots were first machined into rectangular blocks with precise dimensions suitable for PSC testing, ensuring the samples were cut along the rolling direction to maintain the same grain orientation for all samples (as demonstrated in Figure 21), which is important for accuracy and consistency in microscopy analysis. After sectioning, the sample surfaces were ground to achieve a smooth finish, eliminating surface defects that could influence deformation. Finally, dimensional accuracy was confirmed using a micrometre, ensuring the samples met the technical drawing specifications.

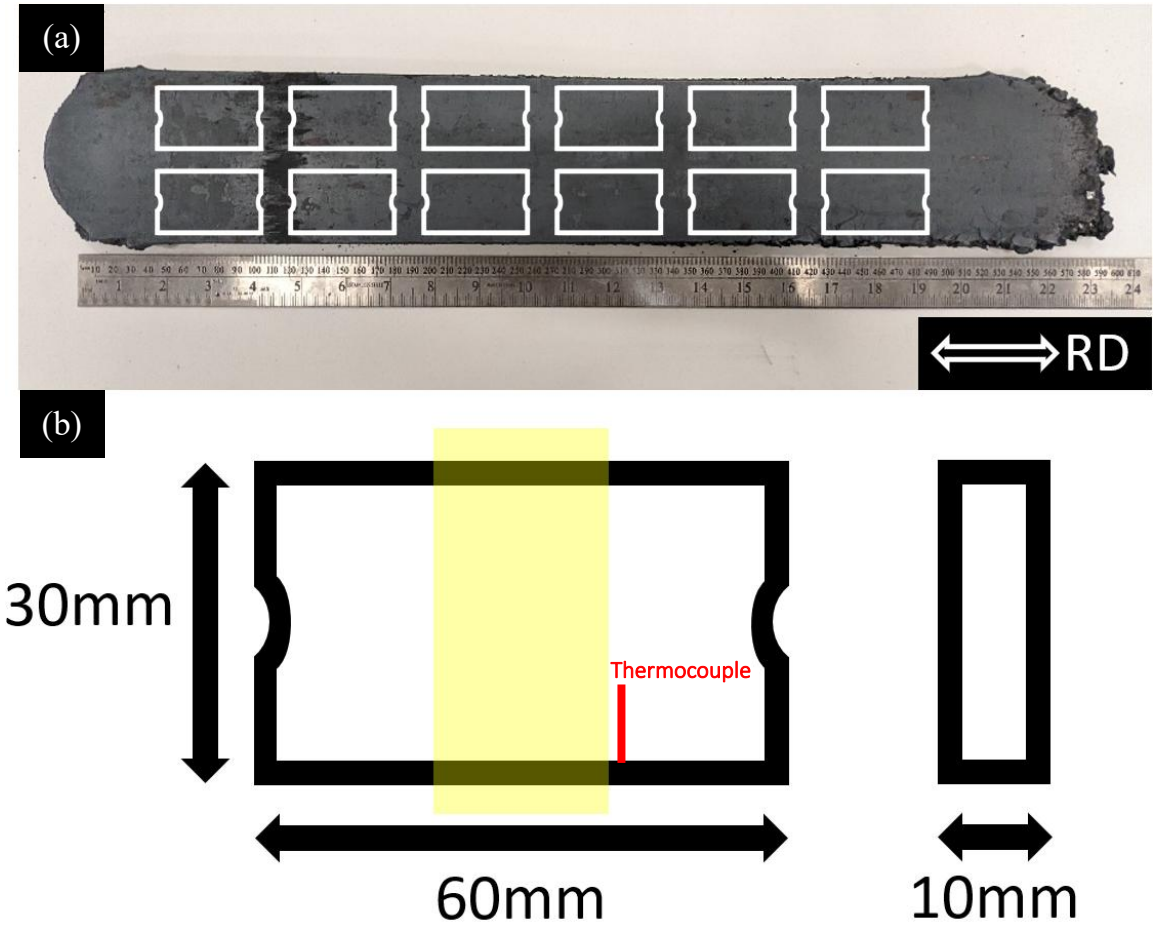

Figure 21: (a) Rolled MA ingot with 12mm final thickness and PSC sample orientation indicated with the rolling direction, RD, and (b) a geometry schematic of a PSC sample dimensions with the deformation zone highlighted in yellow

3.3.2 Final Rolling Simulation using PSC

During industrial rolling, materials experience plane strain deformation, making the plane strain compression (PSC) test the most suitable and widely used method for laboratory simulations of commercial hot rolling. The PSC test offers advantages over other techniques, such as achieving high-strain deformations and involves a larger area of deformed material, which is beneficial for subsequent microstructural and mechanical analysis. PSC tests were conducted to simulate the thermomechanical processing (TMP) of hot rolled sheet metal used in automotive body panels, utilising the servo-hydraulic Thermomechanical Compression (TMC) machine at The University of Sheffield. The TMC machine's fully digitised,

computer-controlled system allows for precise control of deformation parameters, including temperature, strain and strain rate. A full list of the technical capabilities of the TMC machine are summarised in Table 3:

Table 3: Main features of the servo-hydraulic TMC machine [86]

Features	**Machine Characteristics: Servo-hydraulic**
Actuators	Servo-hydraulic
Maximum strain	~2
Maximum strain rate	150-200 /s
Maximum deformation temperature	1200˚C
Maximum load	500kN
Machine Stiffness	410 kN/mm
Maximum FTTU reheating temperature	1300˚C
Full quench start time	< 0.5 seconds from the end of deformation
Controllable cooling variables	Forced air, mist and water quench
Reheating rate	Rapid and controlled heating (up to 1300°C)
Temperature measurement	Up to 3 thermocouples inside the PSC specimen

The purpose of the PSC experiment is to simulate the final rolling step, which is usually performed in manufacturing after a rough rolling procedure. This final step involves defining the imposed strain, strain rate and cooling rate to achieve a desired microstructure and target specific phase transformation during controlled cooling. For this experiment, five different temperature profiles were chosen with a constant strain (ε) of 0.3 and a strain rate of 10/s for two deformation passes. The steps and corresponding temperature profiles in Figure 22 are displayed as follows:

I. Sample is heated to 1250˚C and held for 2 minutes
II. Cooled to 1100˚C at 10˚C/s, then deformed at a strain rate of 10/sec and 0.3 strain
III. Held at 1100˚C for 20 seconds then cooled to 900/1050˚C at 10˚C/s
IV. When 900 or 1050˚C is reached, a second deformation pass is performed using the same strain and strain rate conditions. It is assumed that at 900˚C there is fully unrecrystallised austenite and at 1050˚C there is fully recrystallised austenite.
V. After holding the temperature for 10 seconds, the sample is either quenched or control cooled, where X is the defined cooling rate in ˚C/s. The cooling rates were 30, 2, 0.5 and 0.1˚C/s. The cooling was performed using forced air with mist for 30˚C/s, and forced air alone for 2, 0.5 and 0.1˚C/s. The temperature profile was obtained directly from a thermocouple placed 10mm into the PSC specimen, as indicated in Figure 21.

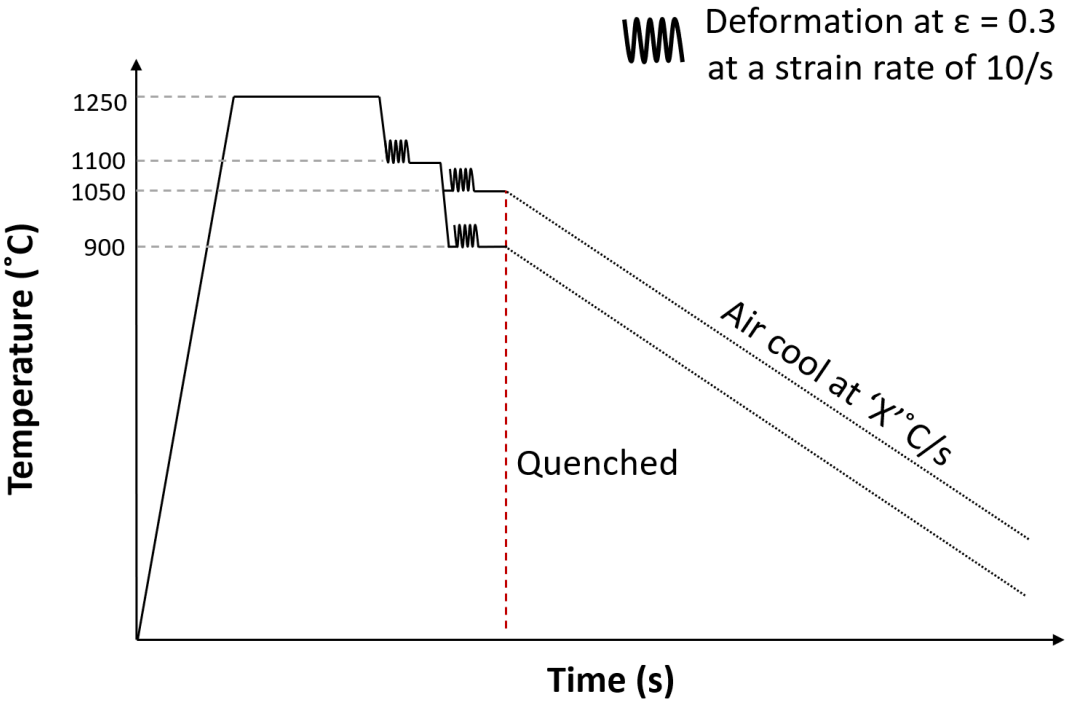

Figure 22: Temperature profile for PSC experiments

The setup of the PSC test is illustrated in (Figure 23). During the PSC test, the specimen is deformed between two flat, parallel tools (15 mm wide at room temperature) while load-displacement data is accurately recorded. The tools, made of a nickel-based superalloy, are sufficiently hard to endure the high loads required for high-temperature deformations.

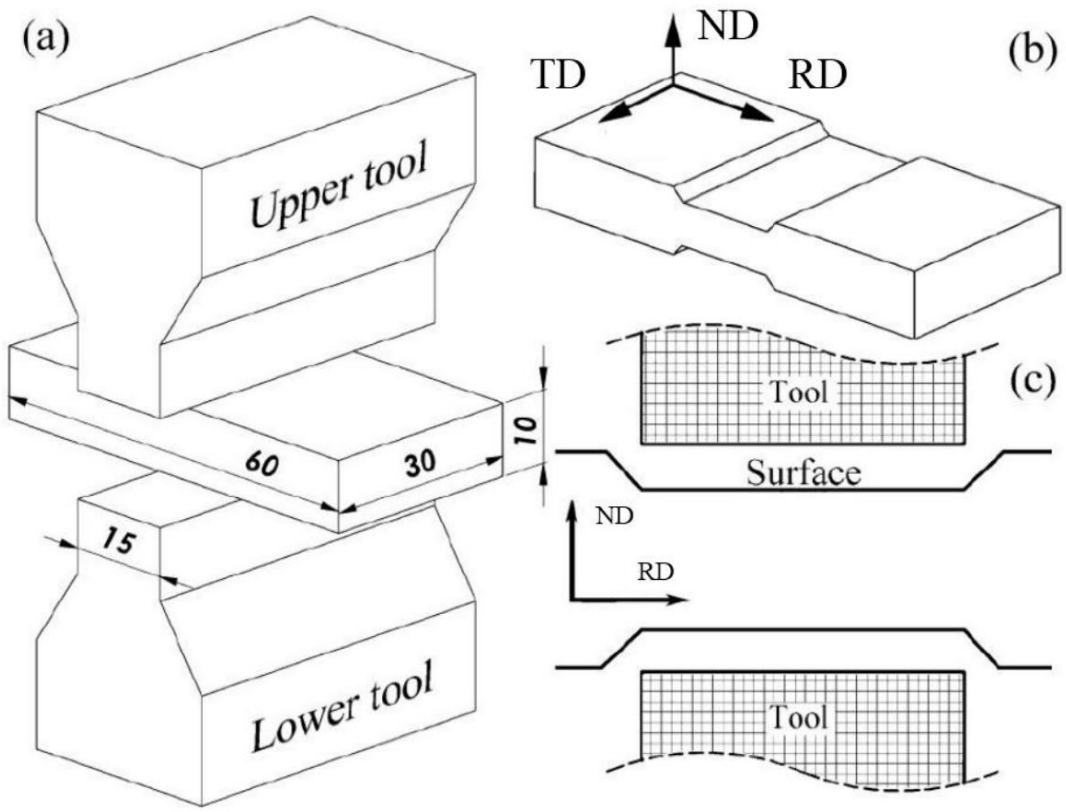

Figure 23: A schematic diagram of the PSC test setup is depicted, showing (a) the positions and geometries of the PSC specimen and deformation tools, (b) the deformed specimen, and (c) the normal direction-rolling direction (ND-RD) plane of the deformed PSC specimen used for microstructure characterisation [87]

An initial rough deformation pass was conducted at 1100˚C with a strain of 0.3. which should demonstrate austenite grain refinement above recrystallisation temperature. A second deformation pass was then carried out at either 900˚C or 1050˚C followed by isothermal holding for 10 seconds. Deformation at 900˚C was chosen to simulate the thermodynamic behaviour of each alloy above the equilibrium temperature A_{e3}, which is defined as the highest temperature at which austenite and ferrite co-exist in equilibrium [88]. The value for A_{e3} was calculated using JMatPro software [89] which is discussed in Chapter 4. At 1050˚C, it is assumed that the austenite recrystallisation temperature $T_{95\%}$, is surpassed [90], [91], which means the deformation and grain behaviour can be studied in a strain-free MA matrix. The MA steel, which becomes the matrix in the MASC alloys, was investigated in-depth to understand the effects of numerous cooling rates and quenching. Ferrite-pearlite (PHFP) was the target phase transformation [10] as high

modulus steels (HMS) predominantly exhibit the excellent ductility of ferrite and stiffness of pearlite. Quenching (to form martensite) of the samples from either 900˚C or 1050˚C was also performed to study the prior austenite grain boundaries (PAGBs) in the MA steel. For the final rolling stage of high-strength low alloy (HSLA) steels used for automotive components, it is common practice to hot roll at strain rates between 1-100/s at a strain of 0.2-1 and a temperature between 800˚C and 1100˚C [92], [93]. An example of a PSC specimen held in a robot arm controlling entry from the fast thermal treatment unit (FTTU) into the furnace with the tooling is shown in Figure 24, alongside a sample before and after two deformation passes:

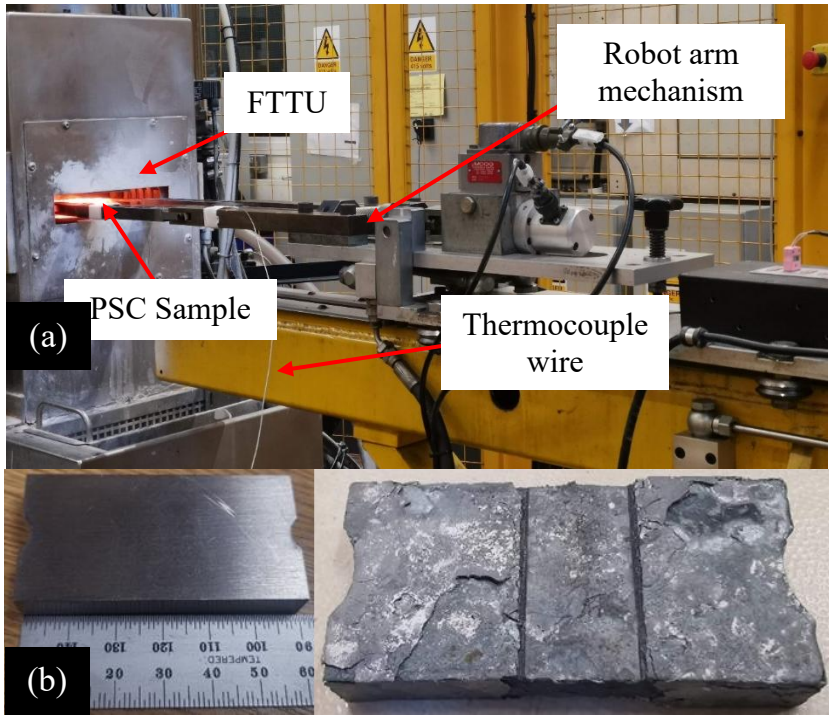

Figure 24: (a) Robot arm of the TMC machine inserting and holding a sample in the FTTU, and (b) an example specimen before and after PSC testing with two deformation passes performed

3.4 Powder Metallurgy

3.4.1 Atomisation

Gas atomisation was utilised to produce fine powders from a microalloyed (MA) steel with the same chemical composition used in the VIM process. Atomisation began with the mounting of an MA steel cylindrical bar (see Figure 25) in a chuck,

kept in a vacuum or inert gas atmosphere, typically argon, to prevent oxidation and contamination. The tip of the bar was then heated with an induction coil (Figure 26), where the steel reached liquid metal form allowing drips to fall. These drips were immediately subjected to high-pressure inert gas jets, which were directed at the molten metal to atomise it into fine droplets. The parameters of the atomisation process, including gas type, pressure, and flow rate, were accurately controlled to optimise particle size and distribution. In this case, argon gas was chosen for its inert properties and its ability to prevent oxidation, ensuring the production of clean, high-quality powder [94].

The high-pressure gas jets rapidly disrupted the molten stream, causing it to break up into fine droplets. These droplets quickly solidified into spherical or near-spherical particles as they cooled while falling through the atomisation chamber. The rapid solidification is essential in preserving the microstructure of the original steel, minimising grain growth and ensuring that the particles retain the desired properties. The solidified powder particles were then collected at the base of the atomisation chamber, often using a cyclone separator to effectively separate the finer particles from the gas stream. Post-atomisation, the powder underwent a rigorous sieving and classification process to segregate particles by size, typically ranging from a few microns to several hundred microns. The final powder was characterised by its morphology, particle size distribution, and surface properties, all of which are critical for subsequent processing steps, such as sintering or additive manufacturing. The fine, spherical particles produced through this atomisation process were particularly well-suited for FAST, ensuring high packing density, flowability, and mechanical performance in the final components.

Figure 25: (a) VIM mould assembly for casting the cylindrical MA steel bar and (b) as-cast MA steel bar with a cone-shaped end for atomisation

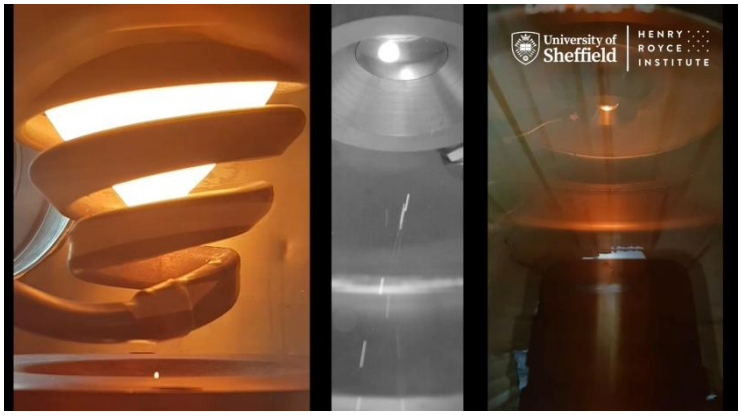

Figure 26: Induction coil and chamber view during gas atomisation at The Henry Royce Institute (HRI), Royce Translational Centre (RTC) [95]

3.4.2 Powder Analysis

Post-atomisation, the powder undergoes analysis to ensure it meets the specific requirements for FAST. The first step involves sieving and classification processes to segregate the powder into various size fractions, typically ranging from <45 μm 500 μm in diameter. This is achieved using a series of sieves with decreasing mesh sizes. The goal is to obtain a narrow particle size distribution that matches the target particle size range. After sieving, the powder is subjected to morphological analysis using techniques such as scanning electron microscopy (SEM). This allows for a detailed examination of the particle shapes, which are ideally spherical or near-spherical, as this morphology ensures better flowability and packing density. Irregularly shaped particles, such as those with sharp edges or elongated forms, are identified and quantified because they can negatively impact the flow characteristics and uniformity of the final product [96]. SEM provides high-resolution images that allow for the identification and classification of powder particles based on their morphology. Keywords commonly used to describe powder shapes include *spherical, near-spherical, irregular, angular, satellite* (where smaller particles are attached to larger ones), and *elongated.* These descriptors are key for understanding how the powder will behave. Spherical or near-spherical particles are typically preferred due to their superior flowability and packing density, which contribute to more uniform sintering and improved mechanical properties in the final product. Irregular or angular particles, on the other hand, may negatively impact flowability and could lead to defects in the final product, such as voids or inconsistencies [96].

For this project, a powder mixture containing 5% volume TiB_2 was calculated with MA steel as the matrix. Using the density of MA steel, determined as 7.71 g/cm^3 via the Archimedes principle, and the known density of TiB_2 as 4.52 g/cm^3 [76], a calculation was performed for a target mass (M) of 15 g in this instance. First, the total mass must be divided into the respective volume fractions of 5% TiB_2 and 95% MA steel. The mass contributions of each component can be calculated by multiplying the density, ρ, with the volume, V.

The volume of components TiB_2 and MA, V_{TiB2} and V_{MA}, is calculated first:

$$V_{TiB2} = \frac{M}{\rho} = 0.05 \times \frac{15}{4.52} = 0.1659 cm^3$$

$$V_{MA} = \frac{M}{\rho} = 0.95 \times \frac{15}{7.71} = 1.848 cm^3$$

The individual masses can then be calculated which sum up to 15 g. These powders can then be placed in a ball milling machine for homogeneous mixing:

$$M_{TiB2} = 4.52 \times 0.1659 = 0.75g$$

$$M_{MA} = 7.71 \times 1.848 = 14.25g$$

3.4.3 Ball Milling

To achieve a homogeneous mixture of <45 μm microalloyed (MA) steel powder with 5% volume TiB_2 powder, a calculation was performed based on the densities of the steel and TiB_2 powders, determining the exact mass of each powder required for a specific volume. The powders were then carefully weighed and loaded into a stainless-steel milling jar. Using the Retsch PM 100 ball milling machine, which features a planetary ball milling setup with two rotational axes, the jar containing the powder mixture was subjected to simultaneous rotations: the jar rotated around its own axis while also rotating around a central axis of the machine. This dual-axis motion generated significant impact and shear forces between the milling balls and the powders, promoting effective mechanical alloying and achieving the desired homogeneity of the mixture. The milling process was conducted at 400 revolutions per minute (rpm) which was selected to optimise the milling efficiency while avoiding excessive heat generation, which could lead to undesirable phase transformations or particle agglomeration. The milling duration was set at 15 minutes to achieve a uniform distribution of TiB_2 particles within the steel matrix, ensuring that the 5% volume fraction was consistently distributed throughout the MA steel powder.

Figure 27: Retsch planetary dual-axis ball milling machine

Figure 28: Mixed MA powder (45-150μm) with 5% vol. TiB_2

3.4.4 Field-assisted Sintering Technology

When setting up the FAST machine (FCT HP D 25, Figure 29), two important aspects need to be addressed: the machine/tooling setup and the software/recipe configuration. The process begins by switching on the chiller and activating the argon and atmosphere valves, which are essential for pyrometer flushing and vacuum release. A 20 mm mould assembly is prepared using upper and lower graphite ram pieces, wear pads, and graphite foil, which is lined along the inner mould walls to prevent powder adhesion during sintering, as illustrated in Figure 30. In some instances, boron nitride (BN) is also applied to prevent the powder from sticking and to mitigate any potential cross-reactions between the carbon foil and steel powder. Additionally, graphite foil discs are placed between the ram and wear pads to ensure smooth operation and to protect the tooling from wear during the sintering process. Finally, a graphite thermal jacket is encased around the assembly to prevent thermal losses during sintering. The setup ensures that the powder remains contained and uncontaminated, allowing for precise and controlled sintering conditions. After layering each component, the powder was pre-pressed using a hydraulic ram and the entire assembly was checked for any loose components or powder leakage Once the mould assembly was placed into the chamber with the thermocouple attached, the vessel was closed and the pistons were moved so that they hold the assembly at 3 kN pressure. This acts as a safety system as the vessel cannot be opened whilst the pistons are providing force. The mass of powder (m) needed is calculated simply through Equation 7:

$$m = \rho_s h_f \pi r^2 \tag{7}$$

where ρ_s is the apparent density of the powder material, h_f is the desired final height of the sample and r is the inner radius of the graphite mould. A recipe was configured using a computer linked to the FAST machine. The important steps involved in a FAST run are vacuuming, pre-hold pressure at 3 kN, increasing the pressure to the desired value, heating up until 400˚C for the top pyrometer to begin reading, raising the temperature at a desired rate (˚C/min), dwelling and finally cooling.

Figure 29: FCT HP D 25 machine

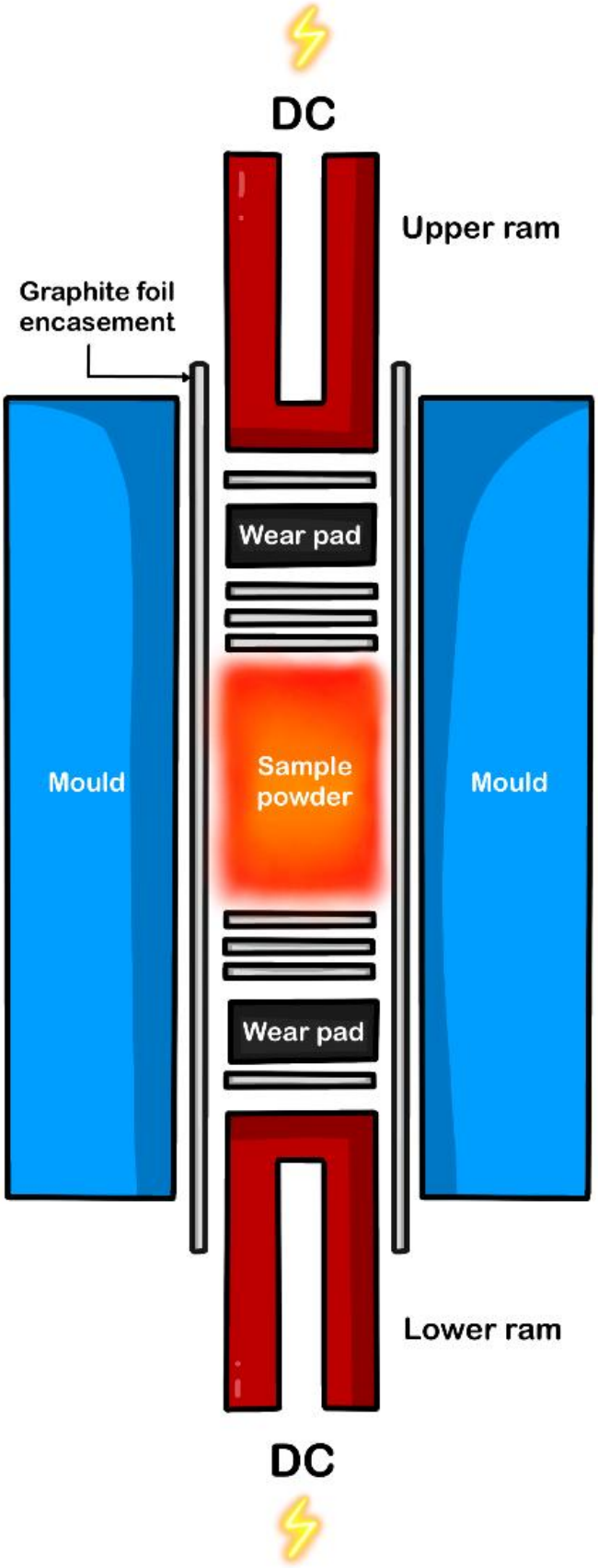

Figure 30: FAST mould assembly for a 20mm diameter sample

3.5 Metallographic Preparation

For microscopy analysis, the as-cast and hot-rolled MA steel using a band saw (Figure 31). To cut the MA steel using a band saw, the process begins by securely clamping the steel workpiece in place to ensure stability and prevent movement and vibration during cutting. Next, the speed of the band saw blade is set according to the hardness of the MA steel. Coolant is applied continuously to the cutting area to reduce friction, dissipate heat, and prevent the blade from overheating. This extends the life of the saw blade and ensures a smoother cut. The band saw is then operated steadily, allowing the blade to gradually work through the material without forcing it, which could lead to blade damage. After cutting, the workpiece is removed, and the cut surface is inspected for quality.

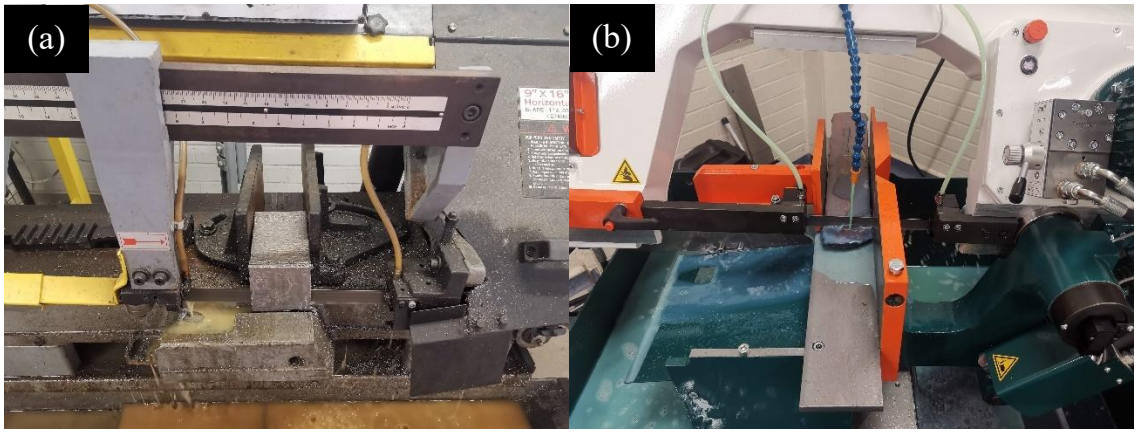

Figure 31: Band saw cutting of (a) as-cast MA ingot and (b) hot-rolled MA steel

The hot rolled ingots and deformed PSC specimens were sectioned along the rolling plane (ND-RD) and mounted in conductive Bakelite, ready for preparation using a grinder-polisher Automet machine. The steel surface was progressively ground with 600, 800, 1200 and 2500 grit silicon carbide papers, with water applied for lubrication. Final polishing was performed using three monocrystalline diamond suspensions of 6µm, 3 µm and 1 µm, respectively, until all visible scratches were removed, resulting in a mirror-like finish on the specimen surface. To preserve the surface before etching, samples were kept in a container of isopropanol alcohol (IPA) to prevent oxidation.

3.6 Etching

Etching is used to reveal and highlight the microstructural features such as grains, grain boundaries, and phase distributions. The process involves applying an acidic or alkaline solution to the polished surface of the steel, which selectively attacks and dissolves regions with lower surface energy, typically at grain boundaries and within specific microstructural phases. This differential attack creates contrast on the etched surface, making the microstructural features visible under optical or electron microscopy [97].

For microalloyed steels which have been heating treated, grain size measurements, in particular, prove to be difficult due to the number of alloying elements found in the chemical composition. Garcia et al. [98] sought to investigate the best procedure to reveal prior-austenite grain boundaries (PAGBs) by using different microalloyed steel compositions and several chemical etchants. These etchants varied from the traditional 2% nital solution to picric acid accompanied by different wetting agents. Revealing PAGBs is important due to their influence on mechanical properties (ductility, strength and fracture toughness) [16] [17]. All tested microalloyed steels were medium carbon (~0.3-0.4wt.%) with small additions of either Ti or V. Full saturation of carbon was allowed for the three separate heat treatments specified by Garcia; this was done to allow austenitisation of the steel matrix. To retain the prior grain boundaries, rapid cooling at 100˚C/s using water quenching was performed to trap the carbon atoms and prevent them from diffusing and forming carbon diffusion-related phases such as ferrite, pearlite and bainite; this left a lath martensitic structure which was fairly acicular and hard to characterise with nital alone, hiding the PAGBs. All three sheets of steel yielded poor results when picric acid with sodium tridecyl benzene sulfonate wetting agent was used. Between 6 to 12 drops of hydrochloric acid (HCl) were also added in a test to improve pitting around the grain boundaries, however, this also yielded noisy results (Figure 32). This could be due to low chromium content in the steels, making them highly susceptible to corrosion.

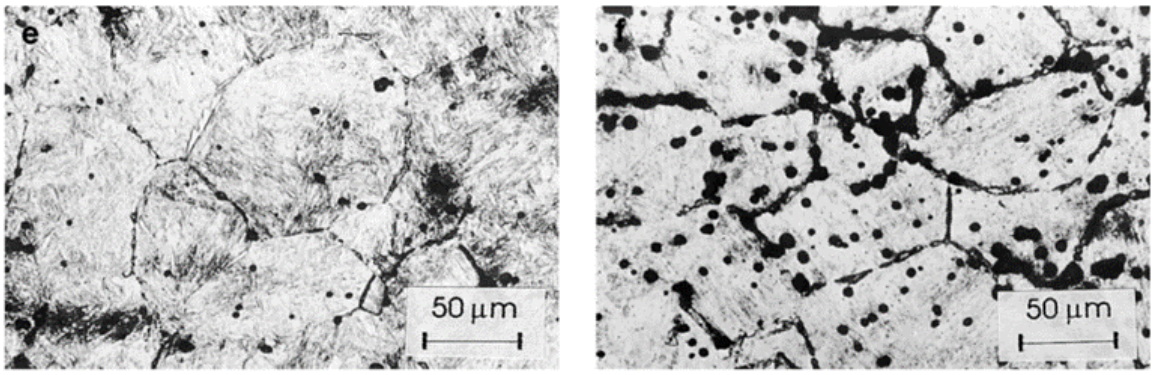

Figure 32: PAGBs of Ti+V steel at austenitisation temperatures 1150˚C (left) and 1200˚C (right), with pitting present as dark spots [98]

Garcia et al. also studied thermal etching as an option to reveal PAGBs, as grain boundary grooves are formed during transport mechanisms that take place at grain boundaries under cooling. These mechanisms are evaporation-condensation, surface and volume diffusion [101]. The grooves are what characterise the grain boundaries, where the mechanisms stated can be promoted by thermal etching. Unlike chemical etching, thermal etching only requires basic metallurgical preparation with the final step being a 1µm diamond polish finish. The samples were heated in a radiation furnace at 5˚C/s up until austenitisation temperature. This was done under vacuum to avoid oxidation on the top layer of the prepared sample. After cooling to room temperature at a rate of 1˚C/s, distinct PAGB's were observed in all microalloyed steel types at all temperatures. Though a slow cooling rate promotes carbon diffusion and other phases to form, only PAGBs are revealed in the matrix. This paper provides clarity as to which etching technique demonstrates a clear reveal for PAGBs. The total amount of data and microstructural analysis gives confidence to researchers, and a constructive approach is strictly followed which indicates consistency between runs on each microalloyed steel.

3.6.1 Nital

Nital (2% nitric acid 98% IPA) is a common etchant used in steels to reveal ferrite and pearlite in microstructures, and can also reveal bainite with stronger nitric acid concentration [102]. It is expected that ferrite and pearlite phases will be present in all cases excluding the quenched PSC samples; therefore, a simple etch was performed in a fume cupboard. The prepared samples were all initially checked under an optical Nikon microscope to ensure that the surface was free of any major scratches that could hinder characterisation. Nital etchant was pre-prepared and 20ml was poured into a small glass beaker. Using a cotton swabbing technique, etching occurred quickly in all cases (12 seconds) as the mirror finish of the sample's surface began to dull. To stop the etching process, a beaker of IPA was used to submerge the samples, followed by a rinse with distilled water and a spray of IPA again allowing for easy drying of the sample surface.

3.6.2 Picric Acid

Picric acid is often used to reveal PAGBs due to its effectiveness in selectively etching these boundaries while preserving the overall microstructure. Picric acid reacts with the steel, preferentially attacking the areas around the grain boundaries, making them more visible under a microscope. This etching technique highlights the PAGBs clearly, allowing for detailed analysis of grain size, shape, and distribution, which are important for understanding the material's thermal history and mechanical properties. The controlled etching process ensures that the grain boundaries are distinctly revealed without over-etching or damaging the sample surface [103].

A saturated picric acid solution (yellow liquid as Figure 33 highlights) with a sodium dodecyl sulphate (SDS) wetting agent was used on the quenched PSC samples to see if this would reveal PAGBs. There are many factors which affect the attack rate and etching quality of picric acid. These are the wetting agent used, the temperature at which etching occurs and the use of hydrogen chloride (HCl) to promote pitting at grain boundaries. 100ml of picric acid solution was measured and

1g of SDS was added. The acid was left to stir on a hot-plate magnetic stirring machine up until 80-85˚C was reached on the thermometer; after which 6 drops of HCl was added. Three dummy samples were placed in the solution for 5 minutes each to mature the etching solution as the rate of attack was initially very high in the picric acid. This darkened the solution to a desired colour as displayed in Figure 34 [103]. After some evaporation time (approximately 1.5 hrs) and the use of dummy samples, the same process used for nital was implemented to stop etching, with an additional step of swabbing with Teepol first to immediately stop the etching process. The etched surface was then examined using a Nikon Eclipse LV150 optical microscope to observe the prior austenite grains.

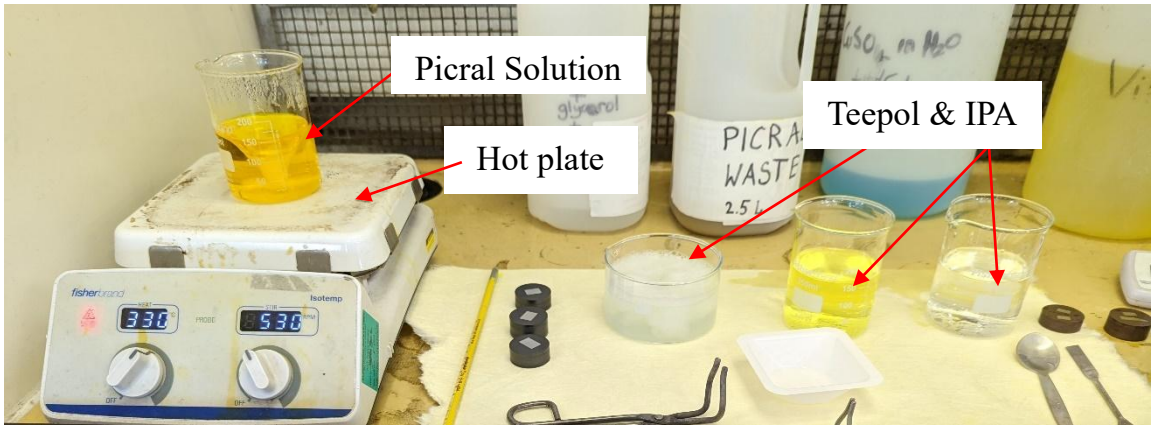

Figure 33: Setup of different solutions used during the picric acid etching process

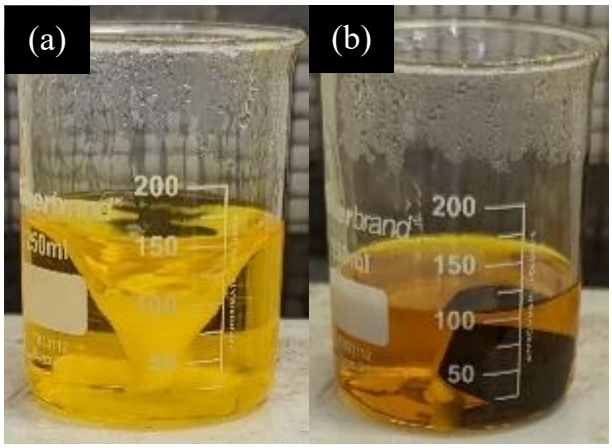

Figure 34: Picric acid solution (a) before and (b) after maturing the solution with three dummy samples

3.7 Microscopy

3.7.1 Optical and Scanning Electron Microscopy

To analyse the morphology of TiB_2 particles and the phases and grains in all etched samples, both optical and scanning electron microscopy (SEM) were employed.

Optical Microscopy: The etched samples were first examined under an optical microscope (Nikon Eclipse LV150) to observe the overall grain structure and the distribution of phases, as well as check that the polished surfaces before etching were clear of deep scratches. This step provided a broad overview of the microstructural features, such as grain boundaries and phase distribution.

SEM Analysis: Detailed morphological analysis was then conducted using an FEI Inspect F50 SEM. The mounted samples were placed under vacuum, and both secondary electron (SE) and backscattered electron (BSE) imaging modes were used. SE imaging highlighted surface topography, revealing the fine details of acicular ferrite (AF), TiB_2 particles and other phase structures, while BSE imaging provided contrast based on atomic number differences, allowing for the identification of different phases and particles within the matrix. This dual imaging approach ensured a comprehensive understanding of the microstructural features and the distribution of TiB_2 precipitates within the MASC alloys. Additionally, X-ray energy dispersive spectroscopy (X-EDS) was utilised to map the elemental distribution within microstructures, giving more data for the distribution and composition of TiB_2 particles and other phases in the MA matrix.

3.7.2 Electron Backscatter Diffraction

For electron backscatter diffraction (EBSD) imaging, samples were polished further using 0.1 μm colloidal silica with water. It was important to ensure the imaged surface was perfectly parallel to the opposite surface. The samples were also placed in an ultrasonic IPA bath for 5 minutes to ensure no colloidal silica remains were left on the sample. Due to the AF grains present in the quenched MA samples, a precision etching coating system (PECS) machine was used to laser etch the surface

of the sample (1 mm x 1 mm surface area) for 30 minutes at 5 kV power for a smooth finish. This is done to identify small ferrite grain size which can cause a hit loss during indexing. PECS enhances the surface quality of samples by using ion beam milling to remove surface layers and polishing the sample to achieve a high-quality, deformation-free surface. This is crucial for EBSD as it allows for clear and accurate detection of crystallographic orientations, grain boundaries, and phases. Parameters for EBSD using the JEOL JEM 7900 F were as follows:

- RD-ND plane analysed
- Working distance, WD = 164.7mm
- Tilt around RD = 70˚
- Used 0.1 μm step size for acicular ferrite recognition
- Fe-BCC/FCC package in HKL Channel 5 Flamenco
- Boundary & colour mapping obtained

Selecting an appropriate step size is crucial for EBSD mappings. Typically, a step size of one-tenth of the average grain size is used for microtextured and grain misorientation measurements, although the optimal step size also depends on the scale of the features being studied and the condition of the material. For observing the spatial distribution of texture components, a step size equal to the smallest grain size is effective. However, for detailed maps of microstructure morphology or subtle orientation variations within grains, a smaller step size is necessary [104]. Given that the grain size in the quenched MA microstructures was AF dominant, with grains typically ranging from 1.5 to 4.0 μm, and considering the high density of substructures within AF laths, a step size of 0.1 μm was chosen for the analysis of PAGBs.

3.8 Mechanical Testing

3.8.1 Tensile Testing

A standard ASTM E8 tensile test was conducted using a Zwick-Roell ProLine machine on deformed PSC specimens that were machined into dog-bone shapes, as shown in Figure 35, with the gauge area located within the deformation zone.

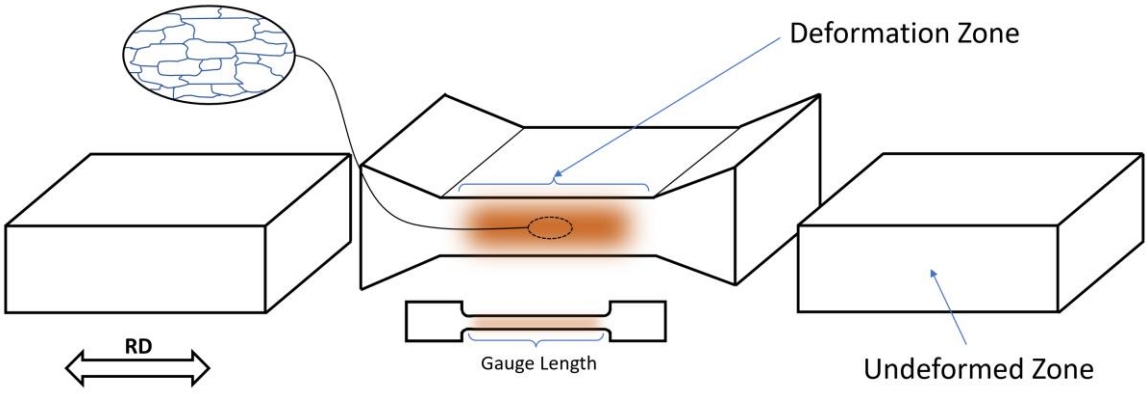

Figure 35: Schematic of how a tensile dog bone specimen is machined from a deformed PSC sample, with the indication of microstructural analysis on the RD plane

The geometry of these dog bone samples is indicated in Figure 36. The specimens were securely hand-clamped in the testing rig using two tool types (Figure 37), and the crosshead movement speed was set to 1 mm/min. The machine's software continuously measured the change in gauge length as the force was applied, generating a live plot of this relationship. To ensure accurate measurements, the gauge length was initially determined by attaching two pins at the start and end points of the gauge area, which were precisely measured with a micrometre. A camera on the tensile machine, aligned perpendicularly to the sample, tracked the pins to estimate the gauge length digitally. As plastic deformation occurred, the pins moved apart, and the digital reading updated, plotting the force against the change in length every second. This data was subsequently translated into a stress-strain curve, enabling the calculation of Young's modulus, yield strength, uniform elongation, and tensile strength. To minimise errors such as elongation measurement fluctuation, good grip contact, lighting and camera alignment were maintained.

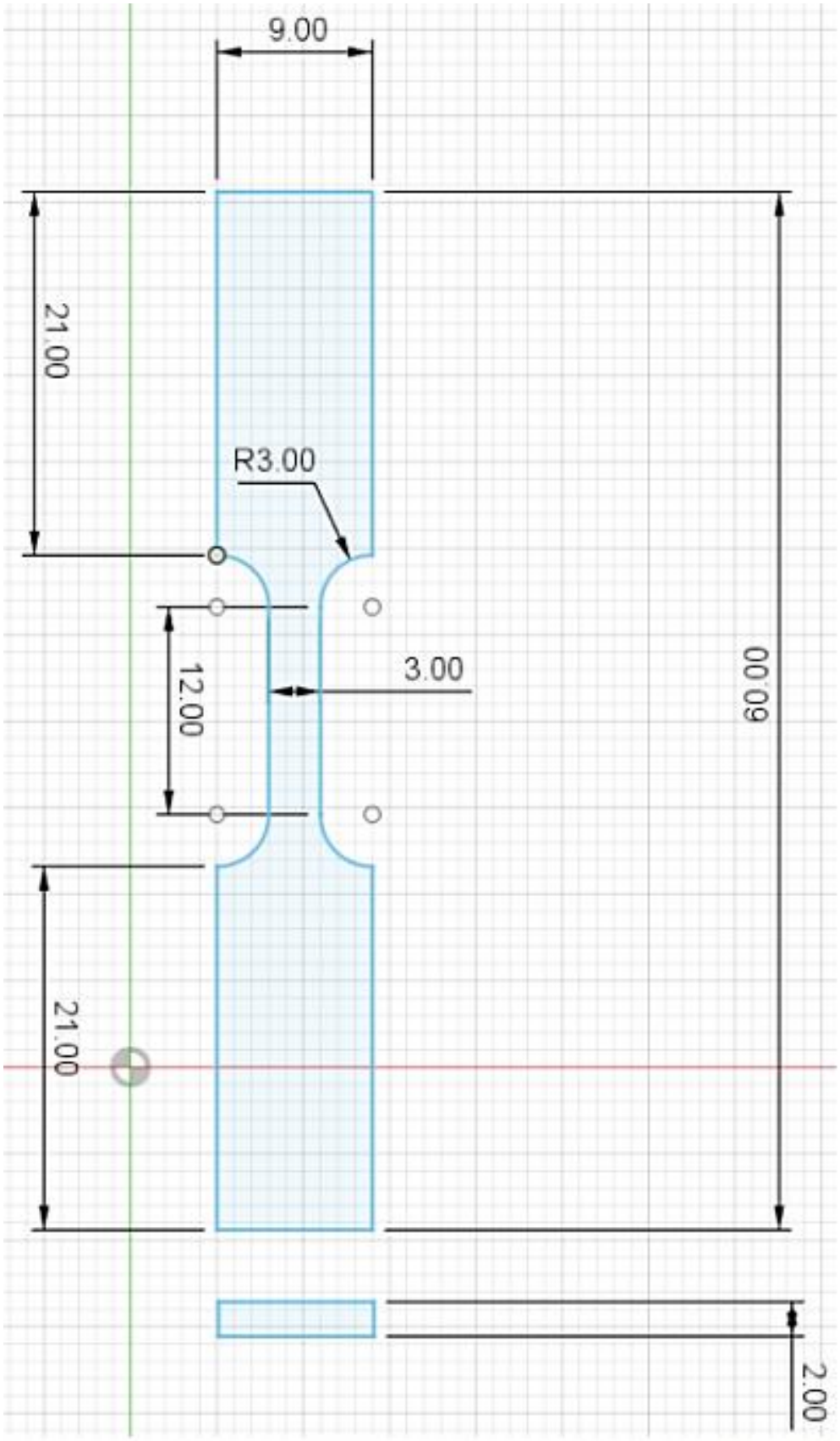

Figure 36: Technical drawing of a tensile bar machined from a deformed PSC sample

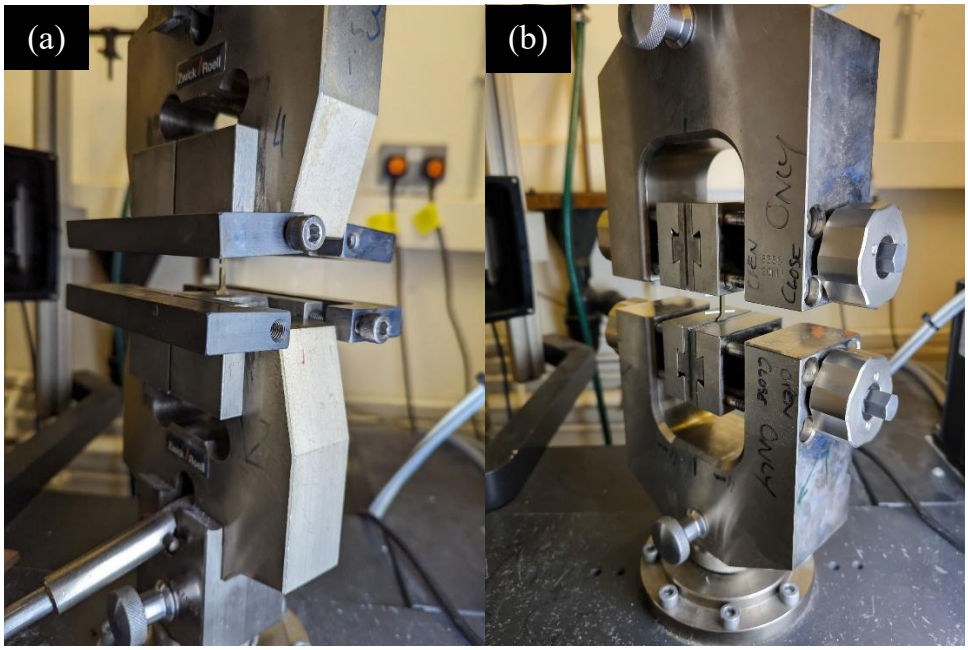

Figure 37: 15 kN tensile tooling with (a) black external clamps holding the dog bone specimen for added force to the grips and (b) revised 15 kN tooling holding a dog bone specimen, with a single bolt grip tightening mechanism

3.8.2 Resonant Frequency Damping Analysis

Resonant frequency damping analysis (RFDA) was used to obtain Young's modulus measures through a non-destructive technique using the integrated material control engineering (IMCE) RFDA Professional (Figure 38). RFDA is an impulse excitation technique (IET) that can gather accurate measurements of elastic modulus through vibrational testing. 'Free-free' testing was used to avoid unnecessary damping and uncertainty of supports; this means that the sample was not clamped at either end. The RFDA experiment is simple, with multiple frequencies being detected by a microphone at the time of impulse excitation, which is a percentage defined by the user through impact strength. The loss rate indicated by the software (Figure 39) is directly linked to the amplitude of the detected wavelengths. As well as the impulse excited detection there are secondary vibrations and ambient noises to account for. The mass of the sample was accurately recorded on a top-pan balance followed by accurate dimensional measurements which were taken with a micrometre. These are needed for the calculation of density, ρ of the samples.

Young's modulus is calculated using an ASTM C 1259/ASTM E 1876/ISO 12680 standard equation presented by Spinner and Teft in the early 1960s [105].

$$E = 0.9465\rho f_r^2 \left(\frac{L^4}{t^2}\right) T_1 \tag{8}$$

where Young's modulus, E, is dependent on the density of the material, ρ, the flexural frequency, f_r, the thickness of the sample, L, a correction factor, T and wave duration, t [106].

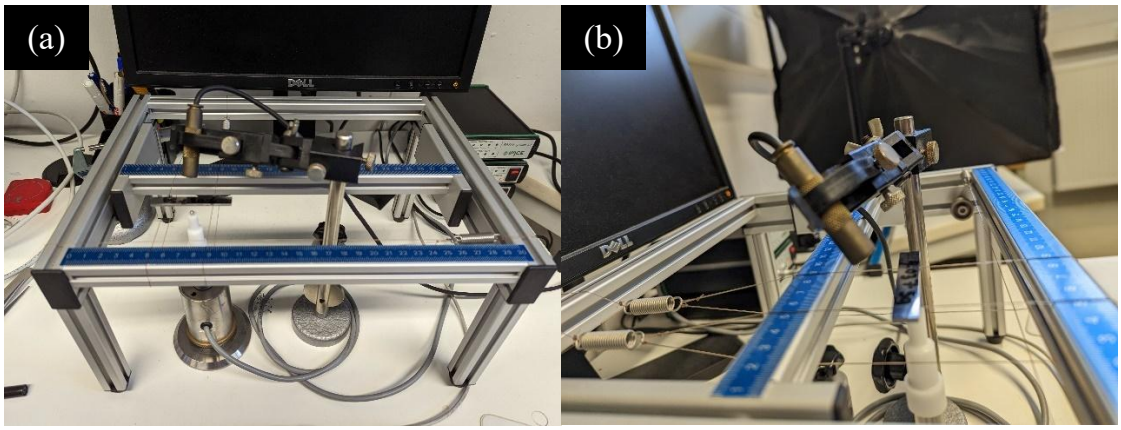

Figure 38: (a) RFDA apparatus and (b) side view of apparatus which illustrates the positioning of the microphone and impulse excitation device directly below the sample

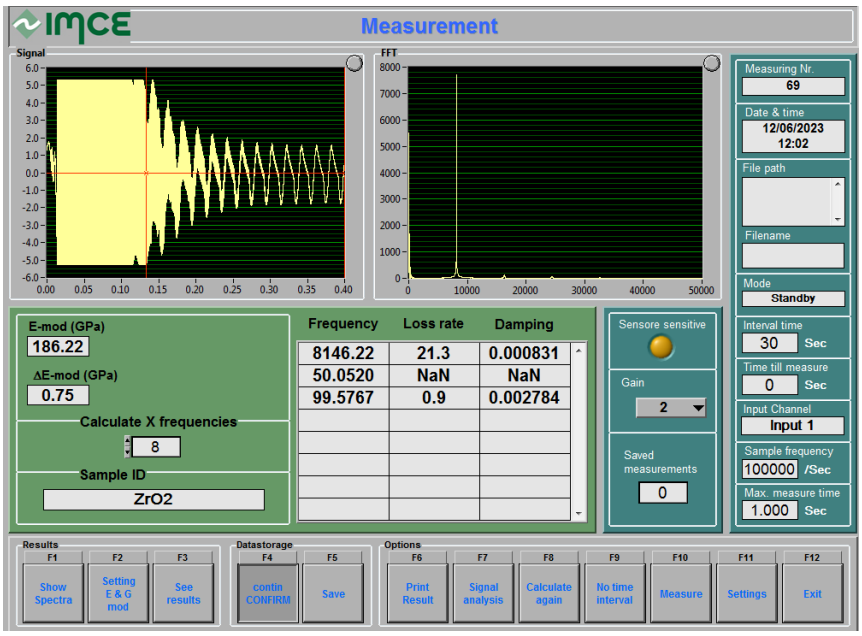

Figure 39: Software GUI from the IMCE RFDA unit, the plot on the top-left displays the signal captured by the microphone, while the top-right plot presents the Fourier analysis of that signal. Below the plots, boxes list the identified peaks and the calculated modulus.

The uncertainty given by the machine can be calculated using a standard deviation technique. An example would be ± 1.79 GPa uncertainty obtained from multiple modulus measurements on the MA steel. This calculation involves determining the variance, squaring deviations, summing them, dividing by the number of observations, and then taking the square root, as illustrated below:

1. **Calculate the Mean:** ∑measurements ÷ number of measurements = (205.0+208.5+210.0+206.0+208.0) ÷ 5 = 207.5 GPa
2. **Calculate the Squared Deviations from the Mean:**
    - For 205.0 GPa: $(205.0-207.5)^2 = 6.25$
    - For 208.5 GPa: $(208.5-207.5)^2 = 1.0$
    - For 210.0 GPa: $(210.0-207.5)^2 = 6.25$
    - For 206.0 GPa: $(206.0-207.5)^2 = 2.25$
    - For 208.0 GPa: $(208.0-207.5)^2 = 0.25$
3. **Sum the Squared Deviations:**
   6.25+1.0+6.25+2.25+0.25 = 16.0
4. **Calculate the Variance:**
   Sum of Squared Deviations ÷ number of measurements =
   16.0 ÷ 5 = 3.2 GPa^2
5. **Determine the Uncertainty:**
   Standard Deviation = Sqrt (Variance)
   Sqrt (3.2) = **± 1.79 GPa**

3.8.3 Vickers Microhardness

Using a Mitutoyo Charpy impact indenter, testing was carried out on all samples obtained throughout this project to see the evolution of Vickers hardness due to adding microalloying elements, TiB_2 and TMP stages including hot rolling and deformation through PSC. On each sample, 10 readings with averaged horizontal and vertical diamond indentation readings (in microns) were taken following the ASTM E384 standard [107], which was translated to HV1 values, using 1 kg mass or a force of 9.81N with a 20-second dwell time.

4. Medium Carbon Microalloyed Steel with Precipitation-hardened Ferritic-Pearlitic (PHFP) Microstructure Fabricated via VIM

4.1 Introduction

The development and optimisation of medium carbon microalloyed (MA) steel with a precipitation-hardened ferritic-pearlitic (PHFP) microstructure are well suited in the automotive industry where the relationship between strength, toughness, and ductility is vital. Medium carbon steels, typically with carbon contents ranging from 0.3% to 0.6%, offer a flexible platform for tailoring mechanical properties through controlled thermomechanical processing (TMP). When microalloying elements such as niobium, vanadium, and titanium are introduced, these steels can undergo significant transformation in their microstructure, particularly through precipitation hardening, which is a key mechanism for enhancing strength and performance.

Precipitation hardening in these steels occurs through the formation of nanoscale carbides, nitrides, or carbonitrides, which impede dislocation motion within the ferritic and pearlitic phases. This results in a significant increase in yield strength and tensile strength while maintaining satisfactory ductility. The fine precipitates serve as pinning points within the microstructure, restricting grain boundary movement and refining the overall grain size. This is particularly important in automotive applications, where components are subjected to complex loading conditions that require materials capable of withstanding both high static and dynamic stresses without yielding to brittle failure.

The vacuum induction melting (VIM) process is fundamental to the fabrication of these advanced steels, providing the precision required to achieve the desired composition, and ensuring that the microalloying elements are evenly distributed throughout the molten metal. This uniformity is crucial in preventing the formation of unwanted phases or inclusions that could compromise the material's mechanical

properties. Additionally, the vacuum environment minimises the presence of gases such as oxygen and nitrogen, which can lead to the formation of non-metallic inclusions that weaken the steel.

In the context of the PHFP microstructure stated by Bleck et al. [10], the ferritic phase provides a matrix that is relatively soft and ductile, allowing for energy absorption and deformation under load, which is essential in applications such as crash-resistant automotive structures. The pearlitic phase offers high strength and hardness, contributing to the wear resistance required for components like gears and bearings. The relationship between these two phases, coupled with the strengthening effect of the precipitates, results in a composite-like behaviour where the material can endure both high loads and impact forces without significant plastic deformation or failure. The microalloyed elements further contribute to the refinement of the pearlitic colonies, enhancing the interlamellar spacing within the pearlite, which in turn increases the strength of the steel [108]. This microstructural refinement is essential for achieving the high fatigue resistance needed in automotive components subjected to cyclic loading.

This chapter researches the process of fabricating a medium carbon MA steel with a PHFP microstructure via VIM, exploring the relationship between microalloying elements, processing parameters, and the resulting microstructural and mechanical properties. By examining the interaction of phases within the microstructure and their influence on the material's behaviour, this work aims to contribute to the ongoing development of high-performance steels tailored to the demanding requirements of the automotive industry.

4.2 Fabrication of a Microalloyed Steel

This section explores the fabrication of an MA steel, utilising the composition outlined by Bleck et al. [10], which Volkswagen recommended as an optimal matrix material before the incorporation of TiB_2 as a composite reinforcement.

4.2.1 VIM and Hot-rolling

The fabrication of the MA steel used in this study was initiated through the VIM process. This method was selected to achieve precise control over the chemical composition, ensuring the successful incorporation of various ferrous alloying elements to match the target PHFP composition proposed by Bleck et al. [10]. As confirmed by the compositional analysis in Table 4, the elements C, Mn, Ti, V, Nb, Si, Cr, and Mo were accurately added to achieve the desired alloy characteristics. Following the VIM process, the as-cast ingot underwent a preliminary heat treatment at 1200˚C for two hours to homogenise the microstructure. This heat treatment was essential to reduce segregation and ensure uniform distribution of the alloying elements throughout the ingot, thus preparing it for subsequent mechanical processing.

The homogenised ingot was then subjected to hot rolling for the elimination of casting defects such as porosity and to refine the grain structure. The rollers were gradually brought closer by 5 mm with each pass to achieve the desired deformation thickness, as well as enhance the mechanical properties and ensure the structural integrity of the material. After hot rolling, the ingot was left to air cool. Samples for plane strain compression (PSC) testing were machined from the rolled ingot.

Table 4: Element composition in weight percent (wt.%) of the target PHFP steel composition [10] *and the actual MA steel composition verified through induction coupled plasma optical emission spectroscopy (ICP-OES)*

Material	Fe	C	Cr	Mn	Mo	Nb	Ni	P	S	Si	Ti	V
PHFP	96.88	0.36	0.15	1.44	0.03	0.029	0.2	0.016	0.008	0.68	0.022	0.19
MA Steel	96.56	0.47	0.13	1.37	0.06	0.030	0.17	0.013	0.010	0.72	0.03	0.18

4.2.2 Construction of CCT Curve

The construction of time-temperature-transformation (TTT) and continuous-cooling-transformation (CCT) curves is an essential part of understanding phase transformations in MA steels. These curves are fundamental tools for predicting the microstructures that develop under different thermal conditions, which in turn determine the mechanical properties of the final material. Generating TTT and CCT curves for the selected MA steel composition was performed using JMatPro version 13.3 [89], a thermodynamic and kinetic simulation software widely used in materials science. TTT curves provide a map of phase transformations at constant temperatures, illustrating how phases such as austenite transform into other microstructures (e.g., pearlite, bainite, martensite) over time when held at specific temperatures. These curves are ideal for understanding isothermal transformation processes, but they do not accurately represent what happens during continuous cooling, which is more typical of industrial processes such as casting, forging, and hot rolling [109].

CCT curves, on the other hand, are more applicable to real-world scenarios where materials are subjected to controlled cooling rather than being held at a constant temperature. CCT curves map out the transformation of austenite under different continuous cooling conditions and are therefore more relevant for processing operations where the cooling rate is a significant parameter. Predictions can be made for the formation of phases such as ferrite, pearlite, bainite, and martensite as a function of cooling rate, making them necessary for developing controlled cooling strategies that achieve desired microstructures and thus, mechanical properties. For instance, as the target microstructure is a dual-phase ferrite-pearlite structure, the CCT curve will indicate the cooling rates at which these phases will form. It will also show the cooling rates to avoid the formation of unwanted phases such as martensite, which could lead to brittleness. Therefore, CCT curves are essential for designing heat treatment processes that produce the desired combination of strength, ductility, and toughness in MA steels.

To construct TTT and CCT curves for the selected MA steel composition, the following steps are undertaken:

I. **Input Material Composition**: The exact chemical composition of the MA steel is input into JMatPro. This includes all alloying elements such as carbon, manganese, niobium, vanadium, and titanium. The software uses this information to calculate the equilibrium phase diagram and predict the phases present at different temperatures and compositions.

II. **Simulation and Analysis**: JMatPro runs the simulation, calculating the time and temperature at which different phases begin to form. The software then generates the TTT and CCT curves, showing the start and finish lines for each phase transformation, as displayed in Figure 40 and Figure 41.

III. **Interpretation of CCT Curve**: The CCT curve is particularly useful for determining the cooling rate required to achieve a ferrite-pearlite microstructure. Identification can be made on the temperature ranges and cooling rates at which ferrite and pearlite begin to form. The curve also reveals the conditions under which other phases, such as bainite or martensite form, allowing us to adjust the cooling rate to avoid these phases as they are undesirable.

According to the calculations, the austenitisation temperature for the material was determined to be 832˚C using JMatPro, which is approximately 114˚C above the eutectoid temperature. At this elevated temperature, carbon is fully dissolved within the austenite matrix, allowing for controlled cooling to achieve the desired ferrite and pearlite microstructures. As indicated in Figure 41, the ferrite start temperature (a_3) is 781˚C, and the pearlite start temperature (a_1) is 728˚C. The cooling curves suggest that a slow cooling rate of 0.1˚C/s is optimal for forming a dual-phase ferrite-pearlite structure. However, at cooling rates between 1˚C/s and 0.1˚C/s, there is a possibility of forming mixed microstructures that include ferrite, pearlite, and potentially bainite in its upper and lower forms.

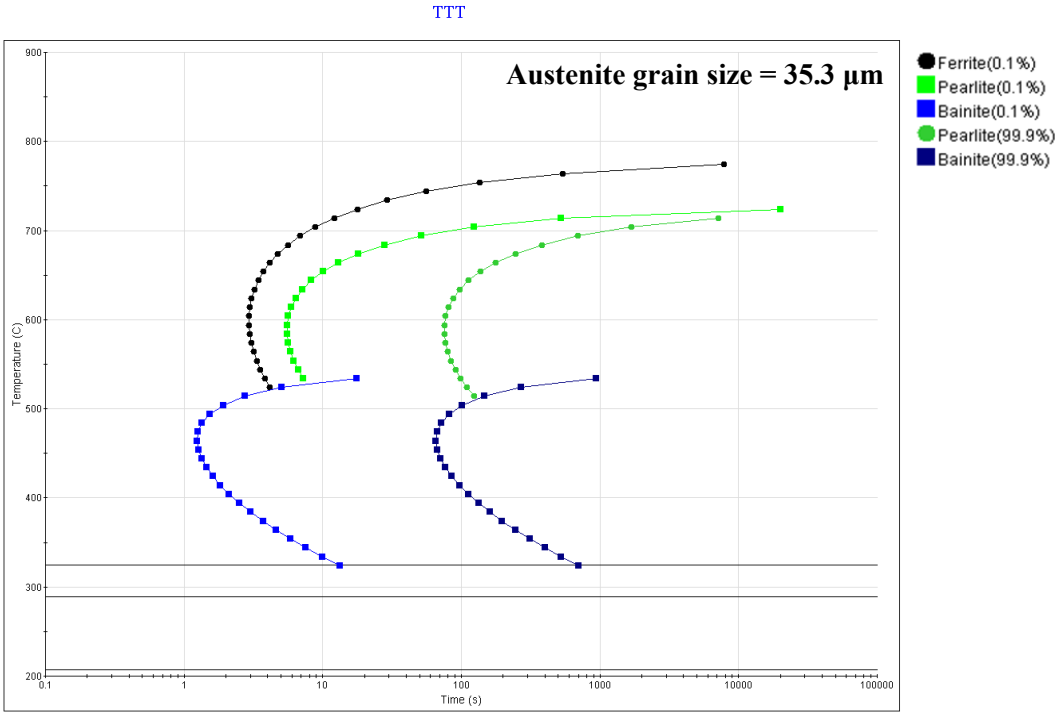

Figure 40: Construction of TTT curve from the MA composition using JMatPro 13.3

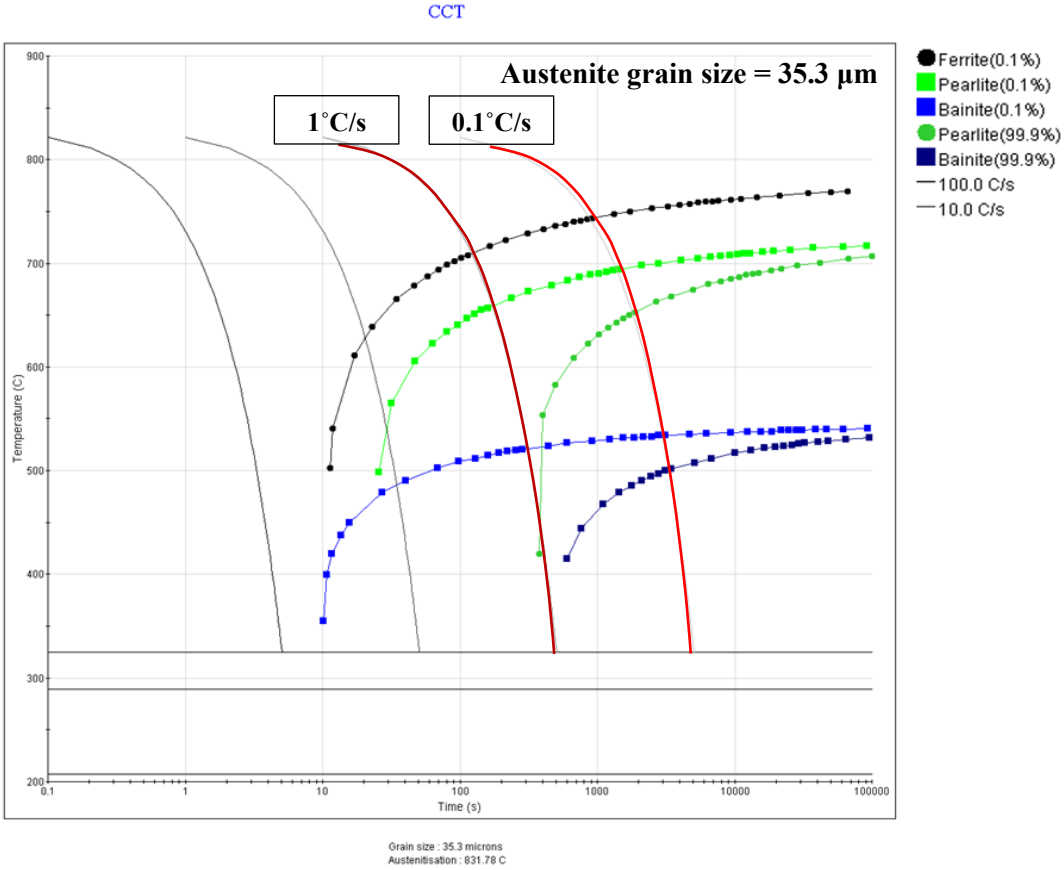

Figure 41: Construction of CCT curve from the MA composition using JMatPro 13.3

4.3 PSC Experiments

4.3.1 Temperature Profiles

As stated in Chapter 3, Section 3.3.2, the cooling rates investigated on the as-rolled MA steels in this study were quenched, 30, 2, 0.5 and 0.1˚C/s from either 900/1050˚C. Mist cooling was used to cool the 30˚C/s sample, forced air cooling was used for the 2, 0.5 and 0.1˚C/s samples and water cooling was used for the quenched samples. Boron nitride (BN) spray was used on the samples to prevent sticking and to minimise oxide scaling on the samples as the furnace was not under vacuum/inert atmosphere. Raw temperature profile data can be found in the appendix of this thesis.

4.3.2 Flow Behaviour

The load-displacement data recorded during the austenite deformation of the MA steel was systematically converted into von Mises equivalent stress-strain data, adhering to a standardised procedure [87]. The experimental setup involved two deformation passes designed to cumulatively achieve a total strain of 0.6, with each pass contributing 0.3 strain. The first deformation pass was conducted at 1100˚C, followed by a second pass at either 900˚C or 1050˚C. The stress-strain behaviour corresponding to these passes is depicted in Figure 42.

During the second deformation at 900˚C, the flow stress exhibited a gradual increase, with a total strain reaching 0.58. This gradual rise indicates a continuous strain hardening characteristic of austenite at lower temperatures. In contrast, at 1050˚C, the total strain achieved was 0.55, and the second deformation pass showed a noticeably lower flow stress value, indicative of dynamic recrystallisation [90], [110]. This reduction in flow stress at higher temperatures reflects the onset of dynamic recrystallisation, where the material undergoes microstructural changes that accommodate deformation more easily, resulting in a decrease in resistance deformation.

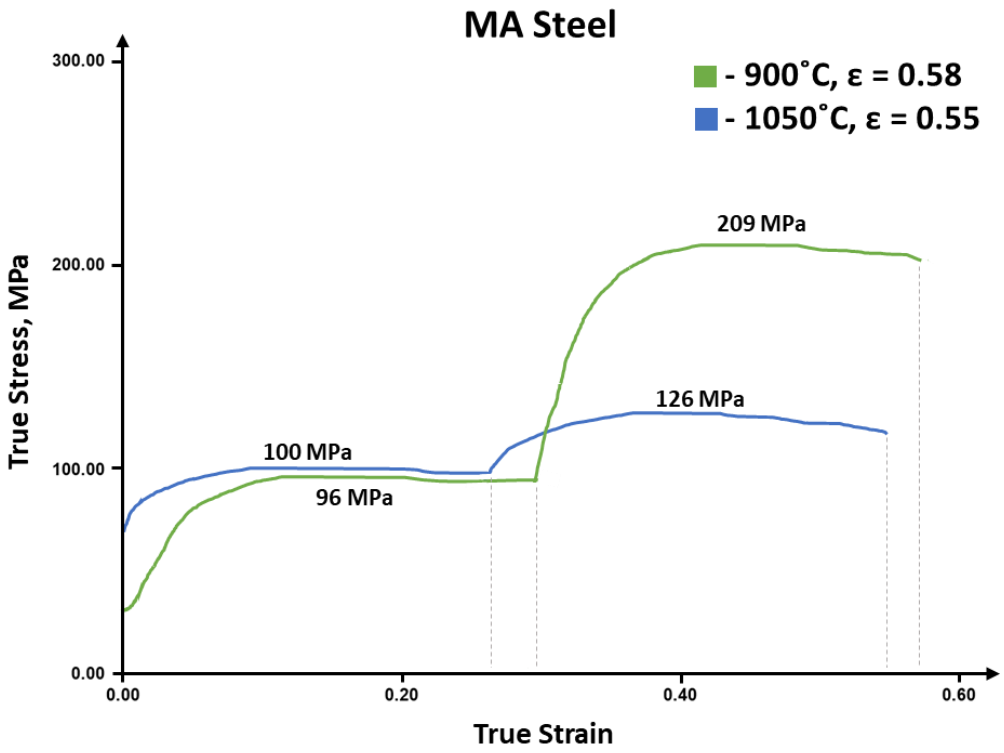

Figure 42: PSC true stress-strain curves during deformation passes of MA steel alloy with peak values of tensile strength indicated for both second deformation temperatures

4.4 Microstructural Characterisation

4.4.1 Prior Austenite Grain Boundaries

Prior austenite grain boundaries (PAGBs) are the boundaries of the austenite grains present in steel before they undergo phase transformation. These boundaries contribute to the determination of the final mechanical properties, as they influence the formation and distribution of subsequent phases during cooling. PAGBs are significant because they serve as sites for the nucleation of new phases during transformation, affecting the grain size and distribution in the final microstructure. For instance, in martensitic steels, the PAGBs can influence the formation of martensitic packets, laths, and block structures [111]. PAGBs are also regions where carbide precipitates and particles can form, which further affects the mechanical properties by hindering dislocation movement. The ability to reveal and analyse PAGBs through techniques such as etching and optical microscopy provides valuable insights into the material's thermal history, phase transformations, and potential for mechanical performance in service.

In examining the quenched MA PSC specimens etched with picric acid, distinct microstructural differences are observed between the samples quenched from 900˚C and 1050˚C. The specimen quenched from 900˚C exhibits a lath martensitic microstructure, with faint, equiaxed prior austenite grain boundaries (PAGBs) visible, as indicated by arrows in Figure 43. Conversely, the specimen quenched from 1050˚C presents interesting banding of dark and bright regions when etched with picric acid, using the same etching method as for the 900˚C specimen. These bands are in the direction of rolling and PAGBs are difficult to observe. The presence of this banding in the 1050˚C specimen likely represents a combination of martensite with some retained austenite or bainite in the darker regions. For this study, numerous attempts at revealing PAGBs using picric acid proved to be challenging, despite using techniques such as varying the HCl drop amounts found in previous literature [103], [112].

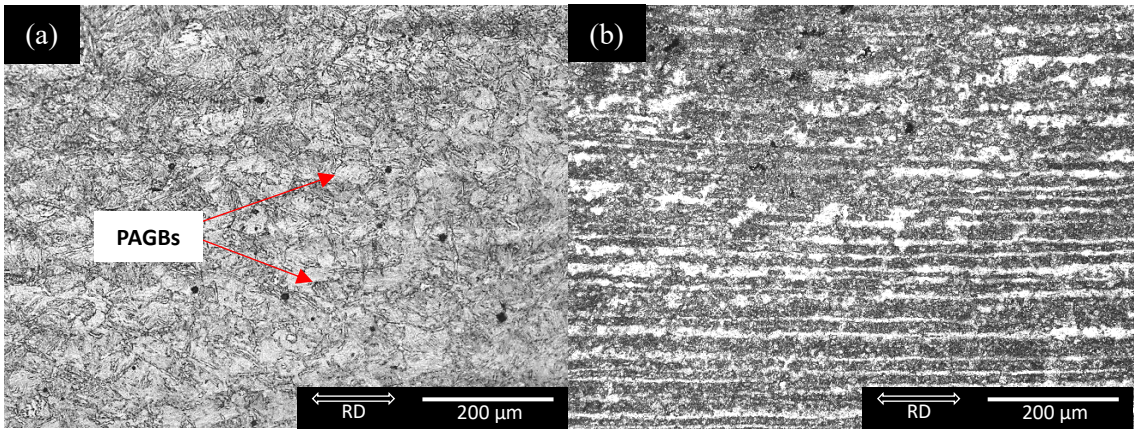

Figure 43: Quenched MA PSC specimens from (a) 900˚C and (b) 1050˚C, etched with picric acid, where 'RD' is the rolling direction

Electron backscatter diffraction (EBSD) was considered a suitable technique for identifying PAGBs due to the lack of indexing at these boundaries and the varying orientations of lath substructures, which could make PAGBs more distinguishable. In the quenched MA steels at 900˚C and 1050˚C, sub-grains were prevalent but small (<10 µm), which posed challenges for achieving a high EBSD hit rate. Despite this, Figure 44 shows the grain misorientation within the prior austenite grains, distinguishing low and high-angle (LA/HA) boundaries.

At 900˚C, PAGs are elongated and lath substructures grow from the grain boundary. At 1050˚C, there is no prevalent grain elongation retention from PSC deformation as the grain boundaries are reformed in an equiaxed state during recrystallisation. The EBSD analysis, with a step size of 0.1 μm, resulted in a moderate hit rate of 60%, taking approximately 2 hours per image. While EBSD is a viable method for identifying and analysing PAGBs, it is time-consuming due to the high magnification required for the small lath substructure size in this unique case. For accurate grain size measurement, additional techniques such as line mapping and converging methods may be necessary. In Figure 44, the most contrasting images from inverse pole figures (IPFs) were chosen to provide the clearest view of the crystallographic orientation of PAGBs.

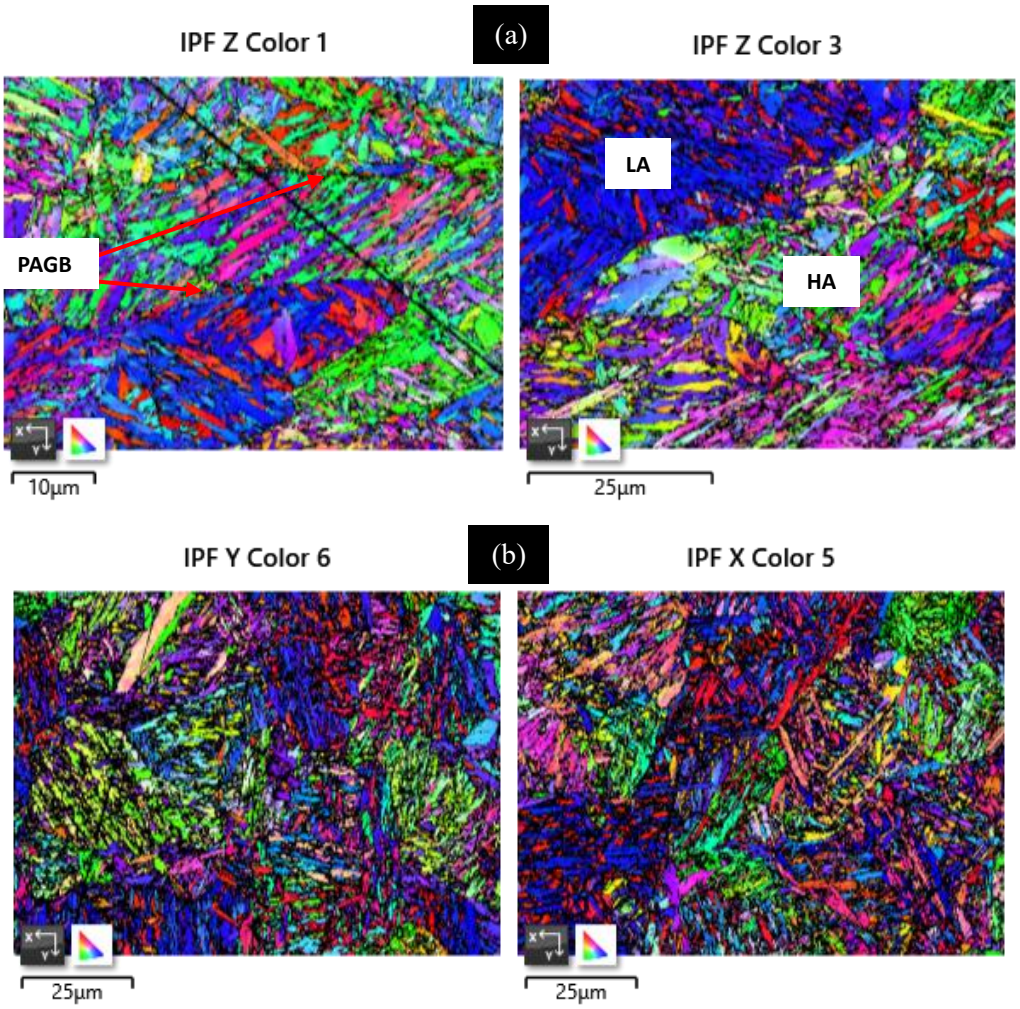

Figure 44: EBSD images at two sites of MA steel quenched from (a) 900˚C and (b) 1050˚C after deformation through PSC

4.4.2 As-cast and Hot Rolled Microstructures

Scanning electron microscopy (SEM) images for the as-cast microalloyed steel are shown in Figure 45. Obtained through a simple 2% nital etch, the as-cast microstructure exhibits acicular ferrite (AF) characteristics as well as cementite aggregates. Overall, the MA as-cast ingot is homogeneous with no non-metallic inclusions or visible precipitates. Both microstructures highlight cross-linked AF with non-uniform shapes and sizes. This matches a study performed by Oliveira et al. [113] who studied MA steel as-cast microstructures and the effects of annealing on mechanical properties. A similar alignment of AF was found, with the exception of polygonal ferrite (PF) being observed in the as-cast microstructure. This could be due to the low carbon content (0.06wt.%), making it difficult for complex phases to form. The fine microstructure from the as-cast state grain refinement effects of microalloying.

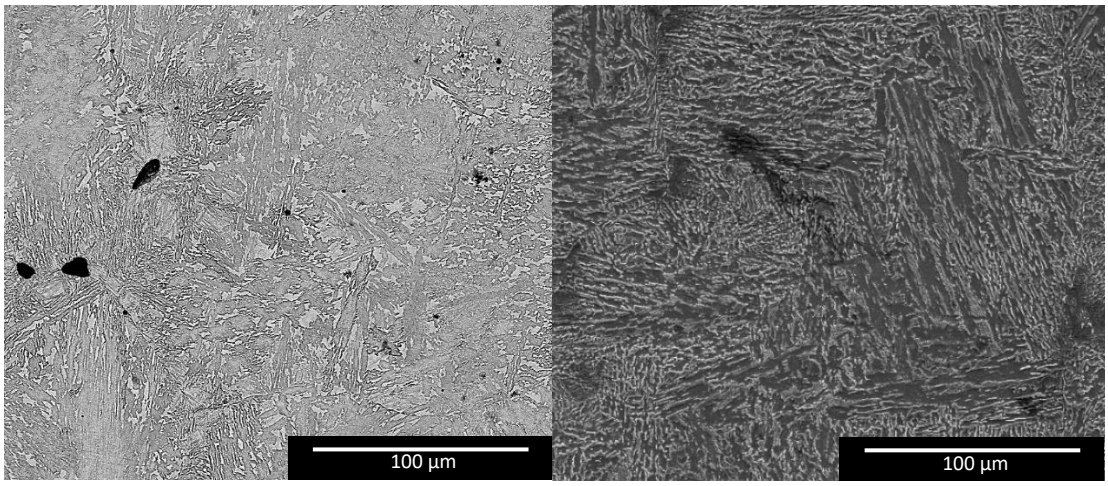

Figure 45: SEM for (a) bottom and (b) top of the as-cast MA steel ingot

The hot rolled ingot was also characterised by the same approach as the cast ingot and the microstructure in Figure 46 highlights similar acicular features through optical microscopy. Brighter regions of elongated PF can faintly be seen along the direction of rolling. This elongation indicates that the destruction and reformation of grain boundaries have taken place. A preliminary heat treatment at 1200˚C for 3 hours was performed before hot rolling to allow for full homogenisation of carbon and ferrous alloying elements that may have been segregated during VIM.

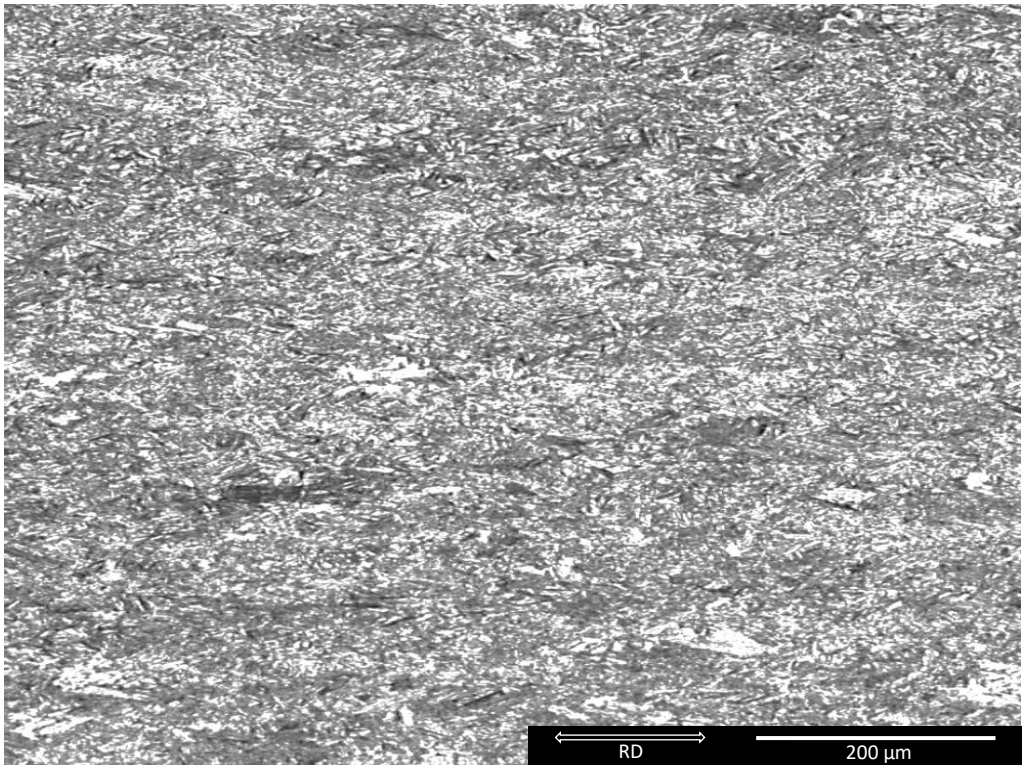

Figure 46: Optical micrograph of the hot-rolled MA steel

4.4.3 Phase Transformation with Modified Cooling Rates

This section focuses on the phase transformation behaviour of the MA steel after cooling from a second deformation pass conducted at either 900˚C or 1050˚C. The cooling rates under investigation are 30˚C/s, 2˚C/s, 0.5˚C/s, and 0.1˚C/s and will be discussed in this order, respectively. Cooling rates ranging from 2-0.1˚C/s target the phases identified from the CCT plot (Figure 41), with the addition of 30˚C/s analysed for Volkswagen to compare the MA steel to a case-hardened steel grade commonly used in the automotive industry, which also undergoes a final cooling rate of 30˚C/s after sheet metal forming. The primary focus of this analysis is to determine whether the grain refinement achieved through prior hot rolling and PSC deformation is preserved as the specimens undergo cooling. Additionally, the study aims to examine the evolution of mechanical properties during the cooling process, providing insight into how these varying rates of cooling influence the final microstructure and mechanical performance of the steel. By understanding the effects of these cooling rates, a prediction can be made on the material's behaviour

in practical applications, ensuring that the desired balance of strength, toughness, and ductility is achieved. For the MA steel cooled at a rate of 30˚C/s, Figure 47 presents SEM microstructures after cooling from both 900˚C and 1050˚C deformation temperatures during PSC. Both cooling conditions yield a similar microstructural outcome, with the formation of a characteristic lath martensitic structure. This lath martensite is marked by its elongated, needle-like features, which form as a result of rapid cooling [114]. Typically, lath martensite is composed of parallel or slightly staggered laths within prior austenite grains, often grouped in packets. This fine, acicular structure is a direct consequence of the high cooling rate, where the rapid transformation from austenite to martensite leaves little time for carbon diffusion. Despite the expectation for potential grain refinement due to the high cooling rate, no significant refinement is visible in the microstructures from either condition.

The 1050˚C SEM image, however, reveals faint PAGBs which can be subtly observed under higher magnification, indicated by a red arrow in the image. The predominant lath martensitic structure in both conditions is associated with high hardness and low ductility. This is primarily because lath martensite, due to its high density of dislocations and its fine structure, acts as a barrier to dislocation motion, thereby increasing hardness. However, this same structural configuration also restricts the ability of the material to undergo plastic deformation, leading to reduced ductility. The rapid cooling traps carbon within the martensite, preventing it from forming softer phases such as ferrite or pearlite, and resulting in a hard, brittle microstructure that is typical of quenched martensitic steels. Consequently, while both the 900˚C and 1050˚C conditions exhibit superior hardness, they are susceptible to low ductility, making them less suitable for applications requiring extensive deformation or toughness.

For the MA steel cooled at 2˚C/s, Figure 48 illustrates the optical microstructures observed after cooling from 900˚C and 1050˚C. Both conditions produce similar microstructural features, predominantly showing a mixture of AF and bainite

needles forming near grain boundaries. There is no noticeable grain refinement in terms of elongation or orientation. Despite the lack of refinement, both conditions are expected to exhibit relatively high hardness and decent ductility. This is because AF and bainite structures typically combine strength with a level of toughness, resulting in a balanced mechanical performance. The presence of bainite, known for its strength and toughness, alongside AF, ensures that the material maintains a good balance between hardness and the ability to deform without fracturing. This microstructural combination is particularly advantageous in applications where a compromise between strength and ductility is required.

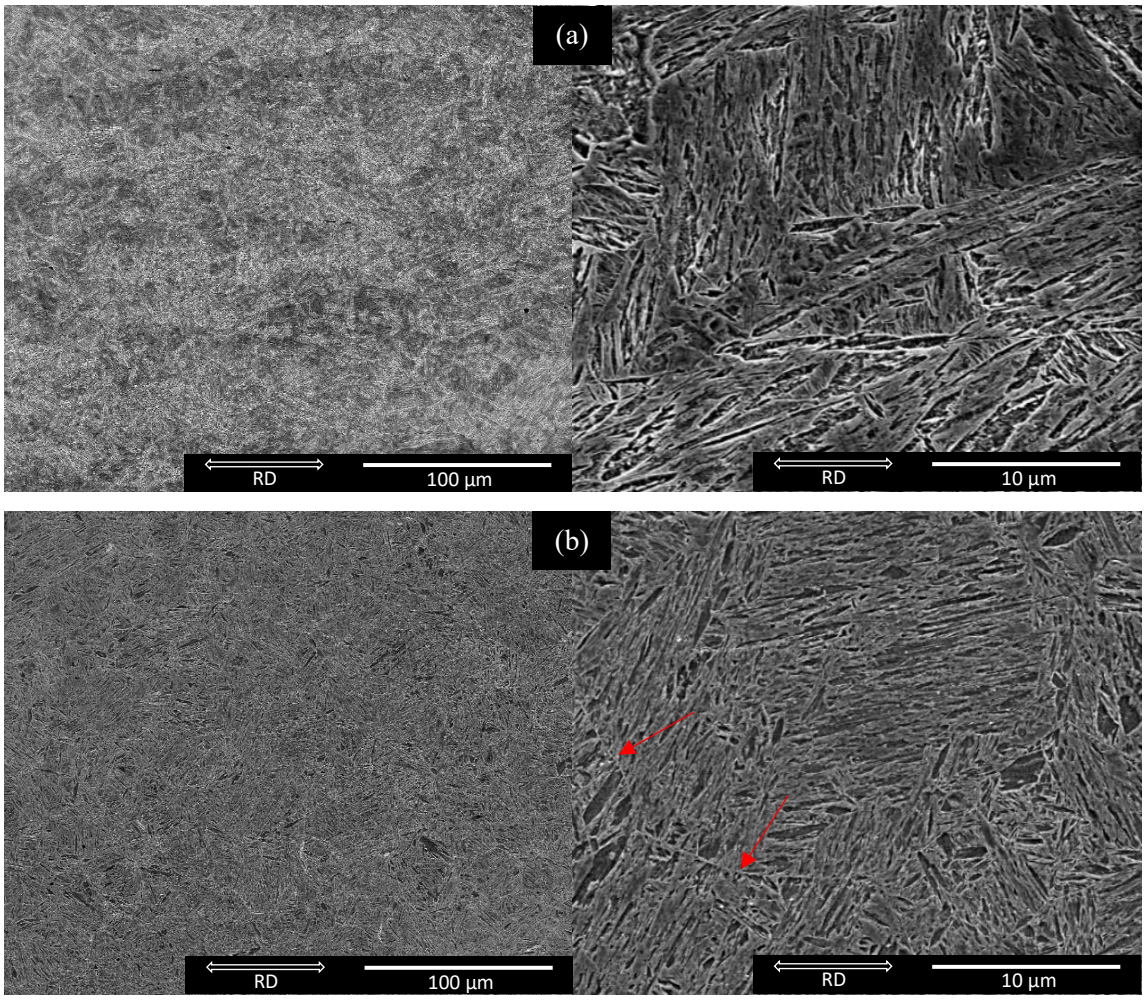

Figure 47: SEM (scanning electron, SE) images at two magnification levels of MA steel tested at (a) 900˚C and (b) 1050˚C deformation temperatures during PSC with a final cooling rate of 30˚C/s

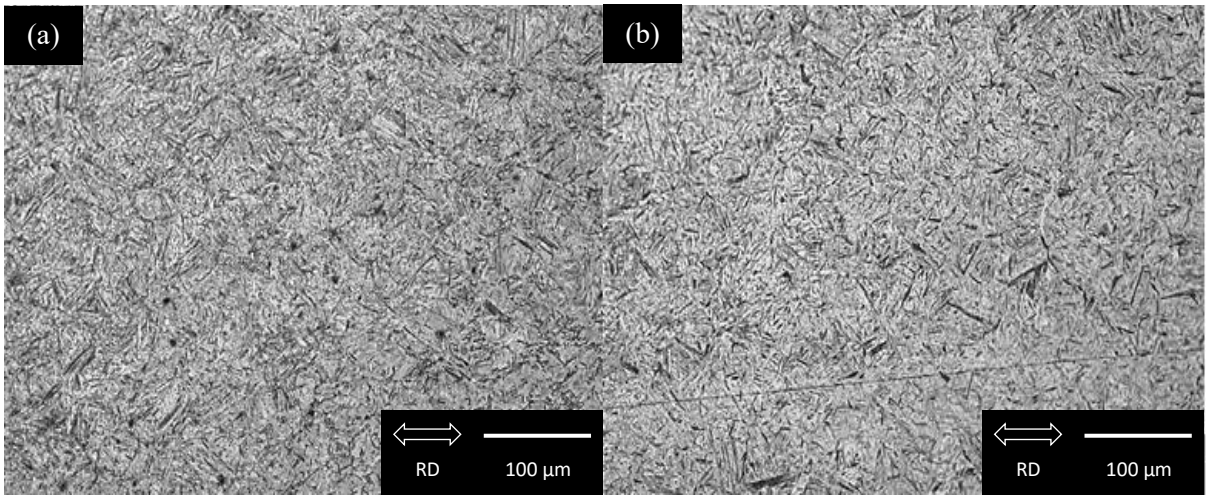

Figure 48: Optical micrographs of air-cooled (2˚C/s) MA PSC samples from (a) 900˚C and (b) 1050˚C

Testing on the MA steel final cooling stage during PSC runs carried out at 2˚C/s led to an unfavourable un-tempered martensitic phase transformation. The target PHFP microstructure was pursued further by reducing the cooling rate to 0.5˚C/s, the micrographs of which are indicated in Figure 49 for both temperatures. The idea of allowing more time for pro-eutectoid ferrite and pearlite to nucleate was partially successful for the 900˚C run, with some regions showing grain elongation in the direction of rolling. The banded regions which show pearlite colonies (P) with PF are clearly indicated in Figure 50. At 1050˚C, the austenite is at a fully recrystallised state which shows no obvious grain refinement retention under cooling, though the formation of PF and pearlite is observed.

Revising the final cooling rate to 0.1˚C/s induces a significant transformation in the microstructure, as evidenced by the optical micrographs in Figure 51. At 900˚C, the microstructure exhibits a distinct lamellar formation of pro-eutectoid ferrite and fine pearlite, oriented along the rolling direction (RD). This lamellar arrangement indicates that the prior austenite grains, which have undergone phase transformation, retain their original grain morphology below the austenite recrystallisation temperature. The slower cooling rate facilitates extended carbon diffusion, allowing sufficient time for the nucleation and growth of pearlite, characterised by alternating layers of ferrite and cementite. The increased time at

elevated temperatures enables the formation of these lamellar structures, with cementite precipitating in the interstices between the ferrite layers [36]. At the higher recrystallisation temperature of 1050˚C, the microstructure evolves into a more refined, equiaxed configuration, with pro-eutectoid ferrite and pearlite grains uniformly distributed across the MA matrix. The grain refinement observed at this temperature is a result of the dynamic recrystallisation process, where the driving force for nucleation is sufficient to produce new grains that are more equiaxed in nature. At slower cooling rates, the extended time for phase transformation allows for the development of lamellar pearlite.

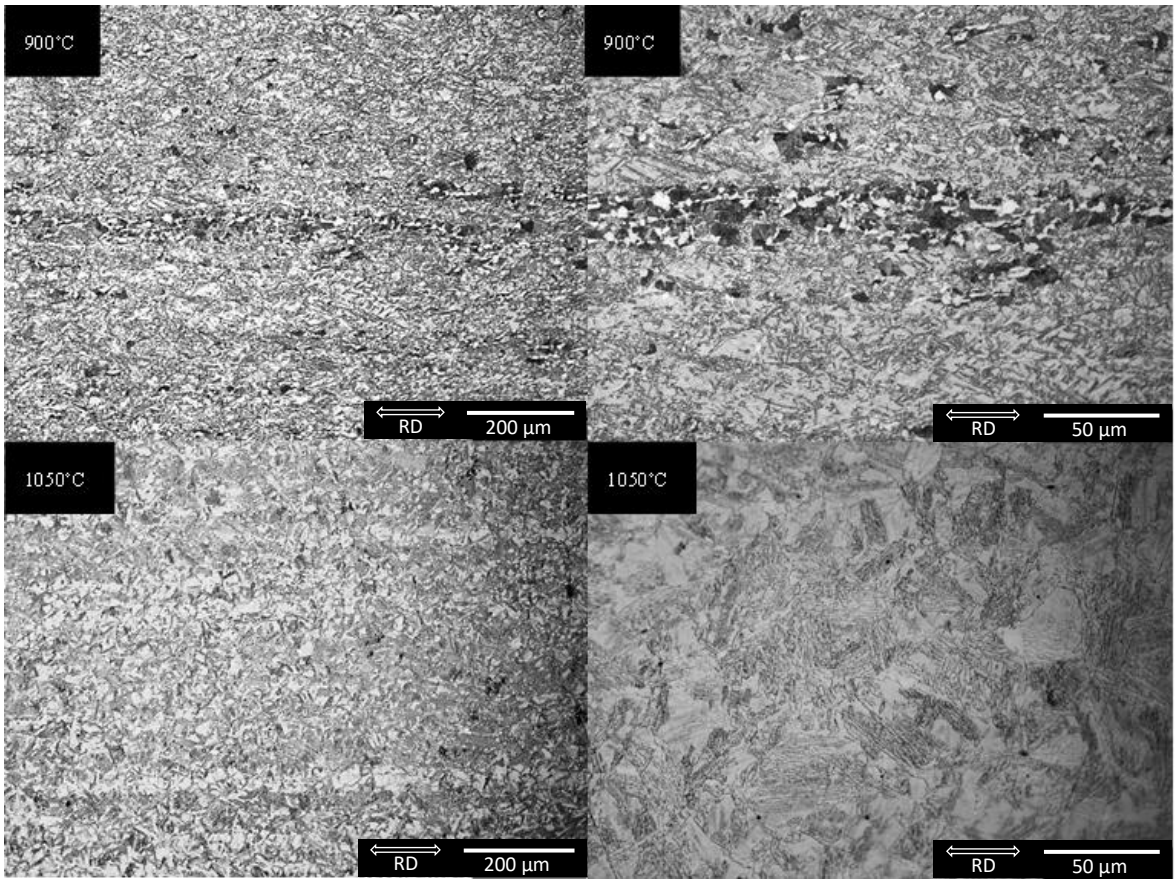

Figure 49: Optical micrographs at two magnification levels of MA steel tested at 900˚C and 1050˚C deformation temperatures with a final cooling rate defined at 0.5˚C/s

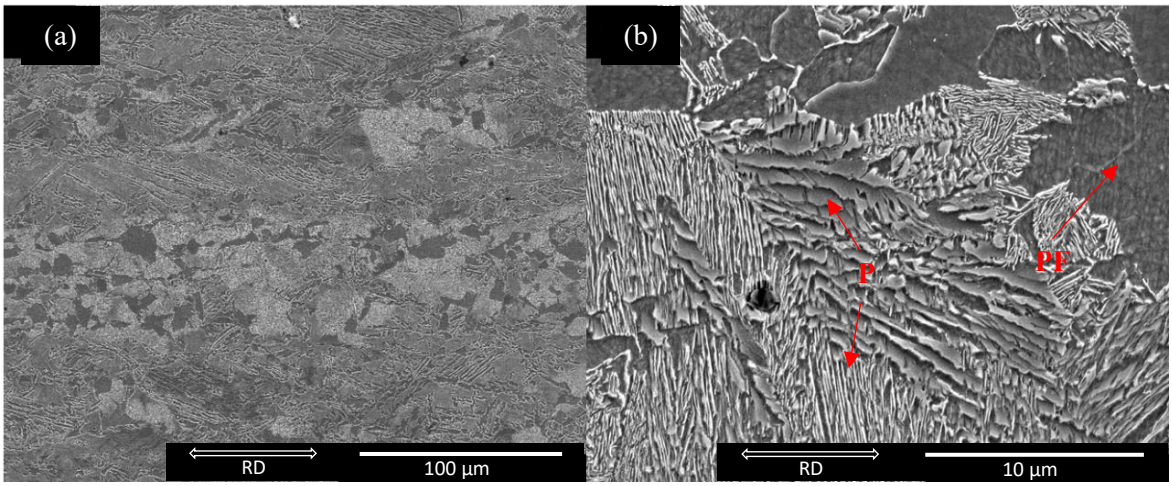

Figure 50: SEM (backscattered electron, BSE) image of 900˚C pearlite region present in Figure 49

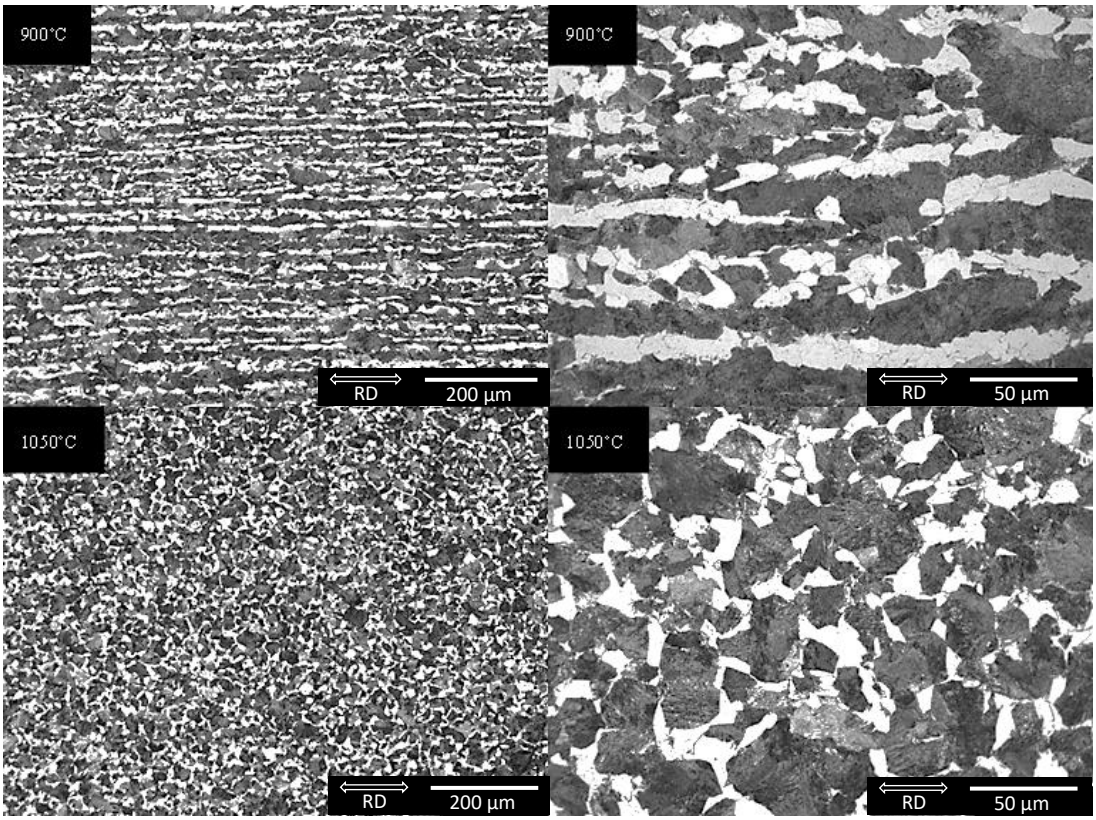

Figure 51: Optical micrographs at two magnification levels of MA steel tested at 900˚C and 1050˚C deformation temperatures with a final cooling rate defined at 0.1˚C/s

4.5 Mechanical Testing

Mechanical testing was conducted to evaluate Young's modulus, yield strength, tensile strength, and uniform elongation of each MA steel under different cooling rate conditions and deformation temperatures. Dog bone specimens, with the gauge area machined so it is located within the deformation zone, were subjected to tensile testing using a Zwick Roell tensile rig, with a consistent crosshead speed of 1 mm/min applied until failure. Young's modulus was determined through the interpretation of the elastic region of the stress-strain curve and a non-destructive resonant frequency damping analysis (RFDA) technique. Additionally, Vickers hardness measurements were performed to further characterise the mechanical properties of the specimens.

4.5.1 Tensile Testing

The engineering stress-strain curves presented in Figure 52 indicate the tensile strength for all tested samples. The highest tensile strength recorded was 1623 MPa, observed in the MA steel cooled at 30˚C/s from 900˚C, corresponding with a low uniform elongation of 6.1%, typical of a martensitic microstructure formed under rapid cooling. Conversely, the lowest tensile strength, 1033 MPa, was observed in the MA steel cooled from 1050˚C at 0.1˚C/s. An average Young's modulus of 208 GPa was determined according to ASTM E111 and ISO 6892-1 standards [115], [116], specifically identifying the gradient between 100 and 300 MPa on the stress-strain curve. This modulus value is typical for medium carbon MA steel. Yield strength and elongation values, presented in Table 5, show a trend of increased ductility with slower cooling rates, which is expected as more time is available for the nucleation of ductile ferrite. The decrease in yield strength with increasing elongation is attributed to the presence of these softer phases, which allow for greater plastic deformation before failure. Additionally, the lower cooling rates reduce internal stresses which makes the material less prone to crack initiation and propagation.

Table 5: Yield strength and uniform elongation values of each MA steel sample

Temp. (˚C) of PSC sample	Cooling Rate (˚C/s)	Yield Strength (MPa)	Uniform Elongation (%)
900	30	1254	6.1
1050	30	1343	5.8
900	2	845	6.2
1050	2	948	6.2
900	0.5	702	9.8
1050	0.5	740	12.0
900	0.1	396	14.3
1050	0.1	438	15.0

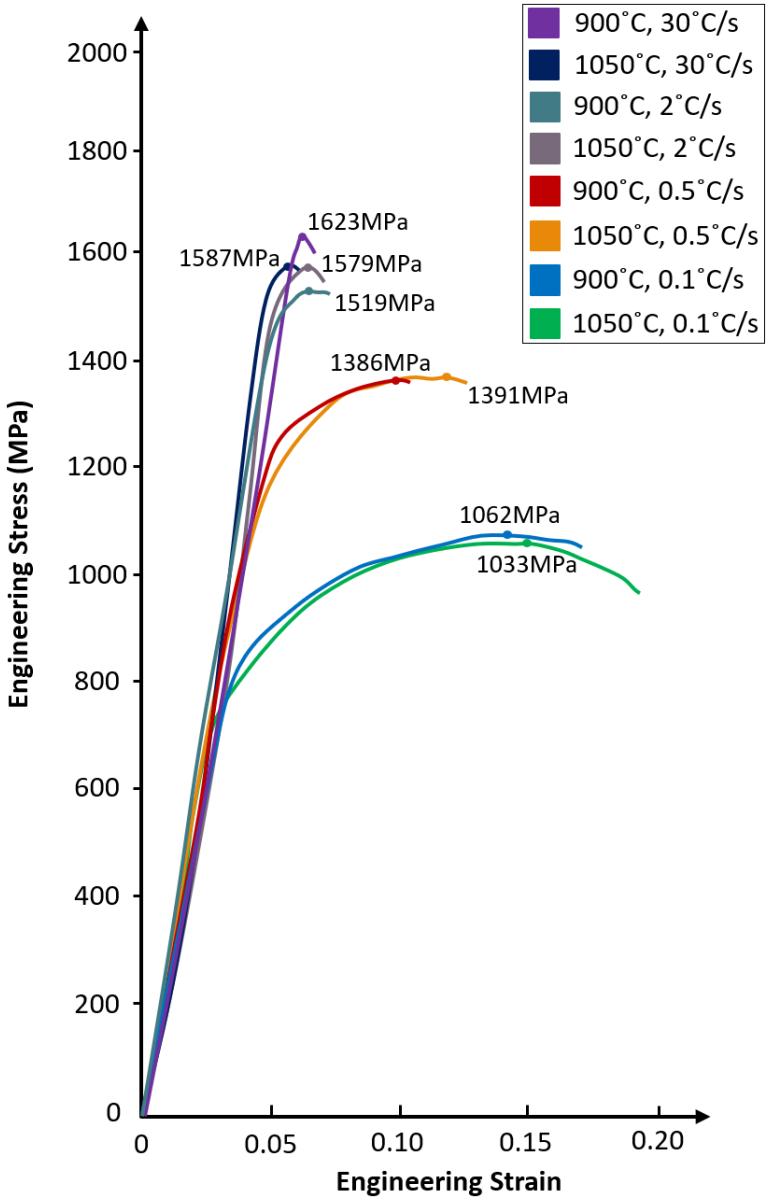

Figure 52: Engineering stress-strain plots of MA steel cooled from 900˚C/1050˚C at various cooling rates. The tensile strength values are stated at the peaks of each plot

Figure 53 illustrates the method used to calculate yield strength using the 0.2% offset strain approach, following the guidelines of ASTM E8. The yield strength is determined by drawing a line parallel to the elastic region of the stress-strain curve, offset by 0.2% strain, where the intersection with the curve indicates the yield point. Additionally, uniform elongation, which represents the strain at the onset of necking or the maximum stress before failure, is also depicted:

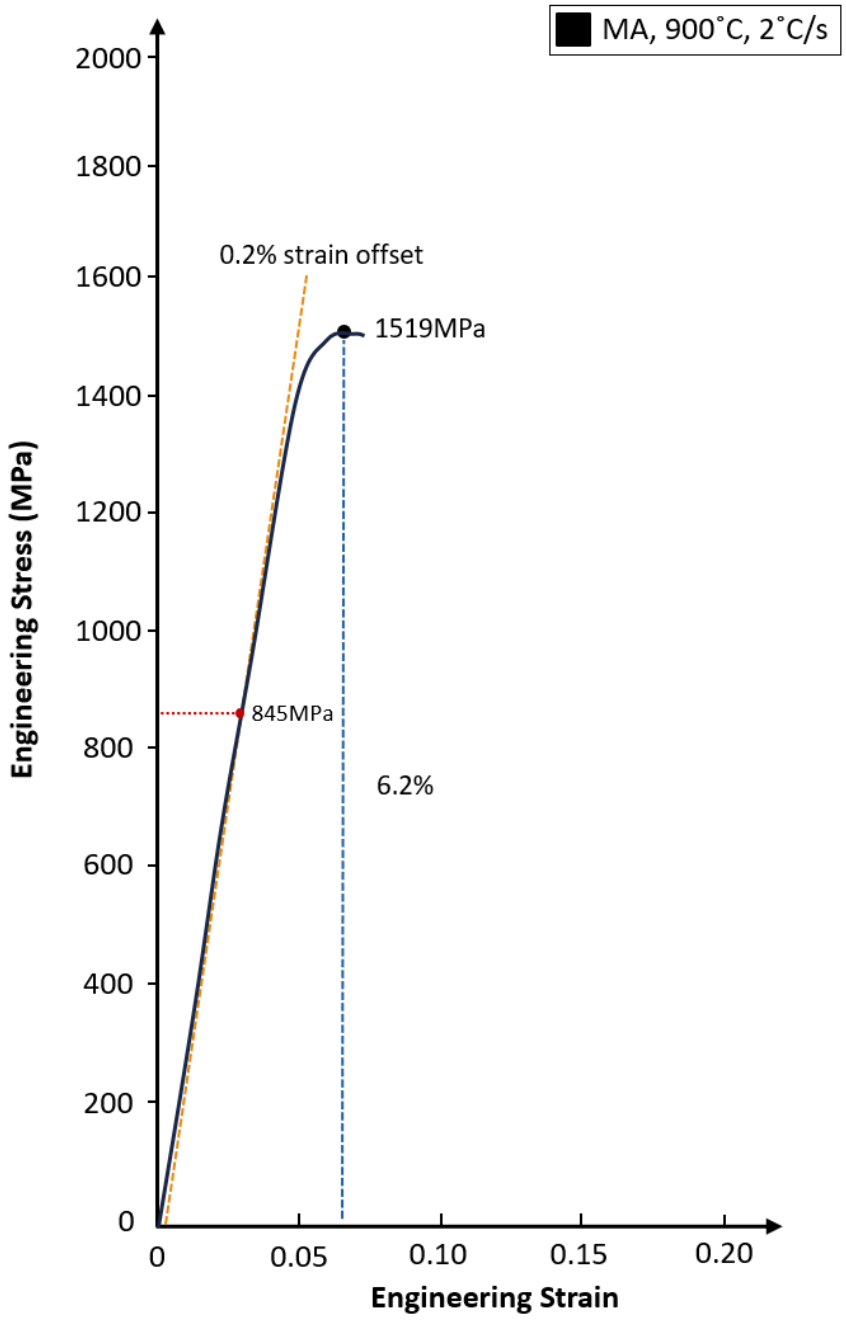

Figure 53: An example of yield strength calculation of MA steel cooled from 900˚C at 0.1˚C/s after PSC, with the uniform elongation annotated

4.5.2 RFDA and Vickers Hardness

RFDA offers a non-destructive method for calculating the Young's modulus of MA steel. Understanding this modulus is essential, especially as it relates to changes with the addition of TiB_2 composite reinforcement later discussed in Chapter 5. Four samples were tested using RFDA, yielding Young's modulus of 207.5 GPa, closely aligning with modulus values calculated from tensile test results. The average value was calculated with a ± 2.45 GPa uncertainty, determined by standard deviation, which involves calculating the variance, squaring deviations, summing them, dividing by the number of observations, and then taking the square root. Vickers hardness values, detailed in Table 6, where HV1 refers to the hardness measurement under a 1 kg load for a 20-second dwell time, shows a progressive increase due to the TMP, including hot rolling and PSC deformation, applied to the MA steel. The martensitic phase present in the quenched and 30˚C/s samples exhibit particularly high hardness, attributable to the rapid cooling, which does not allow sufficient time for carbon atoms to diffuse out of the martensite, leading to a supersaturated, hard structure.

Table 6: Average Vickers hardness (HV1) values for the MA steel at different processing stages

Temp. (˚C) of PSC sample	Cooling Rate (˚C/s)	Vickers Hardness (HV1)
900	30	520.4
1050	30	505.6
900	2	417.9
1050	2	436.4
900	0.5	255.0
1050	0.5	249.3
900	0.1	184.1
1050	0.1	195.1
900	Quenched	516.8
1050	Quenched	517.2

4.6 Summary

This study has highlighted the importance of final cooling on phase transformation and mechanical properties from un-recrystallised and recrystallised states of austenite. The main conclusions from this work are as follows:

I. The successful fabrication of an MA steel with an elemental composition closely matching the target PHFP composition was achieved.

II. Hot rolling and PSC allowed for observation and analysis of flow stress behaviour at 1100, 1050 and 900˚C during final deformation simulations.

III. Phase transformation behaviour under varying cooling rates was thoroughly investigated by modelling a CCT curve using JMatPro. This was complemented by microscopic and mechanical analysis of samples subjected to two deformation passes at a strain of 0.3 and a strain rate of 10/s, enabling a comprehensive understanding of the material's microstructural evolution.

IV. The quenching experiments from 900˚C and 1050˚C offered insights into the morphology of PAGBs in different forms of austenite. Partial observation of these boundaries was achieved through EBSD. Fine sub grains were observed within the PAGBs, showing colour contrasts in the IPF plots due to differences in crystallographic orientation. Although the EBSD mapping provided valuable data, a map convergence approach would be more suitable for this complex microstructure, given the high magnification required for such small grains.

V. Gradual reduction of the cooling rate resulted in the increased formation of ferrite and pearlite colonies, as confirmed by microscopy and mechanical testing. The slower cooling rates improved ductility, though at the expense of reduced tensile and yield strength.

VI. Tensile testing and RFDA consistently indicated that Young’s modulus of the MA steel is approximately 208 GPa.

VII. MA steel is a suitable matrix alloy that can complement the addition of TiB_2 as a ceramic reinforcement. This is because, under hot work, the MA steel presents little to no challenge during fabrication and follows the expected thermodynamic behaviour of medium-carbon steels. At the slowest cooling rate of 0.1˚C/s, the alloy holds a respectable tensile strength of 1062 MPa when cooled from 900˚C, whilst exhibiting excellent ductility (15% uniform elongation).

5. Fabrication and Thermomechanical Processing of a Microalloyed Steel Containing *in situ* TiB_2 Particles for Automotive Applications

5.1 Introduction

With continuous advancements in the electric automotive sector, the need for improving vehicle efficiency through lightweight design and geometric optimisation has become increasingly important. Lightweight design is particularly crucial for enhancing the range and dynamic performance of electric vehicles, including handling, acceleration, and braking. Traditionally, structural steels are favoured in both internal combustion and electric-powered vehicles due to their high modulus, stiffness, and strength. These steel components, which form integral parts of the chassis, body panels, and engine, contribute significantly to a vehicle's overall mass.

The development of high-modulus steels (HMSs) with composite ceramic reinforcement is a well-researched approach for reducing the density of steel components while enhancing stiffness [2], [67], [69], [117]. By lowering the density and maintaining or even increasing strength, vehicle parts can be redesigned with optimised geometries to achieve weight reduction. Alternatively, new composite-reinforced steels can maintain the same geometry as existing parts and deliver similar or superior mechanical properties, reducing the overall weight of electric vehicles without compromising performance. This study focuses on the fabrication and thermomechanical processing (TMP) of a microalloyed steel composite (MASC) containing *in situ* TiB_2 particles, a novel approach aimed at enhancing the mechanical properties of steel through the incorporation of ceramic reinforcements. The use of titanium diboride (TiB_2) as a reinforcing phase is common in low alloy steels due to its exceptional hardness, high melting point (2970˚C, [118]), and stability within a steel matrix. These properties make TiB_2 an ideal candidate for improving Young's modulus and overall strength of steel components, which are

critical factors in automotive applications. The integration of TiB_2 into a microalloyed (MA) steel matrix represents a significant advancement in the development of steel matrix composites (SMCs). Previous studies on MA steels have demonstrated their potential for achieving desirable mechanical properties through precise control of alloy composition and TMP [10], [119], [120], [121], [122]. However, the addition of *in situ* TiB_2 particles introduces a new dimension to this research, offering the possibility of further enhancing the material's performance by utilising the mechanical benefits of composite reinforcement. This chapter aims to improve the modulus and strength of the MA steel studied in Chapter 4 by fabricating an HMS for automotive applications. By using the same manufacturing approach, vacuum induction melting (VIM), coupled with an identical TMP route, a direct comparison can be made to the MA steel. This study will look at the incorporation of TiB_2 at two volume fractions, 5% and 7.5%; these alloys will be referred to as 5MASC and 7.5MASC respectively.

5.2 Fabrication of MASC Alloys

5% and 7.5% volume fractions of TiB_2 were determined using the ThermoCalc2023a volume fraction model [123], with stoichiometric mass fraction calculations for Ti and B also performed in ThermoCalc. Maintaining the correct molar fractions of these elements is important, as excess Ti or B can lead to the formation of undesirable secondary and ternary phases such as Fe_2B and TiB_3 which are denser and more brittle than TiB_2. The stoichiometric composition of TiB_2, approximately 69 weight percent (wt.%) Ti and 31 wt.% B, was carefully adhered to during the elemental composition calculations to avoid these unwanted phases. Figure 54 illustrates the stoichiometric composition of TiB_2 and the overall volume fraction of the main phases expected to form between 700-1300˚C for 5MASC, where 1305˚C is the beginning of the liquid state of iron.

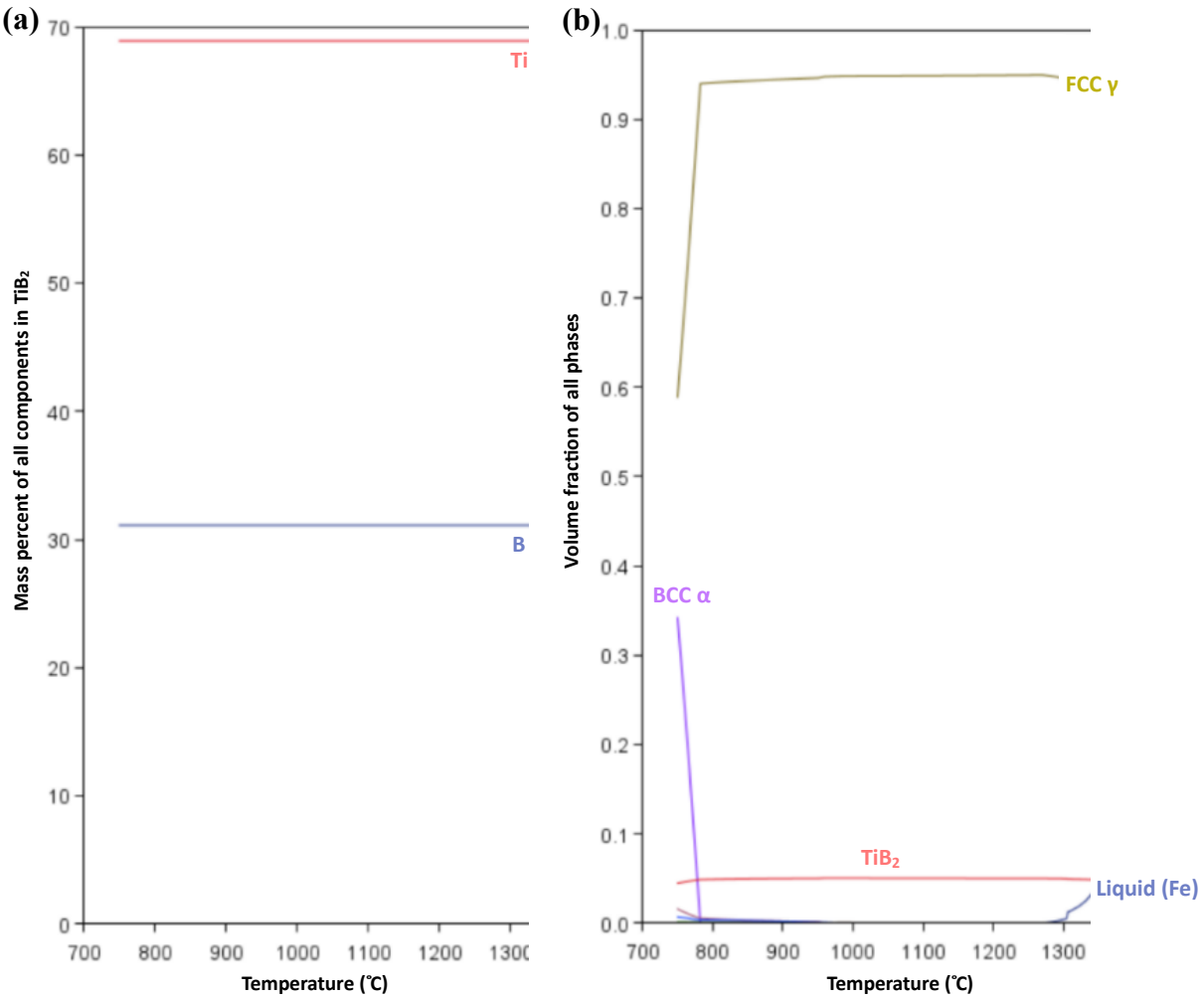

Figure 54: ThermoCalc plots which show (a) stoichiometric composition of TiB_2, (b) example of volume fraction of all phases vs. temperature for 5MASC

Table 7 shows the composition of 5MASC and 7.5MASC, which were recorded using induction coupled plasma optical emission spectroscopy (ICP-OES), these values also closely match the theoretical values used to calculate the volume fraction of TiB_2 in ThermoCalc. For reference, the composition from the MA steel studied in Chapter 4 is also presented:

Table 7: Elemental composition (wt.%) for the MA and MASC ingots fabricated using VIM

Material	Fe	C	Cr	Mn	Mo	Nb	Ni	P	S	Si	Ti	V	B
MA Steel	96.56	0.47	0.13	1.37	0.06	0.030	0.17	0.013	0.010	0.72	0.03	0.18	--
5MASC	94.021	0.43	0.10	1.28	0.07	0.03	0.17	0.011	0.008	0.70	2.05	0.18	0.95
7.5MASC	92.991	0.38	0.11	1.29	0.07	0.03	0.17	0.013	0.006	0.75	2.55	0.19	1.45

5.3 Plane Strain Compression Behaviour

Using the same methodology and parameters for plane strain compression (PSC) testing as applied to the MA steel, the stress and strain values during deformation passes at 1100˚C and 900/1050˚C were calculated. This involved a series of calculations based on a standardised procedure [87], using raw data from the thermomechanical compression (TMC) machine. These calculations help assess the mechanical behaviour of each sample at elevated temperatures, specifically at 900˚C and 1050˚C, where understanding deformation characteristics is essential. This analysis is also particularly valuable in observing how the deformation forces required to achieve specific strain levels change with the introduction of TiB_2 reinforcement.

From the calculated stress-strain plots shown in Figure 55 and Figure 56, true stress values are indicated for the two deformation passes each ingot underwent. During the first deformation pass at 1100C, 5MASC required an average of 184.5 MPa to achieve 0.3 strain whereas 7.5MASC required an average of 157 MPa. The stress required for both MASC ingots at 1050˚C during the second deformation pass is lower than that required at 900˚C. When compared to the MA steel, the inclusion of TiB_2 significantly increases the stress needed to achieve equivalent strain levels due to the particle reinforcement's strengthening mechanism and increased stiffness. At 900˚C, the stress for the 5MASC alloy reaches 188 MPa, representing a 95.8% increase from the base MA steel. This substantial increase indicates that the MASC alloy possesses a stiffer structure with more stress-concentrated regions, necessitating greater energy input to achieve the same strain. Interestingly, the stress values for the 7.5MASC alloy are slightly lower than those for the 5MASC for both deformation passes, which can be attributed to the potential for reduced particle dispersion and possible agglomeration, leading to less effective reinforcement at higher TiB_2 concentrations. This suggests a complex interaction between particle reinforcement and matrix that requires further investigation. In both figures, the total strain (ε) is closely aligned with the target of 0.6.

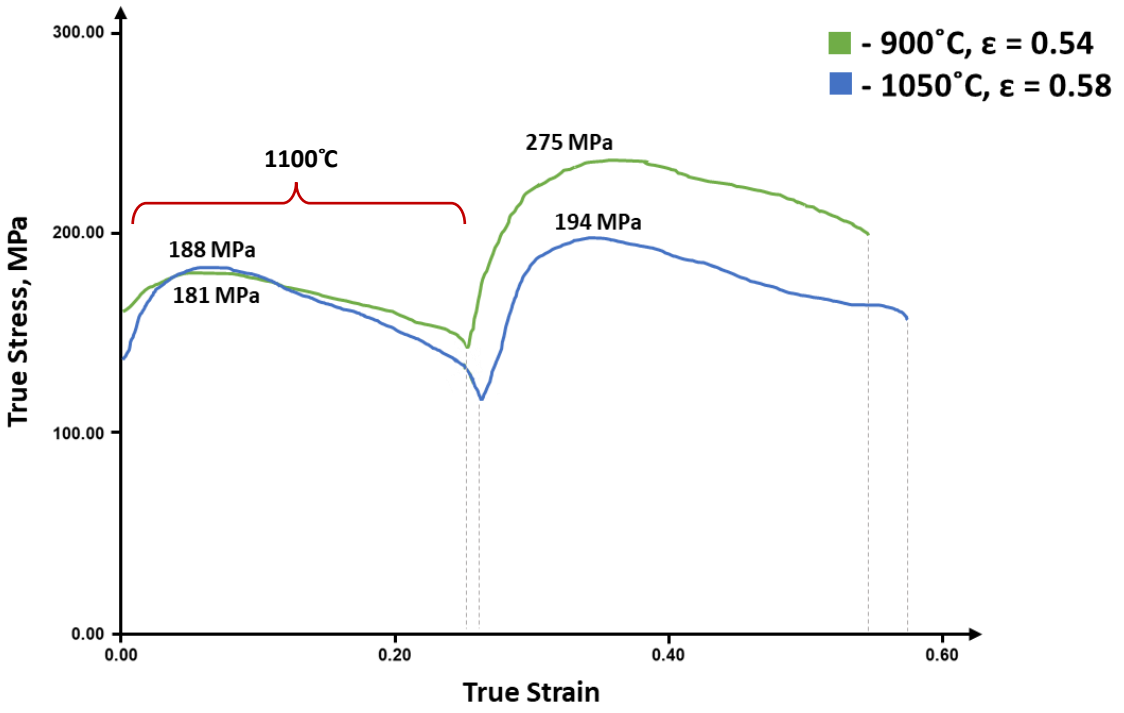

Figure 55: PSC stress-strain curves during deformation passes of 5MASC alloy with peak values of strength indicated for both second deformation temperatures

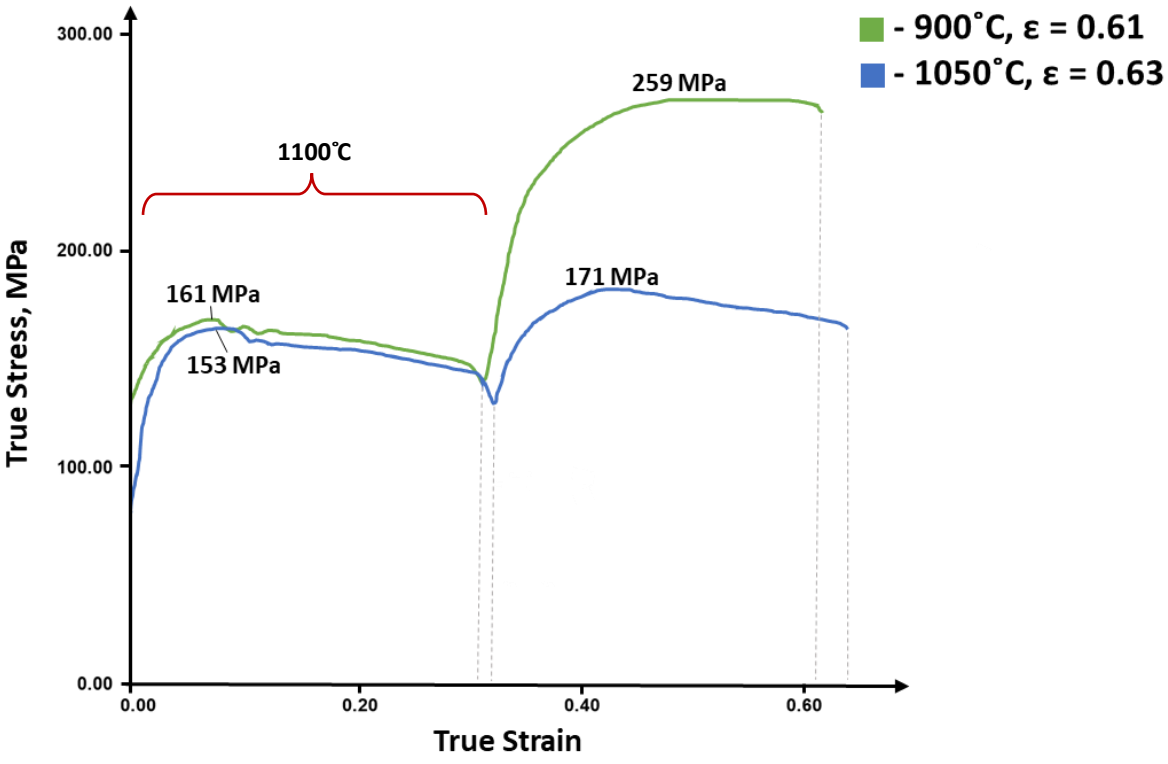

Figure 56: PSC stress-strain curves during deformation passes of 7.5MASC alloy with peak values of strength indicated for both second deformation temperatures

5.4 Microstructural Characterisation

5.4.1 As-cast and Hot Rolled Microstructures

The as-cast 5MASC ingot was analysed through scanning electron microscopy (SEM), where the MA steel matrix with TiB_2 reinforcement is visible. The dark particles scattered throughout the matrix are TiB_2 particles in Figure 57. These particles appear black because they interact differently with the electron beam compared to the surrounding steel matrix, which is shown in lighter grey tones. Partial nucleation of allotriomorphic pro-eutectoid ferrite exists at equiaxed grain boundaries. The TiB_2 particles are distributed along the grain boundaries and within the grains themselves, indicating that they have been well-dispersed during VIM processing. The presence of TiB_2 along these boundaries can enhance the mechanical properties by hindering grain boundary movement, thus increasing the overall strength and hardness of the steel.

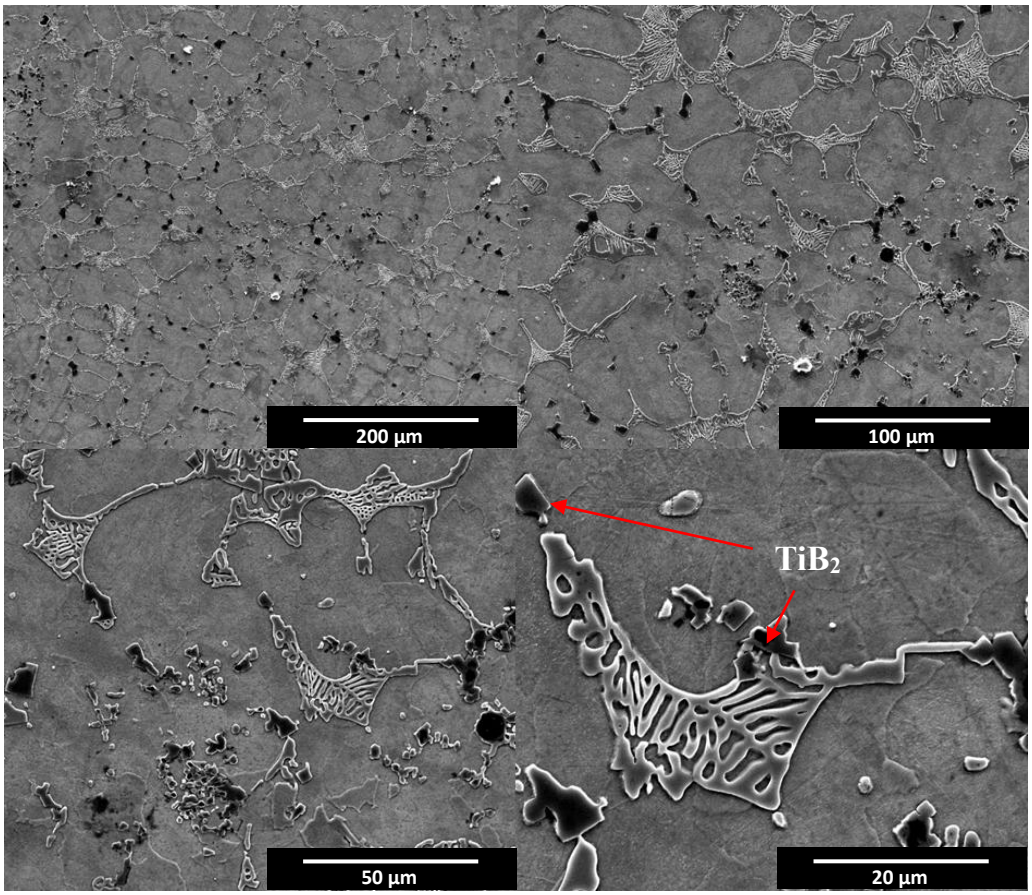

Figure 57: SEM scanning electron (SE) images of 5MASC as-cast from VIM

In Figure 57, TiB_2 generally exhibits a distinctive morphology characterised by its fine, angular, and platelet-like structure; this corresponds to descriptions of TiB_2 found in the relevant literature [76], [124], [125], [126], [127]. However, upon further investigation of the 5MASC alloy in the as-cast state, agglomerated and elongated dark particles were identified as displayed in Figure 58. The contrast of the MA matrix and darker phases was achieved using the backscattered electron (BSE) detector, which is sensitive to the atomic number of the elements present, with heavier elements appearing brighter due to their higher backscattering coefficient. This technique is useful for distinguishing between different phases [128]. The elongated structures could be indicative of another compound that formed during solidification such as carbide phases, which are known to exhibit such morphologies [66].

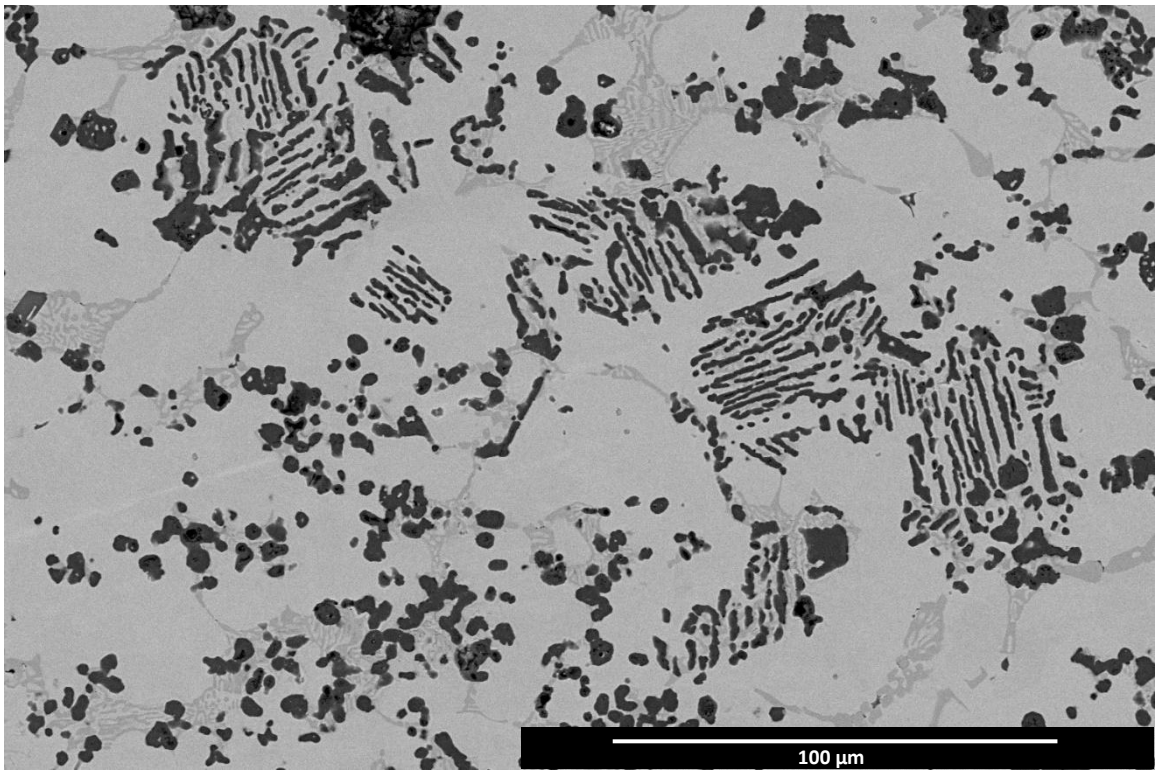

Figure 58: SEM BSE image highlighting particle agglomeration and lamellar formation in as-cast 5MASC

The optical micrograph of the as-rolled 5MASC (Figure 59), etched with 2% nital, shows a mixture of polygonal ferrite (PF) and bainite (B). The nital etching process highlights the ferrite and bainite microstructures, where ferrite typically appears as lighter grains aligned in the direction of rolling, and the bainite being darker due to its higher carbide content. TiB_2 particles are hard to observe in optical microscopy as they appear similar to PF.

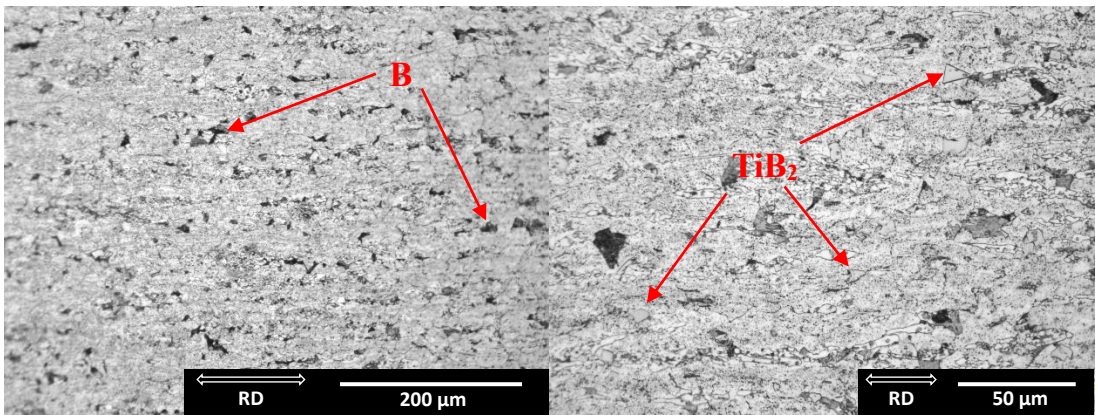

Figure 59: Optical micrograph at two magnification levels of as-rolled 5MASC left to air cool without post-heat treatment, where RD is the rolling direction

5.4.2 Volume Fraction Calculation

To calculate the volume fraction of TiB_2 particles in both MASC alloys, SEM BSE imaging was utilised for its ability to enhance the contrast between the TiB_2 particles and the MA steel matrix. The methodology involves the following steps:

Image Acquisition: Captured 5 x500 magnification BSE images, ensuring clear differentiation between TiB_2 particles and the matrix.

Image Analysis: Used an integrated software measurement tool to find the maximum diameter of each particle in the image (see Appendix for an example). Particles that were partially cut off from the image were neglected.

Area Fraction Calculation: Determined the area fraction by dividing the total area of the TiB_2 particles by the total area of the micrograph. This gives a 2D area fraction, which can be considered equivalent to volume fraction, which is true in this case due to excellent homogeneity.

Multiple Measurements: Measured multiple micrographs from different regions of the sample to account for any variability in particle distribution and size.

Statistical Analysis: Calculated the average volume fraction and use the standard deviation to represent the uncertainty. The standard deviation is calculated by taking the square root of the variance (the average of the squared differences from the mean) of the area fractions from all measured images.

Final Volume Fractions:

5MASC = 5.2% TiB_2

7.5MASC = 7.7% TiB_2

Volume fraction uncertainty = ±0.036%,

TiB_2 particle size = 9.43 μm ±0.045 μm

5.4.3 Phase Transformation with Modified Cooling Rates

5.4.3.1 5MASC

After hot rolling, PSC testing was performed on 5MASC and 7.5MASC samples which all received a final cooling rate of either 30 or 0.1˚C/s after two deformation passes at 1100˚C and 900/1050˚C. 30˚C/s was chosen to simulate current industrial automotive sheet metal processing stated by the industrial sponsor of this project, Volkswagen, and 0.1˚C/s was deemed the most suitable cooling rate to achieve a precipitation-hardened ferrite-pearlite (PHFP) microstructure, as demonstrated in Chapter 4. During the initial heating up to 1200˚C, all MASC samples were prone to oxidation despite a boron nitride (BN) protective coating being applied. Some samples also exhibited small bending after deformation passes which resulted in misaligned deformation and breakage of the samples. One explanation for this could be a high level of incipient oxidation at TiB_2 particle regions which can cause internal weak spots throughout the matrix. With this stated, the runs were performed with normal force and strain readings recorded and micrographs were obtained from all PSC runs.

Due to the limited availability of the 5MASC material, only one sample was tested at a cooling rate of 30˚C/s. This test involved an initial deformation at 1100˚C, with a strain of 0.3 and a strain rate of 10/s. A second deformation pass was conducted under the same conditions at 900˚C. The resulting microstructure, shown in Figure 60 reveals a homogeneously dispersed TiB_2 phase within a martensitic MA matrix. Pro-eutectoid ferrite is observed at the grain boundaries though there is insufficient time for this phase to nucleate, accompanied by martensitic grains. The TiB_2 particles exhibit the same jagged and platelet morphology as seen in the as-cast MASC, reflecting its thermodynamic stability. Deformation has not altered the grain orientation nor affected the TiB_2 morphology in this instance.

Figure 61 presents optical micrographs of 5MASC samples cooled at 0.1˚C/s from 900˚C, 1050˚C, and 1100˚C, respectively, with only one deformation pass performed on the 1100˚C specimen. The 900˚C specimen predominantly exhibits PF with regions of pearlite. The TiB_2 particles, indicated by red arrows on Figure 61, show no alteration in morphology, size, or dispersion despite undergoing hot rolling and subsequent thermomechanical processing. Notably, the 1050˚C specimen demonstrates excellent retention of grain elongation in the rolling direction, predominantly featuring a PF phase. Interestingly, TiB_2 particles are primarily located at grain boundaries. As observed in the MA matrix without composite reinforcement, grain refinement diminishes upon reaching the austenite recrystallisation temperature. However, the grain refinement and retention of deformed grains are evident, likely due to the grain pinning effect attributed to TiB_2 particles [129] . To assess whether the pinning mechanism remains effective at higher temperatures, the 1100˚C specimen was examined, but Figure 61 does not show significant grain refinement or orientation retention in the rolling direction, instead there is an equiaxed microstructure. Although the TiB_2 particles remained well dispersed, they were unable to maintain new dislocation densities during the initial deformation pass in PSC.

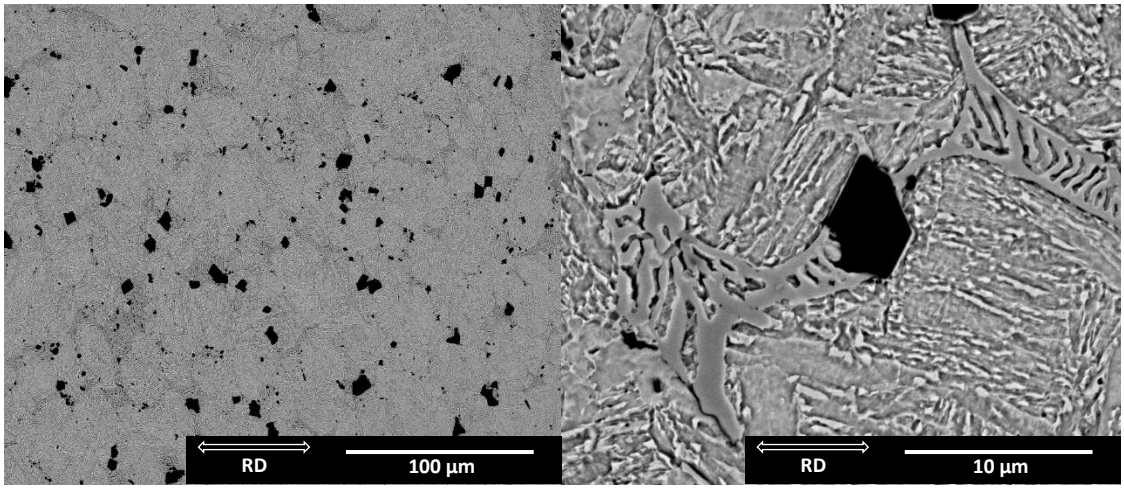

Figure 60: SEM (SE) images of 5MASC at two magnification levels after deformation from PSC, the final cooling rate used was 30˚C/s from 900˚C

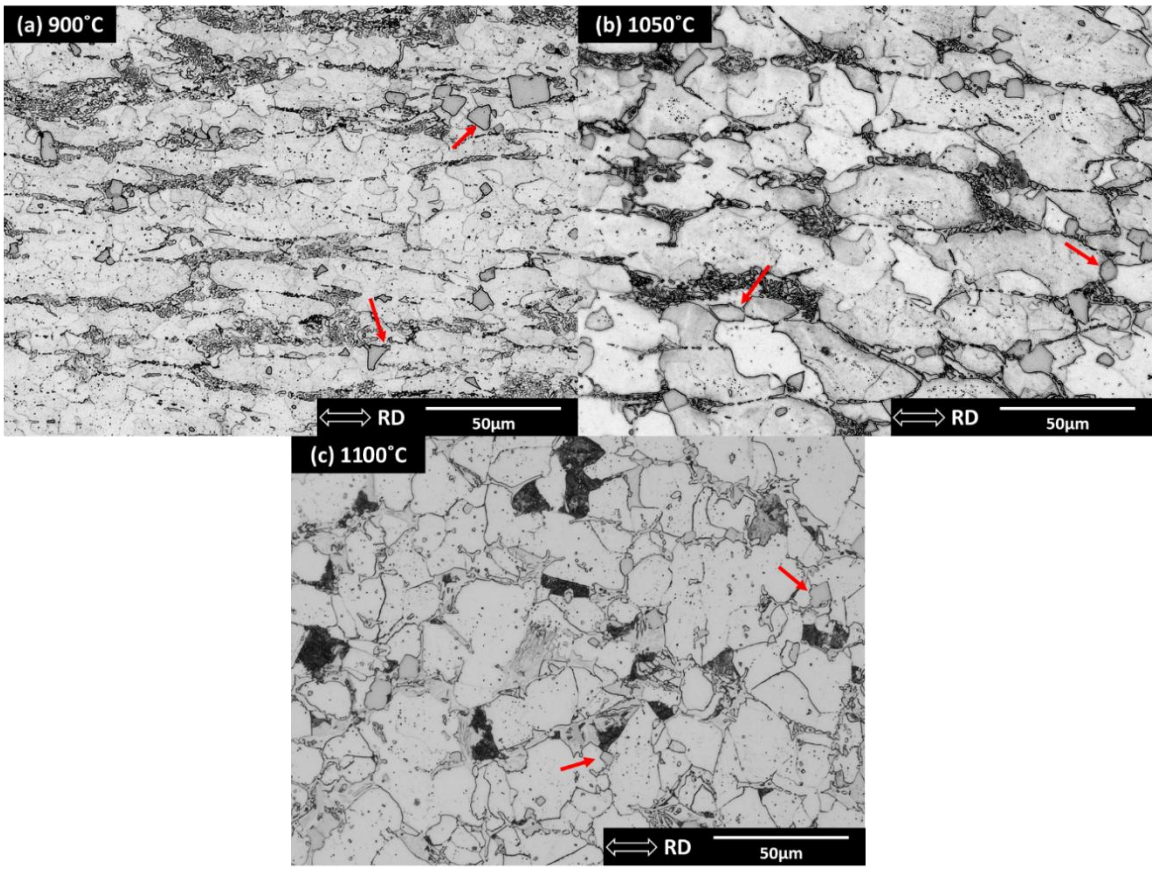

Figure 61: Optical micrographs of 5MASC after deformation using PSC, the final cooling rate used was 0.1˚C/s from (a) 900˚C, (b) 1050˚C and (c) 1100˚C

5.4.3.2 7.5MASC

Using the same PSC testing procedure as the 5MASC alloy, samples were subjected to controlled cooling from the finishing temperatures of 900˚ and 1050˚C at rates of 30˚C/s and 0.1˚C/s, followed by microstructural and mechanical analysis. The resulting microstructure cooled from 30˚C/s, as shown in Figure 62, reveals a homogeneously dispersed TiB_2 phase within a needle-like martensitic MA matrix, similar to the 5MASC ingot. Pro-eutectoid ferrite is observed at the grain boundaries, though insufficient time was available for this phase to fully nucleate. The TiB_2 particles maintain the jagged, platelet morphology seen in the 5MASC. Unlike the 5MASC alloy, elongated grains from TMP are preserved, with TiB_2 particles predominantly positioned at grain boundaries. Increasing the TiB_2 volume fraction by a nominal 2.5% has resulted in a greater number of particles per unit area, as verified in Section 5.4.2.

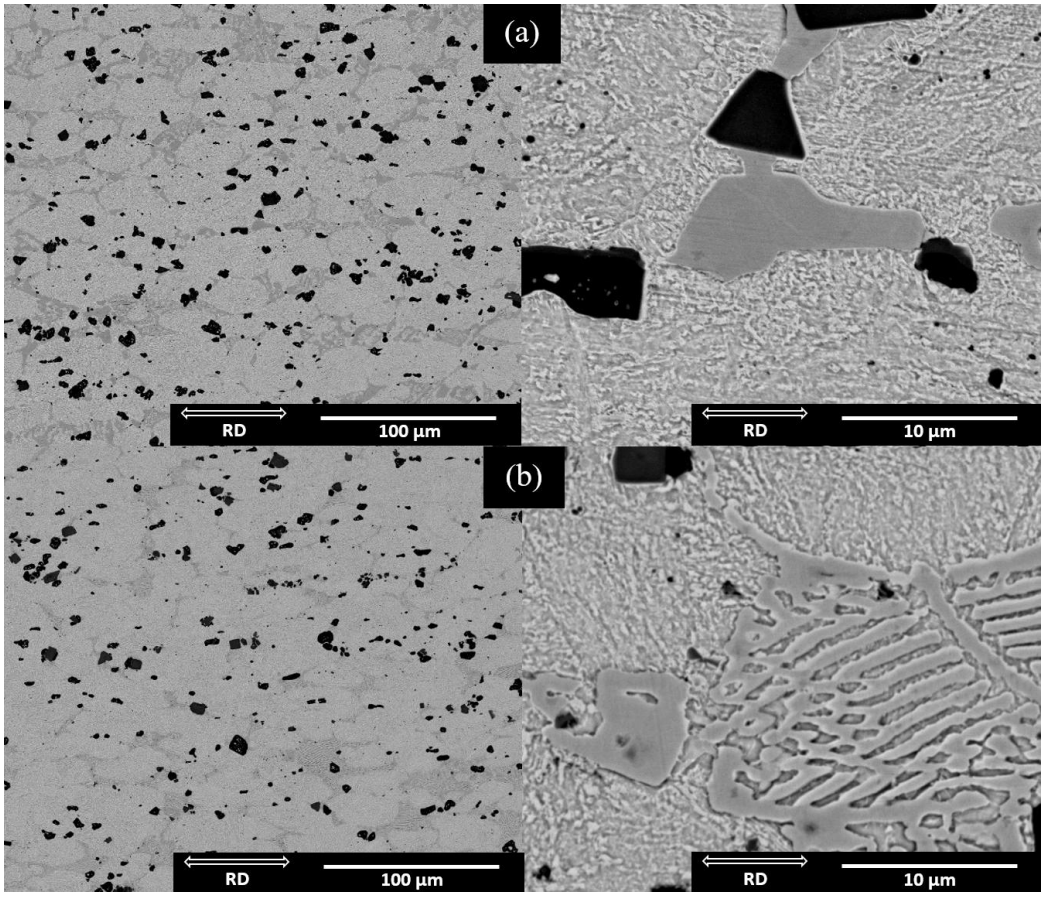

Figure 62: SEM (BSE) images of 7.5MASC after deformation from (a) 900˚C and (b) 1050˚C, with a final cooling rate of 30˚C/s

Similar to the as-cast 5MASC ingot, the 7.5MASC alloy also exhibits an agglomeration of particles within the matrix. An example of this can be seen in Figure 63, where a rounder and significantly larger particle phase begins to form. This phase is distinctly not TiB_2, as indicated by its rounded morphology and slightly lighter appearance in BSE imaging. To accurately characterise this phase, energy dispersive X-ray spectroscopy (X-EDS) analysis will be utilised to acquire different elemental concentrations through map, point and line analysis. The agglomerated particle observed in Figure 63 has a maximum diameter of 35 µm, with smaller surrounding particles ranging from 1 to 5 µm in size. Importantly, this phase appears to be unique and is not commonly found throughout the matrix.

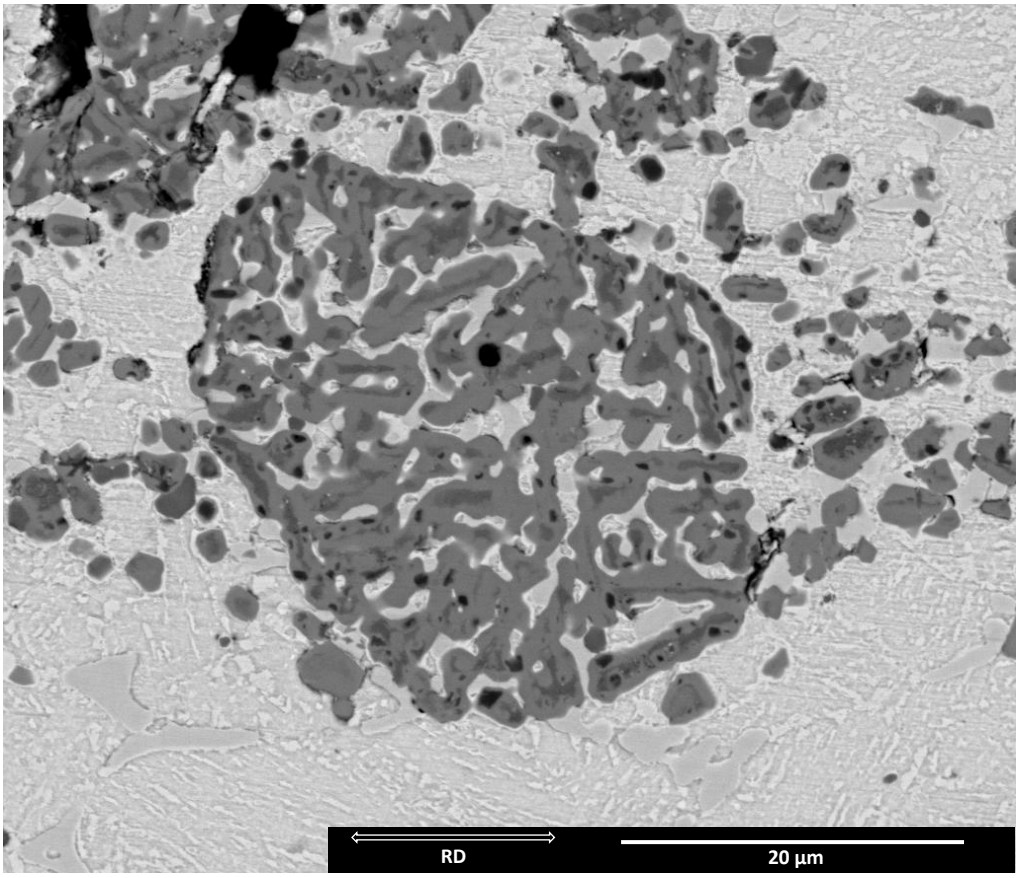

Figure 63: SEM (BSE) images of the foreign phase present in the 7.5MASC after deformation from PSC, the final cooling rate used was 30˚C/s from 900˚C

The microstructure of the 7.5MASC alloy, cooled at a rate of 0.1˚C/s, as depicted in Figure 64, reveals a homogeneously dispersed TiB_2 phase throughout the MA matrix. Despite the slower cooling rate, there remains insufficient time for the complete development of pro-eutectoid ferrite and pearlite. These phases are only faintly discernible in these SE images. Compared to the 5MASC alloy which was slow-cooled at 0.1˚C/s, the 7.5MASC alloy exhibits similar grain refinement due to TMP. Notably, the TiB_2 particles in the 7.5MASC alloy show a tendency to align with the rolling direction. This could cause the material to exhibit different strength, hardness, or ductility in different directions. Despite the slower cooling rate, the MA matrix phase is fine and equiaxed.

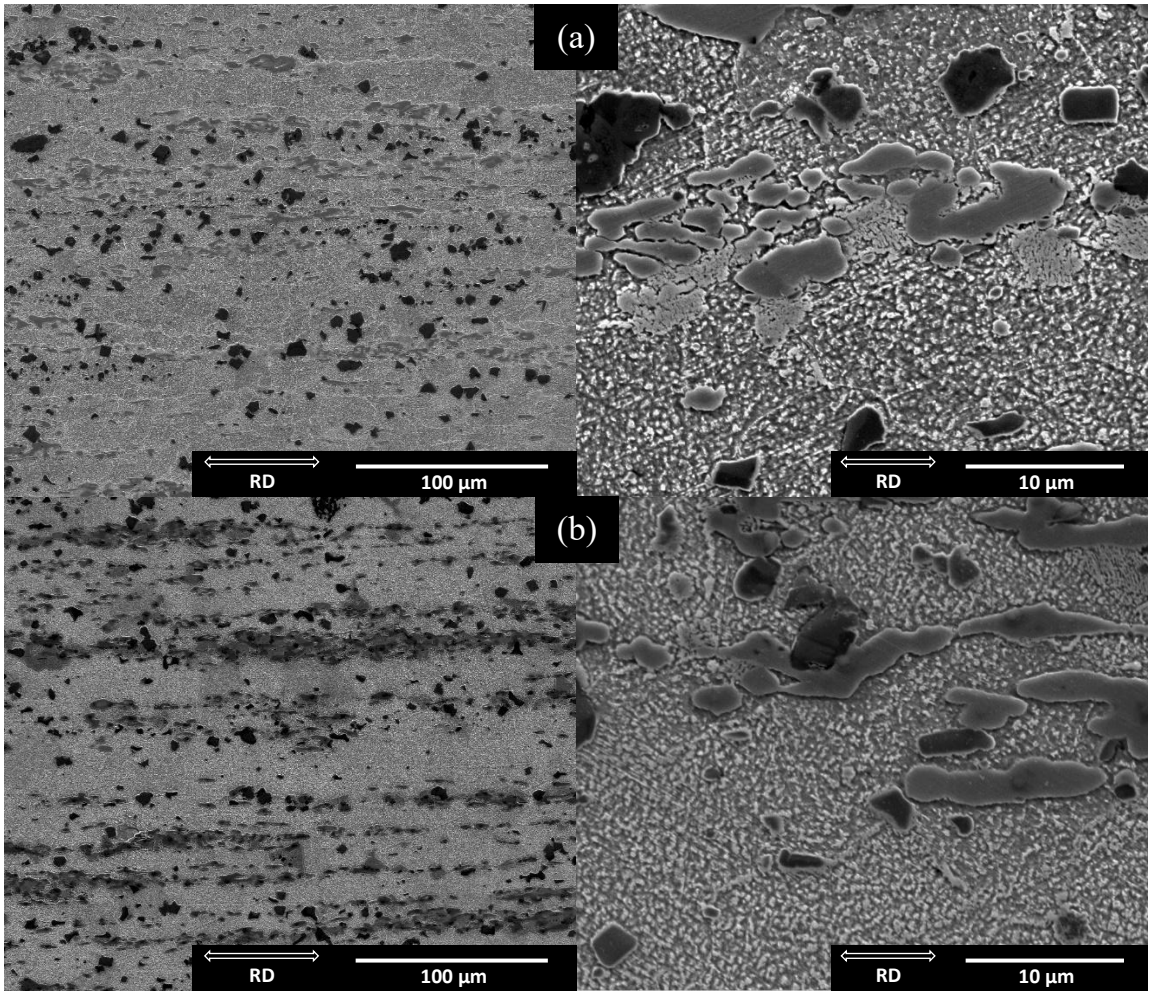

Figure 64: SEM (SE) images of 7.5MASC after deformation using PSC, the final cooling rate used was 0.1˚C/s from (a) 900˚C and (b) 1050˚C

5.5 Energy Dispersive X-Ray Spectroscopy

The presence of TiB_2 in the sample was confirmed through X-EDS analysis. Using the EDS detector on the FEI Inspect F50, elemental scans were conducted, and the resulting map, shown in Figure 65, revealed a high concentration of titanium specifically at the locations of the dark particles, thereby confirming the presence of TiB_2. This observation aligns well with previous literature findings regarding the morphology and size of TiB_2 particles [130], [131], [132]. However, mapping boron proved challenging due to its low atomic weight, which makes it difficult for X-EDS to detect, as the X-ray energies associated with boron are too low for effective detection. Additionally, boron's low energy peaks can be easily overshadowed by noise or other elements' peaks, complicating accurate identification and quantification. This limitation is a known challenge in the analysis of light elements using X-EDS technology.

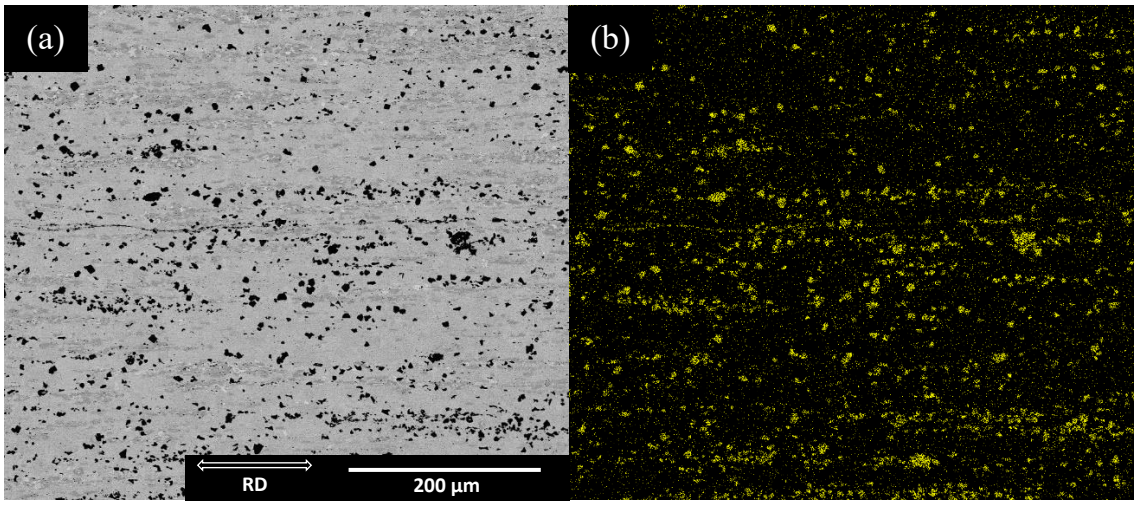

Figure 65: (a) SEM (BSE) image of 7.5MASC example used for X-EDS analysis of TiB_2 particles and (b) Ti map in the MA matrix

Point analysis was conducted on the as-cast 5MASC alloy Figure 66 to analyse the matrix and TiB_2 particles. In Spectrum 1, a high concentration of Ti and Fe was detected, associated with a slightly rounded particle, suggesting the presence of a Ti-rich phase. Spectrum 2 revealed high wt.% of titanium and boron, confirming the identification of a TiB_2 particle. Spectrum 3, which analysed a raised ferrite phase, predominantly showed Fe, with smaller amounts of C and Mn, characteristic of the MA matrix.

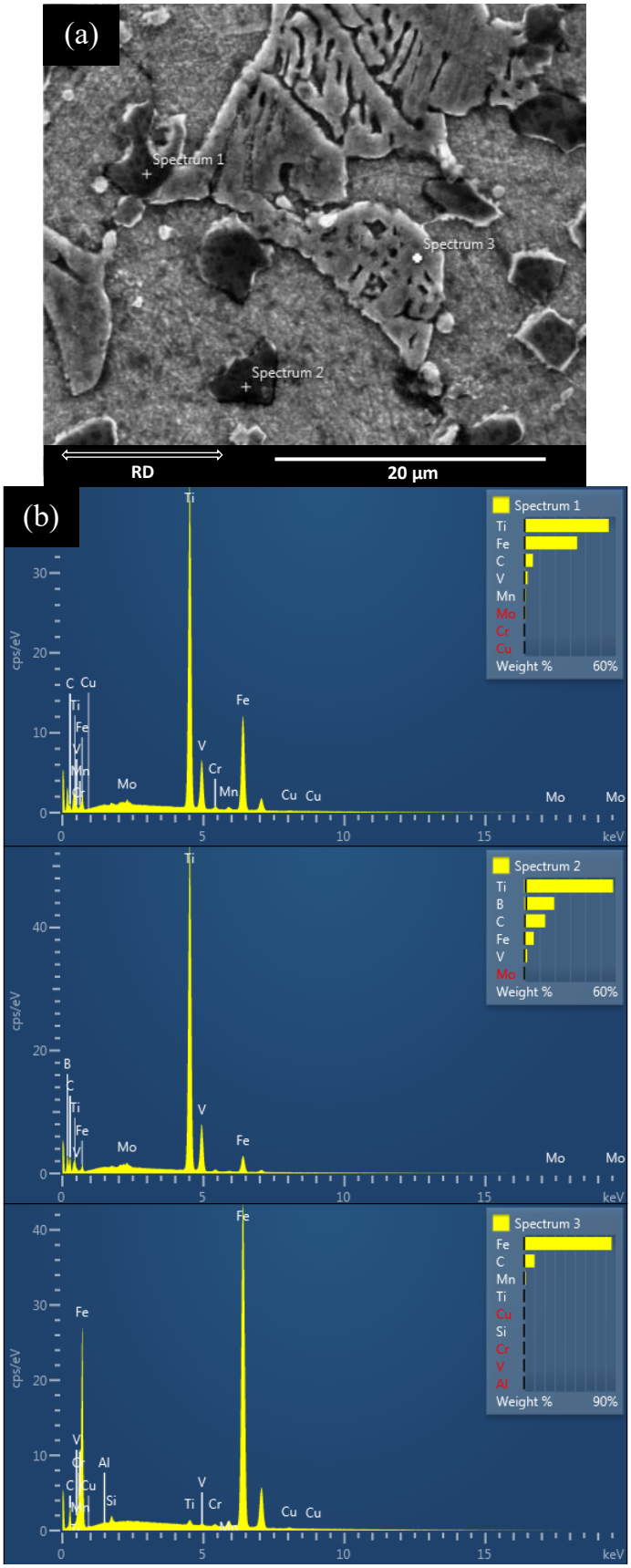

Figure 66: (a) SEM (SE) image of as-cast 5MASC used for X-EDS point analysis and (b) corresponding map spectrums

In the 7.5MASC ingot, cooled from 900˚C at a rate of 0.1˚C/s, an agglomerate phase similar in morphology to the one present in Figure 63 has been identified, as illustrated in the SEM BSE image (Figure 67). The contrast provided by BSE imaging clearly highlights this phase, which, unlike the typical TiB_2 particles, exhibits a rounded morphology, suggesting a different composition. Elemental mapping using X-EDS (Figure 68) has shown that the two large particles within this agglomerate, measuring 20 µm and 25 µm in diameter, consist predominantly of Ti and C. This composition strongly suggests that these particles are titanium carbide (TiC). Although Ti and B are strongly influenced to react with one another by chemical nature (past 1127˚C), excess Ti may have been present in the system after VIM which in turn reacts with free C to form TiC during solidification. The formation and morphology are supported by observations made by Parashivamurthy et al. [133] in TiC. Additionally, the absence of Fe and B in the elemental analysis confirms that this phase is not related to Fe-based carbides or borides. However, its presence is not prevalent in the MA matrix, indicating that the conditions for its formation were not uniformly met across the sample. The identification of TiC in this context allows for an understanding of the interaction of elements during the solidification and cooling of MASC alloys with higher amounts of Ti.

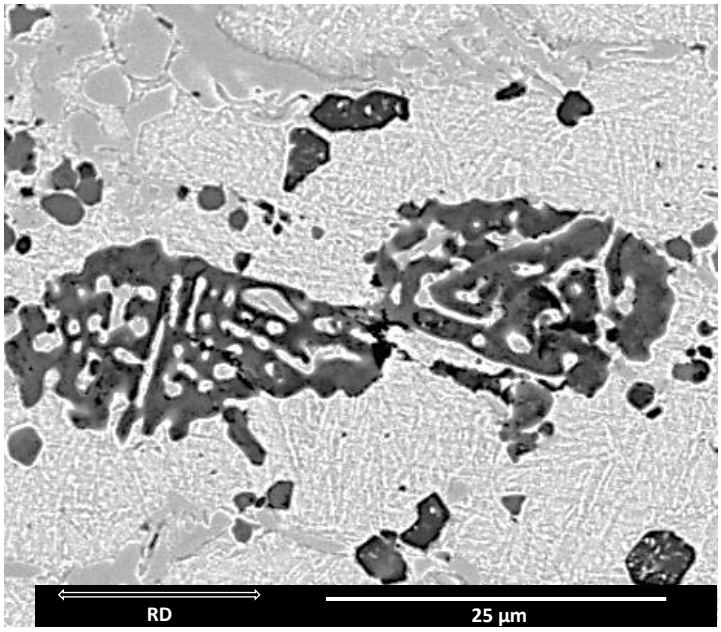

Figure 67: SEM (BSE) image of a foreign phase detected in the 7.5MASC alloy cooled at 0.1˚C/s from 900˚C

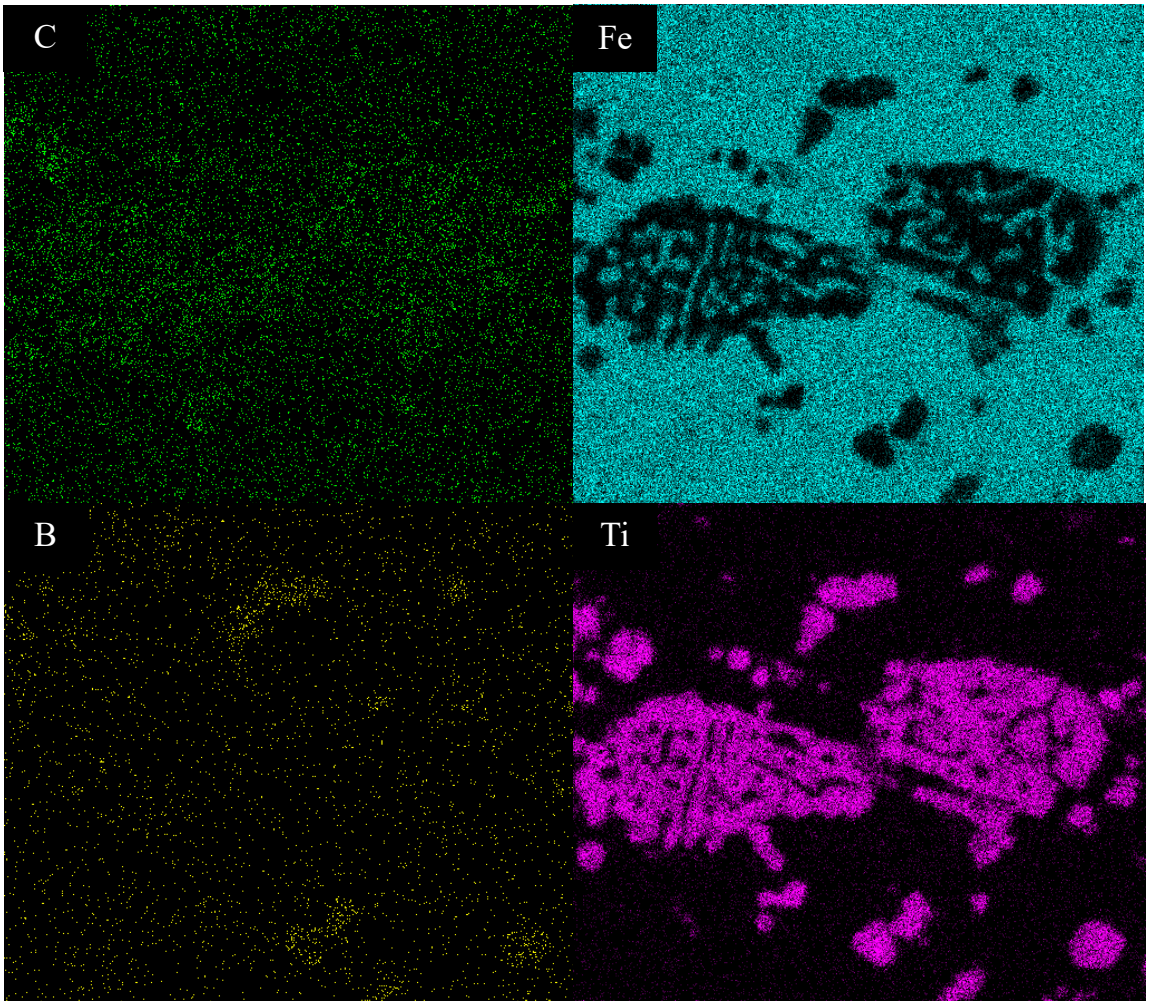

Figure 68: X-EDS map of prominent elements which show high/low wt.% values in the agglomerated phase

5.6 Mechanical Testing

As discussed in Chapter 4 for the MA steel, mechanical properties such as Young's modulus, yield strength, tensile strength, and uniform elongation were investigated for both MASCs. Dog bone specimens were prepared, ensuring the gauge area was positioned within the deformation zone, and subjected to tensile testing on a Zwick Roell tensile rig. Young's modulus was determined by analysing the elastic region of a stress-strain curve and using a non-destructive resonant frequency damping analysis (RFDA) technique. Additionally, Vickers hardness testing was performed to further reveal the mechanical properties of the specimens.

5.6.1 Tensile Testing

The engineering stress-strain curves presented in Figure 69 specify the tensile strength for all tested samples. The highest tensile strength recorded was 1695 MPa, observed in the 7.5MASC cooled at 30˚C/s from 900˚C, corresponding with a low uniform elongation of 5.8%, though interestingly this value is only 0.3% lower than the MA steel alone. It is unusual to observe this, as the presence of TiB_2 typically enhances the material's stiffness and strength at the cost of reduced ductility. The increased rigidity and diminished flexibility are well-known characteristics when reinforcing a material with TiB_2 as this stiffening effect leads to a decrease in the material's ability to undergo plastic deformation. Adding 7.5% volume of TiB_2 has only allowed for a 72 MPa tensile strength improvement. Yield strength was calculated using the same 0.2% offset method for the MA steel (see Figure 53). Maintaining high yield strength ensures that automotive parts can withstand operational stresses without undergoing permanent deformation, thereby preserving the integrity and safety of the vehicle. The highest value of yield strength was recorded from the 7.5MASC alloy cooled from 900C at 30˚C/s (1657 MPa) followed by the same material with an identical cooling rate cooled from 1050˚C (1380 MPa). Conversely, the lowest tensile strength, 1035 MPa, was observed in the 5MASC cooled from 1050˚C at 0.1˚C/s. An average Young's modulus of 230 and 239 GPa was determined for 5MASC and 7.5MASC respectively. All modulus measurements were performed following ASTM E111 and ISO 6892-1 standard [115], [116], specifically identifying the gradient between 100 and 300 MPa on the stress-strain curve. These modulus values closely match the rule-of-mixtures calculation of Young's modulus, which in this instance would take 95 or 92.5 % from the modulus of the MA steel (208 GPa) and add either 5 or 7.5% from the modulus of TiB_2 (565 GPa, [76]). These values are 226 GPa for 5MASC and 240 GPa for 7.5MASC, giving a percentage uncertainty of 1.7% and 0.4% respectively. A representation of Young's modulus values for all alloys is presented in Figure 70.

Table 8: Yield strength and uniform elongation values of each MA steel sample

Material	Temp. (˚C) of PSC sample	Cooling Rate (˚C/s)	Yield Strength (MPa)	Uniform Elongation (%)
5MASC	900	30	1302	5.1
	900	0.1	905	8.0
	1050	0.1	869	7.6
7.5MASC	900	30	1657	5.8
	1050	30	1380	6.1
	900	0.1	1104	7.2
	1050	0.1	949	7.8

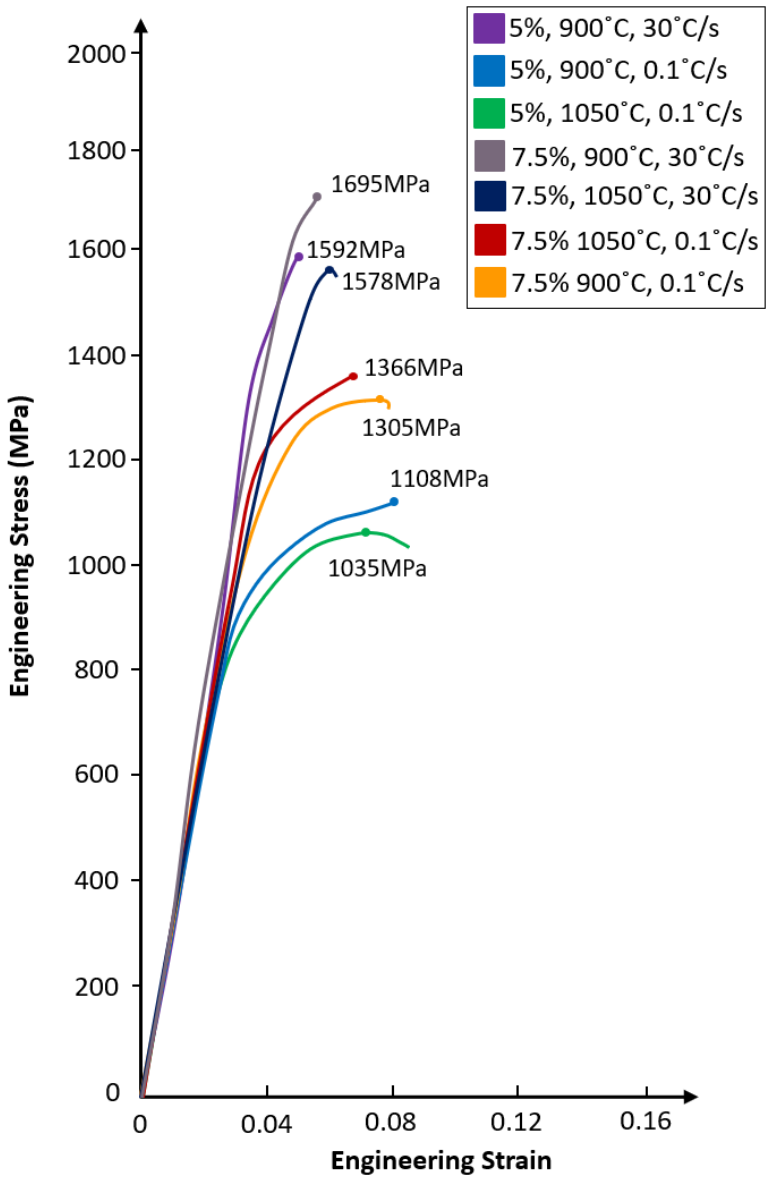

Figure 69: Engineering stress-strain plots of MASC alloys cooled from 900˚C/1050˚C at two cooling rates. The tensile strength values are stated at the peaks of each plot

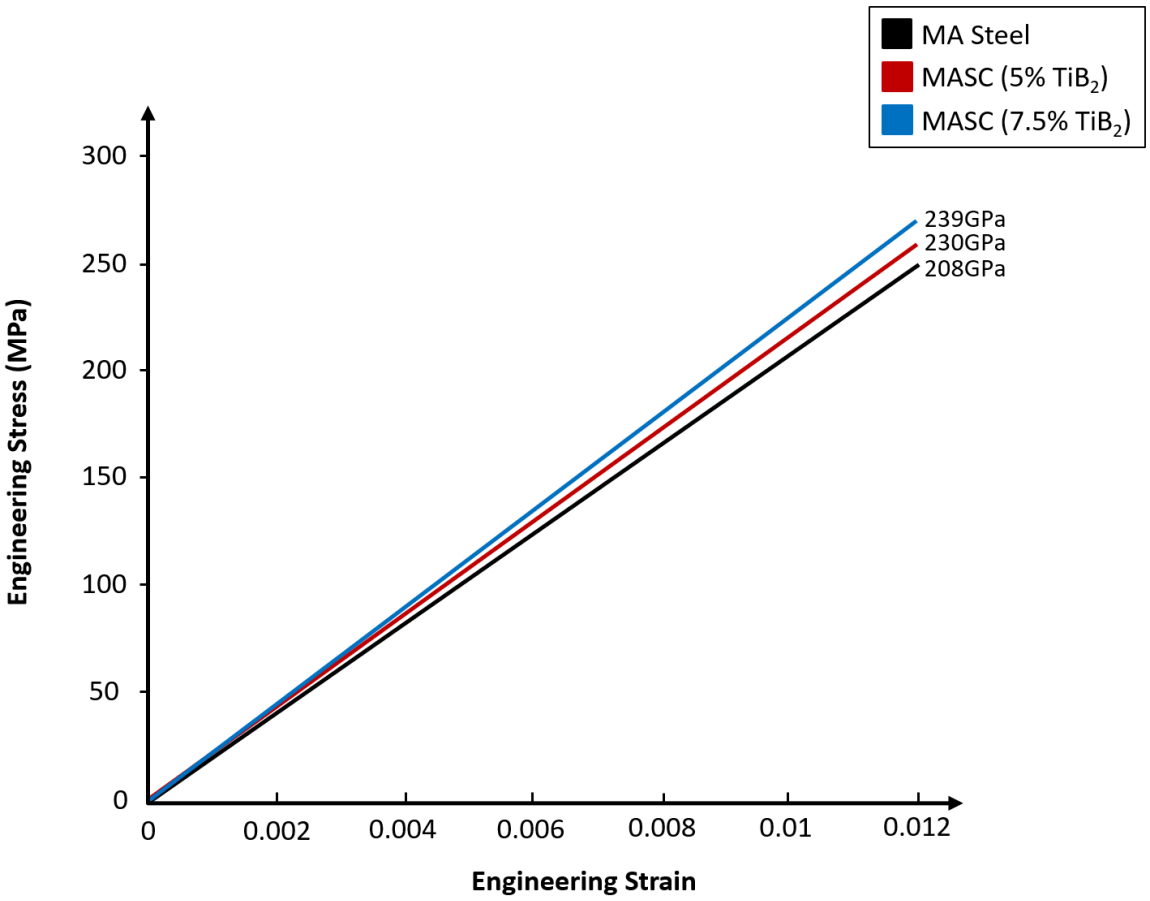

Figure 70: Average elastic region representation of each MA alloy which illustrates the increasing trend in Young's modulus with greater volume fraction additions of TiB_2

5.6.2 Tensile Fracture Analysis

This section focuses on examining the interfacial bonding between TiB_2 particles and the MA matrix under stress until failure. Although the literature on interfacial bonding between high-modulus steels and TiB_2 is limited, existing studies indicate that hot-rolling-induced defects could elevate local stress concentrations, potentially leading to crack coalescence [134], [135], [136]. Optical microscopy (Figure 71) reveals expected necking in the MA steel slow-cooled at 0.1˚C/s from 900˚C, while the MASC alloys exhibit clean fractures, except for a single tear and jagged break line in the 7.5MASC alloy cooled at 30˚C/s from 1050˚C. These micrographs suggest excellent interfacial bonding between the matrix and TiB_2 particles, correlating with observed uniform elongation values. Poor elongation and brittle behaviour would likely result from micro-cracks originating at TiB_2 particle sites.

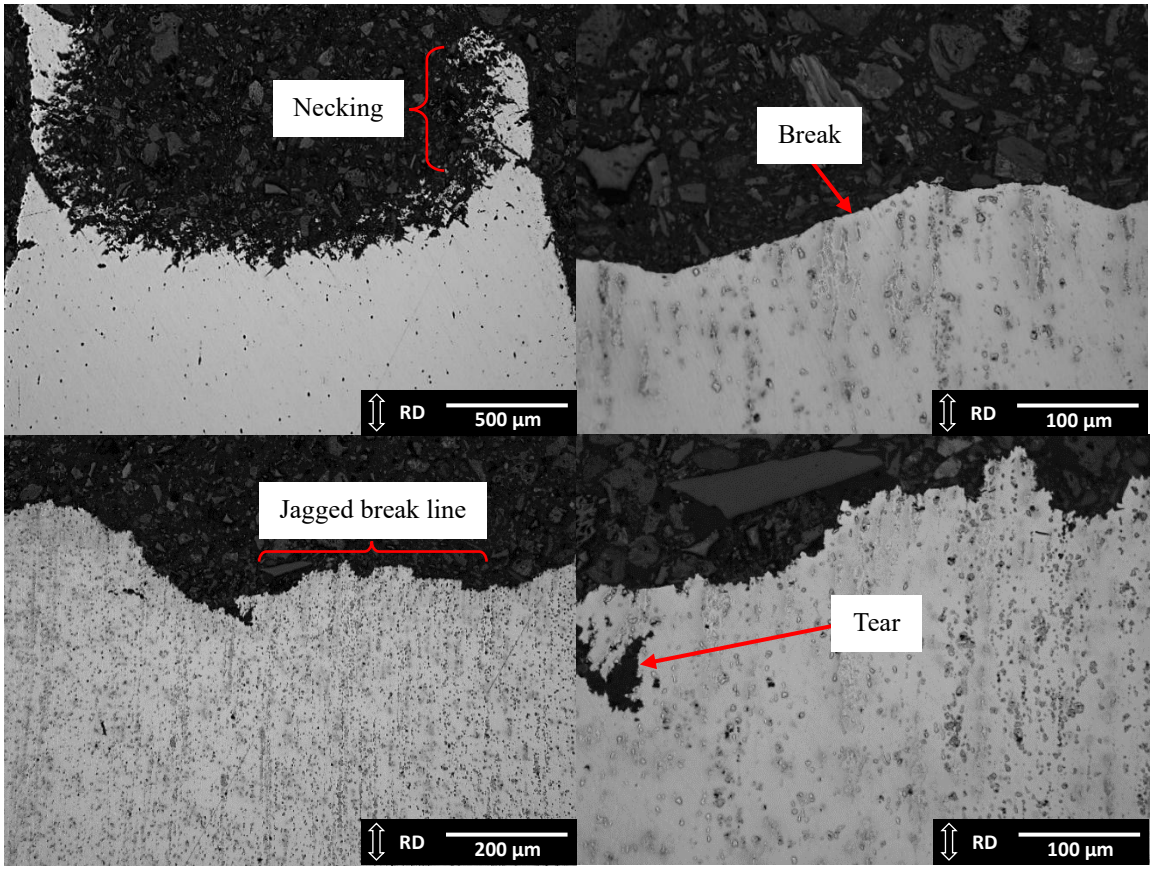

Figure 71: Breakpoints from tensile testing on (a) MA steel cooled from 900˚C at 0.1˚C/s, (b) 5MASC cooled from 900˚C at 30˚C/s and (c) 7.5MASC cooled from 900˚C at 30˚C/s

5.6.3 RFDA and Vickers Hardness

RFDA offers a non-destructive method for calculating Young's modulus of the MASC alloys. Four samples of both MASC alloys were tested using RFDA. When compared to the MA steel without composite reinforcement, RFDA testing revealed an averaged 9.6% improvement in Young's modulus for 5MASC with a value of 229 GPa and an 11.9% improvement for 7.5MASC with a value of 235 GPa. Vickers hardness values, detailed in Table 9 and presented in Figure 72, where HV1 refers to the hardness measurement under a 1 kg load for a 20-second dwell time, shows a progressive increase of hardness using a quicker cooling rate. The MASC alloys cooled from 30˚C/s exhibit high hardness in both MASC alloys due to the high hardness of TiB_2. For comparison, the highest hardness value of 668.8 HV1 from the 7.5MASC cooled from 30˚C/s is 22.2% higher than the MA steel which has undergone identical processing conditions.

Table 9: Average RFDA Young's modulus and Vickers hardness (HV1) values for the MASC alloys using different PSC conditions

Material	Temp. (˚C) of PSC sample	Cooling Rate (˚C/s)	Young's Modulus (GPa)	Vickers Hardness (HV1)
5MASC	900	30	229	624.2
	900	0.1		206.9
	1050	0.1		204.9
	1150	0.1		187.4
7.5MASC	900	30	235	668.8
	1050	30		664.7
	900	0.1		314.1
	1050	0.1		302.0

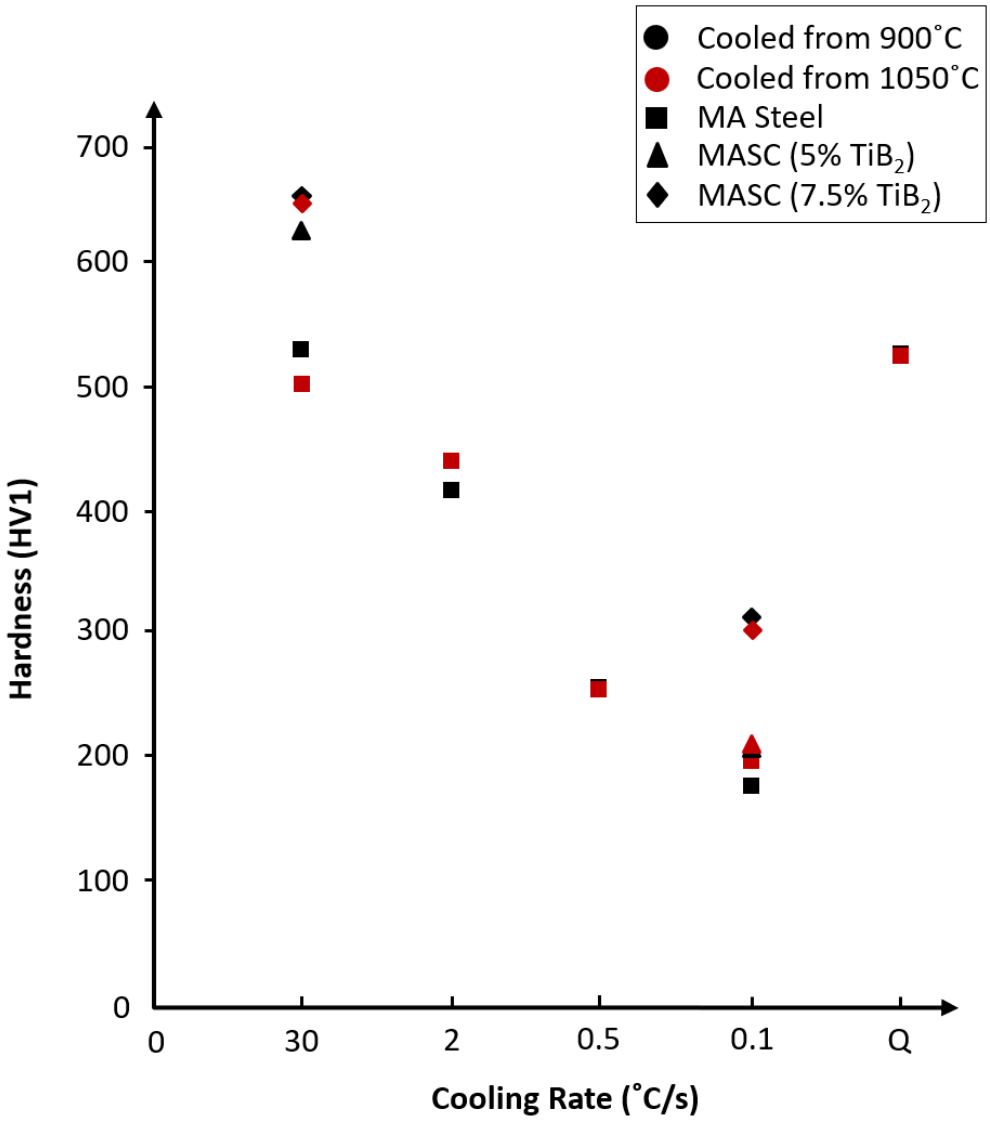

Figure 72: Vickers hardness values (HV1) for all MA alloys with varying cooling rates from 900/1050˚C after the second deformation pass during PSC, where 'Q' is quenched

5.7 Summary

The addition of TiB_2 in an MA steel matrix has proven to be useful in refining and retaining the grain structure of a thermo-mechanically processed VIM ingot. ThermoCalc has proven to be a pivotal tool in accurately calculating the required volume fraction of TiB_2 and providing insights into the multiple phases that form within the liquid region of MASC steel compositions. This computational tool has simplified the identification of optimal alloying conditions for Ti and B, ensuring the successful formation of TiB_2 particles. The TiB_2 particles are homogeneously distributed within the as-cast 5MASC microstructure, exhibiting an irregular hexagonal or jagged morphology. The successful formation of TiB_2 through ferrous additions of Ti and B aligns well with findings from previous studies.

The interface between the composite and matrix remains stable even at elevated temperatures, with grain pinning mechanisms notably effective in the 5MASC alloy, particularly when cooled at 0.1˚C/s from 1050˚C. This stability highlights the high thermodynamic stability of TiB_2. The pinning effect is evidenced by the retention of elongated grains aligned in the rolling direction, which remains consistent at higher temperatures. At a cooling rate of 30˚C/s, both alloys develop a martensitic matrix, with the TiB_2 particles remaining unaffected. However, when the cooling rate is reduced to 0.1˚C/s, the 5MASC alloy displays idiomorphic PF and partially nucleated pearlite. In contrast, the 7.5MASC alloy at this slower cooling rate does not exhibit the same phase transformation. Instead, it shows the nucleation of allotriomorphic ferrite without the presence of pearlite. This variation could be attributed to the thermodynamic impact of TiB_2, which may alter the phase stability and transformation kinetics.

Tensile testing and RFDA results reveal incremental improvements in Young's modulus, from 208 GPa for the base MA steel to 230 GPa and 239 GPa for the 5MASC and 7.5MASC alloys, respectively. This demonstrates the effect of increasing TiB_2 volume fraction on enhancing the material's stiffness. The progressive improvement in modulus reflects the reinforcing role of TiB_2,

contributing to the overall mechanical performance of the alloys. The primary objective of this study was to enhance the stiffness and strength of MA steel through ceramic reinforcement. The tensile results, particularly under conditions that mirror real-life applications where stiffness, yield strength, and uniform elongation are paramount, indicate that the 5MASC alloy cooled from 900˚C at 0.1˚C/s achieves an optimal yield strength of 905 MPa, coupled with a uniform elongation of 8%.

The ultimate goal is to optimise the balance between strength, stiffness, and elongation. The processing parameters chosen in this study were specifically selected to identify an ideal product for automotive components, focusing not on maximising any single property but on optimising the overall performance. The MASC alloys have shown great potential for novel high-modulus applications, and the aim is to provide Volkswagen with a range of processing conditions and alloy compositions, allowing them to determine the most suitable materials for various electric vehicle components.

6. Analysis of Steel 4140 Powder Consolidated using Field-assisted Sintering Technology

6.1 Introduction

The consolidation of S4140 powder using Field-Assisted Sintering Technology (FAST) offers many benefits that are particularly advantageous for the production of high-performance components in demanding industries such as automotive and aerospace. FAST is well-known for its ability to produce fully dense materials at lower temperatures and in shorter times compared to conventional sintering methods. This is achieved by applying a pulsed direct electric current directly through the powder compact, which heats the material rapidly and enhances diffusion processes through Joule heating, leading to accelerated sintering. The combination of high heating rates under vacuum and the application of uniaxial pressure results in a highly controlled sintering environment, allowing for the retention of fine microstructures and the suppression of undesirable grain growth. These characteristics make FAST an ideal technique for consolidating powders into high-strength materials suitable for automotive applications.

AISI S4140 steel or 42CrMo4, a chromium-molybdenum alloy, is widely utilised in the automotive industry for components that require a combination of high strength, toughness, and wear resistance. This alloy is often utilised in the manufacture of gears, bolts and couplings where its ability to withstand high loads and resist wear is essential [137]. The choice of S4140 for this research was driven by the need to familiarise with powder handling, powder analysis, and the FAST process during the initial stages of the PhD project. The COVID-19 pandemic led to the limited availability of atomisation equipment required to produce the desired microalloyed (MA) steel powders at the time. As a result, commercial S4140 powder was selected as a substitute to initiate experimental work as this material is similar to the MA steel in that it is a medium-carbon hypo-eutectoid steel. This allowed for the development of knowledge in various aspects of the project,

including SEM-based powder morphology analysis, ball milling techniques for powder mixing, and the familiarisation and optimisation of FAST processing conditions.

This chapter details the analysis of S4140 powder consolidated using FAST, focusing on how densification is impacted by temperature and dwell time (DT). The study also explores the interaction of S4140 with a commercial titanium diboride (TiB_2) powder, which was mixed with the steel powder using ball milling. The introduction of TiB_2 as a reinforcement phase is of particular interest due to its potential to enhance the mechanical properties of the consolidated matrix material. TiB_2 is known for its high hardness and modulus, which contributes to increased wear resistance and strength in the final composite material [127]. An examination of the microstructural evolution and phase transformations in the S4140 with and without a 5% volume fraction of TiB_2 composite will also be carried out. The knowledge gained from this initial phase of the project is key for the successful application of FAST to an MA steel, allowing for parallel comparison to the VIM work presented in Chapters 4 and 5.

6.2 Material Analysis

6.2.1 Elemental Composition

S4140 powder with a powder particle size of 53-106 μm was provided by Hoganas Sweden, with an average powder particle size determined at 75 μm. The elements, values in weight percent (wt.%), found in S4140 are presented in Table 10 alongside the MA steel composition for comparison:

Table 10: Elemental compositions (wt.%) of MA steel and S4140 powder from Hoganas, Sweden

Material	Fe	C	Cr	Mn	Mo	Nb	Ni	P	S	Si	Ti	V
MA Steel	96.56	0.47	0.13	1.37	0.06	0.030	0.17	0.013	0.010	0.72	0.03	0.18
S4140	97.068	0.40	1.0	0.90	0.20	--	--	0.026	0.006	0.4	--	--

6.2.2 Powder Morphology

The two powders which have been analysed are the Steel 4140 provided by Hoganas Sweden and TiB_2 provided by NewMet. The TiB_2 powder, with particle sizes ranging from 3 to 11 µm, exhibits angular morphology. This appearance reflects the inherently hard and stiff nature of TiB_2, which is also indicative of its brittle behaviour, as shown in Figure 73. The size and morphology of these particles closely resemble the TiB_2 particles observed during the liquid casting process via vacuum induction melting (VIM) used for *in situ* reinforcement, as displayed and discussed in Chapter 5.

In contrast, Figure 74 shows the S4140 powder particles with multiple satellites and some rough particle surfaces in scanning electron microscopy (SEM) imaging. With the increase of particle size of the powder, the probability of collision of the powder increases greatly. Satellite powder is almost unavoidable for powder particles of a certain size. According to a large number of observations and statistics, this critical diameter is about 100 µm [138]. Some particles have good sphericity and a smooth surface with a topographical texture also indicated in Figure 74. This texture shows a uniform distribution of agglomerate sub-particles. This morphology is typical of atomised powders, where rapid solidification during the cooling phase results in a smooth surface, promoting good flowability and packing density.

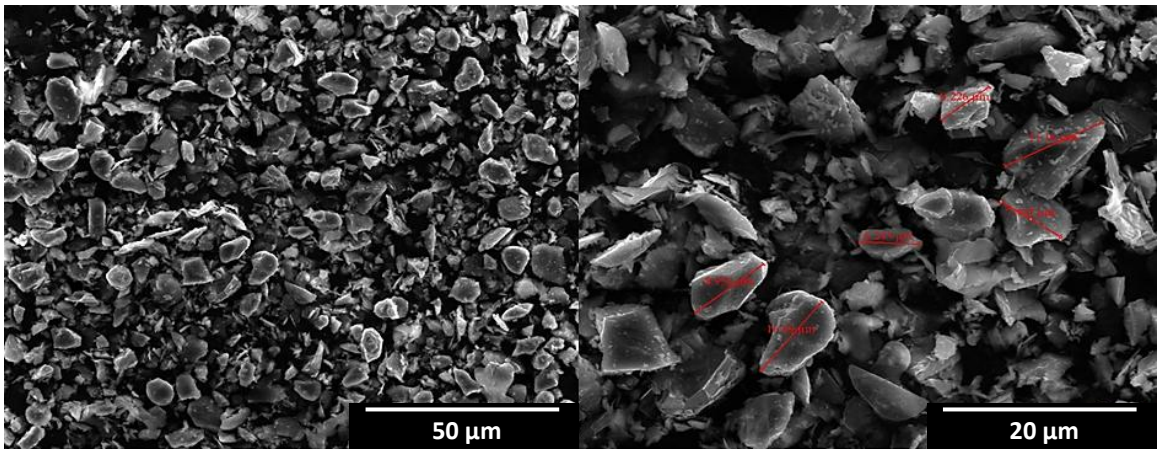

Figure 73: TiB_2 powder under SEM (SE), with an average particle size of approximately 8µm

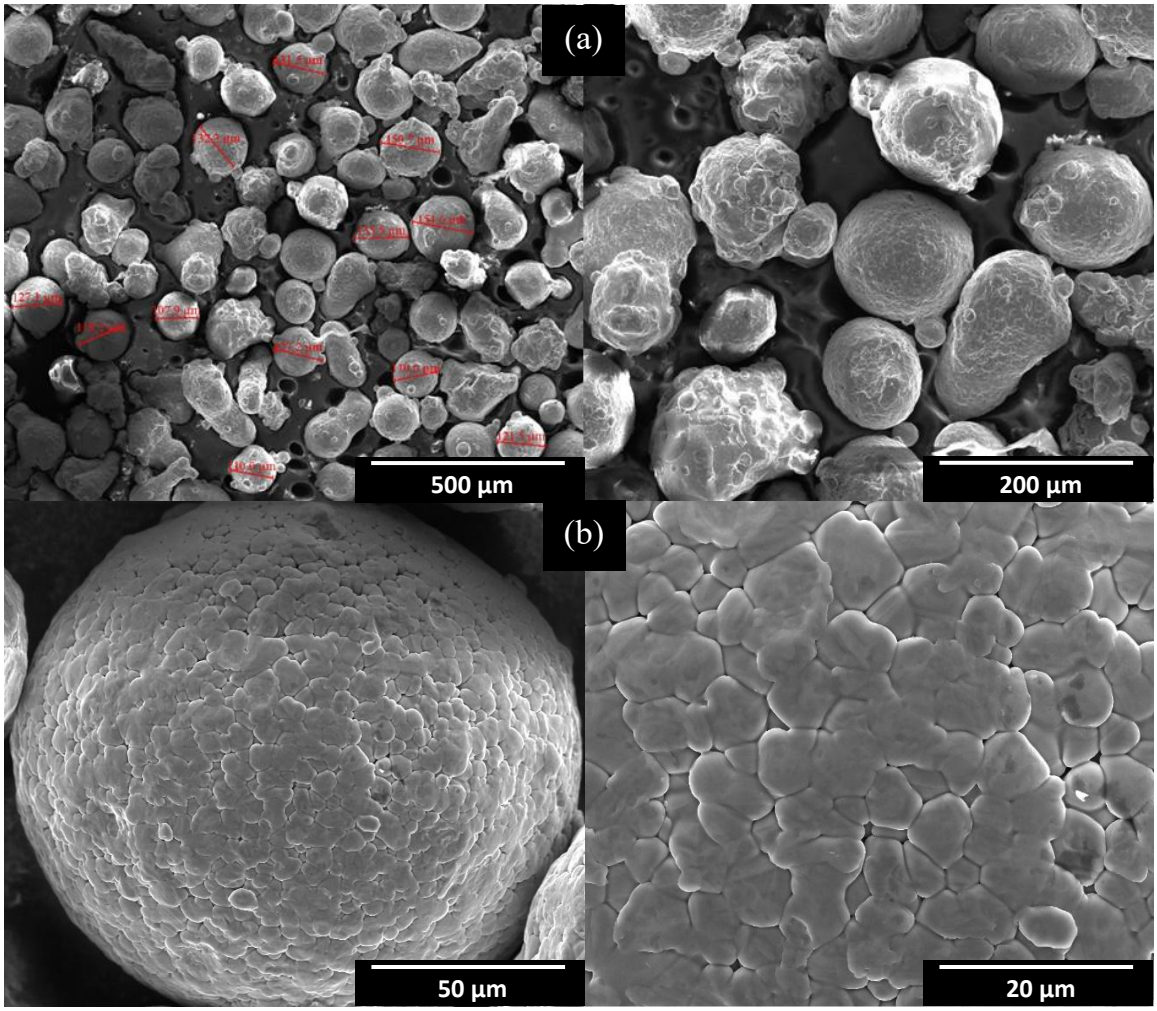

Figure 74: (a) S4140 powder under SEM (scanning electron, SE) and (b) topographical microstructure of a spheroid S4140 particle

6.3 FAST Testing Parameters

The key steps in a FAST run include vacuuming, applying an initial pre-hold pressure of 3 kN, gradually increasing pressure to the desired level, heating to 400˚C for the top pyrometer to begin reading, further temperature increase at the specified rate (˚C/min), dwelling, and cooling. After placing the mould assembly into the chamber and attaching the thermocouple, the vessel is sealed, and the pistons apply 3 kN pressure, ensuring the vessel remains closed during operation. Table 11 outlines the parameters for each FAST run (R1, R2…), maintaining a consistent mass of 12 grams for all 20 mm diameter samples. SEM and energy dispersive X-ray spectroscopy (X-EDS) analysis was conducted using the FEI Inspect F50 machine for both S4140 and S4140 with 5% volume TiB_2 compositions.

Table 11: FAST processing parameters used to investigate consolidation of S4140 with and without 5% volume fraction addition of TiB_2

Material	Dwell Pressure (MPa)	Hold Temperature (˚C)	DT (min)	
S4140	35	1050	5	R1
	35	1150	5	R2
	50	1050	5	R3
	50	1150	5	R4
	50	1150	5, 7.5, 10, 15	
S4140 + 5% TiB_2	50	1150	5, 10	

6.4 Microstructural Characterisation

This section will focus on the phase transformations observed in S4140, both with and without the addition of 5% volume TiB_2. The purpose of this study is to investigate how variations in pressure, temperature, and DT affect these transformations, providing insights into the material's behaviour under different FAST processing conditions.

6.4.1 S4140

Before investigating phase transformations, it is key to first comprehend the uncontrolled cooling rate used in the FAST machine, as this allows for a more accurate interpretation and estimation of the phases present within the S4140 matrix. Using in-built software to retrieve data from the machine, approximately 1,600 temperature data points from the top pyrometer were analysed for each run. To determine the cooling rate from Figure 75, particularly for the R3 run in this instance (all runs had nearly identical cooling gradients), the slope function in Excel was employed to calculate the gradient, revealing the rate of temperature change. Specifically, a gradient of -3.4 was calculated between 1050˚C and 600˚C, a critical

range for phase transformations in steels. Given that the heating rate was set at 100˚C/min, the gradient between 500˚C and 800˚C during heating was calculated at 1.68, indicating an average cooling rate of approximately 200˚C/min or 3.33˚C/s post-dwelling. This cooling rate may be too high for the formation of ferrite and pearlite and more favourable for martensite and bainite to form.

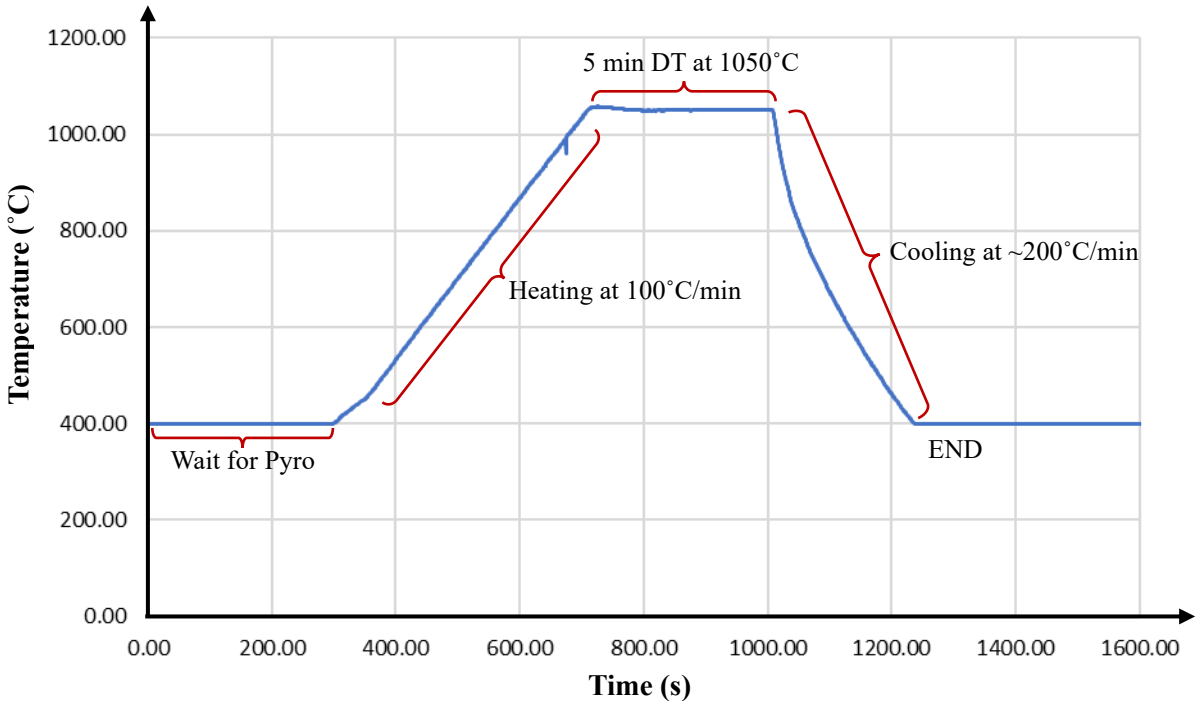

Figure 75: Temperature profile run for the FAST processing of S4140 at 1050˚C, 50MPa

From the collection of micrographs in Figure 76, it is evident that densification improves as temperature and/or pressure increase. For example, in R2 and R3, distinct regions where individual particles remain visible indicate incomplete diffusion bonding. In contrast, R4 demonstrates more advanced particle bonding, although some areas of incomplete bonding and porosity, highlighted by red arrows, are still present. The optical micrograph in R1 showcases idiomorphic ferrite (IF) and plate-like cementite (Fe_3C) phases characteristic of bainite. These phases are homogeneously distributed within the S4140 matrix, with needle-like cementite embedded in a lath ferrite microstructure.

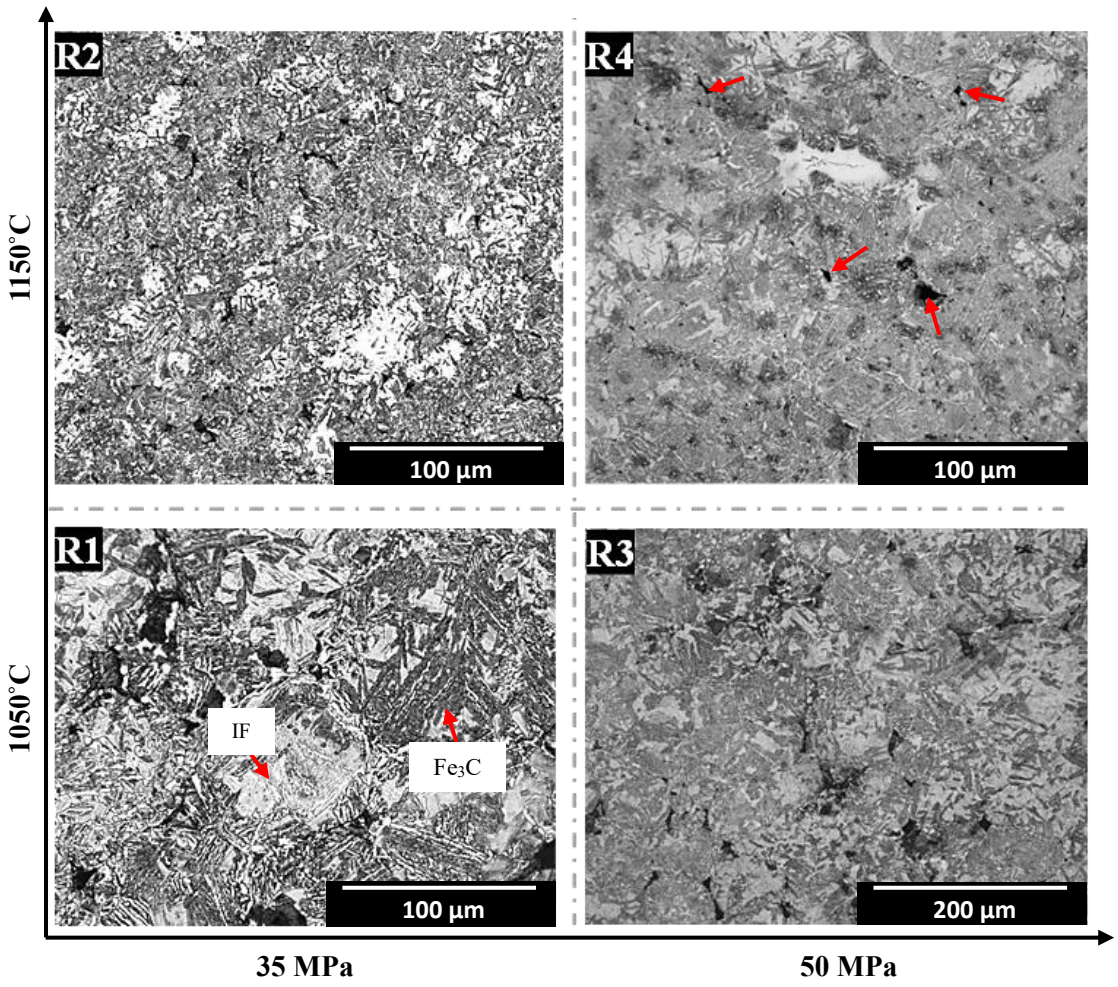

Figure 76: Optical micrograph grid for each FAST run of S4140, all samples are etched with 2% nital solution

An investigation into the effect of varying DT was conducted to determine whether holding S4140 at 1150˚C under 50 MPa for extended periods impacts key factors such as diffusion bonding between particles and phase transformations. DTs ranging from 5 to 15 minutes were tested, with the corresponding optical micrographs presented in Figure 77. The results indicate a progressive improvement in densification as DT increases, evidenced by a reduction in the number of pores. The consistent observation of bainite suggests that the cooling rate was sufficiently rapid to suppress the formation of ferrite and pearlite, leading to the development of bainite through the diffusion-less transformation of austenite. The presence of bainite typically enhances the material's strength and toughness, though it may reduce ductility compared to a fully ferritic or pearlitic structure.

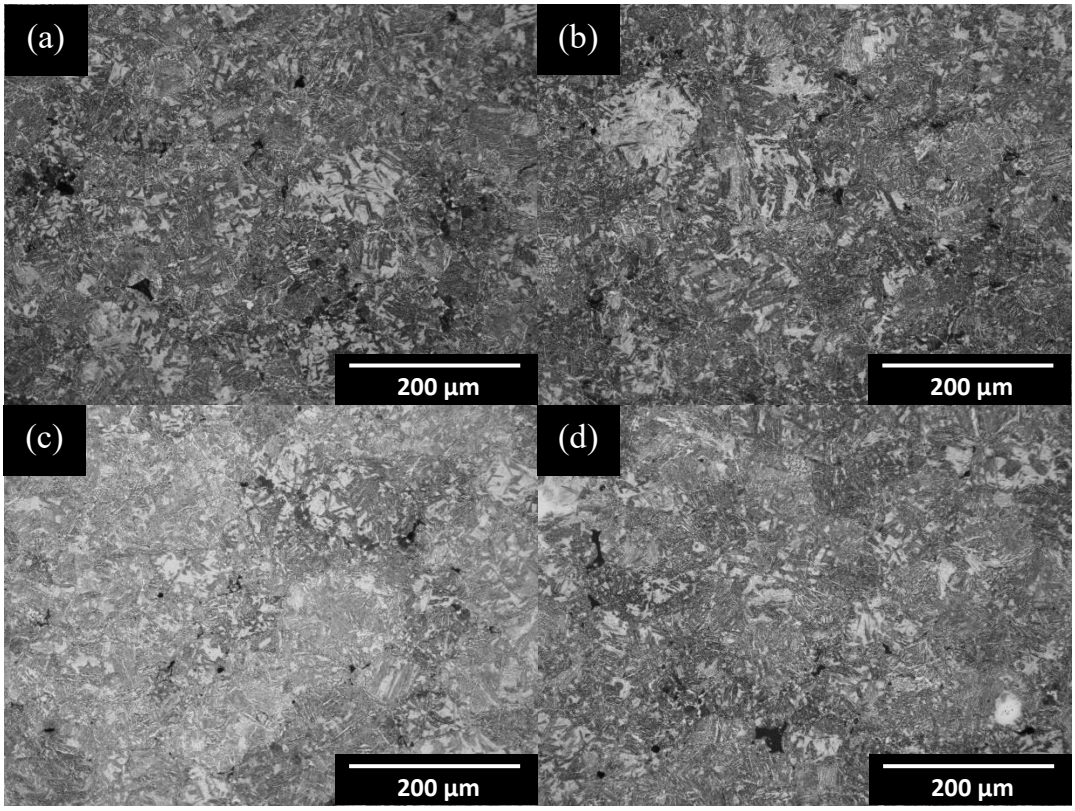

Figure 77: Optical microstructures of S4140 consolidated at 1150˚C, 50MPa holding pressure at (a) 5 min, (b) 7.5 min, (c) 10 min and (d) 15 min dwell times

Only one study by Yamanoglu et al. [139] has been published that investigates the effects of temperature and DT on the consolidation of S4140 using FAST. This study supports the conclusion that sintering temperature significantly influences the densification of S4140. Yamanoglu et al. demonstrated that the heating rate notably impacts the final relative density, particularly at lower temperatures, with higher heating rates increasing density, which then decreases with rising sintering temperatures above 900˚C. Additionally, the study confirmed that extending DT improves final density. The research also noted that sintering in a graphite die causes carbon to diffuse into the near-surface, forming hard martensite and that increased carbon content lowers the martensite start temperature, leading to retained austenite at the surface. Interestingly, Yamanoglu et al. identified optimal densification parameters as 1000˚C with an 8-minute DT and a 200˚C/min heating rate. However, these findings do not align with the results of this study, where porosity was observed at 1150˚C with a 15-minute DT.

6.4.2 S4140 with 5% Volume TiB_2

The study of S4140 was extended to understand its interaction with TiB_2 powder. Using the known apparent densities and masses of S4140 and TiB_2, the volume fraction of TiB_2 was calculated to be 5%. After calculating the appropriate proportions, the powders were mixed using a ball milling technique to ensure homogeneity. The ball milling process involved rotating the powders in a stainless-steel milling jar which facilitated the uniform distribution of TiB_2 particles within the S4140 matrix. Following this, the mixed powders were subjected to FAST, and SEM images (Figure 78) were captured for samples sintered with DTs of 5 and 10 minutes. The TiB_2 particles, averaging 8 μm in size, positioned themselves between neighbouring S4140 matrix particles, thereby hindering the diffusion bonding between adjacent S4140 particles. This is attributed to the high thermodynamic stability of TiB_2. As a result, full consolidation of the samples was not achieved, and porosity measurement proved challenging due to the dark appearance of TiB_2 in both SE and BSE imaging, which resembled pores or voids within the microstructure.

At 5 minutes DT, the microstructure in Figure 78 illustrates TiB_2 particles agglomerating at interconnecting spheroid S4140 particles, where these particles themselves still show a bainite phase previously identified. Densification improved significantly with a 10-minute dwell time (DT), resulting in a microstructure characterised by larger IF grains and allotriomorphic ferrite (AF) grains positioned at particle boundaries, as illustrated in Figure 78. The extended DT likely provided sufficient time for complete austenitisation and enhanced carbon diffusion, enabling the nucleation of ferrite at grain boundaries. The presence of these larger grains suggests that by manipulating the powder particle size, it is possible to control the grain size in the final sintered product.

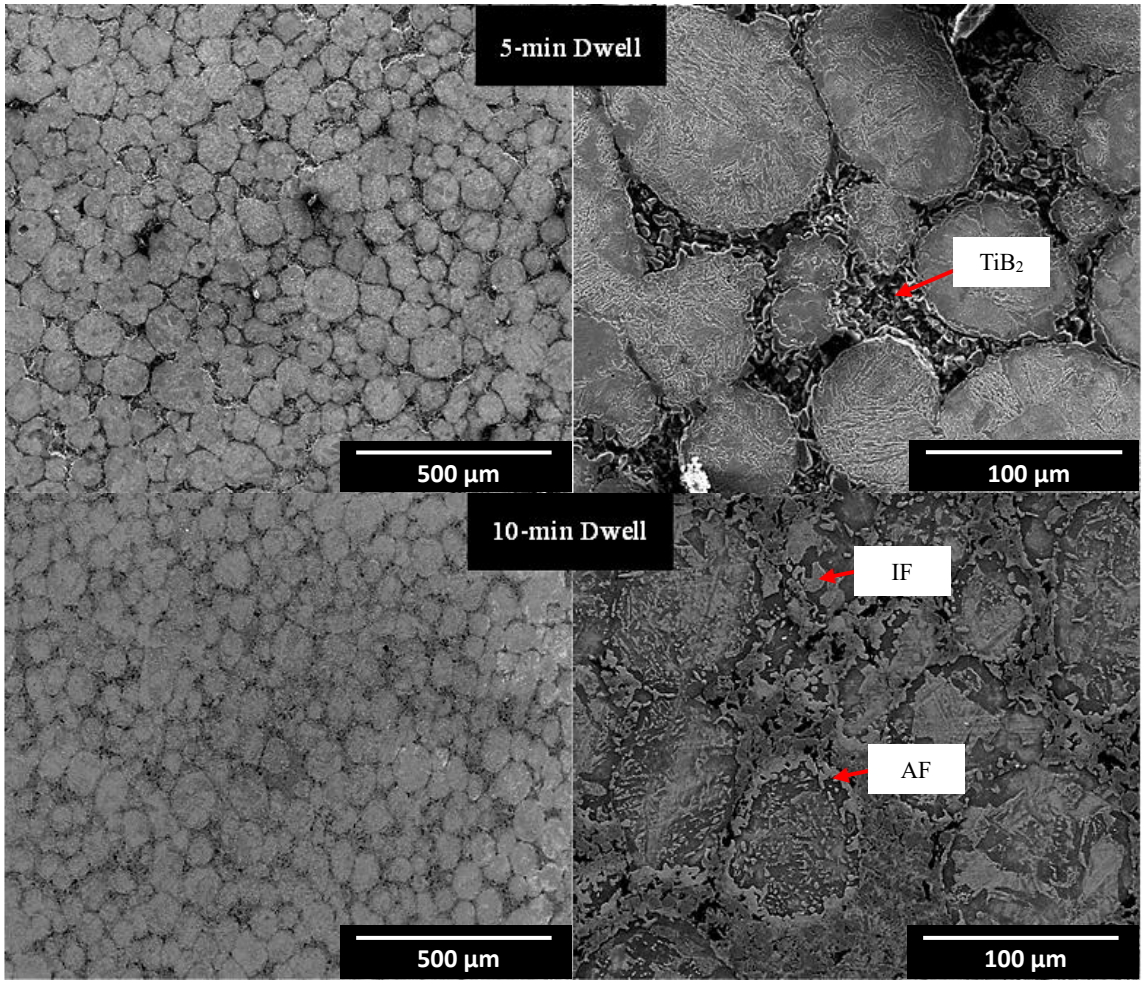

Figure 78: SEM (SE) images of S4140 with 5% volume TiB_2 sintered using two DTs at 1150˚C with a holding pressure of 50MPa

6.5 Energy Dispersive X-Ray Spectroscopy

Figure 79 presents both secondary electron (SE) and backscattered electron (BSE) SEM images of the S4140 alloy containing 5% TiB_2, which reveal the agglomerated TiB_2 phase situated at the particle boundaries of the S4140 matrix. There appears to be limited interfacial bonding between the thermodynamically stable TiB_2 and the surrounding S4140 matrix. However, further analysis using X-EDS will allow for a more detailed elemental examination of the matrix and composite phases.

In Figure 80, high concentrations of titanium are observed specifically in the regions corresponding to the dark powder particles, confirming the presence of TiB_2. Although mapping boron posed challenges due to its low atomic weight, concentrations aligning with the bright spots of titanium were also detected, further

substantiating the presence of TiB_2 and corroborating previous studies on the morphology and size of these particles [130], [131], [132]. Interestingly, carbon segregation was observed, as indicated by the bright spots in the X-EDS element map. Carbon segregation occurs due to the diffusion of carbon atoms to specific regions and can influence the formation of carbides or other carbon-rich phases, potentially affecting the mechanical properties and phase stability of the composite [140]. Additionally, oxygen was detected in the void regions, indicating that the S4140 composite, under the processing conditions of a 5-minute DT at 1150˚C and 50 MPa, exhibits some porosity. The area of higher concentration of oxygen also correlates with the areas of increased carbon concentration which suggests that during the sintering process, carbon may have migrated to areas where oxygen was present.

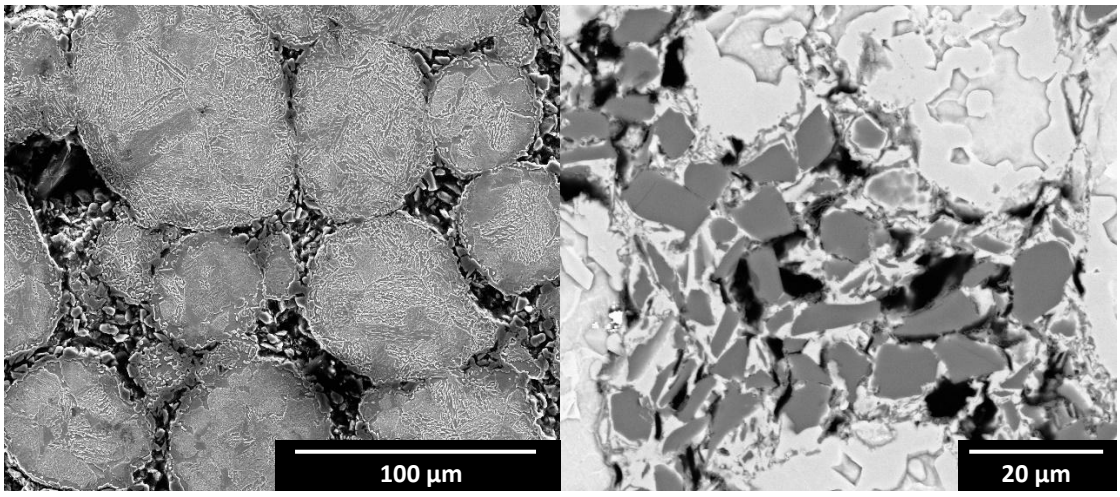

Figure 79: SEM images at two magnification levels of S4140 with 5% vol. TiB_2 fabricated using FAST: 5 min DT, 1150˚C and 50 MPa holding pressure

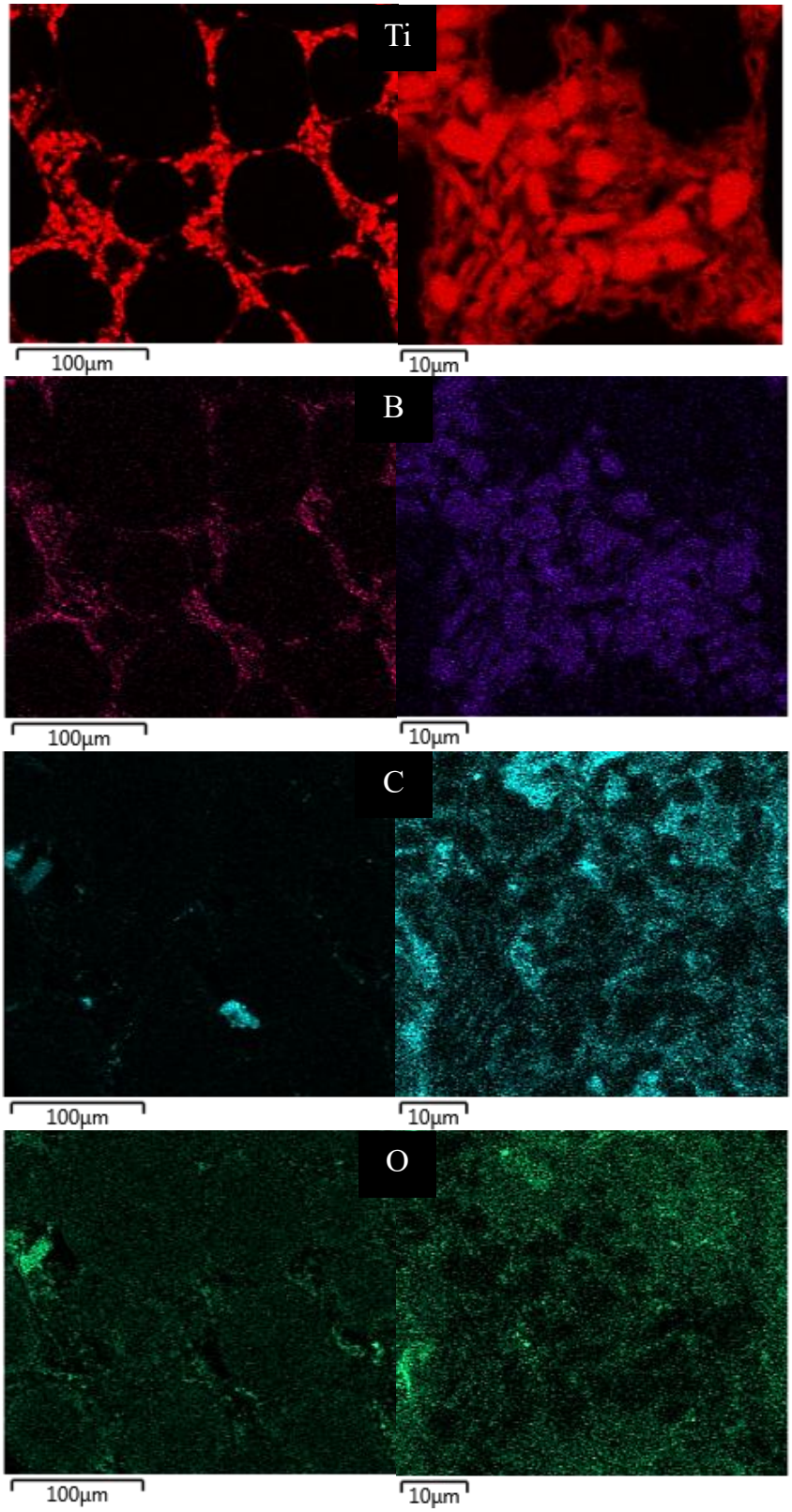

Figure 80: Element maps of Ti, B, C and O found in S4140 with 5% volume TiB_2 using X-EDS

6.6 Summary

This study has effectively utilised FAST as a processing method for the consolidation of S4140 powder. While this steel composition is not directly comparable to the MA steel, the insights gained from this research are valuable. The study has provided a comprehensive understanding of how powder particles can be characterised and the effects of varying DT and temperature on the densification of the final sintered product. The main conclusions from this work are as follows:

I. The morphology of S4140 and TiB_2 powder particles was examined using SEM. The S4140 particles exhibit a rough texture with some spheroidal shapes and satellite agglomerates, while the TiB_2 powder morphology is consistent with that observed in liquid metallurgy fabrication routes.

II. Microstructural characterisation showed that increasing the pressure or temperature during dwelling improves densification, with fewer voids and pores observed. Notably, S4140 particles were not deformed in the uniaxial compression direction during FAST, indicating their stiffness.

III. A bainitic microstructure was consistently observed in the centre of each S4140 sample. Further research is recommended to characterise phase transformations near the sample surface, particularly to investigate whether the graphite mould promotes carbon diffusion and martensitic transformation [139].

IV. When adding 5% volume of TiB_2, it was observed that the matrix particles experienced impeded diffusion bonding, with TiB_2 particles acting as barriers. X-EDS analysis revealed carbon segregation and oxygen in void regions. While increasing the DT from 5 to 10 minutes improved densification, further mechanical analysis is necessary to assess the strength of the particle interfacial bonding under stress. This analysis will provide insights into the durability and performance of the composite material in practical applications, helping to determine the optimal processing conditions for achieving desired mechanical properties.

7. Analysis of a Microalloyed Steel Composite Consolidated by Field-assisted Sintering Technology

7.1 Introduction

The fabrication of microalloyed (MA) steels using field-assisted sintering technology (FAST) is a novel approach that has yet to be thoroughly explored, particularly in the context of microalloyed steel composites (MASC). This study aims to delve into the consolidation of an MA steel which is entirely manufactured using facilities at the Henry Royce Institute at The University of Sheffield. These facilities include vacuum induction melting (VIM) and gas atomisation.

The introduction of 5% volume TiB_2 into the MA steel matrix (5MASC) through powder metallurgy presents a unique opportunity to explore FAST as a potentially feasible processing route for the manufacturing of MASC automotive components. This chapter will include measurements of Young's modulus, which will allow for a direct comparison with the 5MASC alloy discussed in Chapter 5. The research undertaken in this chapter aims to bridge the gap between traditional steel processing techniques previously presented with FAST for the production of high-modulus steel composites, providing new insights into the potential of FAST as a method for producing high-performance MASCs.

From the previous analysis of S4140 powder in Chapter 6, it is important to investigate various processing parameters used in FAST, such as dwell time (DT), temperature, and mould size; This will consequently impact phase transformation, particle diffusion bonding, consolidation, and microstructural evolution. These investigations are first conducted on the MA steel alone, providing a comprehensive understanding of its behaviour under various conditions. Following this, the study incorporates 5% TiB_2 into the MA steel, creating a microalloyed steel composite, referred to as 5MASC throughout this study.

7.2 Material Analysis

7.2.1 Fabrication and Elemental Composition

Given the exclusive composition of the MA steel investigated in this project, as detailed in Table 12 with elemental values expressed in weight percent (wt.%), a commercially available powder of this specific composition was not accessible. Consequently, VIM was utilised to produce a cylindrical bar, specifically designed with a cone-shaped end to enable droplet formation during the subsequent gas-atomisation process.

This entire process was uniquely personalised to align with the MA composition examined in Chapter 4 given by Bleck et al. [10], ensuring consistency across different experimental stages. By adhering to the same composition, this study enables a more precise comparison between powder metallurgy and conventional casting followed by thermomechanical processing (TMP).

Table 12: Element composition in wt.% of as-cast ma steel composition, verified through induction coupled plasma optical emission spectroscopy (ICP-OES)

Material	Fe	C	Cr	Mn	Mo	Nb	Ni	P	S	Si	Ti	V
MA Steel	96.56	0.47	0.13	1.37	0.06	0.030	0.17	0.013	0.010	0.72	0.03	0.18

7.2.2 Powder Morphology

Three distinct size fractions of gas-atomised MA steel powder were analysed, utilising the advanced facilities at the Royce Translational Centre (RTC) in Sheffield, UK [95]. These fractions, categorised by particle size sub 45 µm, 45-150 µm, and 150-300 µm, were separated using stainless steel sieves with corresponding mesh sizes. The surface morphology of these powders was examined using scanning electron microscopy (SEM), as depicted in Figure 81. The SEM analysis reveals that the sub 45 µm and 45-150 µm particles exhibit a well-spheroidised shape with minimal ‘satelliting’, a phenomenon where smaller particles agglomerate onto

larger ones. Conversely, the spherical morphology results from the surface tension that acts on the droplets before they fully solidify, promoting a rounder shape as particle size decreases. The smaller the particle size, the greater the sphericity, reducing the likelihood of abnormal or satellite formations due to the shorter cooling and spheroidising time. Larger particles, which have longer cooling and spheroidising times, are more susceptible to collisions that can disrupt their surface morphology before they fully solidify [138].

Additionally, bright spheroidal particles, as indicated by red arrows in Figure 81, could suggest the presence of contaminant particles possibly left from previous atomisation runs. Also, the topography of the powder can influence brightness. Particles that are more exposed or have a favourable orientation towards the detector can appear brighter due to increased electron emission. This effect is particularly noticeable in non-flat surfaces, such as powders

In the context of FAST processing, the presence of non-spheroidal particles and satellites is less concerning. This is due to the superior compaction and diffusion bonding achieved through Joule heating, which can mitigate the effects of such irregularities. The powder particle sizes were verified using the measuring software integrated into the FEI Inspect F50 SEM, ensuring accuracy in size distribution for further processing and analysis.

Smaller particles, due to their sphericity, enable superior packing density and diffusion bonding, thereby promoting more efficient consolidation. In this particular case, the gas-atomisation process yielded approximately 75% mass of powder from the cylindrical ingot, with less than 200 grams of particles under 45 μm, 500 grams within the 45-150 μm range, and nearly 1 kg in the 150-300 μm range. Consequently, the 150-300 μm fraction was predominantly utilised during FAST experimentation due to its abundance.

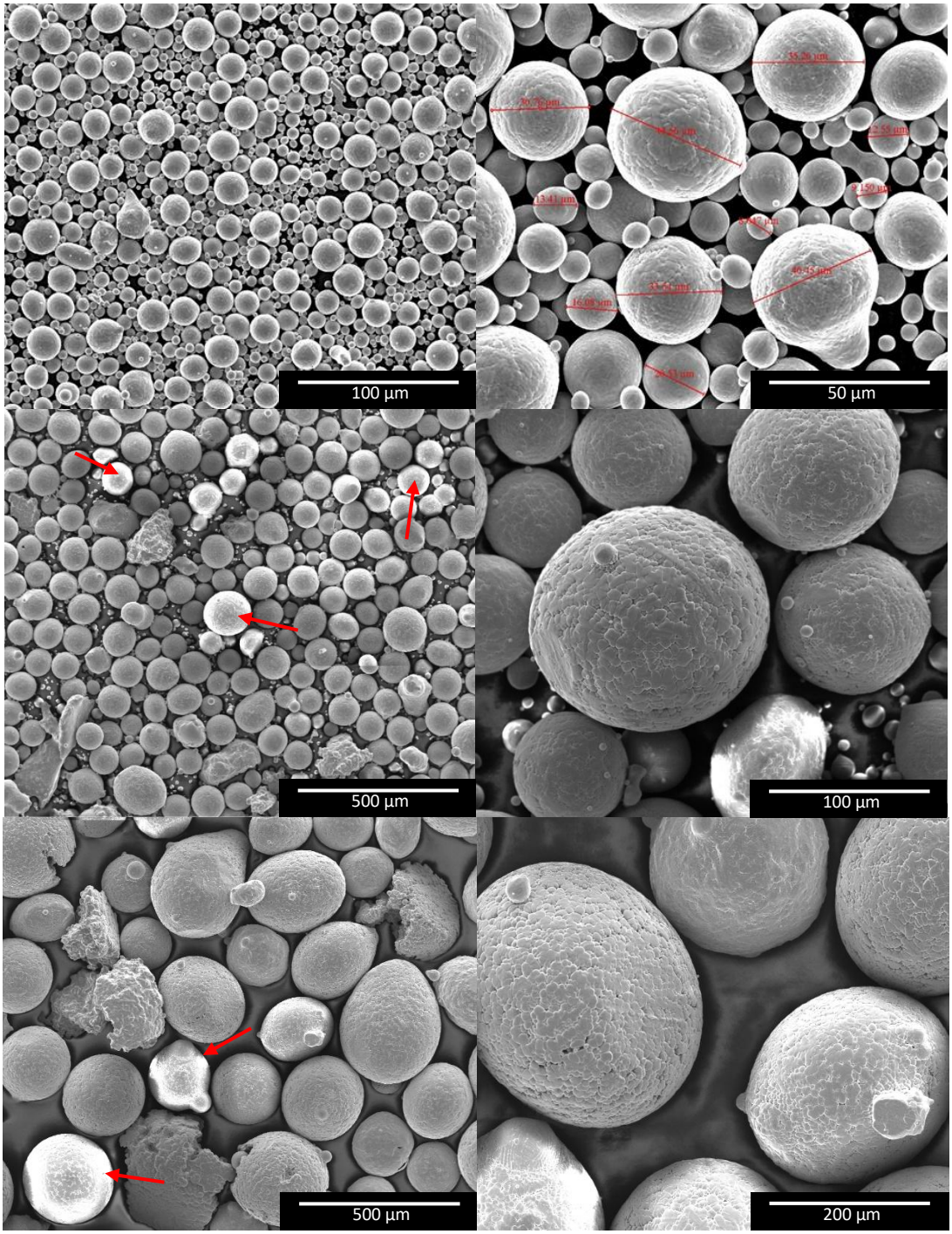

Figure 81: MA steel powder under SEM (scanning electron, SE) at (a) <45µm, (b) 45-150µm and 150-300 µm diameter

7.3 FAST Testing Parameters

The study examines the effects of varying temperature, DT and mould size on the consolidation, densification, diffusion bonding, and phase transformation of MA steel during FAST processing. By altering these parameters, the research aims to identify the optimal conditions for achieving excellent consolidation and microstructural refinement in MA steel before the investigation continues to incorporate *in situ* TiB_2. Table 13 details the specific parameters used for each FAST run for both MA and 5MASC alloys, ensuring a consistent sample mass of 12 grams for 20 mm diameter samples and 560 grams for 80 mm diameter samples. These masses were calculated to achieve a consistent sample thickness of 15 mm. Holding pressure for all FAST runs was kept at 50 MPa for 20 mm runs and 40 MPa for 80 mm. The lower pressure was chosen for the larger mould as breakage would occur at 50 MPa. The 80 mm mould runs were specifically conducted to evaluate the practical application potential of larger samples, which can also be subjected to mechanical analysis.

Table 13: FAST processing parameters used to investigate consolidation of MA steel powder with and without 5% volume fraction addition of TiB_2

Material	MA Particle Size (µm)	Hold Temperature (˚C)	DT (min)
MA Steel	45-150	900	5
	150-300	1000, 1100, 1200	5
	150-300	1100	0, 5, 10, 30
	45-150*	1100	5
5MASC	45-150	1100	0, 10*

**80 mm diameter mould used.*

7.4 Microstructural Characterisation

This section will investigate the phase transformations and consolidation behaviour observed in the MA steel, both with and without the incorporation of 5% volume TiB_2. The study aims to explore how variations in temperature, DT and mould size influence these transformations, offering insights into the material's response under different FAST processing conditions. Optimal processing conditions can be determined for the FAST processing of MA steel before the fabrication of a 5MASC alloy.

7.4.1 MA Steel

7.4.1.1 Changing Temperature

Temperature variations during FAST processing can significantly impact the rate of diffusion bonding between particles. Higher temperatures typically enhance consolidation, as corroborated by previous literature [139], [141], [142], [143]. In this study, temperatures of 900˚C, 1000˚C, 1100˚C, and 1200˚C were selected as dwell temperatures, with each held for 5 minutes to investigate their effects on the MA steel. The SEM images from these runs, shown in Figure 82, illustrate the progression of consolidation. A noticeable decrease in porosity is observed with increasing temperature, particularly between 900˚C and 1000˚C, and a clear improvement is seen between 1000˚C and 1100˚C. At 900˚C, partial diffusion bonding (DB) is evident, with significant porosity reduction occurring as the temperature reaches 1100˚C, indicating that the energy threshold required for effective diffusion bonding between MA steel particles is achieved at this range. At 1100˚C, nearly full consolidation is observed, and further increasing the temperature to 1200˚C does not yield any additional improvements in densification. The phases observed across all four temperature conditions remain consistent, with martensite being the predominant phase. This martensitic phase is characterised by its sharp, needle-like morphology within the matrix. This transformation leads to a hard and brittle microstructure, which is typical of quickly cooled steels.

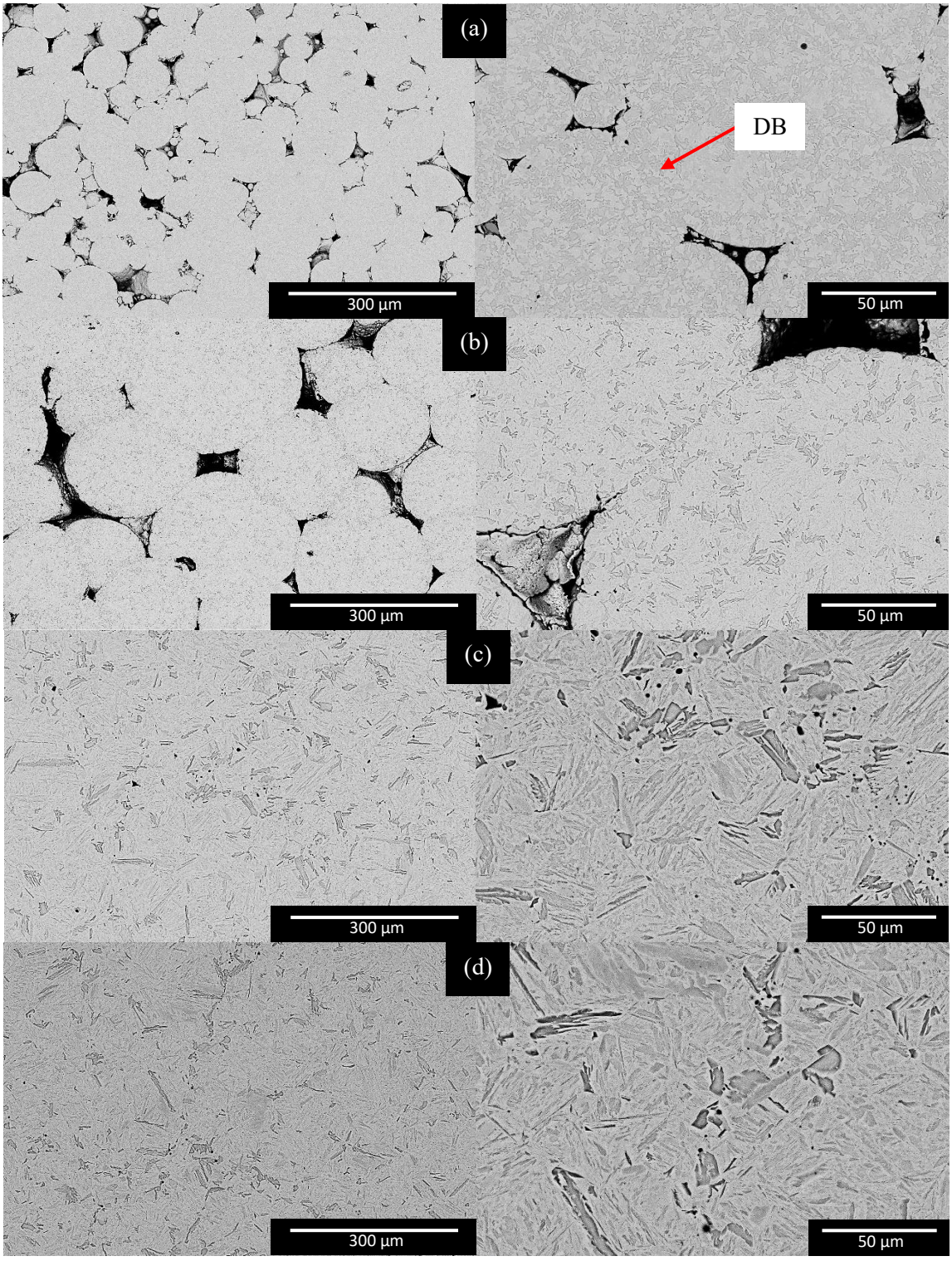

Figure 82: SEM (backscatter electron, BSE) micrographs of the MA steel powder sintered at (a) 900˚C, (b) 1000˚C, (c) 1100˚C and (d) 1200˚C for 5min at 50MPa

7.4.1.2 Changing Dwell Time

Investigating the effects of DT on the consolidation characteristics and phase transformations in MA steel is key to understanding how to optimise FAST processing. Previous studies indicate that increasing DT generally enhances the relative density of a material, though this effect tends to plateau after a certain duration [82], [139], [144]. This plateau is influenced by the material's properties, such as deformability (stiffness) and thermal conductivity, as well as the hold temperature during the dwelling phase.

For this investigation, all runs were conducted at 1100˚C and 50 MPa, using MA steel particles within the 150-300 μm range. The DTs examined were 0, 5, 10, and 30 minutes. As shown in Figure 83, the progressive densification of the MA steel aligns with existing literature, with noticeable improvements in porosity indicated by black voids in the microstructure. However, the difference between 10 and 30 minutes of DT is minimal, suggesting that near-complete consolidation is achieved within 10 minutes at the given temperature and pressure conditions. The effectiveness of diffusion bonding increases with longer DT, as it allows more time for atomic diffusion to occur, thus improving the overall consolidation of the MA steel.

The phase transformations observed during the rapid and uncontrolled cooling from the FAST machine offer intriguing insights. Unlike the microstructures depicted in Figure 82, a bainitic microstructure can be observed, identified by the presence of plate-like cementite indicated as darker regions of the micrographs which were etched in 2% nital. These cementite phases also nucleate at the prior particle boundaries, indicating the potential to manipulate grain size by controlling the initial powder particle size during sintering. The nucleation of cementite at grain boundaries likely results from the interaction between particle diffusion bonding and carbon segregation, where carbon atoms migrate to grain boundaries.

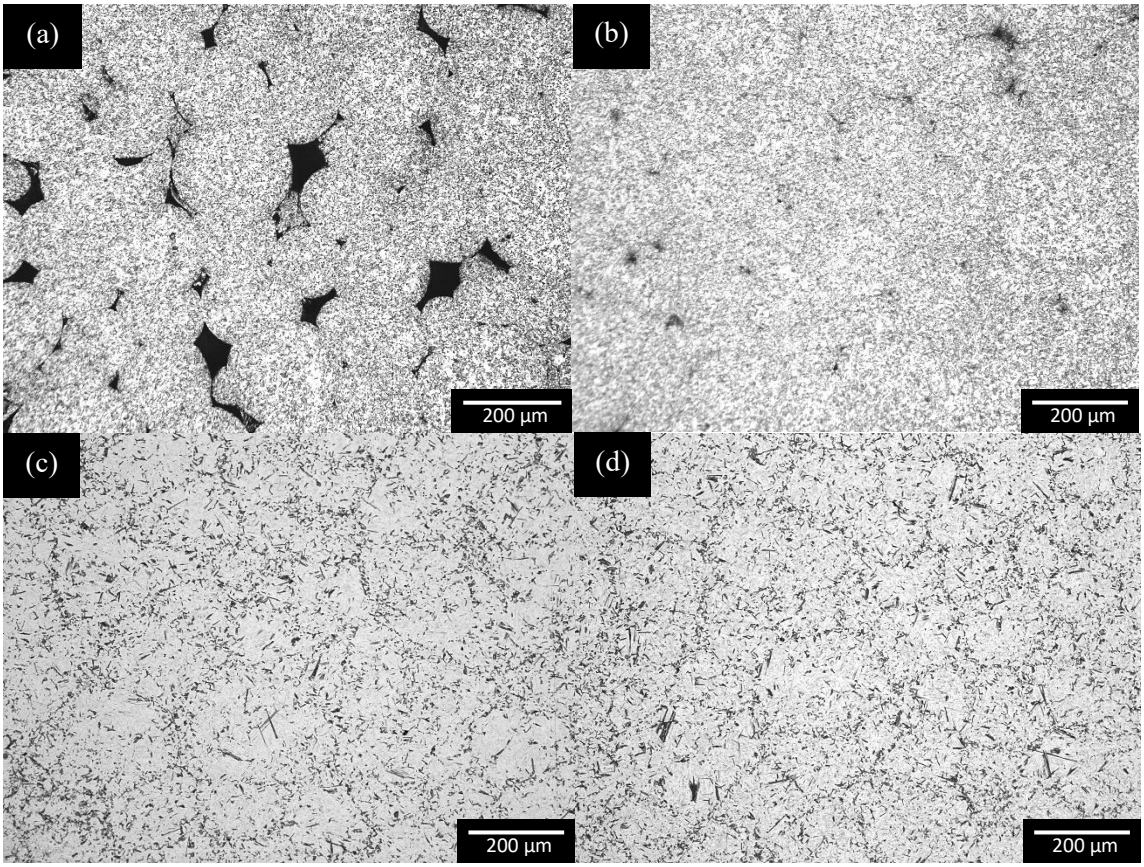

Figure 83: Optical micrographs of 150-300 µm MA steel powder sintered at 1100˚C held at 50MPa for (a) 0min, (b) 5min, (c) 10min and (d) 30min

7.4.1.3 80 mm Mould FAST Run

The microstructural investigation of both the edge and centre of an 80 mm MA FAST sample was undertaken to ensure homogeneity in phase distribution and consolidation throughout the specimen. Despite the inclusion of a thermal jacket (porous graphite) around the mould, a temperature gradient may still exist, as the temperature distribution within the tooling and specimen might not be uniform during FAST processing of larger mould sizes, as noted by Vanmeensel et al. [145]. Figure 84 illustrates the microscopic analysis of both the centre and edge regions, revealing a martensitic microstructure at the edge of the sample, similar to Figure 82. In contrast, the centre exhibits pro-eutectoid ferrite forming allotriomorphically at grain boundaries, with a fine pearlite phase observed within the grains.

The distinct contrast between these phases indicates a significant variation in cooling rates across the sample, with the edges cooling more rapidly than the centre. This differential cooling rate allows for the nucleation and growth of ferrite and pearlite in the slower-cooled central region, while the edge solidifies more rapidly, leading to the formation of martensite. This inhomogeneity in the microstructure is not ideal for FAST processing, as it results in variations in strength and hardness across the sample, compromising its mechanical performance and integrity. Previous investigations and analysis in Chapter 4 suggest that the cooling rate at the centre of the sample is approximately 0.1˚C/s, whereas the near-surface cooling rate ranges between 5-30˚C/s.

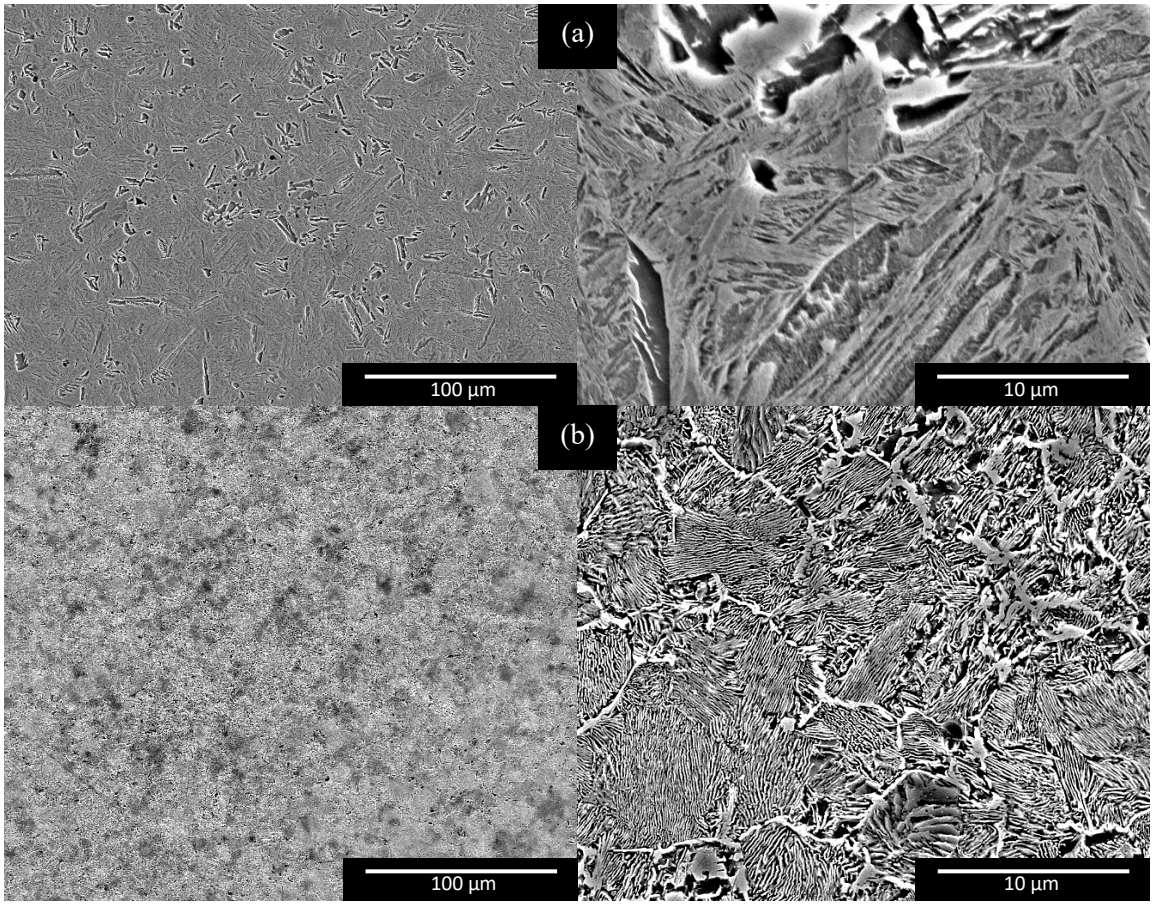

Figure 84: SEM (SE) micrographs of 45-150µm MA steel powder sintered with an 80 mm mould at 1100˚C for 5 minutes at 50MPa holding pressure, (a) edge and (b) centre of the sample

7.4.2 5MASC

The investigation into MA steel was expanded to investigate its interaction with TiB_2 powder. By calculating the apparent densities and masses of MA and TiB_2, the volume fraction of TiB_2 was determined to be 5%, resulting in the 5MASC alloy. To ensure homogeneity, the powders were mixed using a ball milling technique, where a stainless-steel milling jar was rotated on two axes at 400 rpm for 15 minutes. This process was used to prevent the agglomeration of fine TiB_2 particles, ensuring their uniform distribution within the MA matrix. Subsequently, the mixed powders were subjected to FAST, and SEM images (Figure 85) were taken for samples sintered with DTs of 0 and 10 minutes at a temperature of 1100˚C. This temperature was chosen based on prior experiments with the MA steel matrix alone, where near-complete consolidation and excellent diffusion bonding were observed.

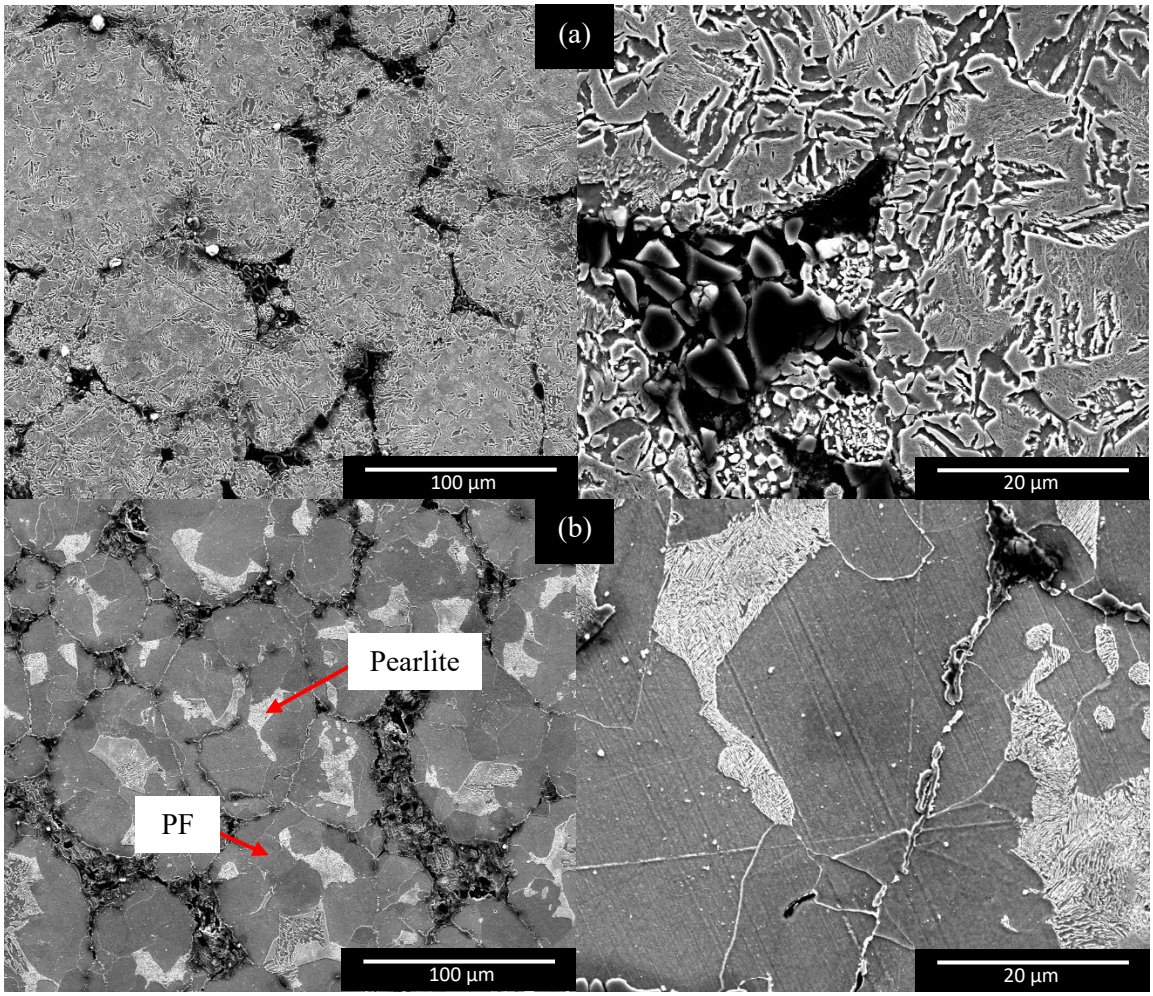

Figure 85: SEM (SE) micrographs of the sintered 5MASC alloy (45-150µm), dwell at 1100˚C for (a) 0 min and (b) 10 min

In the 0-minute DT samples, TiB_2 particles, averaging 8 μm in size, were found to position themselves between neighbouring MA matrix particles, impeding diffusion bonding due to the high thermodynamic stability of TiB_2. Consequently, full consolidation was not achieved, and a martensitic phase was observed in the MA matrix, consistent with earlier FAST runs with short dwell times.

Conversely, in the 10-minute DT samples, phase transformation to a polygonal ferrite (PF) and pearlite phase was observed, indicating that the longer DT allowed sufficient time for diffusion bonding between adjacent MA particles and full carbon saturation. Despite some large regions of TiB_2 agglomeration, effective diffusion bonding is observed between MA particles, reinforcing the steel and highlighting the importance of adequate DT for improving mechanical properties. Some small inclusions are also present within the PF grains.

7.5 Energy Dispersive X-Ray Spectroscopy

To further understand the microstructural characteristics and the effectiveness of diffusion bonding within the 5MASC alloy, energy dispersive X-ray spectroscopy (X-EDS) was utilised. This technique is useful for mapping and identifying the elemental composition of the alloy at a microstructural level. X-EDS also allows for the precise localisation of key elements such as Ti, B, Fe and C within the microstructure, helping to determine their distribution, concentration, and interactions with the MA steel matrix.

By analysing the elemental maps generated by X-EDS, regions of successful diffusion bonding can be identified, along with any areas where bonding may be impeded, such as near TiB_2 agglomerates. This analysis is essential for confirming the presence and stability of the composite phase, understanding the microstructural evolution, and assessing the overall quality of the FAST consolidated 5MASC.

An initial BSE image was captured of a broader region of the 5MASC alloy to locate and verify the distribution of TiB_2 particles, as shown in Figure 86. Despite the thorough mixing achieved through ball milling, the image in Figure 86 reveals instances of TiB_2 agglomeration. The finer TiB_2 particles tend to collect around the MA steel particles, as indicated by the X-EDS mapping of titanium. However, the presence of larger agglomerates of TiB_2 is undesirable, as this inhomogeneity can introduce brittle zones within the microstructure, negatively affecting the alloy's mechanical properties. Such agglomeration not only compromises the uniform distribution of reinforcement but also increases the likelihood of stress concentration points, which could lead to premature failure under mechanical loading. Moreover, these large agglomerates reduce the available surface area for effective diffusion bonding between MA particles, leading to weaker interparticle bonds and potential inconsistencies in the material's overall strength and durability.

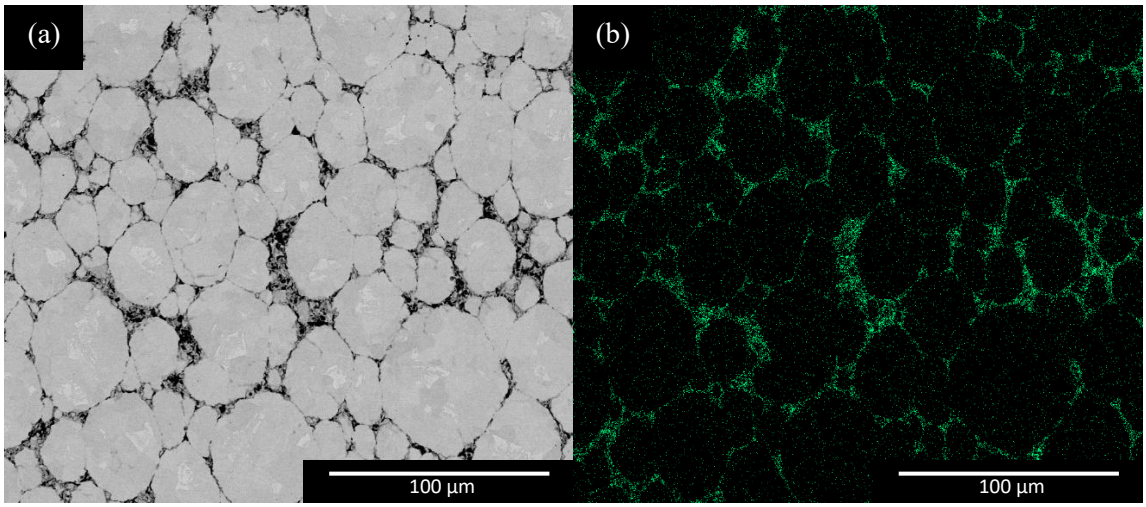

Figure 86: (a) SEM (BSE) micrograph of FAST 5MASC at 1100˚C, 10 min DT at 40MPa and (b) corresponding X-EDS map of Ti

Understanding the nature of agglomerate zones within the 5MASC alloy is key for assessing the microstructural integrity and mechanical properties of the material. X-EDS was used to analyse this zone, with the results presented in Figure 87. The elemental maps for Fe, Ti, O, C, and B were generated to identify the distribution and concentration of these elements. BSE imaging was specifically chosen for this analysis because it offers excellent contrast between the TiB_2 particles and the MA

steel matrix, due to the difference in atomic number. In particular, diffusion bonding is indicated by the presence of Fe between the boundaries of MA particles, suggesting that atomic diffusion has occurred. The presence of Ti and B in this region confirms the incorporation of TiB_2 within the matrix. However, the detection of oxygen spots in these zones signals the presence of porosity, which can negatively impact the mechanical properties of the material by introducing weak points where cracks can initiate and propagate. Additionally, a higher concentration of C in these regions is observed, which can be attributed to the diffusion bonding process where carbon migrates to grain boundaries and interfaces. This migration is not due to a reaction with TiB_2 as this phase is thermodynamically stable at 1100˚C [76], but rather because carbon tends to segregate in regions where diffusion bonding is active. The line analysis in Figure 88 further supports these observations, showing that lighter regions correspond to Fe, while darker regions are identified as TiB_2. The correlation between C and Ti peaks is intriguing, suggesting that carbon accumulates near TiB_2 particles, possibly due to the localised diffusion processes during sintering.

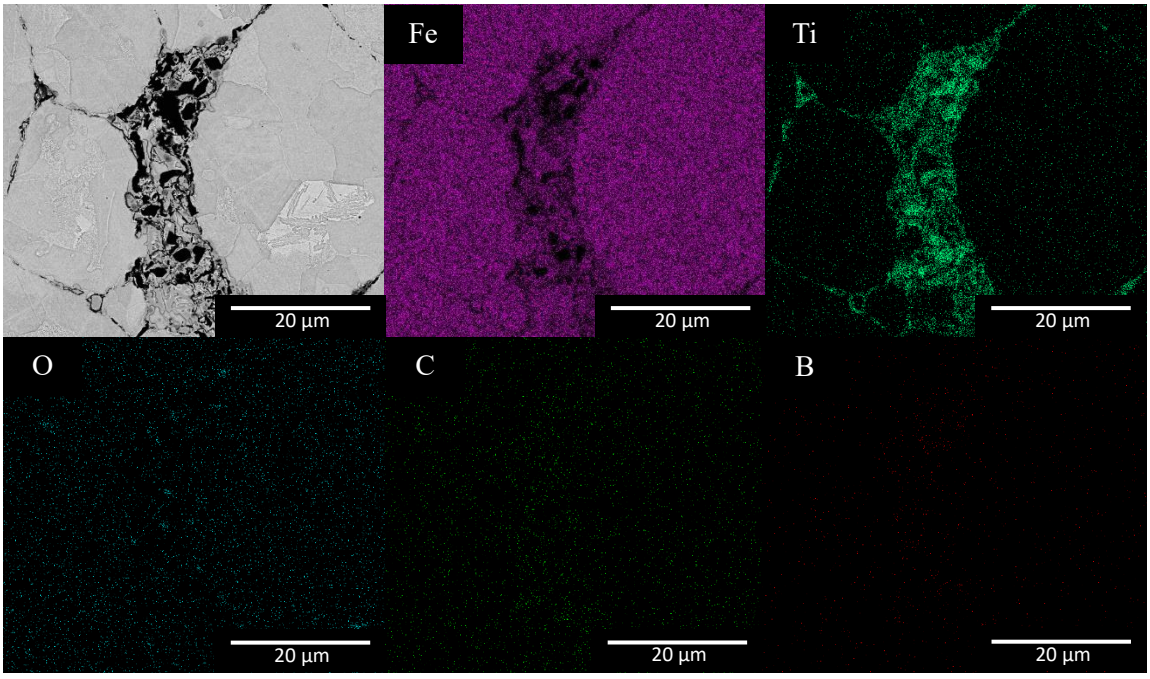

Figure 87: SEM (BSE) micrograph of FAST 5MASC at 1100˚C, 10 min DT at 40MPa and (b) corresponding X-EDS map of appropriate elements

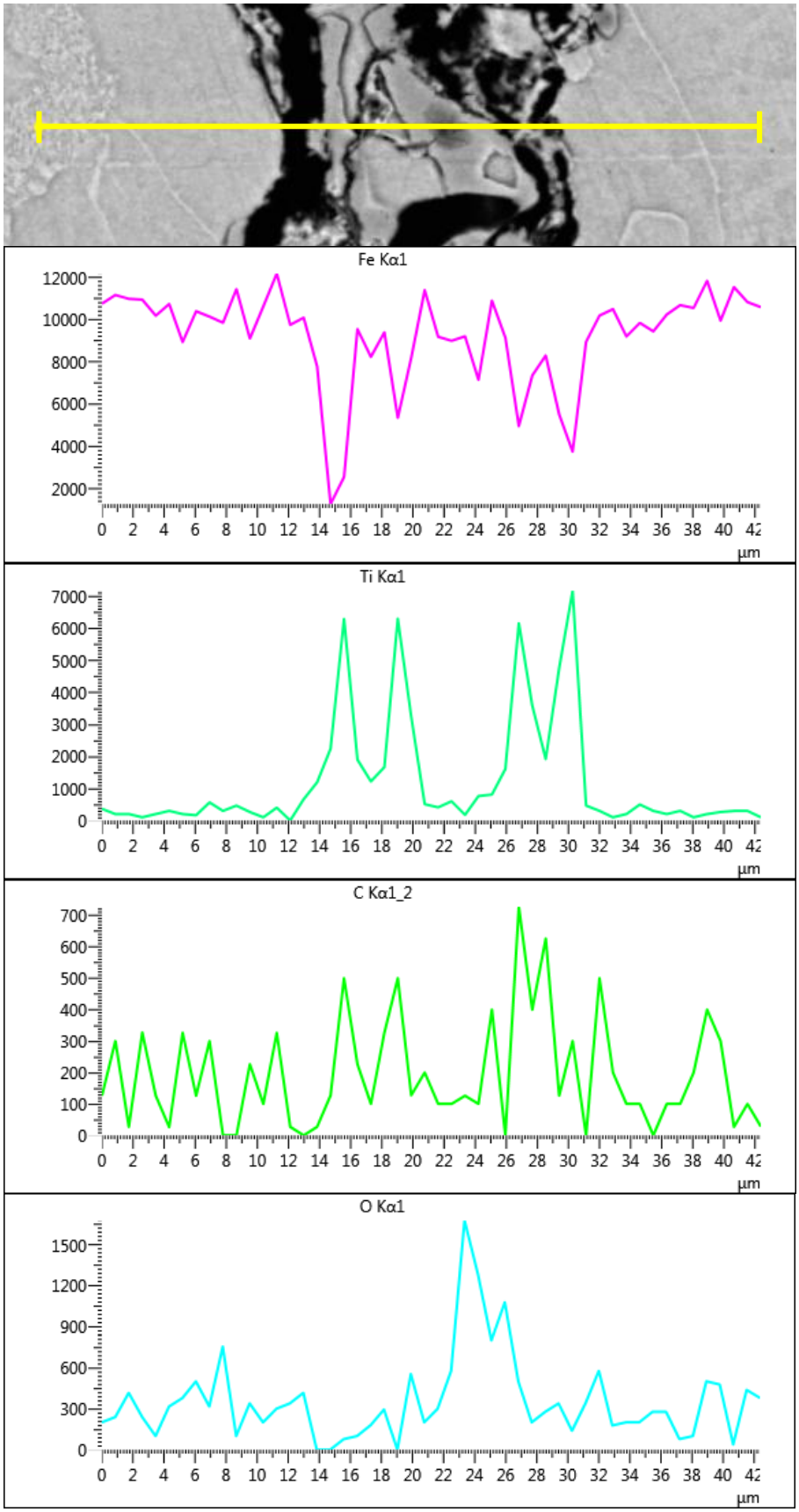

Figure 88: Line scan of a diffusion-bonded region in the FAST 5MASC sample

7.6 Young's Modulus Measurements

The elastic modulus of the 5MASC FAST sample was examined for direct comparison with the 5MASC alloy subjected to TMP and evaluated in Chapter 5. Dog bone specimens were prepared with identical geometries to those used in tensile tests for the VIM-fabricated samples and subsequently tested on a Zwick Roell tensile rig. Young's modulus was calculated by analysing the elastic region of a stress-strain curve, complemented by non-destructive resonant frequency damping analysis (RFDA). As illustrated in Figure 89, the 80 mm 5MASC sample, held at 1100˚C for a DT of 10 minutes, exhibited brittle failure before reaching the plastic deformation stage. This brittle behaviour is attributed to incomplete diffusion bonding and the presence of porosity within the microstructure, as evidenced by the SEM and X-EDS results.

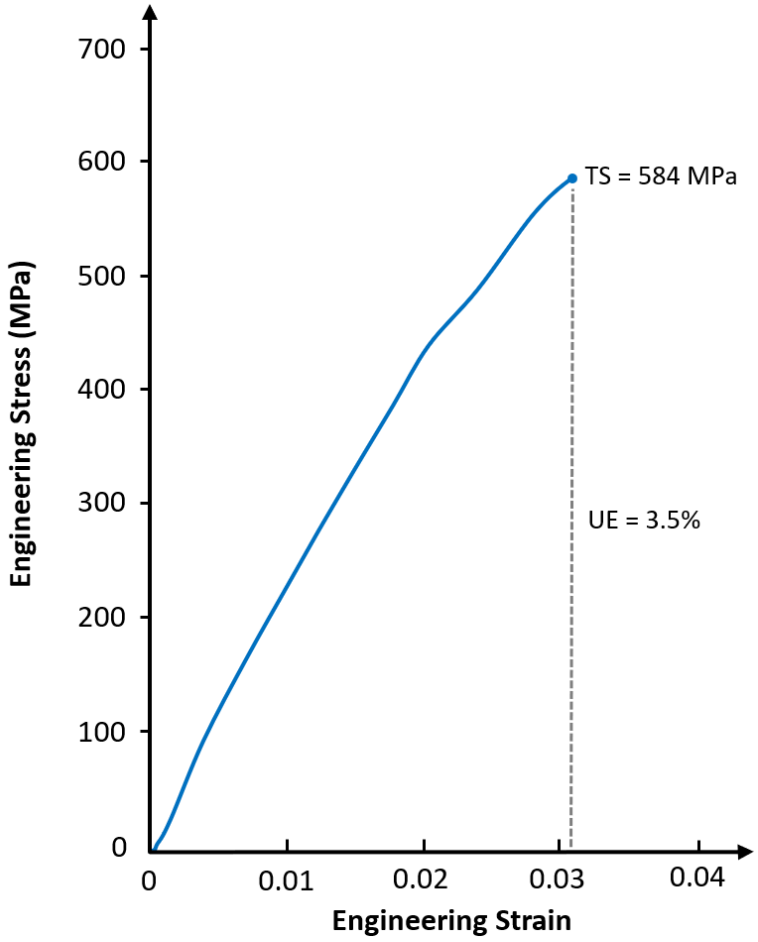

Figure 89: Engineering stress-strain plot of 5MASC FAST alloy sintered at 1100˚C for 10 min with the tensile strength (TS) and uniform elongation (UE) values stated

The Young's modulus for this sample was measured at 206 GPa, which is 24 GPa lower than the value obtained from the VIM-fabricated 5MASC alloy. A similar trend was observed in the RFDA results, where a modulus of 214 GPa was recorded, 16 GPa lower than that of the VIM-fabricated alloy discussed in Chapter 5. These reduced modulus values link back to the porosity and inadequate diffusion bonding at the interface between the MA matrix and TiB_2 particles. For RFDA, samples must exhibit minimal porosity, as this significantly affects the frequency response after impulse excitation. In the presence of porosity, the frequency is dampened due to the energy absorption by voids, leading to a distorted resonance and lower measured modulus.

7.7 Summary

This research successfully used FAST as a processing method for consolidating MA steel powder that was fabricated, sieved, and analysed in-house. The study provided valuable insights into powder characterisation and the impact of varying hold temperature, DT and mould size on the densification and phase transformations of the final sintered product, both with and without TiB_2 as a reinforcing ceramic phase. Through this work, an understanding of the interaction between these parameters has been established, allowing for the identification of optimal conditions required for producing high-quality, consolidated MASC alloys. The main conclusions from this work are as follows:

I. SEM analysis of MA steel powder revealed that larger particles (150-300 μm) have a rough texture with some spheroidal shapes and satellite agglomerates, while smaller particles (<45 μm) are well-spheroidised due to quicker cooling and reduced collision likelihood during solidification.
II. Microstructural characterisation of MA steel revealed that increasing dwelling temperature enhances densification, reducing voids and pores. The MA particles also remained undeformed during uniaxial compression in FAST, highlighting their high stiffness.

III. Investigating the effects of DT on MA steel consolidation reveals that longer DT generally improves densification through enhanced diffusion bonding, with significant consolidation achieved within 10 minutes at 1100˚C and 50 MPa. A bainitic microstructure was observed with plate-like cementite forming at prior MA particle boundaries,

IV. The microstructural investigation of both the edge and centre of an 80 mm MA FAST sample revealed significant inhomogeneity, with a martensitic microstructure at the faster-cooled edge and pro-eutectoid ferrite and fine pearlite at the slower-cooled centre. This variation in cooling rates across the sample indicates a temperature gradient, leading to differences in phase distribution. Such inhomogeneity is not ideal for FAST processing, as it compromises the mechanical integrity of the sample.

V. When adding 5% volume of TiB_2, it was observed that the matrix particles experienced impeded diffusion bonding, with TiB_2 particles acting as barriers. X-EDS analysis revealed carbon segregation and oxygen in void regions. While increasing the DT from 5 to 10 minutes improved densification, further mechanical analysis is necessary to assess the strength of the particle interfacial bonding under stress. This analysis will provide insights into the durability and performance of the composite material in practical applications, helping to determine the optimal processing conditions for achieving desired mechanical properties.

VI. In the 0-minute DT 5MASC samples, TiB_2 particles impeded diffusion bonding due to their high thermodynamic stability, leading to incomplete consolidation and a martensitic microstructure. However, in the 10-minute DT samples, a phase transformation to polygonal ferrite and pearlite occurred, indicating that the extended DT allowed for better diffusion bonding between MA particles.

VII. The 5MASC FAST sample exhibited lower modulus values from tensile and RFDA testing compared to the VIM-fabricated alloy, this is due to porosity and incomplete diffusion bonding in the sample.

8. Feasibility of VIM and FAST Processing Routes for High Modulus Steel Development

8.1 Vacuum Induction Melting

Vacuum Induction Melting (VIM) offers distinct advantages and limitations when considered as a processing route for the development of high-modulus steels, particularly in the context of microalloyed (MA) steels and steel composites. The VIM process, known for its ability to produce high-purity alloys, is especially advantageous for fabricating MA steels, where precise control over the alloying elements and minimal contamination is important.

8.1.1 Advantages of VIM

One advantage of VIM is its ability to produce high-purity steel with minimal contamination from unwanted elements. In traditional steelmaking processes, contamination from the surrounding environment, particularly from gases such as oxygen, nitrogen, and hydrogen, can lead to the formation of undesirable phases and inclusions. These can detrimentally affect the mechanical properties of the final product. VIM, operating under a vacuum, significantly reduces the risk of such contamination, allowing for the production of slagless steel ingots with very low levels of impurities.

For MA steels, VIM is particularly beneficial as the process allows for the accurate addition of microalloying elements such as titanium, niobium, and vanadium in ferrous forms. The control over the alloying process in VIM ensures that these elements are uniformly distributed throughout the melt, leading to a homogenous microstructure in the final product due to electromagnetic stirring. In the fabrication of steel matrix composites (SMCs), particularly those reinforced with ceramic particles like TiB_2, VIM provides the advantage of uniform distribution of the reinforcing phase, as demonstrated in Chapter 5.

VIM also offers advantages in terms of energy efficiency and process control. The inductive heating used in VIM allows for rapid melting and precise temperature control, which is essential for the processing of high-modulus steels where the thermal profile can significantly influence the final microstructure and properties (assuming no further thermomechanical processing is undertaken). Additionally, the vacuum environment reduces the risk of oxidation, particularly of reactive elements such as titanium and boron, which were used to fabricate the microalloyed steel composite (MASC) alloys.

8.1.2 Limitations of VIM

A drawback of VIM is the cost associated with the process. The need for a vacuum environment, inductive heating, and precise control of alloying elements makes VIM more expensive compared to conventional steelmaking processes. This can be significant, particularly for large-scale production where cost efficiency is vital.

Another limitation of VIM is the potential for inhomogeneity in the distribution of alloying elements and reinforcing phases, particularly in larger ingots that weigh more than 20 kg. While inductive stirring helps to some extent, achieving complete homogeneity in large melts can be challenging. This can lead to variations in the microstructure and mechanical properties of the final product. In the context of SMCs, while VIM allows for the incorporation of ceramic reinforcements, there is a risk of agglomeration of these particles during solidification. This can lead to the formation of regions with high concentrations of the reinforcing phase, which can act as stress concentrators and reduce the toughness of the composite.

8.1.3 Thermomechanical Processing: Hot Rolling and PSC

Following VIM, the ingots typically undergo two stages of hot rolling as a form of thermomechanical processing (TMP), with PSC simulating final rolling in the case of this project. Hot rolling allows for the improvement of the as-cast microstructure by elimination of any micro-porosity and grain refinement, thus, enhancing mechanical properties. The uniform microstructure obtained from VIM is

advantageous for hot rolling, as it reduces the likelihood of defects such as cracks and inclusions that can occur during deformation. However, the effectiveness of hot rolling is partially dependent on the initial microstructure obtained from VIM. If the VIM process results in a microstructure with significant inhomogeneities, these can be exacerbated during rolling (such as crack propagation), leading to anisotropy in the final product.

VIM offers significant advantages for the development of high-modulus steels, particularly in terms of purity and control over the alloying process. However, the limitations of VIM, particularly in terms of cost and potential inhomogeneities, must be considered. The success of subsequent TMP, including hot rolling and PSC, is somewhat dependent on the quality of the initial microstructure obtained from VIM.

8.2 Field-assisted Sintering Technology

Field-assisted sintering technology (FAST) offers advantages for the consolidation of metal powders into dense, high-performance materials. This process has been sparsely studied for its application in MA steels and medium-carbon steel composites with ceramic particles such as TiB_2. While FAST holds considerable promise, it also presents several limitations that must be considered, especially when applied to MA steels.

8.2.1 Advantages of FAST

One of the most compelling advantages of FAST is its ability to produce near-net-shape components. This is particularly valuable in industries where complex geometries are required, such as in aerospace and automotive applications. Near-net-shape processing minimises material waste and reduces the need for extensive post-processing, enhancing the overall efficiency and cost-effectiveness of the manufacturing process. In the context of MA steels and MASCs, FAST allows for the precise control of sintering conditions such as temperature, dwell time (DT) and applied pressure.

FAST distinguishes itself from traditional sintering techniques such as hot isostatic pressing (HIP) through its unique application of uniaxial pressure combined with a pulsed direct electric current. This results in quick sintering at relatively low temperatures and with shorter DTs. In the production of steel composites, FAST also provides an easy method of incorporating *in situ* TiB_2 using powder forms of matrix and composite reinforcement.

8.2.2 Limitations of FAST

A limitation associated with FAST is the size and geometry constraints imposed by the graphite moulds used in the process. While FAST performs well in the production of small to medium-sized cylindrical components, scaling up to larger and more complex tailored parts can be problematic. Geometric complexity and custom moulds must be thoroughly tested and researched to ensure graphite moulds can withstand high pressures without failure. This investigation is time-consuming and cost-intensive. Additionally, as mould sizes increase, the risk of temperature gradients within the mould also increases, potentially leading to inhomogeneities in the final product. This has also been demonstrated in Chapter 7. These inhomogeneities can manifest as variations in grain size and phase distribution.

Another significant limitation of FAST is its application to medium-carbon MA steels. While extensive research has been conducted on stainless steels like 316L, which are low-carbon steels that are well-suited to the FAST process, medium-carbon steels present unique challenges. The rapid heating and cooling cycles inherent in FAST can lead to undesirable phases in transformation-sensitive MA steels studied in this project, such as the formation of martensite, which can embrittle the material.

Furthermore, the initial capital investment required for FAST equipment is substantial. The specialised equipment, including the power supply, chiller, tooling, and control systems, is expensive, which can be a barrier to entry for some manufacturers. While the reduced post-processing costs and material savings can offset this initial investment, the high upfront cost remains a consideration.

8.2.3 Challenges in MASC Fabrication

When considering the fabrication of MA steels and steel composites, the limitations of FAST become even more apparent. The high thermodynamic stability of TiB_2, for example, impedes diffusion bonding between MA particles, making it difficult to achieve full consolidation of the composite material. This issue is worsened by the presence of TiB_2 agglomerates, which can create brittle spots within the microstructure. Despite these challenges, FAST offers the potential to fast-forge components, which mitigates some of the limitations associated with mould size and geometric complexity. Fast-forging combines the benefits of FAST with traditional forging techniques, allowing for the production of larger and more complex components while still taking advantage of the rapid sintering and fine microstructural control offered by FAST [146]. While FAST presents certain limitations, particularly regarding the processing of MASCs and the constraints imposed by mould sizes, it remains a powerful tool for the development of SMCs, as suggested by extensive work presented in previous literature [117], [147], [148], [149].

8.3 Final Comparison

VIM is a well-established method in the steel industry, particularly for the production of high-performance alloys and steels. Its ability to produce homogenous melts with precise control over elemental composition makes it highly suitable for the development of high-modulus steels. The process is particularly effective for producing large, uniform ingots that can be further processed through TMP. The strengths of VIM lie in its scalability and the ability to produce large quantities of material, which is essential for the automotive industry where production volumes are high. Additionally, VIM is versatile in terms of the range of alloys it can produce, making it a feasible option for a variety of steel grades, including those with complex chemistries required for high-modulus applications.

FAST, on the other hand, offers a modern and innovative powder metallurgy approach to steel fabrication, particularly advantageous for producing near-net-shape smaller components. This capability is particularly appealing in the automotive sector, where material efficiency and weight reduction are important. One of the significant advantages of FAST is its ability to rapidly consolidate materials with minimal energy consumption compared to VIM. The process is relatively quick, with shorter cycle times that contribute to lower operational costs. However, FAST also has notable limitations. The size of the components that can be produced is restricted by the size of the vacuum chamber, current output and therefore, mould size, which is a significant drawback for the automotive industry where larger components are often required. The application of FAST to the unique MA composition used in this project proved to be challenging as interfacial bonding between TiB_2 particles and MA particles was weak, as evidenced through tensile testing.

For the production of high-modulus MASCs, particularly where large ingots or billets are needed for further processing, VIM is the more feasible option. Its scalability, ability to handle large volumes, and versatility in alloy production and manipulation make it better suited for the demands of the automotive industry. FAST, while highly innovative and efficient for smaller, complex components, is currently less feasible for MASC-related automotive production due to its limitations in component size and the challenges associated with porosity and the diffusion bonding of particles.

9. Conclusions

This thesis has demonstrated the feasibility of using vacuum induction melting (VIM) and field-assisted sintering technology (FAST) for developing high-modulus steels, with a focus on incorporating titanium diboride (TiB_2) into a microalloyed (MA) steel matrix.

1. **Novel Findings**: The successful integration of TiB_2 into MA steel significantly enhances mechanical properties, with the 7.5MASC alloy achieving a maximum modulus of 239 GPa. The study also highlights the high thermodynamic stability of TiB_2 and its role in grain pinning.
2. **Phase Transformation and Mechanical Properties**: The MA steel exhibited optimal tensile strength of 1062 MPa and a uniform elongation of 15% at a cooling rate of 0.1°C/s, suitable for automotive applications. The 5MASC alloy showed strong potential for high-modulus electric vehicle components, achieving 905 MPa strength and 8% elongation at the same cooling rate.
3. **Processing Methods**: VIM proved superior to FAST for MA steel composites, offering better consolidation, microstructural uniformity, and mechanical properties. FAST, while effective for S4140 steel, showed limitations in achieving complete consolidation and uniformity in MA steel composites.
4. **Microstructural Analysis**: Microscopy revealed that larger MA steel powder particles had a rough texture, while smaller particles were well-spherodised. Increasing dwelling temperature during FAST improved densification, but inhomogeneity was observed in larger samples due to temperature gradients.

5. **Diffusion Bonding**: TiB_2 particles acted as diffusion barriers in both VIM and FAST processes, affecting consolidation and phase transformation. Longer dwelling times in FAST improved bonding and microstructural evolution, but VIM remained the preferred method for high-modulus MA steels.

Overall, this research provides valuable insights into the processing and properties of high-modulus steels, offering practical recommendations for automotive applications and highlighting the advantages of VIM over FAST for producing MA steel composites.

9.1 Further Work

9.1.1 Carbon Extraction Replica and Precipitate Analysis

To further understand the behaviour of the MA steel and its composites, a detailed analysis of precipitates within the matrix should be conducted using the carbon extraction replica technique. This method will allow for the isolation and examination of nanoscale precipitates such as vanadium carbide (VC), titanium carbide (TiC), and niobium carbide (NbC) at the transmission electron microscope (TEM) level. This will offer insights into the distribution, morphology, and size of these precipitates, which are vital in influencing the mechanical properties of the MA alloy. By characterising these precipitates, their role in grain refinement and pinning mechanisms can be better understood.

9.1.2 Exploration of Alternative Ceramic Reinforcements

While TiB_2 has proven effective as an *in situ* ceramic reinforcement, other reinforcements for MA steel can be considered. Investigating other boride-based reinforcements such as CrB_2 and ZrB_2 could yield SMCs with improved hardness, stiffness, and wear resistance. These additions to the MA matrix in particular could be studied to assess their impact on mechanical properties, phase transformations, and grain boundary strengthening. Expanding the range of potential reinforcements could lead to the development of novel high-modulus steel composites.

9.1.3 Advanced Characterisation of TiB_2 Agglomeration

While TiB_2 was successfully incorporated into the MA matrix through VIM, agglomeration of these particles and unidentified phases were observed. Electron backscatter diffraction (EBSD) can be used for phase identification and mapping the crystallographic orientation of foreign particles to the surrounding MA matrix. This will help analyse how these clusters affect phase transformation behaviour and diffusion dynamics.

9.1.4 Modelling of Thermal Gradients in FAST

Thermal gradients present a challenge during FAST processing, particularly in larger mould sizes where inconsistent heating can affect phase transformation. Using finite element analysis (FEA) software such as COMSOL, thermal gradients within the FAST system should be modelled to predict the impact on phase transformations and densification across MASC alloys. By simulating different mould sizes and processing parameters, this work can provide a strong understanding of how temperature gradients affect microstructure homogeneity and mechanical properties.

9.1.5 Tensile Testing of MA Steel Fabricated through FAST

The work presented in Chapter 7 only highlighted the mechanical properties of the 5MASC alloy which had poor interfacial bonding. A focused investigation into the mechanical behaviour of the MA steel matrix was not possible as there was not enough powder to create the required 80 mm sample. This study would involve performing tensile tests on MA steel samples consolidated via FAST under similar conditions to those used in the composite samples. Comparing mechanical properties to the 5MASC would provide a clearer picture of diffusion-bonded interface strength with and without TiB_2.

References

[1] C. Baron, H. Springer, and D. Raabe, 'Combinatorial screening of the microstructure–property relationships for Fe–B–X stiff, light, strong and ductile steels', *Mater Des*, vol. 112, pp. 131–139, 2016, doi: 10.1016/j.matdes.2016.09.065.

[2] Y. Z. Li and M. X. Huang, 'Revealing the interfacial plasticity and shear strength of a TiB2-strengthened high-modulus low-density steel', *J Mech Phys Solids*, vol. 121, pp. 313–327, 2018, doi: 10.1016/j.jmps.2018.08.010.

[3] S. Lartigue-Korinek, M. Walls, N. Haneche, L. Cha, L. Mazerolles, and F. Bonnet, 'Interfaces and defects in a successfully hot-rolled steel-based composite Fe-TiB2', *Acta Mater*, vol. 98, pp. 297–305, 2015, doi: 10.1016/j.actamat.2015.07.024.

[4] K. k C. N. Chawla, 'Metal-Matrix composites in Ground Transportation', *Low-Cost Composites in Vehicle Manufacture*, vol. 130, no. 2, pp. 67–70, 2006.

[5] J. H. Schmitt and T. Iung, 'New developments of advanced high-strength steels for automotive applications', *C R Phys*, vol. 19, no. 8, pp. 641–656, 2018, doi: 10.1016/j.crhy.2018.11.004.

[6] K. W. Allen, 'The physical metallurgy of microalloyed steels', *Choice Reviews Online*, vol. 35, no. 05, pp. 35-2725-35–2725, 1998, doi: 10.5860/choice.35-2725.

[7] G. Thomas, 'Physical Metallurgy and Alloy Design of Dual Phase Steels.', *Materials Science Monographs*, vol. 26, pp. 89–123, 1985.

[8] J. C. Villalobos, A. Del-Pozo, B. Campillo, J. Mayen, and S. Serna, 'Microalloyed steels through history until 2018: Review of chemical composition, processing and hydrogen service', *Metals (Basel)*, vol. 8, no. 5, 2018, doi: 10.3390/met8050351.

[9] J. Adamczyk, 'Development of the microalloyed constructional steels', *Journal of Achievements in Materials and Manufacturing Engineering*, vol. 14, no. 1, pp. 9–20, 2006.

[10] W. Bleck, M. Bambach, V. Wirths, and A. Stieben, 'Microalloyed engineering steels with improved performance - An overview', *HTM - Journal of Heat Treatment and Materials*, vol. 72, no. 6, pp. 346–354, 2017, doi: 10.3139/105.110339.

[11] F. Bonnet, V. Daeschler, and G. Petitgand, 'High modulus steels: New requirement of automotive market. How to take up challeng?', *Canadian Metallurgical Quarterly*, vol. 53, no. 3, pp. 243–252, 2014, doi: 10.1179/1879139514Y.0000000144.

[12] B. T. L. Zhang, ‘State of the Art in the Control of Inclusions during Steel Ingot Casting’, *Metallurgical and Materials Transactions B*, vol. 37B, pp. 733–761, 2005, doi: 10.1017/cbo9781139174244.010.

[13] X. Xuan, ‘Joule heating in electrokinetic flow’, *Electrophoresis*, vol. 29, no. 1, pp. 33–43, 2008, doi: 10.1002/elps.200700302.

[14] N. A. S. Sharma, Nidhi, *Fundamentals of Spark Plasma Sintering (SPS): An Ideal Processing Technique for Fabrication of Metal Matrix Nanocomposites: Advances in Processing and Applications*, no. February. 2019. doi: 10.1007/978-3-030-05327-7.

[15] A. V. Sverdlin and A. R. Ness, ‘Fundamental concepts in steel heat treatment’, *Steel Heat Treatment: Metallurgy and Technologies*, pp. 165–211, 2006, doi: 10.1201/nof0849384523-7.

[16] M. Detrois, P. D. Jablonski, and J. A. Hawk, ‘Evolution of Tantalum Content During Vacuum Induction Melting and Electroslag Remelting of a Novel Martensitic Steel’, *Metallurgical and Materials Transactions B: Process Metallurgy and Materials Processing Science*, vol. 50, no. 4, pp. 1686–1695, 2019, doi: 10.1007/s11663-019-01614-z.

[17] G. Jarczyk and H. Franz, ‘Vacuum melting equipment and technologies for advanced materials’, *Materials Science and Engineering*, vol. 56, no. 2, pp. 82–88, 2012.

[18] M. Koreoki, A. Brewka, and E. Wofowiec-Korecka, ‘Devices for modern vacuum heat treatment’, *Archives of Materials Science and Engineering*, vol. 95, no. 2, pp. 77–85, 2019, doi: 10.5604/01.3001.0013.1732.

[19] Y. Tan *et al.*, ‘Removal of aluminum and calcium in multicrystalline silicon by vacuum induction melting and directional solidification’, *Vacuum*, vol. 99, pp. 272–276, 2014, doi: 10.1016/j.vacuum.2013.06.015.

[20] P. S. SCHAFFER, *Theoretical and Practical Aspects of Vacuum Induction Melting of High-Strength Steels*. 1960.

[21] P. G. MICHELENA, ‘Vacuum Induction Melting through Numerical and Experimental Investigation’, Arrasate-Mondragón, 2023.

[22] J. Frenzel, Z. Zhang, K. Neuking, and G. Eggeler, ‘High quality vacuum induction melting of small quantities of NiTi shape memory alloys in graphite crucibles’, *J Alloys Compd*, vol. 385, no. 1–2, pp. 214–223, 2004, doi: 10.1016/j.jallcom.2004.05.002.

[23] R. Hasenhündl, P. Presoly, W. Schützenhöfer, R. Tanzer, and F. Hildebrand, ‘Vacuum Induction Melting – Optimisation of Pressure Dependent Reactions’, *Lmpc 2007*, pp. 289–294, 2007.

[24] H. U. Kessel *et al.*, *" FAST " field assisted sintering technology- a new process for the production of metallic and ceramic sintering materials*, no. October 2015. 2008.

[25] O. Guillon *et al.*, 'Field-assisted sintering technology/spark plasma sintering: Mechanisms, materials, and technology developments', *Adv Eng Mater*, vol. 16, no. 7, pp. 830–849, 2014, doi: 10.1002/adem.201300409.

[26] R. K. Bordia, S. J. L. Kang, and E. A. Olevsky, 'Current understanding and future research directions at the onset of the next century of sintering science and technology', *Journal of the American Ceramic Society*, vol. 100, no. 6, pp. 2314–2352, 2017, doi: 10.1111/jace.14919.

[27] S. Chanthapan, A. Kulkarni, J. Singh, C. Haines, and D. Kapoor, 'Sintering of tungsten powder with and without tungsten carbide additive by field assisted sintering technology', *Int J Refract Metals Hard Mater*, vol. 31, pp. 114–120, 2012, doi: 10.1016/j.ijrmhm.2011.09.014.

[28] S. Rothe, S. Kalabukhov, N. Frage, and S. Hartmann, 'Field assisted sintering technology. Part I: Experiments, constitutive modeling and parameter identification', *GAMM Mitteilungen*, vol. 39, no. 2, pp. 114–148, 2016, doi: 10.1002/gamm.201610009.

[29] R. D. Doherty, 'Recrystallization and texture', *Prog Mater Sci*, vol. 42, no. 1–4, pp. 39–58, 1997, doi: 10.1016/s0079-6425(97)00007-8.

[30] MARTYN R. DRURY and JANOS L., 'Deformation-related recrystallization processes', *Tectonophysics*, vol. 172, pp. 235–253, 1990, doi: 10.1109/IMFEDK.2013.6602261.

[31] C. M. Sellars, 'Recrystallization of metals during hot deformation', *Philosophical Transactions of the Royal Society of London. Series A, Mathematical and Physical Sciences*, vol. 288, no. 1350, pp. 147–158, 1978, doi: 10.1098/rsta.1978.0010.

[32] T. Sakai, A. Belyakov, R. Kaibyshev, H. Miura, and J. J. Jonas, 'Dynamic and post-dynamic recrystallization under hot, cold and severe plastic deformation conditions', *Prog Mater Sci*, vol. 60, no. 1, pp. 130–207, 2014, doi: 10.1016/j.pmatsci.2013.09.002.

[33] B. López and J. M. Rodriguez-Ibabe, 'Recrystallisation and grain growth in hot working of steels', in *Microstructure Evolution in Metal Forming Processes*, 2012, pp. 67–113. doi: 10.1533/9780857096340.1.67.

[34] H. Hallberg, 'Approaches to modeling of recrystallization', *Metals (Basel)*, vol. 1, no. 1, pp. 16–48, 2011, doi: 10.3390/met1010016.

[35] Y. C. Lin, M. Chen, and J. Zhong, 'Study of static recrystallization kinetics in a low alloy steel', *Comput Mater Sci*, vol. 44, no. 2, pp. 316–321, 2008, doi: 10.1016/j.commatsci.2008.03.027.

[36] D. A. Porter, K. E. Easterling, and K. E. Easterling, *Phase Transformations in Metals and Alloys (Revised Reprint)*, 3rd Editio. 2009. doi: 10.1201/9781439883570.

[37] S. Cho, K. Kang, and J. J. Jonas, 'The Dynamic , Static and Metadynamic Recrystallization of a Nb-microalloyed Steel', vol. 41, no. 1, pp. 63–69, 2001.

[38] F. J. Humphreys and M. Hatherly, *Recrystallization and Related Annealing Phenomena*. 2012. doi: 10.1016/C2009-0-07986-0.

[39] Z. C. et al. Cordero, 'Six Decades of the Hall–Petch Effect – a Survey of Grain-Size Strengthening Studies on Pure Metals', *International Materials Reviews 61*, no. Institute of Materials, Minerals and Mining and ASM International, Jul. 2016.

[40] Y. Li, A. J. Bushby, and D. J. Dunstan, 'The Hall – Petch effect as a manifestation of the general size effect Subject Areas ':, *rspa.royalsocietypublishing.org*, vol. 1, May 2016.

[41] C. S. Pande and K. P. Cooper, 'Progress in Materials Science Nanomechanics of Hall – Petch relationship in nanocrystalline materials', vol. 54, pp. 689–706, 2009, doi: 10.1016/j.pmatsci.2009.03.008.

[42] Y. Z. Zhu, S. Z. Wang, B. L. Li, Z. M. Yin, Q. Wan, and P. Liu, 'Grain growth and microstructure evolution based mechanical property predicted by a modified Hall – Petch equation in hot worked Ni76Cr19AlTiCo alloy', vol. 55, pp. 456–462, 2014, doi: 10.1016/j.matdes.2013.10.023.

[43] E. Ghassemali, M. Riestra, T. Bogdanoff, and B. S. Kumar, 'ScienceDirect Hall-Petch equation in a hypoeutectic Al-Si cast alloy : grain size vs . secondary dendrite arm spacing', *Procedia Eng*, vol. 207, pp. 19–24, 2017, doi: 10.1016/j.proeng.2017.10.731.

[44] J. W. Morris, 'The Influence of Grain Size on the Mechanical Properties of Steel', *University of California, Berkeley and Center for Advanced Materials*, 2001.

[45] E. J. Palmiere, C. I. Garcia, and A. J. DeArdo, 'Thermomechanical processing of Steel', *Metals Handbook, Tenth Edition*, vol. 4, pp. 237–255, 1991.

[46] D. Gaude-Fugarolas and H. K. D. H. Bhadeshia, 'A model for austenitisation of hypoeutectoid steels', *J Mater Sci*, vol. 38, no. 6, pp. 1195–1201, 2003, doi: 10.1023/A:1022805719924.

[47] B. Pawłowski, 'Pawłowski, B. (2011). Critical points of hypoeutectoid steel-prediction of the pearlite dissolution finish temperature Ac1f. Journal of Achievements in Materials and Manufacturing Engineering, 49(2), 331-337..pdf', vol. 49, no. 2, pp. 331–337, 2011.

[48] B. Pawłowski, ‘Determination of critical points of hypoeutectoid steels’, *Archives of Metallurgy and Materials*, vol. 57, no. 4, pp. 957–962, 2012, doi: 10.2478/v10172-012-0106-4.

[49] K. K. Ray and D. Mondal, ‘The effect of interlamellar spacing on strength of pearlite in annealed eutectoid and hypoeutectoid plain carbon steels’, *Acta Metallurgica Et Materialia*, vol. 39, no. 10, pp. 2201–2208, 1991, doi: 10.1016/0956-7151(91)90002-I.

[50] E. Rozniata and R. Dziurka, ‘The phase transformations in hypoeutectoid steels Mn-Cr-Ni’, *Archives of Metallurgy and Materials*, vol. 60, no. 1, pp. 497–502, 2015, doi: 10.1515/amm-2015-0080.

[51] T. N. Baker, ‘Microalloyed steels’, *Ironmaking and Steelmaking*, vol. 43, no. 4, pp. 264–307, 2016, doi: 10.1179/1743281215Y.0000000063.

[52] S. Gunduz, M. A. Erden, H. Karabulut, and M. Turkmen, ‘The Effect of Vanadium and Titanium on Mechanical Properties of Microalloyed PM Steel’, *Powder Metallurgy and Metal Ceramics*, vol. 55, no. 5–6, pp. 277–287, 2016, doi: 10.1007/s11106-016-9803-2.

[53] W. jun Hui, C. wei Shao, Y. jian Zhang, S. lian Chen, and H. Dong, ‘Influence of Vanadium on Fracture Splitting Property of Medium Carbon Steel’, 2016. doi: 10.1016/S1006-706X(16)30075-9.

[54] S. Cho, K. Kang, and J. J. Jonas, ‘The Dynamic , Static and Metadynamic Recrystallization of a Nb-microalloyed Steel’, vol. 41, no. 1, pp. 63–69, 2001.

[55] R. D. K. Misra, H. Nathani, J. E. Hartmann, and F. Siciliano, ‘Microstructural evolution in a new 770 MPa hot rolled Nb – Ti microalloyed steel’, vol. 394, pp. 339–352, 2005, doi: 10.1016/j.msea.2004.11.041.

[56] F. A. Khalid, M. Farooque, A. Haq, and A. Q. Khan, ‘Role of ferrite / pearlite banded structure and segregation on mechanical properties of microalloyed hot rolled steel Role of ferrite / pearlite banded structure and segregation on mechanical properties of microalloyed hot rolled steel’, no. October 1999, 2017, doi: 10.1179/026708399101505121.

[57] I. Gutie, ‘Role of the Particle-Matrix Interface on the Nucleation of Acicular Ferrite in a Medium Carbon Microalloyed Steel’, *Centro de Estudios e Investigaciones TeÂcnicas de GuipuÂzcoa (CEIT)*, vol. 47, no. 3, pp. 951–960, 1999.

[58] S. Vervynckt *et al.*, ‘Modern HSLA steels and role of non- recrystallisation temperature Modern HSLA steels and role of non-recrystallisation temperature’, vol. 6608, 2013, doi: 10.1179/1743280411Y.0000000013.

[59] A. J. Deardo, ‘Niobium in modern steels’, *Maney for the Institute of Materials, Minerals and Mining and ASM International.*, 2003.

[60] S. Mengaroni, M. Calderini, G. Napoli, C. Zitelli, and A. Di Schino, 'Micro-alloyed steel for forgings', *Materials Science Forum*, vol. 941, pp. 1603–1606, 2018, doi: 10.4028/www.scientific.net/MSF.941.1603.

[61] R. D. Verlinden, B., Driver, J., Samajdar, I., & Doherty, *Thermo-Mechanical Processing of Metallic Materials*, vol. 11. 2007. [Online]. Available: http://www.sciencedirect.com/science/article/pii/S1470180407800186

[62] S. Guk, D. Milisova, and K. Pranke, 'Influence of deformation conditions on the microstructure and formability of sintered Mg-PSZ reinforced TRIP-matrix-composites', *Key Eng Mater*, vol. 684, pp. 86–96, 2016, doi: 10.4028/www.scientific.net/KEM.684.86.

[63] S. V. S. N. Murty, S. Torizuka, and K. Nagai, 'Microstructural evolution during simple heavy warm compression of a low carbon steel: Development of a processing map', *Materials Science and Engineering A*, vol. 410–411, pp. 319–323, 2005, doi: 10.1016/j.msea.2005.08.173.

[64] M. S. Loveday *et al.*, 'Measurement of flow stress in hot plane strain compression tests', *Materials at High Temperatures*, vol. 23, no. 2, pp. 85–118, 2006, doi: 10.3184/096034006782739394.

[65] Z. Wang, T. Lin, X. He, H. Shao, B. Tang, and X. Qu, 'Fabrication and properties of the TiC reinforced high-strength steel matrix composite', *Refractory Metals and Hard Materials*, vol. 58, no. 58, pp. 14–21, 2016, doi: 10.1016/j.ijrmhm.2016.03.013.

[66] W. H. Kan *et al.*, 'A study on novel AISI 304 stainless steel matrix composites with NbTiC', *International Journal on the Science and Technology of Friction Lubrication and Wear*, pp. 220–226, 2018.

[67] R. Chen, W. Li, B. Li, and C. Jiang, 'In situ experimental study on fracture toughness and damage mechanism of TiB2-reinforced steel matrix composites', *Fatigue Fract Eng Mater Struct*, vol. 46, no. 1, pp. 17–31, 2023, doi: 10.1111/ffe.13843.

[68] C. T. L. J. P. Kershaw, *Metal Matrix Composites*. Taylor & Francis Group. doi: 10.31399/asm.tb.scm.t52870537.

[69] H. Zhang, H. Springer, R. Aparicio-Fernández, and D. Raabe, 'Improving the mechanical properties of Fe – TiB2 high modulus steels through controlled solidification processes', *Acta Mater*, vol. 118, pp. 187–195, 2016, doi: 10.1016/j.actamat.2016.07.056.

[70] B. H. Li, Y. Liu, L. He, H. Cao, S. J. Gao, and J. Li, 'Fabrication of in situ TiB2 reinforced steel matrix composite by vacuum induction melting and its microstructure and tensile properties', *International Journal of Cast Metals Research*, vol. 23, no. 4, pp. 211–215, 2010, doi: 10.1179/136404609X12580240348974.

[71] M. Sadhasivam, S. Raman Sankaranarayanan, and S. P. Kumaresh Babu, ‘Synthesis and characterization of TiB2 reinforced AISI 420 stainless steel composite through vacuum induction melting technique’, in *Materials Today: Proceedings*, 2019, pp. 2550–2558. doi: 10.1016/j.matpr.2020.03.385.

[72] H. H. Pariser, N. R. Backeberg, O. C. M. Masson, and J. C. M. Bedder, ‘Changing nickel and chromium stainless steel markets - A review’, *J South Afr Inst Min Metall*, vol. 118, no. 6, pp. 563–568, 2018, doi: 10.17159/2411-9717/2018/V118N6A1.

[73] L. Ceschini, A. Marconi, C. Martini, A. Morri, and A. Di Schino, ‘Tensile and impact behaviour of a microalloyed medium carbon steel: Effect of the cooling condition and corresponding microstructure’, *Mater Des*, vol. 45, pp. 171–178, 2013, doi: 10.1016/j.matdes.2012.08.063.

[74] W. H. Kan *et al.*, ‘Fabrication and characterization of microstructure of stainless steel matrix composites containing up to 25 vol% NbC’, *Mater Charact*, vol. 119, pp. 65–74, 2016, doi: 10.1016/j.matchar.2016.07.019.

[75] C. lei Zhang, W. Fang, B. run Cai, X. hang Sun, and Y. zheng Liu, ‘Austenite grain growth and its effect on splitting fracture property of a V–N microalloyed medium carbon steel connecting rod’, *Journal of Iron and Steel Research International*, vol. 26, no. 8, pp. 875–881, 2019, doi: 10.1007/s42243-019-00288-w.

[76] R. G. Munro, ‘Material Properties of Titanium Diboride’, *J Res Natl Inst Stand Technol*, vol. 105, no. 5, pp. 709–720, 2000, doi: 10.6028/jres.105.057.

[77] K. Tanaka and T. Saito, ‘Phase equilibria in TiB2-reinforced high modulus steel’, *Journal of Phase Equilibria*, vol. 20, no. 3, pp. 207–214, 1999, doi: 10.1361/105497199770335730.

[78] S. C. Tjong, G. S. Wang, and Y. W. Mai, ‘Erratum to “Low-cycle fatigue behavior of Al-based composites containing in situ TiB2, Al2O3 and Al3Ti reinforcements” [Mater. Sci. Eng. A 358 (1–2) (2003) 99–106]’, *Materials Science and Engineering: A*, vol. 366, no. 2, p. 426, 2004, doi: 10.1016/j.msea.2003.08.037.

[79] M. Sadhasivam, N. Mohan, S. R. Sankaranarayanan, and S. P. K. Babu, ‘Investigation on mechanical and tribological behaviour of titanium diboride reinforced martensitic stainless steel’, *Mater Res Express*, vol. 7, no. 1, pp. 0–13, 2019, doi: 10.1088/2053-1591/ab6488.

[80] R. H. R. Castro and K. van Benthen, *Sintering - Mechanisms of Convention Nanodensificatioon and Filed Assisted Processes*, vol. 35, no. 3. Davis, CA, 2013. [Online]. Available: https://www.tandfonline.com/doi/full/10.1080/08940886.2017.1316123%0Ahttps://link.springer.com/10.1007/978-3-642-31009-6

[81] I. Sulima, P. Hyjek, L. Jaworska, and M. Perek-Nowak, 'Influence of ZrB2 on microstructure and properties of steel matrix composites prepared by spark plasma sintering', *Materials*, vol. 13, no. 11, 2020, doi: 10.3390/MA13112459.

[82] B. Li, Y. Liu, J. Li, H. Cao, and L. He, 'Effect of sintering process on the microstructures and properties of in situ TiB2-TiC reinforced steel matrix composites produced by spark plasma sintering', *J Mater Process Technol*, vol. 210, no. 1, pp. 91–95, 2010, doi: 10.1016/j.jmatprotec.2009.08.008.

[83] I. Sulima, P. Putyra, P. Hyjek, and T. Tokarski, 'Effect of SPS parameters on densification and properties of steel matrix composites', *Advanced Powder Technology*, vol. 26, no. 4, pp. 1152–1161, 2015, doi: 10.1016/j.apt.2015.05.010.

[84] M. Tokita, 'Recent and future progress on advanced ceramics sintering by Spark Plasma Sintering', *Nanotechnol Russ*, vol. 10, no. 3–4, pp. 261–267, 2015, doi: 10.1134/S1995078015020202.

[85] M. G. de Miranda Salustre, T. B. Gonoring, J. B. R. Martins, H. D. A. Lopes, and M. T. D. A. Orlando, 'Study of steel matrix composite samples with 12%Wt TiB2 produced by spark plasma sintering', *Mater Chem Phys*, vol. 302, no. March, pp. 1–9, 2023, doi: 10.1016/j.matchemphys.2023.127736.

[86] E. Pineda-Martinez, 'Study of the Microstructural Refinement of a High Niobium Microalloyed Steel Under Controlled Hot Deformation. PhD Thesis.', no. July, pp. 76–76, 2020.

[87] M. S. Loveday *et al.*, 'Measurement of flow stress in hot plane strain compression tests', *Materials at High Temperatures*, vol. 23, no. 2, pp. 85–118, 2006, doi: 10.3184/096034006782739394.

[88] A. Ali and H. K. D. H. Bhadeshia, 'Microstructure of high strength steel refined with intragranularly nucleated Widmanstätten ferrite', *Materials Science and Technology (United Kingdom)*, vol. 7, no. 10, pp. 895–903, 1991, doi: 10.1179/mst.1991.7.10.895.

[89] N. Saunders, Z. Guo, X. Li, A. P. Miodownik, and J. P. Schillé, 'Using JMatPro to model materials properties and behavior', *Jom*, vol. 55, no. 12, pp. 60–65, 2003, doi: 10.1007/s11837-003-0013-2.

[90] G. Hopkin and H. K. D. H. Bhadeshia, 'Recrystallisation of Austenitic Stainless Steels', University_of_Cambridge.

[91] V. N. Urtsev *et al.*, 'Formation of the Structural State of a High-Strength Low-Alloy Steel upon Hot Rolling and Controlled Cooling', *Physics of Metals and Metallography*, vol. 120, no. 12, pp. 1233–1241, 2019, doi: 10.1134/S0031918X19120160.

[92] P. C. M. Rodrigues, E. V. Pereloma, and D. B. Santos, ‘Mechanical properities of an HSLA bainitic steel subjected to controlled rolling with accelerated cooling’, *Materials Science and Engineering: A*, vol. 283, no. 1–2, pp. 136–143, 2000, doi: 10.1016/s0921-5093(99)00795-9.

[93] K. H. Jitendra Patel, Christian Klinkenberg, ‘Hot Rolled HSLA Strip Steels for Automotive and Construction Applications’, Jan. 2003.

[94] L. Achelis and V. Uhlenwinkel, ‘Characterisation of metal powders generated by a pressure-gas-atomiser’, *Materials Science and Engineering: A*, vol. 477, no. 1–2, pp. 15–20, 2008, doi: 10.1016/j.msea.2007.07.095.

[95] ‘The Henry Royce Institute - Royce Translational Centre Facilities’, 2023, *Sheffield*.

[96] and V. G. G. Neikov, Oleg D., Dina V. Lotsko, ‘Powder Characterization and Testing’, *Handbook of non-ferrous metal powders 2*, pp. 611–628, 2009, doi: 10.1002/9781118773727.ch25.

[97] H. Colpaert, *Metallography of Steels —Interpretation of Structure and the Effects of Processing*. Ohio: ASM International, 2018.

[98] C. García De Andrés, M. J. Bartolomé, C. Capdevila, D. San Martín, F. G. Caballero, and V. López, ‘Metallographic techniques for the determination of the austenite grain size in medium-carbon microalloyed steels’, *Mater Charact*, vol. 46, no. 5, pp. 389–398, 2001, doi: 10.1016/S1044-5803(01)00142-5.

[99] G. Vander Voort, ‘Revealing Prior Austenite Grain Boundaries.pdf’, 2014, *Georgevandervoort.com*.

[100] V. Sinha, E. J. Payton, M. Gonzales, R. A. Abrahams, and B. S. Song, ‘Delineation of Prior Austenite Grain Boundaries in a Low-Alloy High-Performance Steel’, *Metallography, Microstructure, and Analysis*, vol. 6, no. 6, pp. 610–618, 2017, doi: 10.1007/s13632-017-0403-4.

[101] C. G. De Andrés, F. G. Caballero, C. Capdevila, and D. S. Martín, ‘Revealing austenite grain boundaries by thermal etching : advantages and disadvantages’.

[102] R. D. Lawson, D. K. Matlock, and G. Krauss, ‘An etching technique for microalloyed dual-phase steels’, *Metallography*, vol. 13, no. 1, pp. 71–87, 1980, doi: 10.1016/0026-0800(80)90023-3.

[103] K. F. Rodriguez-Galeano, L. F. Romano-Acosta, E. J. Palmiere, and W. M. Rainforth, ‘A new approach to etching low-carbon microalloyed steels to reveal prior austenite grain boundaries and the dual-phase microstructure’, *J Microsc*, vol. 289, no. 2, pp. 73–79, 2023, doi: 10.1111/jmi.13153.

[104] V. Randle and O. Engler, *Introduction to Texture Analysis: Macrotexture, & Orientation Microtexture Mapping*. Boca Raton: Taylor & Francis Group, LLC, 2000.

[105] L. Barboni, G. R. Gillich, C. P. Chioncel, C. O. Hamat, and I. C. Mituletu, 'A Method to Precise Determine the Young's Modulus from Dynamic Measurements', *IOP Conf Ser Mater Sci Eng*, vol. 416, no. 1, 2018, doi: 10.1088/1757-899X/416/1/012063.

[106] B. Bollen, 'The Impulse Excitation technique, an innovative NDT method for microstructure and mechanical properties characterization of refractory materials used in the aluminum industry.', 2016, *IMCE- RFDA Professional, Aachen, Belgium*. [Online]. Available: http://dx.doi.org/10.1016/j.ceramint.2013.01.038%0Ahttps://doi.org/10.1016/j.ceramint.2017.10.010%0Ahttp://dx.doi.org/10.1016/j.jeurceramsoc.2011.10.048%0Ahttp://dx.doi.org/10.1016/j.ceramint.2015.12.134%0Ahttp://dx.doi.org/10.1016/j.commatsci.2008.04.024

[107] ASTM, 'Standard Test Method for Microindentation Hardness of Materials', 2009, *ASTM International, PA, USA*. [Online]. Available: www.astm.org,

[108] K. K. Ray and D. Mondal, 'The effect of interlamellar spacing on strength of pearlite in annealed eutectoid and hypoeutectoid plain carbon steels', *Acta Metallurgica Et Materialia*, vol. 39, no. 10, pp. 2201–2208, 1991, doi: 10.1016/0956-7151(91)90002-I.

[109] N. Saunders, Z. Guo, X. Li, A. P. Miodownik, and J.-P. Schillé, 'The Calculation of TTT and CCT diagrams for General Steels', *JMatPro Software Literature*, pp. 1–12, 2004.

[110] F. J. Humphreys and M. Hatherly, *Recrystallization and Related Annealing Phenomena*. 2012. doi: 10.1016/C2009-0-07986-0.

[111] G. Vander Voort, 'Revealing Prior Austenite Grain Boundaries', Aug. 14, 2014, *Georgevandervoort.com*.

[112] R. Thackray, E. J. Palmiere, and O. Khalid, 'Novel etching technique for delineation of prior-austenite grain boundaries in low, medium and high carbon steels', *Materials*, vol. 13, no. 15, 2020, doi: 10.3390/MA13153296.

[113] B. F. de Oliveira, M. P. Oliveira, L. A. H. Terrones, M. G. de Azevedo, and L. B. Godefroid, 'Microstructure and mechanical properties of as-cast and annealed high strength low alloy steel', *Journal of Materials Science Research*, vol. 8, no. 4, p. 1, 2019, doi: 10.5539/jmsr.v8n4p1.

[114] M. Detrois, P. D. Jablonski, and J. A. Hawk, 'Evolution of Tantalum Content During Vacuum Induction Melting and Electroslag Remelting of a Novel Martensitic Steel', *Metallurgical and Materials Transactions B: Process*

Metallurgy and Materials Processing Science, vol. 50, no. 4, pp. 1686–1695, 2019, doi: 10.1007/s11663-019-01614-z.

[115] S. Suttner and M. Merklein, 'A new approach for the determination of the linear elastic modulus from uniaxial tensile tests of sheet metals', *J Mater Process Technol*, vol. 241, pp. 64–72, Mar. 2017, doi: 10.1016/j.jmatprotec.2016.10.024.

[116] B. H.-J. K. B. H. F. R. and C. W. Johannes Aegerter, 'Tensile Testing: Initial Experience from the Practical Implementation of the New Standard', Marl, Germany, 2011.

[117] M. G. de Miranda Salustre, T. B. Gonoring, J. B. R. Martins, H. D. A. Lopes, and M. T. D. A. Orlando, 'Study of steel matrix composite samples with 12%Wt TiB2 produced by spark plasma sintering', *Mater Chem Phys*, vol. 302, no. March, pp. 1–9, 2023, doi: 10.1016/j.matchemphys.2023.127736.

[118] K. Tanaka and T. Saito, 'Phase equilibria in TiB2-reinforced high modulus steel', *Journal of Phase Equilibria*, vol. 20, no. 3, pp. 207–214, 1999, doi: 10.1361/105497199770335730.

[119] D. Bhattacharya, 'Microalloyed Steels for the Automotive Industry', *Tecnol Metal Mater Min*, vol. 11, no. 4, pp. 371–383, 2014, doi: 10.4322/tmm.2014.052.

[120] J. Adamczyk, 'Development of the microalloyed constructional steels', *Journal of Achievements in Materials and Manufacturing Engineering*, vol. 14, no. 1, pp. 9–20, 2006.

[121] S. Kato, T. Kano, M. Hobo, Y. Yamada, T. Miyazawa, and Y. Okada, 'Development of microalloyed steel for fracture split connecting rod', *SAE Technical Papers*, no. 724, 2007, doi: 10.4271/2007-01-1004.

[122] B. Dutta and C. M. Sellars, 'Strengthening of austenite by niobium during hot rolling of Microalloyed steel', no. August, 2016, doi: 10.1179/026708386790123521.

[123] 'ThermoCalc 2023', Dec. 01, 2023, *MDPI AG*. doi: 10.3390/ma12234006.

[124] K. Tanaka, 'Ultra High Modulus Steel Reinforced with Titanium Boride Particles', *R&D Review of Toyota CRDL*, vol. 35, no. 1, p. 2000, 2000.

[125] M. Sadhasivam, N. Mohan, S. R. Sankaranarayanan, and S. P. K. Babu, 'Investigation on mechanical and tribological behaviour of titanium diboride reinforced martensitic stainless steel', *Mater Res Express*, vol. 7, no. 1, pp. 0–13, 2019, doi: 10.1088/2053-1591/ab6488.

[126] W. J. Liu, J. Li, C. Bin Shi, and X. D. Huo, 'Effect of Boron and Titanium Addition on the Hot Ductility of Low-Carbon Nb-Containing Steel', *High*

Temperature Materials and Processes, vol. 34, no. 8, pp. 813–820, 2015, doi: 10.1515/htmp-2014-0145.

[127] C. Baron, H. Springer, and D. Raabe, 'Efficient liquid metallurgy synthesis of Fe-TiB2 high modulus steels via in-situ reduction of titanium oxides', *Mater Des*, vol. 97, pp. 357–363, 2016, doi: 10.1016/j.matdes.2016.02.076.

[128] M. T. Postek, A. E. Vladár, J. S. Villarrubia, and A. Muto, 'Comparison of electron imaging modes for dimensional measurements in the scanning electron microscope', *Microscopy and Microanalysis*, vol. 22, no. 4, pp. 768–777, Aug. 2016, doi: 10.1017/S1431927616011430.

[129] S. Mengaroni, M. Calderini, G. Napoli, C. Zitelli, and A. Di Schino, 'Micro-alloyed steel for forgings', *Materials Science Forum*, vol. 941, pp. 1603–1606, 2018, doi: 10.4028/www.scientific.net/MSF.941.1603.

[130] K. Rane and N. Dhokey, 'On the formation and distribution of in situ synthesized tib2 reinforcements in cast aluminium matrix composites', *Journal of Composites Science*, vol. 2, no. 3, pp. 1–11, 2018, doi: 10.3390/jcs2030052.

[131] M. Sadhasivam, S. Raman Sankaranarayanan, and S. P. Kumaresh Babu, 'Synthesis and characterization of TiB2 reinforced AISI 420 stainless steel composite through vacuum induction melting technique', in *Materials Today: Proceedings*, 2019, pp. 2550–2558. doi: 10.1016/j.matpr.2020.03.385.

[132] B. H. Li, Y. Liu, L. He, H. Cao, S. J. Gao, and J. Li, 'Fabrication of in situ TiB2 reinforced steel matrix composite by vacuum induction melting and its microstructure and tensile properties', *International Journal of Cast Metals Research*, vol. 23, no. 4, pp. 211–215, 2010, doi: 10.1179/136404609X12580240348974.

[133] K. I. Parashivamurthy, R. K. Kumar, S. Seetharamu, and M. N. Chandrasekharaiah, 'Review on TiC reinforced steel composites', 2001.

[134] R. Chen, B. Li, and K. Xu, 'Effect of particle morphology on fatigue crack propagation mechanism of TiB2-reinforced steel matrix composites', *Eng Fract Mech*, vol. 274, Oct. 2022, doi: 10.1016/j.engfracmech.2022.108752.

[135] B. Li *et al.*, 'On the fatigue crack propagation mechanism of a TiB2-reinforced high-modulus steel', *Compos B Eng*, vol. 190, Jun. 2020, doi: 10.1016/j.compositesb.2020.107960.

[136] R. Chen *et al.*, 'Revealing the fatigue crack initiation mechanism of a TiB2-reinforced steel matrix composite', *Int J Fatigue*, vol. 130, Jan. 2020, doi: 10.1016/j.ijfatigue.2019.105276.

[137] A. H. Meysami, R. Ghasemzadeh, S. H. Seyedein, and M. R. Aboutalebi, 'An investigation on the microstructure and mechanical properties of direct-

quenched and tempered AISI 4140 steel', *Mater Des*, vol. 31, no. 3, pp. 1570–1575, Mar. 2010, doi: 10.1016/j.matdes.2009.09.040.

[138] H. Qi, X. Zhou, J. Li, Y. Hu, and L. Xu, 'Performance testing and rapid solidification behavior of stainless steel powders prepared by gas atomization', *Materials*, vol. 14, no. 18, Sep. 2021, doi: 10.3390/ma14185188.

[139] R. Yamanoglu, W. Bradbury, E. A. Olevsky, and R. M. German, 'Sintering and microstructure characteristics of 42CrMo4 steel processed by spark plasma sintering', *Metals and Materials International*, vol. 19, no. 5, pp. 1029–1034, 2013, doi: 10.1007/s12540-013-5015-1.

[140] G. Krauss, *Solidification, Segregation, and Banding in Carbon and Alloy Steels*, vol. 34B. Metallurgical and Materials Transactions B, 2003.

[141] A. Salomon, M. Emmel, S. Dudczig, D. Rafaja, and C. G. Aneziris, 'Dynamic, in situ generated interfaces between carbon-bonded alumina filters and steel during spark plasma sintering/field-assisted sintering', *Adv Eng Mater*, vol. 15, no. 12, pp. 1235–1243, 2013, doi: 10.1002/adem.201300119.

[142] R. Yamanoglu, W. Bradbury, E. A. Olevsky, and R. M. German, 'Sintering and microstructure characteristics of 42CrMo4 steel processed by spark plasma sintering', *Metals and Materials International*, vol. 19, no. 5, pp. 1029–1034, 2013, doi: 10.1007/s12540-013-5015-1.

[143] S. Jin Oh, J. H. Jun, M.-H. Lee, I.-J. Shon, and S. J. Lee, 'Microstructure and Mechanical Properties of Highly Alloyed FeCrMoVC Steel Fabricated by Spark Plasma Sintering', *Metals and Materials International*, vol. 24, pp. 597–603, 2018, [Online]. Available: www.jsw.co.jp

[144] S. Chanthapan, A. Kulkarni, J. Singh, C. Haines, and D. Kapoor, 'Sintering of tungsten powder with and without tungsten carbide additive by field assisted sintering technology', *Int J Refract Metals Hard Mater*, vol. 31, pp. 114–120, 2012, doi: 10.1016/j.ijrmhm.2011.09.014.

[145] K. Vanmeensel, A. Laptev, J. Hennicke, J. Vleugels, and O. Van Der Biest, 'Modelling of the temperature distribution during field assisted sintering', *Acta Mater*, vol. 53, no. 16, pp. 4379–4388, Sep. 2005, doi: 10.1016/j.actamat.2005.05.042.

[146] N. S. Weston and M. Jackson, 'FAST-forge − A new cost-effective hybrid processing route for consolidating titanium powder into near net shape forged components', *J Mater Process Technol*, vol. 243, pp. 335–346, 2017, doi: 10.1016/j.jmatprotec.2016.12.013.

[147] H. U. Kessel *et al.*, *" FAST " field assisted sintering technology- a new process for the production of metallic and ceramic sintering materials*, no. October 2015. 2008.

[148] A. Mukhopadhyay, T. Venkateswaran, and B. Basu, ‘Spark plasma sintering may lead to phase instability and inferior mechanical properties: A case study with TiB2’, *Scr Mater*, vol. 69, no. 2, pp. 159–164, 2013, doi: 10.1016/j.scriptamat.2013.02.027.

[149] K. Feng, Y. Yang, M. Hong, J. Wu, and S. Lan, ‘Intensified sintering of iron powders under the action of an electric field: Effect of technologic parameter on sintering densification’, *J Mater Process Technol*, vol. 208, no. 1–3, pp. 264–269, 2008, doi: 10.1016/j.jmatprotec.2007.12.117.